Investigation of Photomechanical Surface Patterning in Azobenzene Materials

Kevin G. Yager

A thesis submitted to McGill University in partial fulfilment of the requirements for the degree of

Doctor of Philosophy

Department of Chemistry,
McGill University, Montreal
Quebec, Canada

Your file Votre référence
ISBN: 978-0-494-32254-3
Our file Notre référence
ISBN: 978-0-494-32254-3

Abstract

Detailed modeling and experiments were conducted in order to elucidate the nature of photo-induced surface patterning in azobenzene materials. Using a cellular automaton simulation, it was established that both the absolute temperature rise, and the thermal gradient, in a film during patterning are negligibly small. These results, confirmed experimentally by patterning samples on substrates of differing thermal conductivity, eliminate purely thermal mechanisms as candidate explanations for mass transport. The length-scale of patterning was probed by monitoring the formation and thermal erasure of gratings as a function of film thickness. In both cases, film dynamics deviate from bulk behavior when film thickness decreases below ~150 nm. Moreover, mass transport is completely hindered below 40 nm. This deviation of polymer dynamics implies that photo-induced mass transport involves the coordinated motion of many polymer chains in the depth of the material, and not merely surface diffusion of individual chains.

Neutron reflectometry was applied to measure in detail the photomechanical response of azobenzene materials. A significant photo-expansion effect, up to 17%, was observed at 25°C, attributed to the molecular free volume requirement of azo isomerization. Above a well-defined crossover temperature, which occurs at ~50°C for poly(disperse red 1 acrylate), the material response is inverted. At these elevated temperatures, photo-contraction effects, of more than –15%, were instead measured. In this case the combination of photo-induced motion and thermally-enabled mobility enables aggregation, aromatic stacking, and crystallization of the azobenzene dipoles. Using localized surface patterning experiments, it was confirmed that the mass transport phenomenon exhibits the same trend and phase relationship as the photomechanical effect. It is argued that the fundamental origin of surface mass transport in azo materials is in fact this newly identified photomechanical effect. This suggestion enables explanation of a variety of previously contradictory results in the literature.

Résumé

L'origine de la photo-fabrication des structures topographiques dans les matériaux azobenzene a été élucidée en utilisant des modèles et expériences. En utilisant une simulation cellulaire d'automate, il a été établi que pendant l'irradiation, l'élévation de température absolue ainsi que le gradient thermique du film, sont assez petits pour être négligés. Ces résultats, confirmés expérimentalement par illumination d'échantillons assemblés sur des substrats ayant différentes propriétés thermiques, peuvent être utilisés éliminer les mécanismes uniquement thermiques comme explication de la formation de structures topographiques. Les propriétés spatiales du processus ont été déterminées en surveillant la formation et l'effacement thermique des structures topographiques, en fonction de l'épaisseur du film. Dans les deux cas, les dynamiques du film dévient du comportement macroscopique quand l'épaisseur de film est dessous ~150 nm. En plus, le processus topographique est complètement arrêté dans les films <40 nm. Cette déviation des dynamiques de polymère indique que le transport de matière, causé par la lumière, exige le mouvement coordonné de plusieurs chaînes de polymère dans la profondeur du matériel, et non seulement par la diffusion de chaînes sur la surface de ce deriner.

La réflectométrie de neutron a été utilisée pour mesurer la réaction photomécanique des matériaux d'azobenzene. Une photo-expansion à 25°C, allant jusqu'à 17%, a été observée, et attribuée au volume moléculaire nécessaire pour l'isomérisation d'azobenzene. Au-dessus d'une température bien résolue, par exemple à ~50°C pour le poly (disperse red 1 acrylate), la réaction du matériel est inversée. À ces températures plus élevées, un effet de photo-contraction, de plus de –15%, a été mesuré. Dans ce cas, la combinaison du mouvement causé par la lumière et la mobilité thermique permet l'agrégation, l'empilement aromatique, et la cristallisation des dipôles d'azobenzene. En fabriquant des structures topographiques de façon localisée, il a été confirmé que le phénomène de photo-fabrication a la même tendance et phase que l'effet photomécanique. Il est alors proposé que l'origine fondamentale de la photo-fabrication est en fait un phénomène photomécanique. Cette hypothèse permet l'explication d'une variété de résultats dans la littérature qui était auparavant contradictoires.

Foreword

This dissertation is based upon a review chapter, a review paper, and five original research papers. The review chapter and review paper have been published, and form the basis of the introduction. The first two research papers have also been published in scientific journals. The last three research chapters are based upon papers that have been submitted for publication to peer-reviewed scientific journals. The last chapter of the thesis provides perspectives on future directions of the research program.

Contribution of Authors

All papers presented in the thesis were entirely written by Kevin Yager. All papers were co-authored with Prof. Christopher J. Barrett (Department of Chemistry, McGill University), who acted as research advisor. All of the research presented in this dissertation was planned, performed, and critically analyzed by the author. For the work presented in two of the chapters, technical assistance was provided by co-authors, as described below.

Chapter 1 is a thorough review of the field of study, and is based upon a book chapter and a review article, both of which were entirely researched and written by the author, with guidance from Prof. Christopher J. Barrett. The book chapter has been published in a volume entitled "Light-Induced Nanostructure Formation using Azobenzene Polymers," and the review article appears in the *Journal of Photochemistry and Photobiology A*.

Chapter 2 is an experimental chapter, whose objective is to describe the details of a unique sample cell built specifically for experiments conducted at the Canadian Neutron Beam Centre (National Research Council, Canada) Chalk River Laboratories. The cell in question was designed and built by Mike Watson at the NRC, in consultation with experimental requirements described by the author. The cell was then tested and validated in a first series of experiments conducted at Chalk River Laboratories, where Dr. Helmut Fritzsche acted as a local contact. These experiments were conducted by the author, with the technical assistance of Oleh M. Tanchak. The data analysis and all

writing for the paper were conducted entirely by the author. The results of this analysis were published in *Review of Scientific Instruments* in 2006.

Chapter 3 describes temperature modeling initiated and performed by the author under the supervision of Prof. Christopher J. Barrett. The author performed all computer programming, data analysis, and the manuscript preparation required for this project. The work was published in *Journal of Chemical Physics* in 2004.

Chapter 4 describes a series of pattern erasure experiments conducted by the author at the suggestion of Prof. Christopher J. Barrett. The sample preparation, experiments, data analysis and manuscript writing were all performed by the author.

Chapter 5 is a neutron reflectometry study. The experiments in question were performed at the Canadian Neutron Beam Centre (NRC, Canada), using the sample cell already mentioned. The work was done in collaboration with Dr. Helmut Fritzsche at the NRC, who provided instrument training. The experiments were performed by the author, with technical assistance from Oleh M. Tanchak and Chris Godbout. The extensive data analysis, interpretation of results, and the final manuscript preparation were all conducted solely by the author.

Chapter 6 is a patterning study conducted by the author. Experimental design, data interpretation, and manuscript writing were performed solely by the author, with guidance from Christopher J. Barrett.

I hereby give copyright clearance for the inclusion of the following manuscripts, of which I am a co-author, in the dissertation of Kevin G. Yager.

Yager, K.G.; Barrett, C.J. "Light-Induced Nanostructure Formation using Azobenzene Polymers" Chapter 8 in *Polymeric Nanostructures and their Applications*, Nalwa, H.S., ed. American Scientific Publishers, **2006**, Los Angeles. ISBN: 1-58883-068-3

Yager, K.G.; Barrett, C.J. "Novel Photoswitching using Azobenzene Functional Materials" *Journal of Photochemistry and Photobiology A: Chemistry* **2006**, *published online 23 May.*

Yager, K.G.; Barrett, C.J. "Temperature Modeling of Laser-Irradiated Azo Polymer Films" *Journal of Chemical Physics* **2004**, *120*, 1089.

Yager, K.G.; Tanchak, O.M.; Barrett, C.J.; Watson, M.J.; Fritzsche, H. "Temperature-controlled neutron reflectometry sample cell suitable for study of photoactive thin films" *Review of Scientific Instruments* **2006**, *77*, 045106.

Yager, K.G.; Barrett, C.J. "Confinement of Surface Patterning in Azo-Polymer Thin Films" *Macromolecules* **2006**, *submitted.*

Yager, K.G.; Tanchak, O.M.; Godbout, C.; Fritzsche, H.; Barrett, C.J. "Photomechanical Effects in Azo-Polymers Studied by Neutron Reflectometry" *Macromolecules* **2006**, *submitted.*

Yager, K.G.; Barrett, C.J. "Photomechanical Surface Patterning in Azo-Polymer Materials" *Macromolecules* **2006**, *submitted.*

Professor Christopher J. Barrett
Department of Chemistry
McGill University
Quebec, Canada

July 28 '06

Date

Acknowledgments

This thesis represents not only a contribution to science, but also a testament to my growth as a scientist and person. My education over the course of my doctoral work did not occur in a vacuum, and I owe a tremendous thanks to all the people who helped me complete this project. The entire Department of Chemistry helped create a stimulating and enriching environment, where my talents could flourish and be recognized. Professors Lennox and Ronis, who acted as departmental chairs during my doctoral work, deserve considerable credit in this regard. I also wish to thank my committee members, Professors Eisenberg and Wiseman, who monitored my progress and provided critical insights. I will fondly remember Professor Gray's influence, which runs from lively scientific discussion to canoeing at the cottage. I am also indebted to Dr. Wilczek, who contributed considerably to my development as a teacher and academic.

Other students in the department helped make my stay at McGill enjoyable and rewarding. Susan, Annie, Rashida, Hassan, and more recently Chris and Mehul, were always fun to have around. A special thanks to Oleh, with whom I spent more lunchtimes than I care to count. Oleh acted as a sounding board for ideas and frustrations, and will always feature prominently in my memories of graduate school. My collaboration with the Canadian Neutron Beam Centre was extremely fruitful, and I wish to thank all the hardworking people at the NRC. In particular, Dr. Helmut Fritzsche was always helpful and insightful, even when working into the twilight hours.

Critical to the completion of this thesis were the enduring efforts of my thesis supervisor, Professor Chris Barrett. His infectious enthusiasm for science was an asset during the early years, when I was trying to find my way. Throughout my degree, he worked to ensure that I had the resources and opportunities not only to perform high-level research, but also to grow as a scientist. Perhaps most importantly, he always believed in me. Critically, he believed in the quality of my work when even I was not convinced. In short, he gave me a much-needed push to succeed.

I also wish to acknowledge my friends and family, who were unwaveringly supportive of my decisions and unnervingly optimistic about my future. 'The boys' not only helped me by livening my mood, but also by teaching me to know the joy of

enduring hardship. I thank my sister, Nique, a kindred spirit who has never judged, and always understood. I also wish to thank Kira and Kaden, for enriching my life at just the right moment, and my parents, Beverley, Barry, and Antoinette, for always believing in me and always respecting my choices. Importantly, I thank Emily, whose inspiration was itself inspiring, and whose support and commitment were never-ending. I would not have been able to complete my degree without her continual help as a friend and confidant.

Lastly, I wish to thank the society that enabled this research, and my education, to take place. Of course, all of the funding that I received, for living and research, were provided by the people of this country. More important than that, however, is to acknowledge a society that is committed to science and the fundamental pursuit of knowledge. I believe it is critical to our future as a species to pursue knowledge, and share this knowledge widely. I feel exceedingly fortunate to have grown up in a society that also values these ideals, and hope that I can carry on this noble tradition.

Table of Contents

Chapter 2: Temperature-Controlled Neutron Reflectometry Sample Cell Suitable for Study of Photoactive Thin Films

Chapter 3: Temperature Modeling of Laser-Irradiated Azo-Polymer Thin Films

Chapter 4: Confinement of Surface Patterning in Azo-Polymer Thin Films

Chapter 5: Photomechanical Effects in Azo-Polymers Studied by Neutron Reflectometry

Chapter 1
Introduction

This chapter provides a thorough introduction to the research related to azobenzene photochemistry and photo-motions. It is based upon a published book chapter, with inclusion of more recent literature review contained in a published article. The text from the two sources is reprinted, with permission, from:

Yager, K.G.; Barrett, C.J. "Light-Induced Nanostructure Formation using Azobenzene Polymers" Chapter 8 in *Polymeric Nanostructures and their Applications*, Nalwa, H.S., ed. American Scientific Publishers, **2006**, Los Angeles. ISBN: 1-58883-068-3. Copyright 2006 American Scientific Publishers.

and

Yager, K.G.; Barrett, C.J. "Novel Photoswitching using Azobenzene Functional Materials" *Journal of Photochemistry and Photobiology A: Chemistry* **2006**, *in press, published online 23 May.* Copyright 2006, Elsevier.

1.1. Preamble

The formation of useful nanostructures, and interfacing these with macro-world devices, is an ongoing research challenge. The microelectronics industry has a wide variety of optical tools available for patterning using light, and has achieved remarkable control over material properties. It is therefore attractive to investigate future patterning techniques that take advantage of this visible-light lithographic infrastructure. Azobenzene molecules exhibit numerous photo-responsive properties, which can be exploited to locally modify material properties. Specifically, irradiation of azobenzenes with light causes a fast and efficient change of the molecule's configuration. This photo-isomerization can be exploited as a photoswitch, to orient the chromophore (which induces birefringence), or even to perform all-optical surface topography patterning. These photo-motions enable many interesting applications, ranging from optical components and lithography to sensors and smart materials.

This chapter will discuss the many unique properties of the azobenzene chromophore, and the exceptional material control enabled when these chromophores are

incorporated in a polymeric matrix. More specifically, we will attempt to highlight the ways in which azo-polymers could be used as tools in the emerging field of controlled nanostructure formation.

1.2. Azobenzene

Azobenzene is an aromatic molecule formed by an azo linkage (–N=N–) connecting two phenyl rings. In this text, as in most on the subject, we use 'azobenzene' and 'azo' in a more general way: to refer to the class of compounds that exhibit the core azobenzene structure, with different ring substitution patterns (even though, strictly, these compounds should be referred to as 'diazenes'). There are many properties common to nearly all azobenzene molecules. The most obvious is the strong electronic absorption of the conjugated π system. The absorption spectrum can be tailored, via the ring substitution pattern, to lie anywhere from the ultraviolet to the visible-red region. It is not surprising that azobenzenes were originally used as dyes and colorants.[1,2] The geometrically rigid structure and large aspect ratio of azobenzene molecules makes them ideal mesogens: azobenzene small molecules and polymers functionalized with azobenzene can exhibit liquid crystalline phases.[3,4] The most startling and intriguing characteristic of the azobenzenes is their highly efficient and fully reversible photo-isomerization. Azobenzenes have two stable isomeric states: a thermally stable *trans*

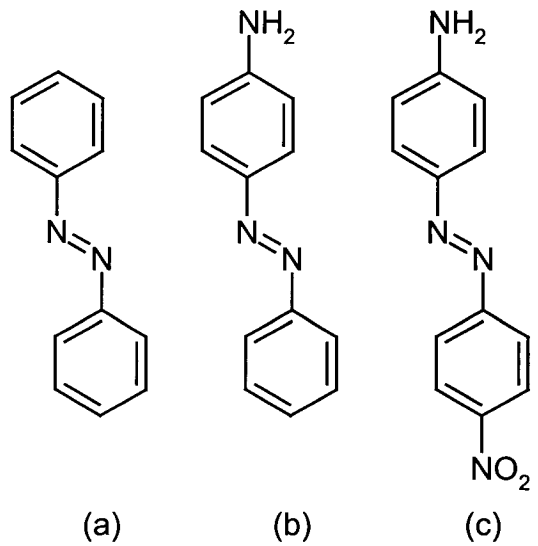

Figure 1.1: Examples of azo molecules classified as (a) azobenzenes, (b) aminoazobenzenes, and (c) pseudo-stilbenes.

configuration, and a meta-stable *cis* form. Remarkably, the azo chromophore can interconvert between these isomers upon absorption of a photon. For most azobenzenes, the molecule can be optically isomerized from *trans* to *cis* with light anywhere within the broad absorption band, and the molecule will subsequently thermally relax back to the *trans* state on a timescale dictated by the substitution pattern. This clean photochemistry is central to azobenzene's potential use as a tool for nanopatterning.

1.2.1 Azobenzene Chromophores

Azobenzenes can be separated into three spectroscopic classes, well described by Rau:[5] azobenzene-type molecules, aminoazobenzene-type molecules, and pseudo-stilbenes (refer to Figure 1.1 for examples). The particulars of their absorption spectra (shown in Figure 1.2) give rise to their prominent colors: yellow, orange, and red, respectively. Many azos exhibit absorption characteristics similar to the unsubstituted azobenzene archetype. These molecules exhibit a low-intensity $n \rightarrow \pi^*$ band in the visible region, and a much stronger $\pi \rightarrow \pi^*$ band in the UV. Although the $n \rightarrow \pi^*$ is symmetry-forbidden for *trans*-azobenzene (C_{2h}), vibrational coupling and some extent of nonplanarity make it nevertheless observable.[6]

Adding substituents to the azobenzene rings may lead to minor or major changes

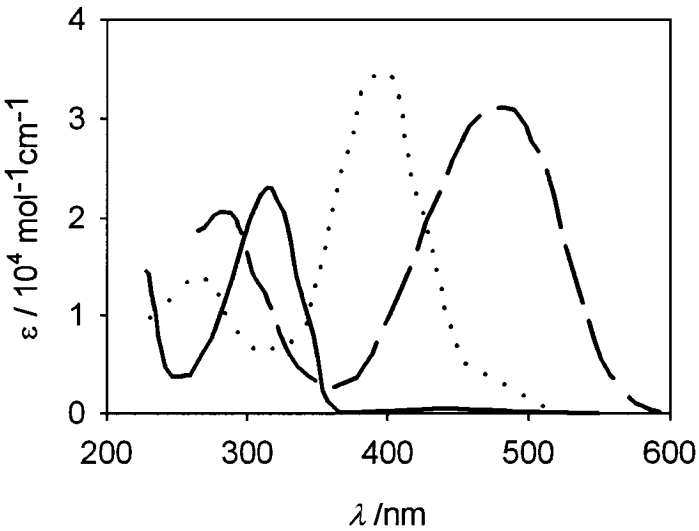

Figure 1.2: Schematic of typical absorbance spectra for *trans*-azobenzenes. The azobenzene-type molecules (solid line) have a strong absorption in the UV, and a low-intensity band in the visible (barely visible in the graph). The aminoazobenzenes (dotted line) and pseudo-stilbenes (dashed line) typically have strong overlapped absorptions in the visible region.

in spectroscopic character. Of particular interest is ortho- or para- substitution with an electron-donating group (usually an amino, $-NH_2$), which results in a new class of compounds. In these aminoazobenzenes, the $n \rightarrow \pi^*$ and $\pi \rightarrow \pi^*$ bands are much closer. In fact, the $n \rightarrow \pi^*$ may be completely buried beneath the intense $\pi \rightarrow \pi^*$. Whereas azobenzenes are fairly insensitive to solvent polarity, aminoazobenzene absorption bands shift to higher energy in nonpolar solvents, and shift to lower energy in polar solvents. Substituting azobenzene at the 4 and 4′ positions with an electron-donor and an electron-acceptor (such as an amino and a nitro, $-NO_2$, group) leads to a strongly asymmetric electron distribution (often referred to as a 'push/pull' substitution pattern). This shifts the $\pi \rightarrow \pi^*$ absorption to lower energy, towards the red and past the $n \rightarrow \pi^*$. This reversed ordering of the absorption bands defines the third spectroscopic class, the pseudo-stilbenes (in analogy to stilbene, phenyl–C=C–phenyl). The pseudo-stilbenes are very sensitive to local environment, which can be useful in some applications.

Especially in condensed phases, the azos are also sensitive to packing and aggregation. The π-π stacking gives rise to shifts of the absorption spectrum. If the azo dipoles have a parallel (head-to-head) alignment, they are called J-aggregates, and give rise to a red-shift of the spectrum (bathochromic) as compared to the isolated chromophore. If the dipoles are antiparallel (head-to-tail), they are called H-aggregates, and lead to a blue-shift (hypsochromic). Fluorescence is seen in some aminoazobenzenes and many pseudo-stilbenes, but not in azobenzenes, whereas phosphorescence is absent in all three classes. By altering the electron density, the substitution pattern necessarily affects the dipole moment, and in fact all the higher-order multipole moments. This becomes significant in many non-linear optical (NLO) studies. For instance, the chromophore's dipole moment can be used to orient with an applied electric field (poling), and the higher-order moments of course define the molecule's non-linear response.[7] In particular, the strongly asymmetric distribution of the delocalized electrons that results from push/pull substitution results in an excellent NLO chromophore.

1.2.2 *Azobenzene Photochemistry*

Key to some of the most intriguing results and interesting applications of azobenzenes is the facile and reversible photo-isomerization about the azo bond, converting between the *trans* (E) and *cis* (Z) geometric isomers (Figure 1.3). This photo-

isomerization is completely reversible and free from side reactions, prompting Rau to characterize it as "one of the cleanest photoreactions known."[5] The *trans* isomer is more stable by approximately 50 kJ/mol,[8,9] and the energy barrier to the photo-excited state (barrier to isomerization) is on the order of 200 kJ/mol.[10] Thus, in the dark, most azobenzene molecules will be found in the *trans* form. Upon absorption of a photon (with a wavelength in the *trans* absorption band), the azobenzene will convert, with high efficiency, into the *cis* isomer. A second wavelength of light (corresponding to the *cis* absorption band) can cause the back-conversion. These photo-isomerizations usually have picosecond timescales.[11,12] Alternately, azos will thermally reconvert from the *cis* to *trans* state, with a timescale ranging from milliseconds to hours, depending on the substitution pattern and local environment. More specifically, the lifetimes for azobenzenes, aminoazobenzenes, and pseudo-stilbenes are usually on the order of hours, minutes, and seconds, respectively. The energy barrier for thermal isomerization is on the order of 90 kJ/mol.[13,14] Considerable work has gone into elongating the *cis* lifetime, with the goal of creating truly bistable photo-switchable systems. Bulky ring substituents can be used to hinder the thermal back reaction. For instance, a polyurethane main-chain azo exhibited a lifetime of 4 days (thermal rate-constant of $k = 2.8\times10^{-6}$ s^{-1}, at 3°C),[15] and an azobenzene para-substituted with bulky pendants had a lifetime of 60 days ($k < 2\times10^{-7}$ s^{-1}, at room temperature).[16] The conformational strain of macrocylic azo compounds can

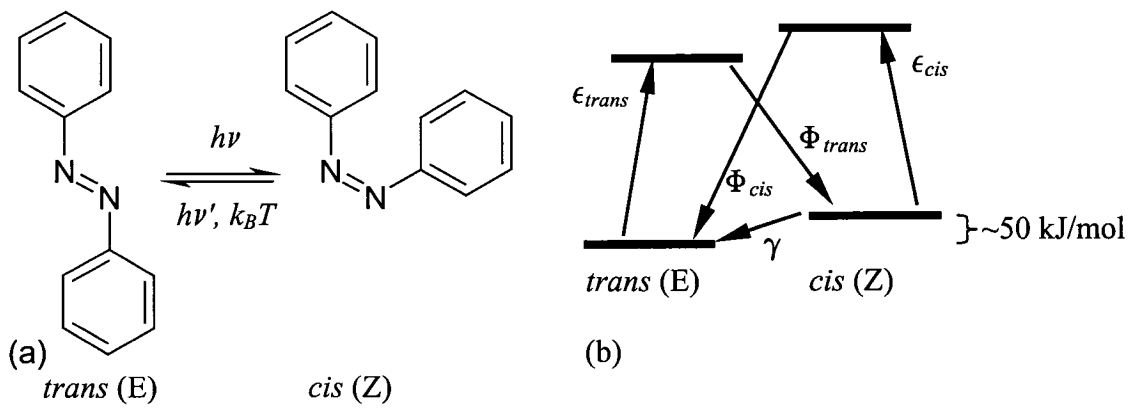

Figure 1.3: (a) Azobenzene can convert between *trans* and *cis* states photochemically, and relaxes to the more stable *trans* state thermally. (b) Simplified state model for azobenzenes. The *trans* and *cis* extinction coefficients are denoted ϵ_{trans} and ϵ_{cis}. The Φ refer to quantum yields of photoisomerization, and γ is the thermal relaxation rate constant.

also be used to lock the *cis* state, where lifetimes of 20 days ($k = 5.9\times10^{-7}$ s^{-1}),[17] 1 year (half-life 400 days, $k = 2\times10^{-8}$ s^{-1}),[18,19] or even 6 years ($k = 4.9\times10^{-9}$ s^{-1})[20] were observed. Similarly, using the hydrogen-bonding of a peptide segment to generate a cyclic structure, a *cis* lifetime of ~40 days ($k = 2.9\times10^{-7}$ s^{-1}) was demonstrated.[21] Of course, one can also generate a system that starts in the *cis* state, and where isomerization (in either direction) is completely hindered. For instance, attachment to a surface,[22] direct synthesis of ring-like azo molecules,[23] and crystallization of the *cis* form[24,25] can be used to maintain one state, but such systems are obviously not bistable photo-switches.

A bulk azo sample or solution under illumination will achieve a photostationary state, with a steady-state *trans*/*cis* composition based on the competing effects of photo-isomerization into the *cis* state, thermal relaxation back to the *trans* state, and possibly *cis* reconversion upon light absorption. The steady-state composition is unique to each system, as it depends on the quantum yields for the two processes (Φ_{trans} and Φ_{cis}) and the thermal relaxation rate constant. The composition also depends upon irradiation intensity, wavelength, temperature, and the matrix (gas phase, solution, liquid crystal, sol-gel, monolayer, polymer matrix, etc.). Azos are photochromic (their color changes upon illumination), since the effective absorption spectrum (a combination of the *trans* and *cis* spectra) changes with light intensity. Thus absorption spectroscopy can be conveniently used to measure the *cis* fraction in the steady-state,[26,27] and the subsequent thermal relaxation to an all-*trans* state.[28-31] NMR spectroscopy can also be used.[32] Under moderate irradiation, the composition of the photostationary state is predominantly *cis* for azobenzenes, mixed for aminoazobenzenes, and predominantly *trans* for pseudo-stilbenes. In the dark, the *cis* fraction is below most detection limits, and the sample can be considered to be in an all-*trans* state. Isomerization is induced by irradiating with a wavelength within the azo's absorption spectrum, preferably close to λ_{max}. Modern experiments typically use laser excitation with polarization control, delivering on the order of 1–100 mW/cm^2 of power to the sample. Various lasers cover the spectral range of interest, from the UV (Ar^+ line at 350 nm), through blue (Ar^+ at 488 nm), green (Ar^+ at 514 nm, YAG at 532 nm, HeNe at 545 nm), and into the red (HeNe at 633 nm, GaAs at 675 nm).

The ring substitution pattern affects both the *trans* and the *cis* absorption spectra, and for certain patterns, the absorption spectra of the two isomers overlap significantly (notably for the pseudo-stilbenes). In these cases, a single wavelength of light effectuates both the forward and reverse reaction, leading to a mixed stationary state, and continual interconversion of the molecules. For some interesting azobenzene photo-motions, this rapid and efficient cycling of chromophores is advantageous, whereas in cases where the azo chromophore is being used as a switch, it is clearly undesirable.

The mechanism of isomerization has undergone considerable debate. Isomerization takes place either through a rotation about the N–N bond, with rupture of the π bond, or through inversion, with a semi-linear and hybrizidized transition state, where the π bond remains intact (refer to Figure 1.4). The thermal back-relaxation is agreed to be via rotation, whereas for the photochemical isomerization, both mechanisms appear viable.[33] Historically the rotation mechanism (as necessarily occurs in stilbene) was favored for photo-isomerization, with some early hints that inversion may be contributing.[34] More recent experiments, based on matrix or molecular constraints to the azobenzene isomerization, strongly support inversion.[35-38] Studies using picosecond

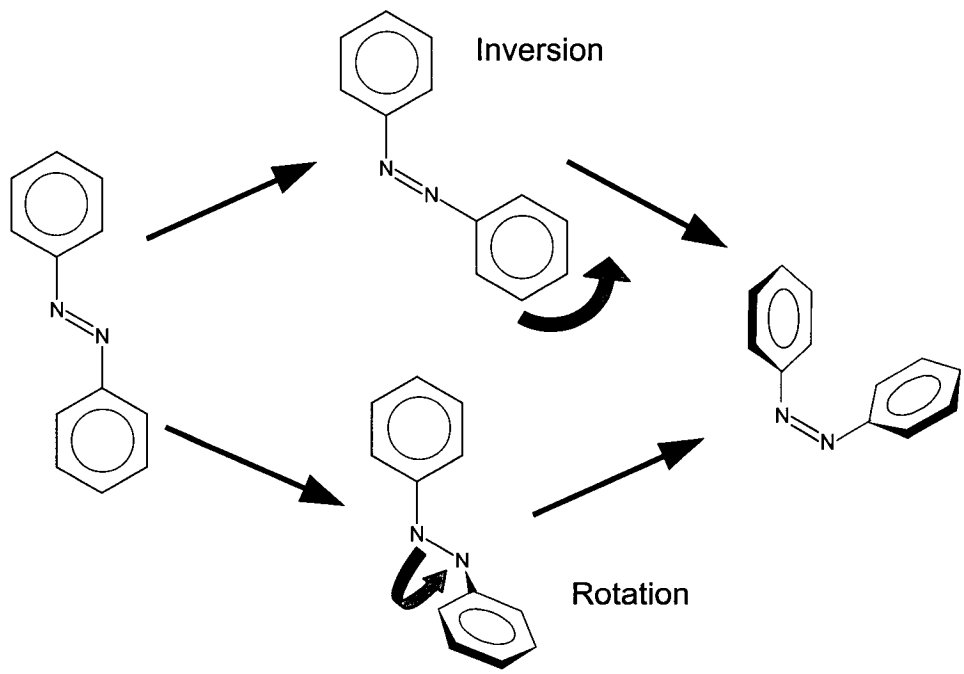

Figure 1.4: The mechanism of azobenzene isomerization proceeds either via rotation or inversion. The *cis* state has the phenyl rings tilted at 90° with respect to the CNNC plane.

Raman and femtosecond fluorescence show a double bond (N=N) in the excited state, confirming the inversion mechanism.[39,40] By contrast, Ho et al.[41] found evidence that the pathway is compound-specific: a nitro-substituted azobenzene photo-isomerized via the rotation pathway. Furthermore, ab initio and density functional theory calculations indicate that both pathways are energetically accessible, although inversion is preferred.[42,43] Thus, both mechanisms may be competing, with a different one dominating depending on the particular chromophore and environment. The emerging consensus nevertheless appears to be that inversion is the dominant pathway for most azobenzenes.[44] The availability of the inversion mechanism explains how azos are able to isomerize easily even in rigid matrices, such as glassy polymers, since the inversion mechanism has a much smaller free volume requirement than the rotation.

The thermal back-relaxation is generally first-order, although a glassy polymer matrix can lead to anomalously fast decay components,[45-48] attributed to a distribution of chromophores in highly strained configurations. Higher matrix crystallinity increases the rate of decay.[49] The decay rate itself can act as a probe of local environment and molecular conformation.[50,51] The back-relaxation of azobenzene is acid-catalyzed,[52] although strongly acidic conditions will lead to side-reactions.[25] For the parent azobenzene molecule, quantum yields (which can be indirectly measured spectroscopically[45,53,54]) are on the order of 0.6 for the $trans \rightarrow cis$ photo-conversion, and 0.25 for the back photo-reaction. Solvent has a small effect, increasing the $trans \rightarrow cis$ and decreasing the $cis \rightarrow trans$ yield as polarity increases.[55] Aminoazobenzenes and pseudo-stilbenes isomerize very quickly and can have quantum yields as high as 0.7–0.8.

1.2.3 Azobenzene Systems

Azobenzenes are robust and versatile moieties, and have been extensively investigated as small molecules, pendants on other molecular structures, or incorporated (doped or covalently bound) into a wide variety of amorphous, crystalline, or liquid crystalline polymeric systems. Noteworthy examples include self-assembled monolayers and superlattices,[56] sol-gel silica glasses,[57] and biomaterials.[58-60] A number of small molecules incorporating azobenzene have been synthesized, including crown-ethers,[61] cyclodextrins,[62,63] proteins such as bacteriorhodopsin,[64] and 3D polycyclics such as

cubane[65] and adamantane.[66] Typically, azo chromophores are embedded in a solid matrix for studies and devices. As a result, matrix effects are inescapable: the behavior of the chromophore is altered due to the matrix, and in turn the chromophore alters the matrix.[67] Although either could be viewed as a nuisance, both are in fact useful: the chromophore can be used as a probe of the matrix (free volume, polarizability, mobility, etc.), and when the matrix couples to chromophore motion, molecular motions can be translated to larger lengthscales. Thus, the incorporation strategy is critical to exploiting azobenzene's unique behavior.

1.2.3.1 Thin Polymer Films

Doping azobenzenes into polymer matrices is a convenient inclusion technique.[68,69] These 'guest–host' systems can be cast or spin-coated from solution mixtures of polymer and azo small molecules, where the azo content in the thin film is easily adjusted via concentration. Although doping leaves the azo chromophores free to undergo photo-induced motion unhindered, it has been found that many interesting photomechanical effects do not couple to the matrix in these systems. Furthermore, the azo mobility often leads to instabilities, such as phase-separation or micro-crystallization. Thus, one of the most attractive methodologies for incorporating azobenzene into functional materials is by covalent attachment to polymers. The resulting materials benefit from the inherent stability, rigidity, and processability of polymers, in addition to

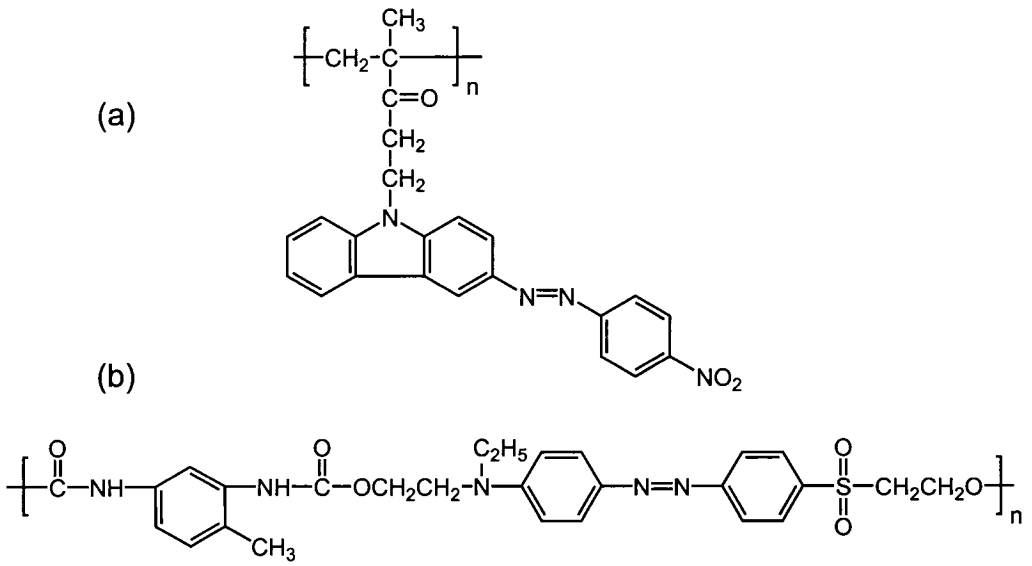

Figure 1.5: Examples of azo-polymer structures, showing that both (a) side-chain and (b) main-chain architectures are possible.

the unusual photo-responsive behavior of the azo moieties. Both side-chain and main-chain azobenzene polymers have been prepared[70] (Figure 1.5). Reported synthetic strategies involve either polymerizing azobenzene-functionalized monomers[71,72] or post-functionalizing a polymer that has an appropriate pendant group (usually a phenyl).[73-75] The first method is preferred for its simplicity and control of sequence distribution. The second takes advantage of commonly available starting materials, but may require more reaction steps. Many different backbones have been used as scaffolds for azo moieties, including imides,[76] esters,[77] urethanes,[78] ethers,[79] organometallic ferrocene polymers,[80] dendrimers,[81,82] and even conjugated polydiacetylenes,[83] polyacetylenes,[84] and main-chain azobenzenes.[85,86] The most common azo-polymers are acrylates,[87] methacrylates,[88] and isocyanates.[89] Thin films are usually prepared by spin-coating,[90-93] although there are also many examples of using solvent evaporation, the Langmuir-Blodgett technique,[94-97] and self-assembled monolayers.[98] Spin-cast films are typically annealed above the polymer glass-transition temperature (T_g) to remove residual solvent and erase any hydrodynamically-induced anisotropy. Recently molecular glasses have been investigated as alternatives to amorphous polymer systems.[99] These monodisperse systems appear to maintain the desirable photomotions and photoswitching properties, while allowing precise control of molecular architecture and thus material properties.[100]

1.2.3.2 Liquid Crystals

Azobenzenes are anisotropic, rigid molecules, and as such are ideal candidates to act as mesogens: molecules that form liquid crystalline (LC) mesophases. Many examples of small-molecule azobenzene liquid crystals have been studied. Some azo-polymers also form LC phases (refer to Figure 1.6 for a typical structure). For side-chain azobenzenes, a certain amount of mobility is required for LC phases to be present; as a rule, if the tether between the chromophore and the backbone is less than 6 alkyl units long, the polymer will exhibit an amorphous and isotropic solid-state phase, whereas if the spacer is longer, LC phases typically form. The photo-isomerization of azobenzene leads to modification of the phase and alignment (director) in LC systems.[67,101] The director of a liquid crystal phase can be modified by orienting chromophores doped into the phase,[102,103] by using an azobenzene-modified 'command surface,'[104-106] using azo copolymers,[107] and, of course, in pure azobenzene LC phases.[108,109] One can force the LC

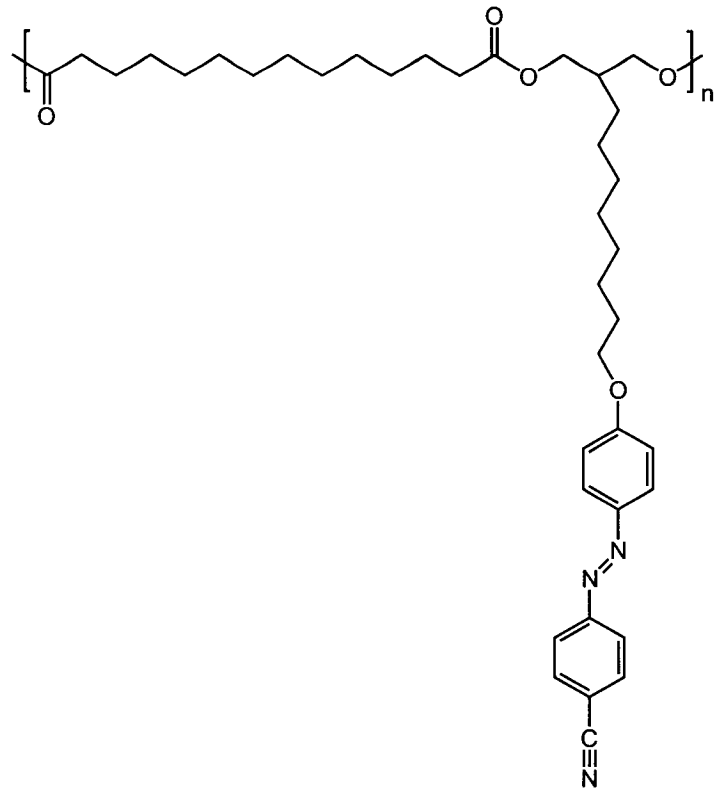

Figure 1.6: A typical liquid-crystalline side-chain azobenzene polymer.

phase to adopt an in-plane order (director parallel to surface), homeotropic alignment (director perpendicular to surface), tilted or even biaxial orientation.[110] These changes are fast and reversible. While the *trans* azobenzenes are excellent mesogens, the *cis* azos typically are not. If even a small number of azo molecules are distributed in an LC phase, *trans* → *cis* isomerization can destabilize the phase by lowering the nematic-to-isotropic phase transition temperature.[111] This enables fast isothermal photo-control of phase transitions.[44,112-114] Since these modulations are photo-initiated, it is straightforward to create patterns.[115] These LC photoswitching effects are obviously attractive in many applications, such as for display devices, optical memories,[104] electro-optics,[116] modulating the polarization of ferroelectric liquid crystals,[117,118] etc.

1.2.3.3 Dendrimers

Dendrimers have been investigated as unique structures to exploit and harness azobenzene's photochemistry.[119-121] Dendritic and branched molecular architectures can have better solubility properties and can be used to control undesired aggregation, resulting in higher-quality films for optical applications.[122,123] Dendrimers with strongly

absorbing pendants can act as antenna: harvesting light and making it available, via intramolecular energy transfer, to the dendrimer core. In dendrimers with azo cores, this allows for the activation of isomerization using a wavelength outside of the azo absorption band (since the dendrimer arms absorb and transfer energy to the core).[124,125] Furthermore the configurational change that results from the core isomerization will translate into a larger-scale geometric change. For instance, in a dendrimer with three azobenzene arms (Figure 1.7), the various isomerization combinations (EEE, EEZ, EZZ, and ZZZ) could all be separated by thin-layer chromatography due to their different physical properties.[126] The conformational change associated with isomerization modifies (typically reduces) the hydrodynamic volume, with the specific extent of conformational change depending strongly on where the azo units are incorporated.[127]

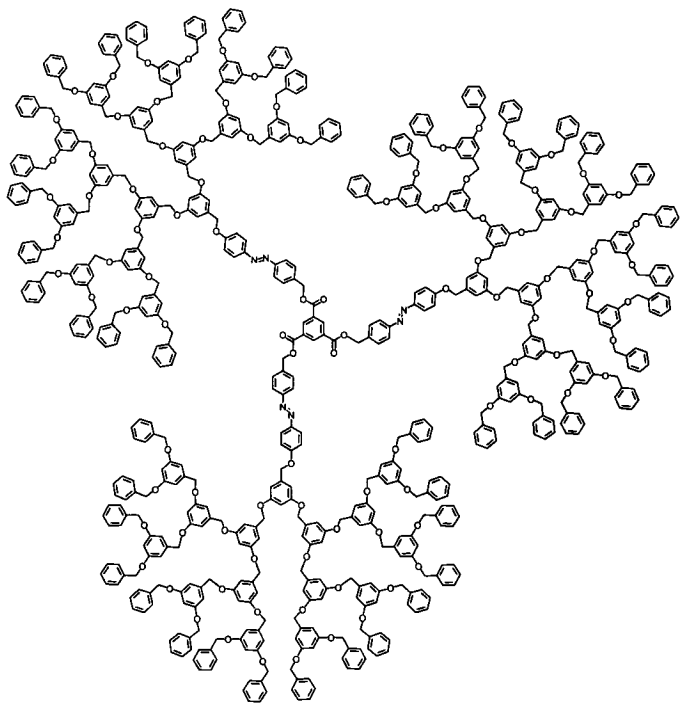

Figure 1.7: An azobenzene dendrimer containing three azo moieties. Each chromophore has two isomerization states (*trans* and *cis*), leading to four distinct photo-isomers for the dendrimer molecule. All four isomers have different physical properties.

1.2.3.4 Polyelectrolyte Multilayers

A new facile and versatile film preparation technique, layer-by-layer electrostatic self-assembly, has become the subject of intensive research since its introduction by Decher.[128-131] In this technique, a charged or hydrophilic substrate is immersed in a solution of charged polymers (polyelectrolytes), which adsorb irreversibly onto the substrate. After rinsing, the substrate is then immersed in a solution containing a polyelectrolyte of opposite charge, which adsorbs electrostatically to the charged polymer monolayer. Because each layer of adsorbed polymer reverses the surface charge, one can build up an arbitrary number of alternating polycation-polyanion layers. These polyelectrolyte multilayers (PEMs) are easy to prepare, use benign (all-aqueous) chemistry, and are inherently tunable.[132-134] Specifically, by adjusting the ionic strength[135-138] or pH[139-142] (in the case of 'weak' polyelectrolytes) of the assembly solution, the polyelectrolyte chain conformation is modified, and hence the resulting film architecture is tuned. For instance, one can control thickness,[136,143] permeability,[144] morphology,[145-147] and density.[148] Recently the technique has been modified to assemble the alternate layers using a spin-coater, which reduces the assembly times and adsorption solution volumes considerably.[149-152]

As a film preparation technique, this method has numerous advantages. The adsorption of the polymers is quasi-thermodynamic, with the chains adsorbing into a local minimum, which makes the films stable against many defects (dewetting, pinhole formation, etc.). Importantly, the technique is not limited to flat surfaces: any geometry that can be immersed in solution (or have solution flowed-through) is suitable. Colloids have been efficiently coated with PEMs,[153,154] and by dissolving the core one can also form hollow PEM micro-capsules.[155] Multilayers can be formed on nearly any material (glass, quartz, silicon, most metals, etc.), and are robust against thermal and solvent treatment.[156] One of the main interests in PEMs is due to their inherent biocompatibility:[157] multilayers have been formed on enzyme microcrystals,[158] used to encapsulate living cells,[159] and to coat arterial walls.[160] Perhaps the most useful feature of the multilayering technique is its ability to incorporate secondary functional groups into the thin film structure. The location of these functional units (which may be small molecules, pendants on the polyelectrolyte chains, or particles) within the multilayer

stack can be controlled with sub-nanometer precision. A wide variety of functionalities have been demonstrated, including organic molecules,[161] synthetic polymers,[162] biopolymers,[163] natural proteins,[164] colloids,[165] inorganic nanoparticles,[166] clay platelets[167] (used as a nacre biomimic[168]), dendrimers,[169] electrochemically active species,[132] functionalized C_{60},[170] and even, counter-intuitively, uncharged and non-polar polymer chains.[171]

Many research groups have investigated the possibility of incorporating optically-responsive azobenzene chromophores into the versatile PEM structures (examples presented in Figure 1.8), including Advincula,[172-175] Kumar and Tripathy,[162,176] Tieke,[177-180] Heflin,[181] and Barrett.[182,183] In some cases, copolymers are synthesized, where some of the repeat units are charged groups, and some are azo chromophores.[184,185] These materials may, however, have solubility issues, as the azo chromophore is typically not water-soluble. Efforts have therefore gone into synthesizing azo-ionomers,[186,187] or polymers where the charge appears on the azobenzene unit.[185,188,189] The azobenzene chromophore may also be created by post-functionalization of an assembled PEM.[176] Azobenzene-functionalized PEMs have demonstrated all of the unique photophysics associated with the chromophore, including induced birefringence,[174,190] and surface mass transport[188] (which will be described in more detail in section 4). It should be noted, however, that in general the quality of the patterning is lower,[189] presumably due to the

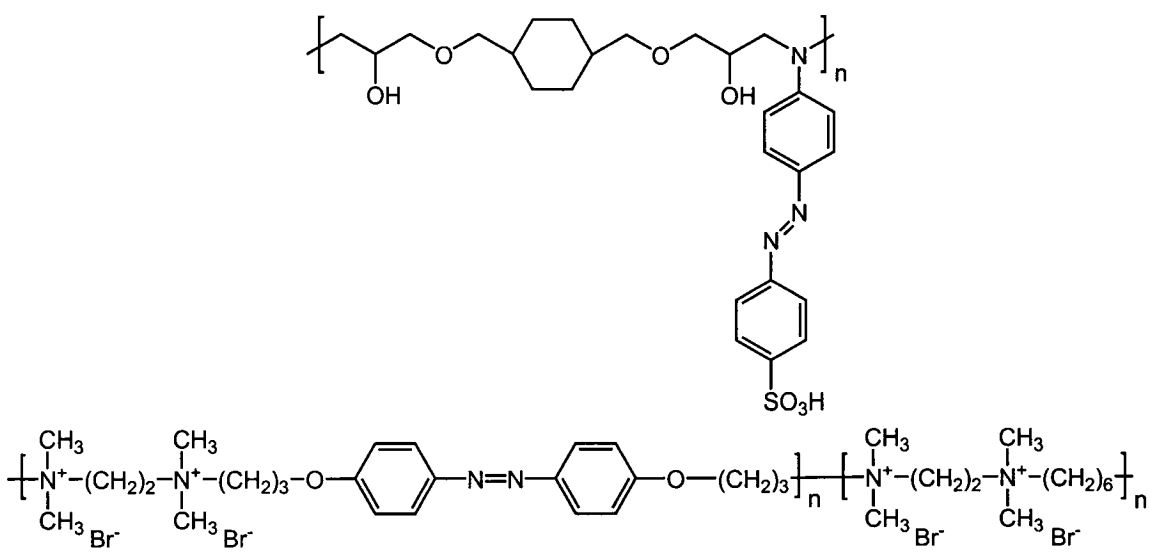

Figure 1.8: Examples of water-soluble azo-polyelectrolytes, which can be used in the preparation of photoactive polyelectrolyte multilayers.

constraints to chain motion that the ionic 'crosslinks' engender. There are many examples of performing the multilayering with a polyelectrolyte and a small molecule azobenzene ionic dye.[148] In contrast to conventional doped systems, the chromophores in these systems do not suffer from aggregation instabilities,[172] and the azo photo-motions do couple to the matrix, as evidenced by birefringence[191,192] and surface patterning.[161,193] These effects can again be attributed to the fact that the ionic attachment points act as crosslinks in a dry PEM sample. The aggregation and photochemical behavior of the azo chromophore (absorbance spectrum, isomerization rate, etc.) vary depending on the nature of the counter-polymer[194] (and of course, is affected by any ionic ring substituent). These may be viewed as undesirable matrix effects, or as a way to tune the chromophore response. The multilayering technique does not offer the precision and reproducibility of conventional inorganic film preparation techniques. It is, however, simple, versatile, and offers the possibility of combining unique structures and functionalities (for instance, it has been used to create superhydrophobic surfaces,[195] to make azo-photochromic hollow shells,[187] and is amenable to patterning[196]). While it is unlikely to replace established techniques for high-performance devices, it may find applications in certain niches (coatings, disposable electronics, biomedical devices, etc.).

1.3. Photoinduced Motions and Modulations

Irradiation with light produces molecular changes in azobenzenes, and under appropriate conditions, these changes can translate into larger-scale motions and even modulation of material properties. Following Natansohn and Rochon,[197] we will describe motions roughly in order of increasing size-scale. However, since the motion on any size-scale invariably affects (and is affected by) other scales, clear divisions are not possible. In all cases, some of the implicated applications, photoswitching, and photo-modulations will be outlined.

1.3.1 Molecular Motion

The fundamental molecular photo-motion in azobenzenes is the geometrical change that occurs upon absorption of light. In *cis*-azobenzene, the phenyl rings are twisted at 90° relative to the C–N=N–C plane.[36,198] Isomerization reduces the distance between the 4 and 4′ positions from 0.99 nm in the *trans* state to 0.55 nm for the *cis*

state.[199-201] This geometric change increases the dipole moment: whereas the *trans* form has no dipole moment, the *cis* form has a dipole moment of 3.1 D.[24] The free volume requirement of the *cis* is larger than the *trans*,[202] and it has been estimated that the minimum free volume pocket required to allow isomerization to proceed via the inversion pathway[36,46] is 0.12 nm^3, and via the rotation pathway[15] approximately 0.38 nm^3. The effects of matrix free volume constraints on photochemical reactions in general have been considered.[203] The geometrical changes in azobenzene are very large, by molecular standards, and it is thus no surprise that isomerization modifies a wide host of material properties.

This molecular displacement generates a nanoscale force, which has been measured in single-molecule force spectroscopy experiments,[204,205] and compared to theory.[206] In these experiments, illumination causes contraction of an azobenzene-polymer, showing that each chromophore can exert pN molecular forces on demand. A pseudo-rotaxane that can be reversibly threaded-dethreaded using light has been called an "artificial molecular-level machine."[207,208] The ability to activate and power molecular-level devices using light is of course attractive, since it circumvents the limitations inherent to diffusion or wiring. The fast response and lack of waste products in azo isomerization are also advantageous. Coupling these molecular-scale motions to do useful work is of course the next challenging step. Progress in this direction is evident from a wide variety of molecular switches that have been synthesized. For example, an azo linking two porphyrin rings enabled photo-control of electron transfer.[209] In another example, dramatically different hydrogen-bonding networks (intermolecular and intramolecular) can be favored based on the isomeric state of the azo group linking two cyclic peptides.[21,210]

1.3.2 Photobiological Experiments

The molecular conformation change of the azo chromophore can be used to switch the conformation, and hence properties, of larger molecular systems to which it is attached. This is particularly interesting in the case of inclusion within molecular-scale biological systems. The bridging of biology and physical chemistry is an ever-expanding research domain. It is no surprise that the clean and unique azo photochemistry has been applied to switching biological systems.[59] One of the earliest investigations of

azobenzene in a biological context involved embedding azobenzene molecules into a model membrane system.[211] Upon isomerization, the lamella were disrupted and rearranged, which also changed the enzymatic activity of membrane-bound proteins. The catalytic activity of a cyclodextrin with a histidine and azobenzene pendant was photo-controllable because the *trans* version of the azo pendant can bind inside the cyclodextrin pocket, whereas the *cis* version liberated the catalytic site.[212] Photo-regulation of polypeptide structure has been an active area of research,[213] with the azobenzenes making significant contributions. Azo-modified poly (L-alanine),[58,214] poly(L-glutamic acid)[215,216] and poly(L-lysine),[217] among others, have been prepared. Depending on the system, photo-isomerization may cause no change,[216] or can induce a substantial conformational change, including transitions from ordered chiral helix to disordered achiral chain,[218-220] changes in the α-helix content, or even reversible α-helix to β-sheet conversions.[221] Also, owing to the change in local electrostatic environment, the pK_a of the polypeptides can be controlled in these systems.

Covalent attachment of azobenzene units to enzymes can modify protein activity by distorting the protein structure with isomerization. This was used to control the enzyme activity of papain[222,223] and the catalytic efficiency of lysozyme.[224] A different methodology is to immobilize the protein of interest inside a photo-isomerizable copolymer matrix, which was used to control α-chymotrypsin.[223,225,226] The azobenzene need not be directly incorporated into an enzyme of interest. In one case, the activity of tyrosinase could be modified by isomerization of small-molecule azo inhibitors.[227] The photo-selective binding of short peptide fragments into enzymes can be used to inhibit, thus control, activity.[228,229] Similarly, the binding of an azo-peptide with a monoclonal antibody was found to be photo-reversible.[230] The photo-response of azobenzene can thus be used to control the availability of key biomolecules. In one case, NAD^+ was modified with an azobenzene group, and introduced into a mixture with an antibody that binds to the *trans* form.[231] This binding makes NAD^+ unavailable, whereas irradiation of the solution with UV light induces the *trans* to *cis* isomerization, and thereby liberates NAD^+.

Bioengineering has more recently been broadened by expanding the natural protein alphabet with artificial amino acids. This enables novel and non-natural protein

sequences to be created, while still exploiting the highly efficient natural synthesis machinery. Chiral azobenzene amino acids have been synthesized, and incorporated into protein sequences.[232] The introduction of artificial photoactive residues opens the possibility of photo-control of biological processes. For instance, *E. coli* variants were selectively evolved that would incorporate azobenzene amino acids into proteins, which enabled photo-control of protein binding in that organism.[233] For instance, photo-control of the binding affinity of a transcription factor to its promoter, allowed for, in essence, light-control of gene expression in the organism. In another case, a (negatively charged) hydrophilic azobenzene amino acid was incorporated into a restriction enzyme, and enabled control of activity with light.[234,235] Specifically, the *trans* azo residue was positioned at the dimer interface, and disrupted association, whereas in the *cis* state, the proteins could aggregate and exhibit normal biological activity. It has also been suggested that the rapid switching of azobenzene could be used as a 'molecular shuttle' for electron transduction in enzyme systems.[236] In effect, this would mean that light could be efficiently used to alter behaviour in yet another class of enzymes. Incorporation of azobenzene into DNA is another interesting way to control biological systems. In one case, the duplex of modified DNA could be reversibly switched,[237] since the *trans* azobenzene intercalates between base pairs, and helps bind the two strands of the double helix together, whereas the *cis* azobenzene disrupted the duplex.[238] By incorporating an azobenzene unit into the promoter region of an otherwise normal DNA sequence, it was possible to photo-control gene expression.[239] In this case, the *trans* versus *cis* states of the azo unit have different interactions with the polymerase enzyme.

These experiments suggest an overall strategy to control biological systems using light. A complex biochemical pathway can be controlled by photo-regulating the activity or availability of a key biomolecule. This allows one to turn a biological process on and off at will, using light. The use inside living organisms is obviously more complicated, but one can reasonably easily apply these principles to control biological processes in industrially relevant settings. The ability to quickly and cleanly switch biological activity using a short light pulse may find application in new microfluidic devices, which need to be able to address specific device regions, and may rely upon natural molecular machinery to carry out certain tasks. Azobenzenes present unique opportunities in the

biological sciences for studying complex biological systems, in addition to controlling them. A bacteriorhodopsin analogue with a central azobenzene molecule, rather than the retinal, was prepared as a model system for studying rhodopsin.[64] As expected, the azobenzene molecule did not interact as favourably with the protein host as strongly as the natural retinal. Despite this, the azo molecules could be coupled into the protein (in the absence of retinal), and led to significant shifts in the physicochemical properties of the complex. Moreover, the azo molecule could be used as a probe of the inner protein domain (sensing pH, for instance). A particularly elegant experiment involved using azobenzenes to monitor protein folding.[240,241] Femtosecond two-dimensional infrared (2D IR) spectroscopy was used as a gauge of the distances between carbonyl groups in the peptide. An azobenzene chromophore, incorporated inside the polypeptide chain, acted as the photoswitch, initiating a conformational change, hence initiating protein folding, on demand. Simultaneous time-resolved measurements of the azo spectra allowed determination of the folding dynamics. This unique measurement of protein folding behaviour was possible because of the photo-triggering nature of the azo unit. Ultrafast laser pulse experiments are being used to study a large number of chemical reactions, providing detail not before possible. This technique is, however, obviously limited to systems where the chemical events can be photo-triggered. By incorporating azobenzene units into new systems, one can generate a photo-triggerable system from an otherwise photo-inactive one. This strategy can thus be applied to a wide range of problems in chemical dynamics, with biological systems being obvious targets.

1.3.3 Photo-Orientation

Azobenzene chromophores can be oriented using polarized light,[67,242] via a statistical selection process, described schematically in Figure 1.9. Azobenzenes preferentially absorb light polarized along their transition dipole axis (long axis of the azo molecule). The probability of absorption varies as $\cos^2\phi$, where ϕ is the angle between the light polarization and the azo dipole axis. Thus, azos oriented along the polarization of the light will absorb, whereas those oriented against the light polarization will not. For a given initial angular distribution of chromophores, many will absorb, convert into the *cis* form, and then revert to the *trans* form with a new random direction. Those chromophores that fall perpendicular to the light polarization will no longer isomerize

and reorient; hence, there is a net depletion of chromophores aligned with the light polarization, with a concomitant increase in the population of chromophores aligned perpendicular (i.e.: orientation hole burning). This statistical reorientation is fast, and gives rise to strong birefringence (anisotropy in refractive index) and dichroism (anisotropy in absorption spectrum) due to the large anisotropy of the azo electronic system. The process is especially efficient due to the mesogen-like cooperative motion that the azobenzene groups facilitate, even in amorphous samples below T_g.[107] Since the process requires cycling of the chromophores between *trans* and *cis* states, the pseudo-stilbenes have the fastest response.

The orientation due to polarized light is reversible. The direction can be modified by using a new polarization direction for the irradiating light. Circularly polarized light will randomize the chromophore orientations. It must be emphasized, however, that there

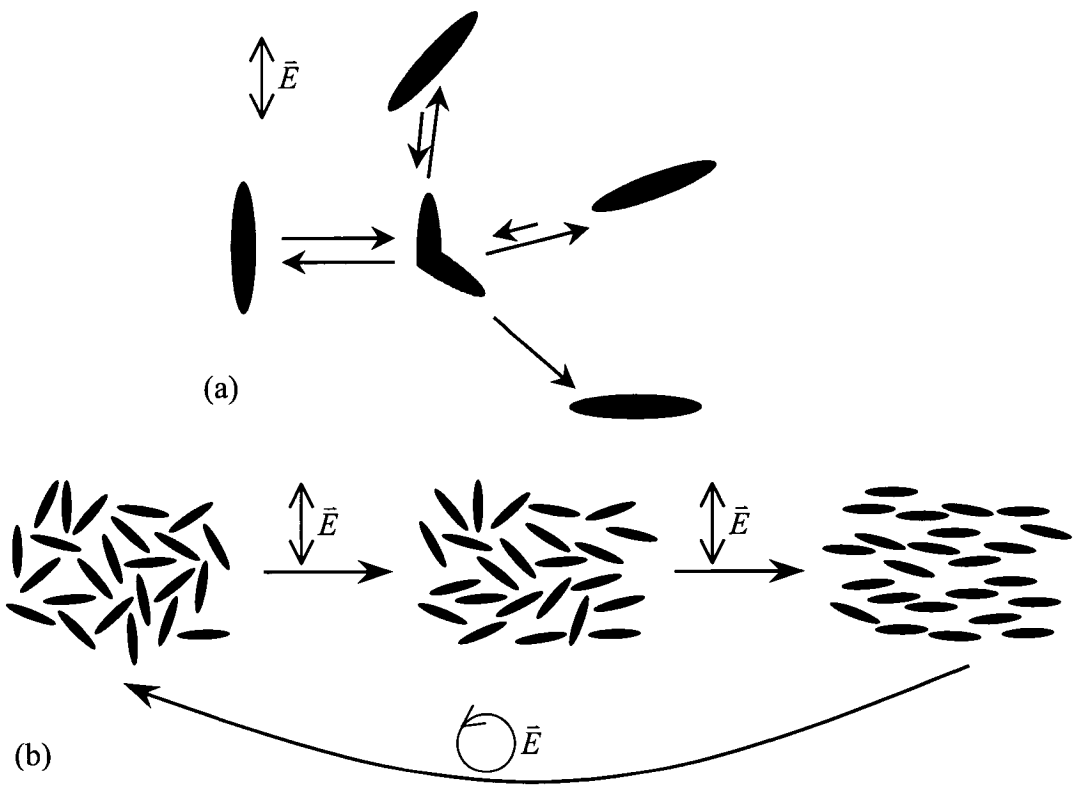

Figure 1.9: Statistical photo-orientation of azo molecules. (a) The molecules aligned along the polarization direction of the incident light absorb, isomerize, and re-orient. Those aligned perpendicular cannot absorb and remain fixed. (b) Irradiation of an isotropic samples leads to accumulation of chromophores in the perpendicular direction. Circularly polarized light restores isotropy.

is another preferential alignment direction during irradiation: along the axis of the incoming light. It is unavoidable that chromophores will efficiently build-up aligned along the irradiation axis, but this is often ignored in the literature, or characterized as 'photo-bleaching' when in fact it is a reversible photo-alignment (albeit one that reduces the absorbance as viewed by any photo-probe). Because unpolarized light can photo-orient (along the axis of illumination),[93] even sunlight is suitable. The motion of the sun through the sky over the course of a day can cause orientation at different tilt angles.[243] This causes chromophores at different depths to be oriented in different directions, which produces a net chiral helical ordering in the film of a particular handedness (based on the hemisphere in which the experiment is performed). The implications of such results to the origin of absolute chirality in biological systems are intriguing.

1.3.3.1 Birefringence

Irradiation with light polarized in the *y*-direction will lead to net alignment of chromophores in the *x*-direction. As a result, the refractive index probed in the *x*-direction, n_x, will measure the azo long axis, and will be larger than n_y. Birefringence is the anisotropy in refractive index: $\Delta n = n_x - n_y$. Photo-alignment in azobenzene systems can achieve extremely high values of Δn, up to 0.3–0.5 at ~633 nm.[244,245] Importantly, very high birefringence values can be obtained far outside of the azo absorption band, which means that the birefringence can be utilized/measured without disturbing the chromophores. An in-plane isotropic state ($n_x = n_y$) can be restored by irradiation with circularly polarized light, and a fully isotropic state can be obtained by heating above the glass-transition temperature.

The exact nature of the orientation can be rigorously quantified using optical techniques. Using surface plasmon resonance spectroscopy or waveguide spectroscopy, the three orthogonal refractive indices in an oriented sample can be measured.[246] Stokes polarimetry can be used to fully characterize the optical anisotropy, separating linear and circular components.[247] The anisotropy of the *cis* population during irradiation can also be measured in some systems,[248,249] where it is found that, as with *trans*, there is an enrichment perpendicular to the irradiation polarization. In some LC systems, however, it may occur that the *cis* population preferentially aligns with the irradiating polarization (which may be attributed to an optical Fréedericksz transition).[250]

The birefringence can be written and erased hundreds of thousands of times, which is important technologically.[251] Amorphous polymer systems with relatively high glass-transition temperatures exhibit good temporal stability of any induced orientation. Upon heating, some order will be lost, with full isotropy restored after heating past T_g. A short spacer between the chromophore and the polymer backbone slows the growth of birefringence yet promotes stability, owing to hindered motion. Surprisingly, main-chain azos can achieve high levels of birefringence, indicating relatively high polymer mobility.[252-254] As might be expected, (nanosecond) pulsed experiments lead to thermal effects, which enhance chromophore motion, and thereby induced greater birefringence, at the same net dose, compared to continuous-wave (cw) experiments.[255,256] At very high pulsed fluence, the thermal effects were too great, and erased the induced birefringence.

The easily inscribed and erased birefringence has a number of unique applications. Most readily, it can be used to create wave-plates,[257] and polarization filters, which can be used to separate right-handed from left-handed circularly polarized light.[258] The strong refractive index contrast, if patterned into a line, can serve as a channel waveguide.[259,260] This offers the unique possibility of optical devices that can be patterned, erased, and reused. In principle, these photonic circuits could be altered during device operation, enabling optical routing of optical signals (i.e.: optical computing). The switching of orientational order can thus be used as an all-optical switch.[261] By illuminating an azo sample with a spatially varying light pattern, birefringence gratings can also be formed.[262-264] These are phase gratings, as opposed to amplitude gratings, and diffract light based on spatial variation of the refractive index. This is the essence of holography: two interfering coherent beams generate a spatially varying light pattern, which is encoded into the material. Under illumination of the material with one of the beams, the diffraction reproduces the other encoded beam. In the case of liquid crystal samples, light induces a spatial pattern of nematic and isotropic zones (which have different refractive indices). These holographic phase grating can be rapidly formed, erased, and switched.[265]

1.3.3.2 Non-Linear Optics

The requirements for non-linear optical (NLO) response in any material is an asymmetric (strictly, anharmonic) response of the electronic system. Pseudo-stilbenes,

which have push/pull substituents, have a strongly asymmetric electron distribution, which makes them ideal NLO molecules (see, for instance, Figure 1.10). For a bulk NLO response, one requires an overall non-centrosymmetric material. This requirement is achieved in many inorganic crystals. In organic systems, the broken symmetry is typically obtained by applying an electric field at a temperature sufficient to allow for the molecular dipoles to align with the field. This process is called electric field poling, and is accomplished using interdigitated or flat electrodes, or a sharp charged needle (or grid) held above a grounded sample (called corona poling). The NLO response is typically quantified using second-harmonic generation (SHG; the emission of light at double the frequency of the incident beam), the electrooptic effect (change of refractive index upon application of an electric field), or wave mixing experiments (where various frequencies of light can be synthesized or enhanced). These also constitute the main applications of NLO materials: they can be used to synthesize new frequencies of light, to electrically switch a beam, or to allow two beams of light to interact and couple (which can form the basis of an all-optical switch).[266]

Azo-polymers have been shown to be excellent NLO materials.[7,267-269] In azo

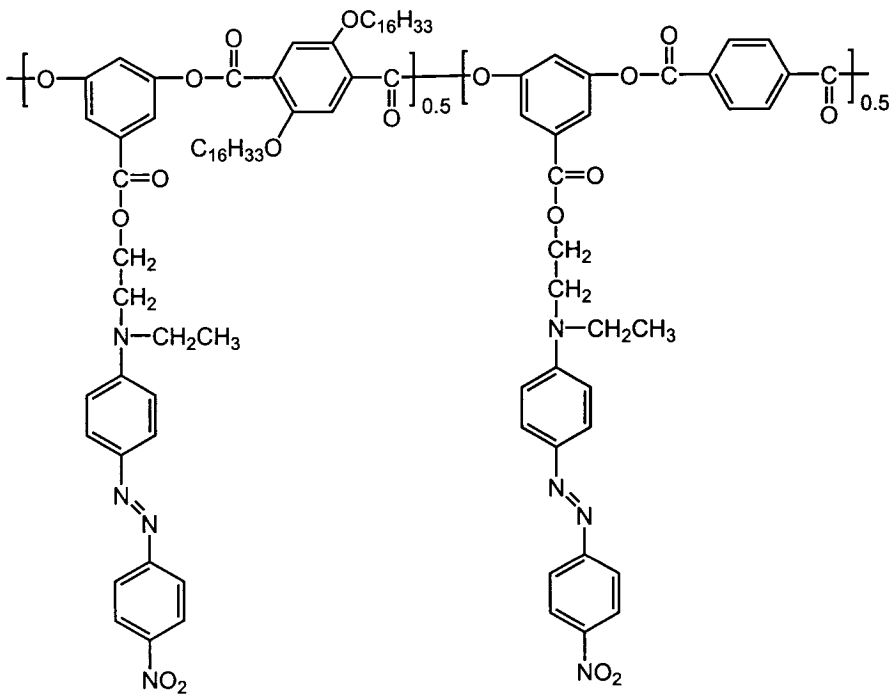

Figure 1.10: Example of a non-linear optic azo-polymer, used for photo-assisted poling.

systems, one has the additional advantage of using light to affect the chromophores. Although photo-alignment orients the chromophore axis, it does not select out a preferred direction for the molecular dipole (thus, an equal number of dipoles point 'left' and point 'right'). In fact, evidence suggests that dipoles in these systems tend to orient antiparallel (H-aggregates),[270,271] thereby canceling polar order. Nevertheless, the photo-alignment can be used to facilitate the electric poling, enabling it to be performed at room temperature and with a small dc field.[272-275] Furthermore, by using polarized light and its harmonic, a net non-centrosymmetry can be obtained in an all-optical process.[276,277] This occurs because the mixture of a primary beam and its second harmonic creates a directional electric field in the material.

Another interesting approach for NLO uses dendrons ('half-dendrimers') with azo functionalities.[278] The dendritic architecture forces all the chromophores within the dendron to align, which strongly enhances the NLO response. The dendron had a first-order molecular hyperpolarizability 20 times larger than the monomer. With regard to applications, the azos have been shown to function as electro-optical switches,[279] and to exhibit photorefraction,[72,280-282] an NLO effect where photoconductivity permits light to establish a space charge grating, whose associated index grating refracts a probe light beam.

1.3.4 Domain Motion

The orientation and reorientation of liquid crystalline domains has already been outlined. The azo chromophores act as mesogens, and their photo-alignment becomes transferred to the LC host. A very small azo content (a few mol%[112]) can lead to orientational control of LC domains. This is an excellent example of amplification of the azo molecular motion. The phase of a liquid crystal can also be switched with light. Irradiation produces *cis* isomers, which are poor mesogens and destabilize the nematic phase, thereby inducing a phase transition to the isotropic state. There are comparatively few examples of photo-triggered increases in LC ordering. In one case, a nanoscale phase separation of the *cis* isomers led to a net increase in the order parameter of the LC phase.[283] In another system, a chiral azo was found to induce a cholesteric phase when it was in the *cis* state.[284]

With liquid crystalline[285] or preoriented amorphous samples,[286] one can photo-induce a chiral domain structure. Incident circularly polarized light becomes elliptically polarized due to the first oriented layer. This ellipse subsequently reorients deeper chromophores, which in turn modify the ellipticity of the light. This reorientation continues throughout the film depth. Overall, a chiral ordering of the chromophore domains is established.[287] Remarkably, one can switch between a right- and left-handed supramolecular helix at will, by changing the incident light handedness. There are many other examples of photo-control of supramolecular order. The pitch of a cholesteric LC can be modified by isomerization.[288] Biomacromolecular variants abound.[59] Azo-modified polypeptides can be photoswitched between ordered states (α-helix or β-sheet) and a random coil.[219,220,289] The duplex of modified DNA can be reversibly switched,[237] and the catalytic activity of histidine can be controlled.[212]

Photo-isomerization can also affect self-assembly behavior at the domain level. On irradiation, one can induce a phase change,[290] a solubility change,[291,292] crystallization,[293] or even reversal of phase separation.[294] The critical micelle concentration (cmc) and surface activity can also be modified.[295] In an amphiphilic polypeptide system, self-assembled micelles were formed in the dark, and could be disaggregated with light.[296] When allowed to assemble as a transmembrane structure, the aggregate could be reversibly formed and destroyed using light, which allowed for reversible photoswitching of ion transport.[297] Related experiments on methacrylates[298,299] and polypeptides[214] showed that a polymer's chiral helix could be reversibly suppressed on irradiation. In a series of polyisocyanate polymers, it could be selected whether irradiation would suppress or increase chirality.[300,301]

1.3.5 *Micron-Scale Motion*

The azos exhibit a unique and remarkable surface-mass transport under light illumination. This optical patterning represents massive material transport at a micrometer and sub-micrometer lengthscale. This mass transport provides a unique opportunity for nanostructure formation, and will be described in detail in section 1.4.

1.3.6 Macroscopic Motion

It is interesting to study whether the azobenzene molecular conformational changes can result in changes to bulk phenomena, or even to macroscopic motion. The first consideration is whether the material expands to an appreciable extent. In monolayers, it is well established that the larger molecular size of the *cis* isomer leads to a corresponding lateral expansion,[302] which can modify other bulk properties. For instance, this allows photo-modulation of a monolayer's water contact angle[303] or surface potential.[304] Using fluorinated azo-polymer, good photo-control[305] and photo-patterning[306] of wettability has been demonstrated. A monolayer of azo-modified calixarene, when irradiated with a light gradient, produced a gradient in surface energy sufficient to move a macroscopic oil droplet,[307] suggesting possible applications in microfluidics. Modest photo-induced contact angle changes for thin polymer films have also been reported.[49] Recently an azobenzene copolymer assembled into polyelectrolyte multilayer showed a modest 2° change in contact angle with UV light irradiation. However, when the same copolymer was assembled onto a patterned substrate, the change in contact angle upon irradiation was enhanced[308] to 70°.[309] That surface roughness plays a role in contact angle is well established, and shows that many systems can be optimized to give rise to a large change in surface properties.

In layered inorganic systems with intercalated azobenzenes, reversible photo-changes in the basal spacing (on the order of 4%) can be achieved.[310,311] In polymer films, there is some evidence that the film thickness increases, as measured by ellipsometry[259] (the refractive index certainly changes,[312] but this is not an unambiguous demonstration of expansion/contraction). Related are experiments that show that external applied pressure tends to hinder photo-isomerization.[313] Photo-contraction for semicrystalline main-chain azos has been measured.[76,314] This photomechanical response presumably occurs because of the shortening of the polymer chains upon *trans* → *cis* conversion. On the other hand, photo-expansion would seem to be contradicted by positron lifetime experiments that suggest no change in microscopic free volume cavity size during irradiation.[315] More conclusive experiments are in order.

The most convincing demonstration of macroscopic motion due to azo isomerization is the mechanical bending and unbending of a free-standing polymer

film.[316,317] The macroscopic bending direction may be selected either with polarized light, or by aligning the chromophores with rubbing. Bending occurs in these relatively thick films because the free surface (which absorbs light) contracts, whereas the interior of the film (which is not irradiated owing to the strong absorption of the upper part of the film) does not contract. Because the direction of bending can be controlled with polarized light, the materials enable full directional photomechanical control.[318] This photomechanical deformation has also been used to drive macroscopic motion of a floating film.[319] That these materials contract (rather than expand) appears again to be related to the main-chain azo groups, and may also be related to the LC nature of the crosslinked gels. For a thin film floating on a water surface, a contraction in the direction of polarized light was seen for LC materials, whereas an expansion was seen for amorphous materials.[320] A related amplification of azo motion to macroscopic motion is the photo-induced bending of a microcantilever coated with an azobenzene monolayer.[321] One can also invert the coupling of mechanical and optical effects: by stretching an elastomeric azo film containing a grating, one can affect its wavelength-selection properties and orient chromophores.[322]

1.3.7 Other Applications of Azobenzenes

1.3.7.1 Photoswitches

As already pointed out, the azo isomerization can be used to photoswitch a wide variety of other properties (at numerous size-scales). In addition to the optical changes already described, it is worth noting that the transient change in material refractive index (due to the different *n* of *cis* and *trans*) can itself act as a photoswitch.[323] The azo photochromism has even been suggested as a possible optical neural network element.[324] Binding and transport properties can also be photoswitched.[91,325] In some systems the redox potential and ionic conductivity can be switched with light.[326] Crown-ethers[327,328] and calixarenes[329] functionalized with azobenzene can be used as reversible ion-binding systems. Thus, ion transport can be photo-regulated. In other cases, the transport properties can be photo-controlled not via binding, but based on changes in pore sizes.[330-332] In a particularly elegant example, the size of nanochannels could be modified by irradiating azo ligands which decorated the channel walls.[333] Azo-derivatized gramicidin

ion channels represent a unique case where ion transport can be photo-controlled by optical manipulation of a biomolecule.[334] In addition to obvious applications in controlled transport, this offers the possibility of studying cells by controlling the timing of ion exchange processes. Photo-induced catalysis is also possible: for instance, using molecules where only the *cis* form is catalytically active.[335] Extension of the molecular imprinting technique to azo-polymers allows for photoswitching of binding activity with respect to the imprinted molecule.[336]

1.3.7.2 Photoprobes

The properties of an azo chromophore (spectrum, isomerization kinetics, etc.) depend strongly on the local environment. This enables the possibility of using the chromophore as a molecular sensing element: a photoprobe. For instance, it has been found that many azo properties depend on local H^+ concentration, to the extent that the azo can in fact be used as a pH meter.[156,337] As already mentioned, the isomerization kinetics can also be used as a probe of free volume,[15,202] local aggregation,[50] or phase transitions. The azo molecule is small and exhibits clean photochemistry, which makes it more versatile and robust than many other photoprobes. The rate of isomerization is also remarkably insensitive to temperature,[338] yet sensitive to local solvent conditions.[50,339] This is an area of research that deserves considerably more attention.

In a more sophisticated example, azo chromophores were used to monitor protein folding.[240,241] Specifically, femtosecond two-dimensional infrared (2D IR) spectroscopy was used to monitor the distances between carbonyl groups in the peptide. An azo chromophore, incorporated inside the polypeptide chain, was used as a photoswitch to initiate a conformational change, hence initiate protein folding, on demand. Combined with time-resolved monitoring of the azo spectrum, this allows the deconvolution of folding dynamics. Pump-probe ultrafast laser pulse experiments are being used to study many different chemical reactions, but are obviously limited to reactions that can be triggered by light. Incorporating azobenzene into the experiment allows a wider range of reactions to be photo-triggered.

1.3.7.3 Optical Data Storage

The azos have been investigated as optical storage media for some time. Early proofs of principle were on Langmuir-Blodgett films, using photochromism[340] or birefringence.[341] Increasingly, amorphous polymer systems are being recognized as promising materials. In these easily processed systems, the birefringence is strong, stable, and switchable, making them ideal for optical memories. A single domain could encode one bit by either being isotropic or birefringent, a difference that is easily probed optically. The Δn values are large enough, in fact, that a gray-level algorithm could be used, where each domain stores more than one bit of data. On the negative side, the photo-alignment generated in the direction of the read/write beam leads to an effective loss of material performance with time. Full anisotropy could be restored with heat, however (which can be local and photo-induced, with appropriate device setup). The feasibility of storing ~30 GBytes of data on a single-layer of a removable disk using this gray-level approach has been demonstrated.[245]

Even the fastest photo-induced birefringence in azo systems requires milliseconds, and is slow compared to most computer timescales. However, optical data storage is amenable to gray-level read/write,[342] and to storing/retrieving full two-dimensional 'pages' of data at a time. In principle, azo systems could achieve high data storage and retrieval speeds. The full three-dimensional volume of a material can be used by encoding many layers of two-dimensional data (pages) one on top of the other.[343,344] This is accomplished by moving the optical focal plane through the material.

An intriguing possibility for high-density storage is to use angular multiplexing.[245] By storing multiple superimposed holograms in a single material, the data density is increased dramatically, and the whole three-dimensional volume of the material is exploited.[345] Volume phase holograms in azo systems can have diffraction efficiencies greater than 90%,[346] making data readout robust. The hologram is encoded by interfering a reference beam and a writing beam inside the sample volume, at a particular angle. The write beam, having passed through a spatial light modulator (SLM), has a pattern corresponding to the data, which is then holographically encoded in the sample. The entire page of data is written at once. By selecting different angles, new pages of data can be written. To readout a page, the azo-sample is set at the correct angle and

illuminated with the reference beam. The resulting diffraction pattern is imaged on a CCD array, which measures the encoded beam pattern (data). The volume of data and transmission rate is clearly large: projections of ~1000 GBytes in a single disk have been made. Since the entire hologram image is stored throughout the material, the technique is fairly insensitive to dust, scratches, and pinpoint defects.

The use of azo-substituted peptide oligomers appears to enable control of the order, hence optimization for holographic applications.[347] Optical memories would be considerably enhanced by using two-photon processes. This allows the addressable volume to be smaller and better defined, while reducing crosstalk between encoded pages. Some azo chromophores exhibit 'biphotonic' phenomena, which could be employed to enhance optical data storage.

1.4. Surface Mass Transport

In 1995, a surprising and unprecedented optical effect was discovered in polymer thin films containing the azo chromophore Disperse Red 1 (DR1), shown in Figure 1.11. The Natansohn/Rochon[348] research team and the Tripathy/Kumar collaboration[349] simultaneously and independently discovered a large-scale surface mass transport when the films were irradiated with a light interference pattern. In a typical experiment, two

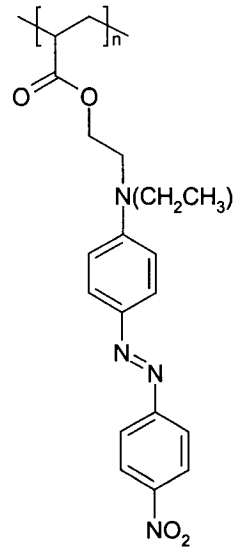

Figure 1.11: Chemical structure of poly(disperse red 1) acrylate, pdr1a, a pseudo-stilbene side-chain azo-polymer that generates high-quality surface-relief structures.

coherent laser beams, with a wavelength in the azo absorption band, are intersected at the sample surface (refer to Figure 1.12). The sample usually consists of a thin spin-cast film (10–1000 nm) of an amorphous azo-polymer on a transparent substrate. The sinusoidal light interference pattern at the sample surface leads to a sinusoidal surface patterning, i.e.: a surface relief grating (SRG). These gratings were found to be extremely large, up to hundreds of nanometers, as confirmed by AFM (Figure 1.13). The SRGs diffract very efficiently, and in retrospect it is clear that many reports of large diffraction efficiency prior to 1995, attributed to birefringence, were in fact due to surface gratings. The process occurs readily at room temperature (well below the T_g of the amorphous polymers used) with moderate irradiation (1–100 mW/cm^2) over seconds to minutes. The phenomenon is a reversible mass transport, not irreversible material ablation, since a flat film with the original thickness is recovered upon heating above T_g. Critically, it requires the presence and isomerization of azobenzene chromophores. Other absorbing but non-isomerizing chromophores do not produce SRGs. Many other systems can exhibit optical surface patterning,[350] but the amplitude of the modification is much smaller, does not involve mass transport, and usually requires additional processing steps. The all-optical patterning unique to azobenzenes has been studied intensively since its discovery, yet there remains controversy regarding the mechanism. The competing interpretations will be discussed and evaluated here. Many reviews of the remarkable body of experimental results are available.[7,70,197,351]

1.4.1 Experimental Observations

1.4.1.1 Dependence on Optical Parameters

The surface mass patterning unique to azobenzenes is a fundamentally optical process, whereby the incident light pattern is encoded in the material. In a surface relief grating experiment, two beams are intersected at an angle 2θ at the sample surface, giving rise to an SRG with period:

$$\Lambda = \frac{\lambda}{2\sin\theta} \tag{1.1}$$

where λ is the wavelength of the inscription light. The amplitude (height) of the SRG depends upon the inscription angle, displaying a maximum at θ~15°.[352,353] Grating height increases non-linearly with irradiation time and power, up to a saturation point.[354,355] At

moderate fluence, the grating efficiency depends only on the net exposure, not on the temporal distribution of irradiation. Gratings can be formed with intensities as low as 1 mW/cm^2, as long as the inscription wavelength is within the azo absorption band. Most chromophores used for SRG formation have a strong overlap of their *trans* and *cis* absorption spectra, allowing both isomers to be excited with a single wavelength. On the other hand, some experiments have been performed using azobenzenes with *trans* absorption in the blue, and *cis* absorption in the red.[356,357] Using an interference pattern of red HeNe beams, inscription only occurs if a blue pump beam concurrently irradiates. This biphotonic phenomenon proves that cycling of chromophores, and not simply isomerization, is required for grating formation.

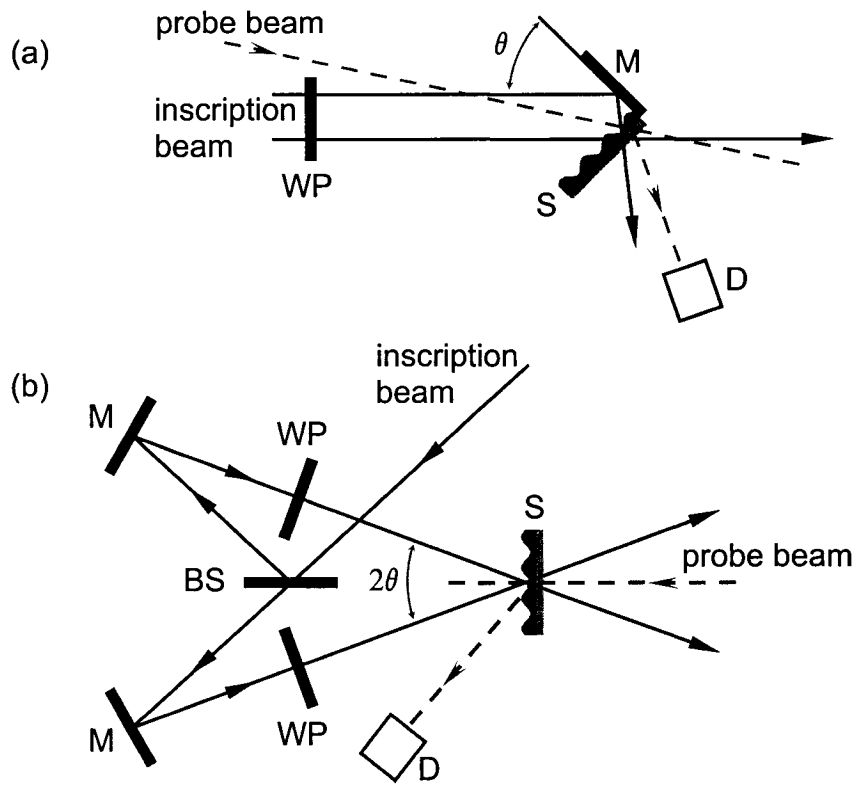

Figure 1.12: Experimental setup for the inscription of a surface relief grating: S refers to the sample, M are mirrors, D is a detector for the diffraction of the probe beam, WP is a waveplate (or generally a combination of polarizing elements), and BS is a 50% beam splitter. The probe beam is usually a HeNe (633 nm) and the inscription beam is chosen based on the chromophore absorption band (often Ar^+ 488 nm). (a) A simple one-beam inscription involves reflecting half of the incident beam off of a mirror adjacent to the sample. (b) A two-beam interference setup enables independent manipulation of the polarization state of the two incident beams.

The phase relationship between the incident light field and the resulting surface deformation is crucial in understanding the mechanism of grating formation (Figure 1.14). Early investigations using the diffraction of an edge,[348,358,359] and single-beam

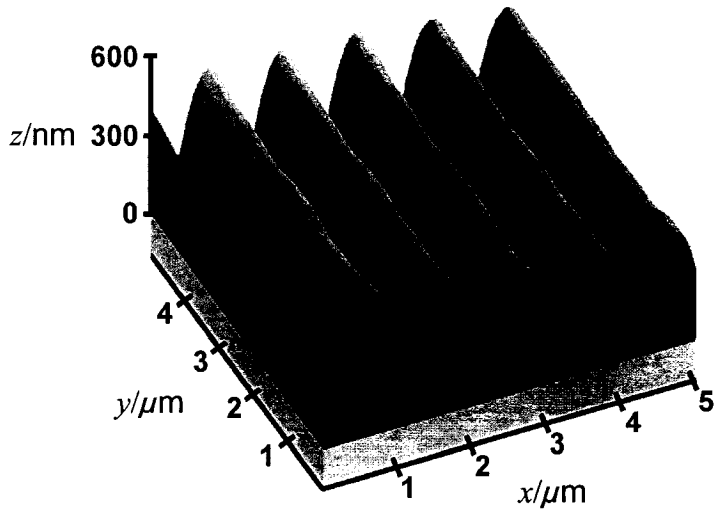

Figure 1.13: AFM image of a typical surface relief grating (SRG) optically inscribed into an azo-polymer film. Grating amplitudes of hundreds of nanometers, on the order of the original film thickness, are easily obtained. In this image, the approximate location of the film-substrate interface has been set to z = 0, based on knowledge of the film thickness.

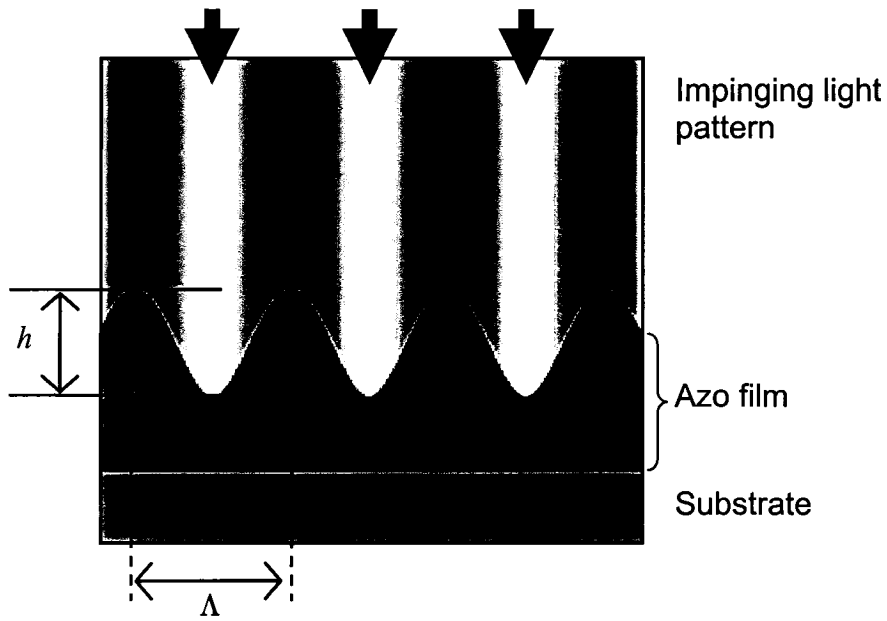

Figure 1.14: Schematic of a grating with spacing Λ and amplitude h. The usual phase relationship is indicated: light intensity maxima correspond to valleys in the surface relief.

surface deformations[360] convincingly showed that the light and surface relief are 180° out of phase. That is, light intensity maxima correspond to valleys in the surface relief. In effect, material is moved out of the light and into the dark regions. This rule appears to hold in the majority of cases, yet in a number of systems the phase relationship seems to be exactly inverted, with mass transport into illuminated regions. Specifically, in certain liquid crystalline systems, the phase behavior is inverted.[320,361,362] In one study, an amorphous material exhibited the 'usual' phase behavior, and a thin film of this polymer floating on water expanded in the direction of the light polarization. A similar LC azo-polymer exhibited inverted phase behavior in SRG experiments, and contracted in the direction of polarized illumination as a floating film. The tempting conclusion is that amorphous and polymeric systems exhibit opposite photomechanical response, which translates into opposite phase behavior in grating inscription. A possibly relevant experiment showed that for LC systems, the *cis* chromophores may become preferentially oriented along the light polarization direction, instead of perpendicular to it.[250] It should be pointed out, however, that some LC systems exhibit the 'usual' phase relationship,[363] and in one LC system, modification of a single ring substituent led to opposite phase behavior.[362]

Adding to the complexity of the phase relationship, it was observed that at high irradiation power (>300 W/cm^2) the behavior was inverted in amorphous systems.[354] Single-beam experiments at high power showed a central peak instead of a depression. By exposing a sample to a gradient two-beam intersection, a film was inscribed with a continuum of laser intensitites. An in-phase grating was found in the high-power region, and a conventional out-of-phase SRG in the low-power region. The intermediate region clearly showed interdigitation of the peaks from the two regimes, resembling a doubling of grating period observed by others. These double-period gratings can be formed in a number of amorphous systems, using the polarization combinations of (*p*, *p*) or (+45°, –45°), with indications that even the (*s*, *s*) and (*p*, *s*) combinations function to a certain extent.[364-367] Observations of a double-frequency orientational grating underneath a normal surface relief grating have also been reported.[368] The double-period surface relief gratings were attributed to interference between the diffracted beams from the primary grating, which gives rise to a light modulation, with double the initial frequency, in the

material. Whether these double-period gratings are related to the inverted structures observed in high-intensity experiments and some LC systems is an open question. It is interesting to note that some of the amorphous polymers that exhibit double-frequency behavior have accessible LC phases at higher temperature. These phase behavior results strongly suggest that there are (at least) two mechanisms at play during surface patterning. One dominates at low intensity in amorphous systems, while another appears to dominate at higher intensity and in LC systems. From an applied standpoint, these double-period gratings are of great interest, as they represent a means of generating patterned structures below the usual diffraction limit of far-field optical lithography.

Polarization of beams:	Electric Field in *xy* Plane					SRG Quality
x:	$+\pi$ $+\Lambda/2$	$+\pi/2$ $+\Lambda/4$	0 0	$-\pi/2$ $-\Lambda/4$	$-\pi$ $-\Lambda/2$	
s : s						6 – Poor
s : p						4
p : p *xy* plane *xz* plane	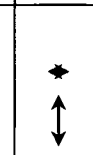					3
+45° : +45°						5
+45° : –45°						2 – Good
RCP : RCP						7 – Worst
RCP : LCP						1 – Best

Table 1.1: Polarization patterns at the sample surface during SRG inscription using a variety of polarized beam combinations. The 'quality' of the SRG (as determined by grating height) is shown for comparison.

Of considerable importance is the fact that the optical inscription process is sensitive to both intensity and polarization.[369] Different polarization combinations lead to different amplitudes, *h*, of the inscribed SRG, as shown in Table 1.1 (the coordinate system is shown in Figure 1.15). An optical field vector component in the direction of light modulation (hence mass transport) appears necessary.[360] Interestingly, SRGs can even be formed via pure polarization patterns, where the light intensity is uniform over

the sample surface.[370] In fact, the (*s*, *s*) and (RCP, RCP) combinations, which correspond to mainly variations in intensity and little to no polarization contrast, produce very poor SRGs. By contrast, the best gratings are obtained with (+45°, –45°) and (RCP, LCP) combinations, which involves primarily variation in polarization state across the film. It should be noted, however, that the exact polarization pattern present inside the material is not known. The pattern impinging on the sample is readily calculated from knowledge of the input polarizations, yet in the bulk of the material the light pattern will be redirected and re-polarized based on the detailed three-dimensional structure of the surface, refractive index, and birefringence. The optical erasure of an SRG, performed by homogenous irradiation, is also polarization-dependant.[371,372] Thus, the gratings possess a memory of the polarization state during inscription, encoded in the orientational distribution of chromophores at various grating positions. Typically, gratings inscribed with highly favorable polarization combinations will be optically erased more quickly. The *s*-polarization state, which produces poor gratings, is generally optimal for performing the erasure. These results are obviously related to the orientational distribution of chromophores after surface patterning, and their subsequent interaction with the erasing polarization.

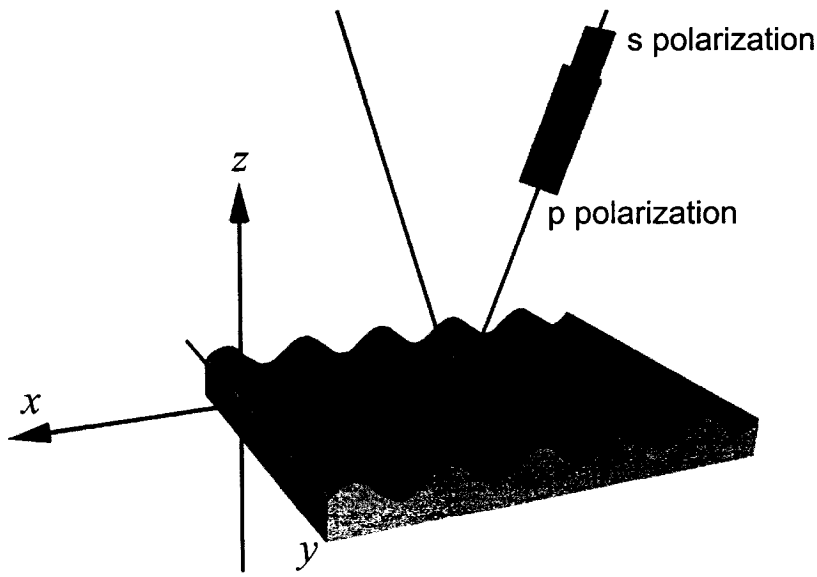

Figure 1.15: Coordinate system used to describe surface relief grating inscription, with *x* running along the direction of light modulation. The two incident beams have their polarization state controlled. The *s* polarization is parallel to the surface, whereas the *p* state is parallel to the plane-of-incidence.

1.4.1.2 Patterning

In a typical inscription experiment, a sinusoidally-varying light pattern is generated at the sample surface. What results is a sinusoidal surface profile: a surface relief grating (SRG). This is the pattern most often reported in the literature, because it is conveniently generated (by intersecting two coherent beams) and easily monitored (by recording the diffraction intensity at a non-absorbing wavelength, usually using a HeNe laser at 633 nm). However, it must be emphasized that the azo surface mass transport can produce arbitrary patterns. Essentially, the film encodes the impinging light pattern as a topography pattern. Both the intensity and the polarization of light are encoded. What appears to be essential is a *gradient* in the intensity and/or polarization of the incident light field. For instance, a single focused gaussian laser spot will lead to a localized depression, a gaussian line will lead to an elongated trench, etc.[360] In principle, any arbitrary pattern could be generated through an appropriate mask, interference/holographic setup, or scanning of a laser spot.[197]

Concomitant with the inscription of a surface relief is a photo-orientation of the azo chromophores, which depends on the polarization of the incident beam(s). The orientation of chromophores in SRG experiments has been measured using polarized Raman confocal microspectrometry.[365,367,373] The strong surface orientation is confirmed by photoelectron spectroscopy.[374] What is found is that the chromophores orient perpendicular to the local polarization vector of the impinging interference pattern. Thus, for a (+45°, –45°) two-beam interference: in the valleys ($x = 0$) the electric field is aligned in the y-direction, so the chromophores orient in the x-direction; in the peaks ($x = \Lambda/2$) the chromophores orient in the y-direction; in the slope regions ($x = \Lambda/4$) the electric field is circularly polarized and thus the chromophores are nearly isotropic. For a (p, p) two-beam interference, it is observed that the chromophores are primarily oriented in the y-direction everywhere, since the impinging light pattern is always linearly polarized in the x-direction. Mass transport may lead to perturbations in the orientational distribution, but photo-orientation remains the dominant effect.

The anisotropy grating that is submerged below a surface relief grating apparently leads to the formation of a density grating under appropriate conditions. It was found that upon annealing an SRG, which erases the surface grating and restores a flat film surface,

a density grating began growing beneath the surface (and into the film bulk).[375,376] This density grating only develops where the SRG was originally inscribed. It appears that the photo-orientation and mass transport leads to the nucleation of liquid crystalline 'seeding aggregates' that are thermally grown into larger-scale density variations. The thermal erasure of the SRG, with concomitant growth of the density grating, has been measured[377] and modeled.[378] Separating the components due to the surface relief and the density grating is described in a later section. Briefly, the diffraction of a visible-light laser primarily probes the surface relief, whereas a simultaneous x-ray diffraction experiment probes the density grating. The formation of a density grating is similar to, and consistent with, the production of surface topography[379] and surface density patterns,[380] as observed by tapping mode AFM, on an azo film exposed to an optical near field. In these experiments, it was found that volume is not strictly conserved during surface deformation,[381] consistent with changes in density.

1.4.1.3 Dependence on Material Properties

For all-optical surface patterning to occur, one necessarily requires azobenzene chromophores in some form. There are, however, a wide variety of azo materials that have exhibited surface mass patterning. This makes the process much more attractive from an applied standpoint: it is not merely a curiosity restricted to a single system, but rather a fundamental phenomenon that can be engineered into a wide variety of materials. It was recognized early on that the gratings do not form in systems of small molecules (for instance, comparing unreacted monomers to their corresponding polymers). The polymer molecular weight (MW), however, must not be too large.[353] Presumably a large MW eventually introduces entanglements which act as crosslinks, hindering polymer motion. Thus intermediate molecular weight polymers (MW ~ 10^3, arguably oligomers) are optimal. That having been said, there are many noteworthy counterexamples. Weak SRGs can be formed in polyelectrolyte multilayers, which are essentially crosslinked-polymer systems.[161,176,188,193] Efficient grating formation has also been demonstrated using an azo-cellulose with ultra-high molecular weight (MW ~ 10^7).[382,383] In a high molecular weight polypeptide (MW ~ 10^5), gratings could be formed where the grating amplitude was dependant on the polymer conformation.[384] Restricted conformations (α-helices and β-sheets) hindered SRG formation.

The opposite extreme has also been investigated: molecular glasses (amorphous non-polymeric azos with bulky pendants) exhibited significant SRG formation.[385-387] In fact, the molecular version formed gratings more quickly than its corresponding polymer.[388] Another set of experiments compared the formation of gratings in two related arrangements: (1) a thin film of polymer and small-molecule azo mixed together, and (2) a layered system, where a layer of the small-molecule azo was deposited on top of the pure polymer.[389] The SRG was negligible in the layered case. Whereas the authors suggest that 'layering' inhibits SRG formation, it may be interpreted that coupling to a host polymer matrix enhances mass transport, perhaps by providing rigidity necessary for fixation of the pattern. A copolymer study did in fact indicate that strong coupling of the mesogen to the polymer enhanced SRG formation,[390] and molecular glasses with hindered structures also enhanced grating formation.[391]

Gratings have also been formed in liquid crystalline systems.[361,362] In some systems, it was found that adding stoichiometric quantities of a non-azo LC guest greatly improved the grating inscription.[392,393] This suggests that SRG formation may be an inherently cooperative process, related to the mesogenic nature of the azo chromophore. The inscription sometimes requires higher power (>1 W/cm^2) than in amorphous systems.[394] In dendrimer systems, the quality of the SRG depends on the generation number.[395]

Maximizing the content of azo chromophore usually enhances SRG formation,[355] although some studies have found that intermediate functionalization (50–80%) created the largest SRG.[396,397] Some attempts have been made to probe the effect of free volume. By attaching substituents to the azo-ring, its steric bulk is increased, which presumably increases the free volume requirement for isomerization. However, substitution also invariably affects the isomerization rate-constants, quantum yield, refractive index, etc. This makes any analysis ambiguous. At least in the case of photo-orientation, the rate of inscription appears slower for bulkier chromophores, although the net orientation is similar.[398,399] For grating formation, it would appear that chromophore bulk is of secondary importance to many other inscription parameters. The mass transport occurs readily at room temperature, which is well below the glass-to-rubber transition temperature (T_g) of the amorphous polymers typically used. Gratings can even be formed

in polymers with exceptionally high T_g,[252] sometimes higher than 370°C.[400] These gratings can sometimes be difficult to erase via annealing.[401]

1.4.1.4 Photo-Softening

The formation of an SRG involves massive material motion. It would appear that the process is in some way a surface phenomenon, since non-azo capping layers tend to inhibit the phenomenon.[402] Many other experiments, however, confirm that azos deeper in the film (which still absorb light) contribute to the mass transport.[403] It is clear that the azobenzene isomerization is necessary to permit bulk material flow well below the polymer T_g. It is usually postulated that repeated *trans*→*cis*→*trans* cycles 'photo-soften' or 'photo-plasticize' the polymer matrix, enhancing polymer mobility by orders of magnitude. While this explanation is very compelling, its direct observation has proved ambiguous. Clearly motion is enabled during isomerization, as demonstrated by mass transport, increases in gas permeability,[404] the segregation of some material components to the free surface,[405] and the ability to optically erase SRGs.[356,371,372] The fact that incoherent illumination during SRG inscription enhances grating formation may also be interpreted as evidence that photo-softening is a dominant requirement for mass transport.[406] Numerous reports have confirmed a reduction in the viscosity of polymer solutions upon *trans* to *cis* conversion.[407-409] This photo-thinning can be attributed to both chain conformation (reduced hydrodynamic size) and interchain interactions. The extent to which such results can be extended into bulk films is debatable. It is also worth noting that a depression of T_g near the surface of a polymer film is now well-established.[410] One might be tempted to explain the mass transport by suggesting that an ultra-thin layer of polymer material at the surface is sufficiently mobile (below T_g) to move, thereby exposing 'fresh surface' which then becomes mobile. However, the T_g depressions typically measured are not sufficient to account for the process (especially in high-T_g samples). Moreover, this does not explain why the mass patterning is only observed in samples that contain azobenzene.

Despite compelling indirect experiments, there are few results that directly suggest photo-softening in bulk samples. Hints from AFM response,[359] experiments with a quartz crystal microbalance,[411] and electromechanical spectroscopy[411-413] all indicate that photo-softening is occurring. However, the magnitude of the effect is quite small

(<10% change in modulus), and certainly much smaller than the change in mechanical response that occurs upon heating a polymer to T_g. Thus, although mobility appears to be comparable to a polymer above T_g, other mechanical properties are only slightly modified. It may indeed be that isomerization merely enables localized molecular motion, but that the continual creation of molecular free volume pockets, which are then re-occupied by neighboring isomerizing chromophores, enables a net cooperative movement of material, akin to the displacement of a vacancy defect in a crystal or a hole in a semiconductor.[412] More investigations, for instance using AFM in the force-distance mode,[414] may help to settle these questions.

1.4.1.5 Measuring Gratings

The formation of an SRG is typically monitored via the diffraction of a probe laser beam. One must be careful in analyzing this diffraction efficiency, however, because a number of simultaneous gratings will be generated in an azo-sample during illumination with a light pattern (Figure 1.16). A light intensity pattern will lead to a

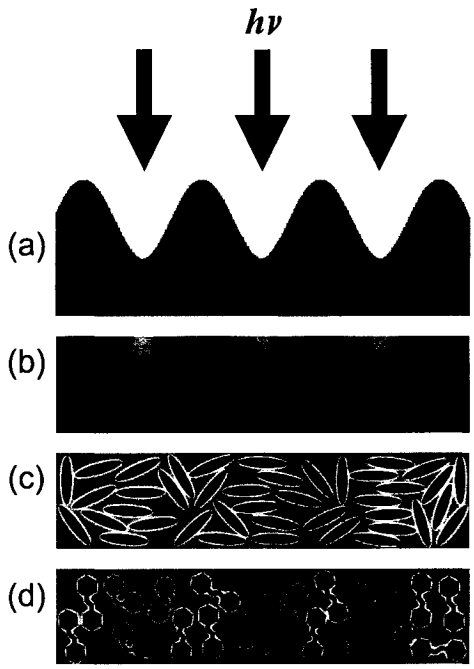

Figure 1.16: Schematic of the different gratings that are formed during illumination of an azo sample. (a) Surface relief grating (SRG). (b) Density grating (DG). (c) Birefringence (orientational) grating. (d) Chemical (*trans/cis*) grating. All the gratings contribute to the observed diffraction efficiency, to varying extents. Gratings (b), (c) and (d) are all refractive-index gratings.

chemical grating, since illuminated regions will be more *cis*-rich than dark regions. The resultant spatial variation of absorbance and refractive index will lead to various optical effects, including diffraction. This grating is temporary, persisting only during irradiation. Simultaneously, a birefringence grating will be inscribed. These birefringence patterns are stable and contribute to the observed final diffraction efficiency. A surface relief grating is of course induced if there is any spatial variation in intensity and/or polarization, and diffraction from this grating is very large, sometimes overwhelming other effects. Lastly, a density grating appears to be seeded beneath the material surface, which will also lead to periodic variation of refractive index.

The contributions to diffraction due to the surface relief and birefringence gratings can be deconvoluted using a Jones matrix formalism applied to polarized measurements of the 1st-order diffracted beams.[69,390,415-417] Similarly, scattering theory[378,418] was used to fit visible-light and x-ray diffraction data,[377,403,419-421] in order to deconvolute contributions due to surface relief and density (refractive index) gratings. For scattering from an SRG, the x and z components of the momentum transfer are:

$$\begin{aligned} q_x &= k(\sin\theta_f - \sin\theta_i) \\ q_z &= nk(\cos\theta_i + \cos\theta_f) \end{aligned} \tag{1.2}$$

where θ_i and θ_f are the incident and reflected angles, and $k = 2\pi/\lambda$. For the visible diffracted peak of order m (i.e., when $q_x = m2\pi/\Lambda$), the scattering intensity was derived to be:

$$I_{vis} \approx \left| J_m(q_z h) - e^{iq_z d} J_m(q_z \Delta n_m d) \right|^2 \tag{1.3}$$

where d is the film thickness, h is the grating height, Δn_m is the m-th Fourier component of the refractive-index grating, and J_m the m-th Bessel function. These Bessel functions can give rise to oscillations in the diffraction signal (Figure 1.17). Thus, one must be careful not to implicitly assume a linear dependence between grating amplitude and diffraction efficiency. Clearly, both the density and surface relief gratings contribute to the signal. For the x-ray signal, the scattering amplitude is given by:

$$A_{x-ray} \approx J_m(q_z h) - e^{iq_z d} \frac{B_m}{2} \tag{1.4}$$

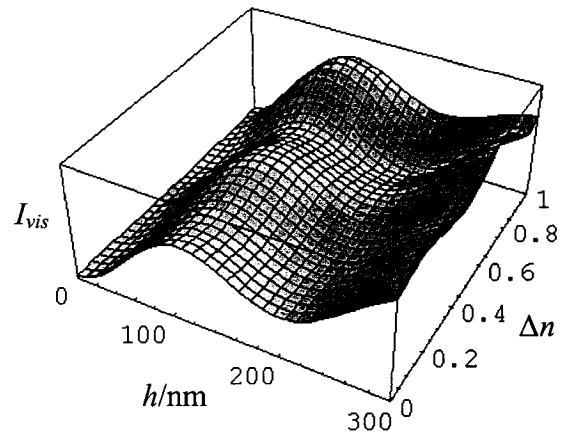

Figure 1.17: Diffraction intensity of a 700 nm thick film as a function of the inscribed grating height, h, and induced refractive-index grating (Δn), based on equation (3). The diffraction intensity is not a linear function of either variable. Oscillations in the signal can complicate analysis of experiments.

where one must now use the q_z appropriate for x-rays, and B_m represents the Fourier component of the density modulation (which is presumably identical to the index-modulation). The intensity is not simply the square of A, but can be determined using Fresnel transmission functions. The visible scattering is mostly sensitive to the surface-relief, and the x-ray scattering is due primarily to the density modulation. Using both measurements, the two contributions can of course be determined.

It is worth noting that chromophores may actually be disturbed by probe beams that are well outside of the azo absorption window. For instance, it was found that illumination using red light (outside of the azo absorption band) made density gratings (formed underneath surface relief gratings) stable against thermal erasure.[376] Others have found that chromophores become slowly aligned even with red laser light, where absorption should be nominal. Luckily the diffraction from azo gratings is intense, enabling the use of heavily attenuated probe beams.

1.4.1.6 Dynamics

Many dynamic measurements of SRG inscription have been made. To a first approximation, the inscription process does not depend on the temporal distribution of laser power, only on the net exposure. Yet this general rule breaks down at high and low power, and for short or interrupted exposures, revealing more complications inherent to the process. The inscription appears to be nonlinear, saturating with inscription time and

power, and being dependent upon history.[422] Interestingly, the growth of the gratings appears to continue for a short time after illumination has ceased, hinting at a photo-induced stress that persists in the dark. This may be due to the relatively slow decay of the *cis* population. For short (<2 s) moderate-power laser pulses, no permanent grating can be formed, even after repeated pulse exposure.[423] For longer (>5 s) pulses, material deformation can be seen after every exposure, and repeated exposure eventually leads to an SRG. These short pulses give rise to localized hills that eventually become a smooth sine wave. This implies that with sufficient power, individual azo chromophores or nano-domains deform, which when summed lead to a grating. Although short exposures do not form permanent gratings, some response is seen, possibly indicating elastic deformation[403,420] in addition to plastic flow.

The formation and erasure of surface relief and density gratings in azo films has been measured and modeled. Using the formalism described in the previous section, one can fit the measured scattering by allowing h and Δn (or B_m) to vary in time. For instance, the erasure of the SRG, and concomitant enhancement and then disappearance of the x-ray signal, can be fit using:[377]

$$h = h_{\max} \frac{1}{1+\exp\left(\frac{T - C_{SRG}T_g}{E_{a,SRG}}\right)}$$
$$B_m = B_{m,\max} \frac{1}{1+\exp\left(\frac{T - C_{DG}T_g}{E_{a,DG}}\right)} \qquad (1.5)$$

where $E_{a,i}$ and C_i are the activation energy and a fitting parameter, respectively, for the surface relief (SRG) and density (DG) gratings. It is found that the surface relief grating begins disappearing ~15 K before T_g. In contrast to this thermal erasure of SRGs, it appears that in some liquid crystalline systems, thermal treatment after SRG formation leads to an enhancement of the grating height.[424,425] In these cases, heating may enable motion and aggregation of chromophores.

1.4.2 Mechanism

Several mechanisms have been described to account for the microscopic origin of the driving force in azobenzene optical patterning. Arguments have appealed to thermal

gradients, diffusion considerations, isomerization-induced pressure gradients, and interactions between azo dipoles and the electric field of the incident light. Considering the large body of experimental observations, it is perhaps surprising that the issue of mechanism has not yet been settled. At present, no mechanism appears to provide an entirely complete and satisfactory explanation consistent with all known observations. On the other hand, viscoelastic modeling of the process has been quite successful, correctly reproducing nearly all experimentally observed surface patterns, without directly describing the microscopic nature of the driving force. Fluid mechanics models provided suitable agreement with observations,[426] and were later extended to take into account a depth dependence and a velocity distribution in the film,[427,428] which reproduces the thickness dependence of SRG inscription. A further elaboration took into account induced anisotropy in the film, and associated anisotropic polymer film deformation (expansion or contraction in the electric field direction).[429] The assumption of an anisotropic deformation is very much consistent with experimental observations.[320] Such an analysis, remarkably, was able to reproduce most of the polarization dependence, predicted phase-inverted behavior at high power, and even demonstrated double-period (interdigitated) gratings. A nonlinear stress-relaxation analysis could account for the nonlinear response during intermittent (pulse-like) exposure.[422] Finite-element linear viscoelastic modeling enabled the inclusion of finite compressibility.[430] This allowed the nonlinear intermittent-exposure results, and, critically, the formation of density gratings, to be correctly predicted. This analysis also demonstrated, as expected, that surface tension acts as a restoring force that limits grating amplitude (which explains the eventual saturation). Finally, the kinetics of grating formation (and erasure) have been captured in a lattice Monte Carlo simulation that takes into account isomerization kinetics and angular redistribution of chromophores.[431-433] Thus, the nonlinear viscoelastic flow and deformation (compression and expansion) of polymer material appear to be well understood. What remains to be fully elucidated is the origin of the force inside the material. More specifically, the connection between the azobenzene isomerization and the apparent force must be explained.

1.4.2.1 Thermal Considerations

Models involving thermal effects were proposed when SRG formation was first observed. Although simple and appealing, a purely thermal mechanism would not account for the polarization-dependence that is observed experimentally. The grating formation proceeds at remarkably low laser power, thus thermal mechanisms appear untenable. A more detailed modeling analysis[434] showed that the temperature gradient induced in a sample under typical SRG formation conditions was on the order of 10^{-4} K. This thermal gradient is much too small for any appreciable spatial variation of material properties. The net temperature rise in the sample was found to be on the order of 5 K, which again suggests that thermal effects (such as temperature-induced material softening) are negligible. On the other hand, high-intensity experiments have shown the formation of gratings that could not be subsequently thermally erased.[354] It is likely that in these cases a destructive thermal mechanism plays a role. In nanosecond pulsed experiments, gratings can be formed.[435-438] However, these gratings are due to irreversible ablation of the sample surface, a phenomenon well established in high-power laser physics. Moreover, the formation of gratings at these energies does not require azobenzene: any absorbing chromophore will do.[439] Computer modeling confirms temperature rises on the order of ~8000 K for nanosecond pulses,[434] clearly an entirely different regime from the facile room-temperature patterning unique to azo chromophores. Although thermal effects should be considered for a complete understanding of SRG formation (especially the phase-inverted structures observed at higher power), they appear to be negligible for typical irradiation conditions at modest laser power.

1.4.2.2 Asymmetric Diffusion

An elegant anisotropic translation mechanism was developed by Lefin, Fiorini and Nunzi.[440,441] In this model, material transport occurs essentially due to an (orientational) concentration gradient. It is suggested that the rapid cycling of chromophores between *trans* and *cis* states enables transient, random motion of molecules preferentially along their long axis, due to the inherent anisotropy of azo molecules. The probability of undergoing a random-walk step is proportional to the probability of isomerization, which of course depends upon the light intensity and the

angle between the chromophore dipole and the incident electric vector. This predicts a net flux of molecules out of the illuminated areas and into the dark regions, consistent with experiment. This process would be enhanced by pointing dipoles in the direction of the light gradient (towards the dark regions). This would appear to explain the polarization dependence to a certain extent. In contrast to experiment, however, this model implies the best results when using small molecules, not polymers. For polymer chains laden with many chromophores, random motion of these moeities would presumably lead to a 'tug-of-war' that would defeat net transport of the chain. It is at present not clear that the driving force in this model is sufficient to account for the substantial mass transport (well below T_g) observed in experiments.

1.4.2.3 Mean-Field Theory

Mechanisms based on electromagnetic forces are promising since they naturally include the intensity and polarization state of the incident light field. In the mean-field model developed by Pedersen et al.,[442,443] each chromophore is subject to a potential resulting from all the other chromophore dipoles in the material. Irradiation orients chromophores, and this net orientation leads to a potential that naturally aligns other chromophores. Furthermore, there is an attractive force between side-by-side chromophores that are aligned similarly. This leads to a net force on chromophores in illuminated areas, causing them to order and aggregate. Obviously this model predicts an accumulation of chromophores in the illuminated areas. Thus surface relief peaks will be aligned with light intensity maxima. While this result does not agree with experiments in amorphous samples, it is consistent with many experiments on LC systems. The mean-field model inherently includes intermolecular cooperativity and orientational order, and it appears natural that it would be manifest in mobile liquid crystalline systems. The polarization state of incident light is explicitly included in the model, as it serves to align dipoles and thus enhance the mean-field force. Because of this, even pure polarization patterns lead to gratings in this model. This mechanism appeals to the unique properties of azobenzenes only to explain the photo-orientation of dipoles. If this mechanism is general, one would expect it to operate on non-isomerizing dipoles that had been aligned by other means, which has not yet been observed.

1.4.2.4 Permittivity Gradient Theory

A mechanism involving spatial variation of the permittivity, ϵ, has been suggested by Baldus and Zilker.[444] This model assumes that a spatial modulation of the refractive index, hence permittivity, is induced in the film. This is certainly reasonable given the well-known photo-orientation and birefringence gratings in azo systems. A force is then exerted between the optical electric field and the gradient in permittivity. Specifically, the force is proportional to the intensity of the electric field in the mass transport direction, and to the gradient of the permittivity:

$$\vec{f} = -\frac{\varepsilon_0}{2}\vec{E}^2\nabla\varepsilon \tag{1.6}$$

Mass is thus driven out of areas with a strong gradient in ϵ, which in general moves material into the dark (consistent with the phase relationship in amorphous systems). Here again the mechanism appears general: any system with spatial variation of refractive index should be photo-patternable, yet this is not observed. This model would appear to require that adequate photo-orientation precede mass transport. Most experiments indicate, however, that both orientational and surface relief phenomena begin immediately and continue concurrently throughout inscription. This model was used to explain SRG formation in pulsed experiments,[437,439] where thermal effects were suggested as giving rise to the spatial variation of permittivity, but the resulting force was essentially identical. However, conventional laser ablation appears to be a simpler explanation for those results.[434]

1.4.2.5 Gradient Electric Force

A mechanism was proposed by Kumar et al. based on the observation that an electric field component in the direction of mass flow was required.[359,370,445,446] This force is essentially an optical gradient force.[447-449] Spatial variation of the light (electric field intensity and orientation) leads to a variation of the material susceptibility, χ, at the sample surface. The electric field then polarizes the material. The induced polarization is related to the light intensity and local susceptibility:

$$\vec{P}_i = \varepsilon_0\chi_{ij}\vec{E}_j \tag{1.7}$$

Forces then occur between the polarized material and the light field, analogous to the net force on an electric dipole in an electric field gradient. The time averaged force was derived to be:[370]

$$\vec{f} = \langle (\vec{P} \cdot \nabla)\vec{E} \rangle \tag{1.8}$$

The grating inscription is related to the spatially-varying material susceptibility, the magnitude of the electric field, and the gradient of the electric field. This theory was extended to include near-field optical gradient forces, which have been used for patterning in some experiments.[450] The gradient force model naturally includes the polarization dependence of the incident light, and reproduces essentially all of the polarization features of single-beam and SRG experiments. It has been pointed out,[197] however, that another analysis[451] of forces exerted on polarizable media suggested a dependence on the gradient of the electric field, but not its polarization direction. The gradient force theory requires azobenzene photochemistry to modulate susceptibility via photo-orientation, and also implicitly assumes that 'photo-plasticization' is enabling mass transport. It would appear, however, that the force density predicted by this model is much too small to account for mass transport in real systems. A straightforward analysis presented by Saphiannikova et al.[430] is described here. In the case of two circularly polarized beams (for instance), the force acting in the x-direction, according to the gradient electric force model, would be

$$f = -k\varepsilon_0 \chi E_0^{\,2} \sin\theta(1+\cos^2\theta)\sin(kx\sin\theta) \tag{1.9}$$

where 2θ is the angle between the two beams and $k = 2\pi/\lambda$. Since $E_0^{\,2} = 2Iz_0$, where z_0 is the vacuum impedance and I is the light intensity, the maximum expected force is

$$f_{\max} = \frac{4\pi}{\lambda}\varepsilon_0 z_0 \chi I \tag{1.10}$$

Given that $\varepsilon_0 = 8.854\times10^{-12}\,\mathrm{C^2/(Nm^2)}$, $|\chi| \approx 1$ and z_0 = 377 Ω, and using the typical values I = 100 mW/cm^2 and λ = 488 nm, we obtain a force density of ~100 N/m^3. Not only is this two orders of magnitude smaller than the force of gravity (which itself is presumably negligible), but it falls short of the estimated 10^{11}–10^{14} N/m^3 necessary for mass transport in polymer films to occur.[430]

1.4.2.6 Isomerization Pressure

One of the first mechanisms to be presented was the suggestion by Barrett et al. of pressure gradients inside the polymer film.[353,426] The assumption is that azobenzene isomerization generates pressure due both to the greater free volume requirement of the *cis*, and due to the volume requirement of the isomerization process itself. Isomerization of the bulky chromophores leads to pressure that is proportional to light intensity. The light intensity gradient thus generates a pressure gradient, which of course leads to material flow in a fluid mechanics treatment. Order-of-magnitude estimates were used to suggest that the mechanical force of isomerization would be greater than the yield point of the polymer, enabling flow. Plastic flow is predicted to drive material out of the light, consistent with observations in amorphous systems. At first it would seem that this mechanism cannot be reconciled with the polarization dependence, since the pressure is presumably proportional to light intensity, irrespective of its polarization state. However, one must more fully take orientational effects into account. Linearly polarized light addresses fewer chromophores than circularly polarized light, and would thus lead to lower pressure. Thus, pure polarization patterns can still lead to pressure gradients. Combined with the fact that the polarized light is orienting (and in a certain sense photo-bleaching), this can explain some aspects of the polarization data. The agreement, however, is not perfect. For instance, the (*s*, *s*) and (*p*, *p*) combinations lead to very different gratings in experiments. It is possible that some missing detail related to polarization will help explain this discrepancy.

Combining a variety of results from the literature, it now appears the mechanical argument of a pressure mechanism may be correct. In one experiment, irradiation of a transferred Langmuir-Blodgett film reversibly generated ~5 nm 'hills,' attributed to nanoscale buckling that relieves the stress induced by lateral expansion.[452] This result is conspicuously similar to the spontaneous polarization-dependant formation of hexagonally-arranged ~500 nm hills seen on an amorphous azo-polymer sample irradiated homogeneously.[453,454] In fact, homogeneous illumination of azo surfaces has caused roughening[412] and homogeneous optical erasure of SRGs leads to similar pattern formation.[372] The early stages of SRG formation, imaged by AFM, again show the formation of nano-sized hills.[423] Taken together, these seem to suggest that irradiation of

an azo film leads to spontaneous lateral expansion, which induces a stress that can be relieved by buckling of the surface, thereby generating surface structures. In the case of a light gradient, the buckling is relieved by mass transport coincident with the light field that generated the pressure inside the film. In an experiment on main-chain versus side-chain azo-polymers, the polarization behavior of photo-deformation was opposite.[381] This may be explained by postulating that the main-chain polymer contracts upon isomerization, whereas the side-chain polymer architecture leads to net expansion. Similarly, the opposite phase behavior in amorphous and LC systems may be due to the fact that the former photo-expand and the latter photo-contract.[320] Lastly, many large surface structures were observed in an azo-dye-doped elastomer film irradiated at high power (4 W/cm^2).[455] The formation of structures both parallel and perpendicular to the grating direction could be attributed to photo-aggregation of the azo dye molecules and/or buckling of the elastomeric surface. Thus a purely photomechanical explanation may be able to describe surface mass transport in azo systems. Further investigations into reconciling this model with the polarization dependence of inscription are in order. Presumably photo-orientation will play a key role.

1.4.3 *Applications of Surface Mass Transport*

The rapid, facile, reversible, and single-step all-optical surface patterning effect discovered in a wide variety of azobenzene systems has, of course, been suggested as the basis for numerous applications. Azobenzene is versatile, amenable to incorporation in a wide variety of materials. The mass patterning is reversible, which is often advantageous. On the other hand, one may use a system where crosslinking enables permanent fixation of the surface patterns.[456] Many proposed applications are optical, and fit well with azobenzene's already extensive list of optical capabilities. The gratings have been demonstrated as optical polarizers,[457] angular or wavelength filters,[458,459] and couplers for optical devices.[460] They have also been suggested as photonic band gap materials,[461] and have been used to create lasers where emission wavelength is tunable via grating pitch.[462,463] The process has, of course, been suggested as an optical data storage mechanism.[464] The high-speed and single-step holographic recording has been suggested to enable 'instant holography,'[436] with obvious applications for industry or end consumers. Since the hologram is topographical, it can easily be used as a master to

create replicas via molding. The surface patterning also allows multiple holograms to be superimposed, if desired. A novel suggestion is to use the patterning for rapid prototyping of optical elements.[465] Optical elements could be generated or modified quickly and during device operation. They could thereafter be replaced with permanent components, if required.

The physical structure of the surface relief can be exploited to organize other systems. For instance, it can act as a command layer, aligning liquid crystals.[466-470] The grating can be formed after the LC cell has been assembled, and can be erased and rewritten. Colloids can also be arranged into the grooves of an SRG, thereby templating higher-order structures.[471,472] These lines of colloids can then be sintered to form wires.[473] The surface topography inscription process is clearly amenable to a variety of optical-lithography patterning schemes. These possibilities will hopefully be more thoroughly investigated. One advantage of holographic patterning is that there is guaranteed registry between features over macroscopic distances. This is especially attractive as technologies move towards wiring nanometer-sized components. One example in this direction involved evaporating metal onto an SRG, and then annealing. This formed a large number of very long (several mm) but extremely thin (200 nm) parallel metal wires.[474] Of interest for next-generation patterning techniques is the fact that the azo surface modification is amenable to near-field patterning, which enables high-resolution nanopatterning by circumventing the usual diffraction limit of far-field optical systems. Proof of principle was demonstrated by irradiating through polystyrene spheres assembled on the surface of an azo film. This results in a polarization-dependent surface topography pattern,[379] and a corresponding surface density pattern.[380] Using this technique, resolution on the order of 20 nm was achieved.[475] This process appears to be enhanced by the presence of gold nano-islands.[476] It was also shown that volume is not strictly conserved in these surface deformations.[381] In addition to being useful as a sub-diffraction limit patterning technique, it should be noted that this is also a useful technique for imaging the near-field of various optical interactions.[477] The (as of yet not fully explained) fact that sub-diffraction limit double-frequency surface relief gratings can be inscribed via far-field illumination[364-367] further suggests the azo-polymers as versatile high-resolution patterning materials.

1.5. Thesis Objectives

Azobenzene polymers are versatile and functional materials that exhibit photo-responsive behavior not seen in any other system. They are fundamentally interesting as optical materials. In particular, the surface mass patterning observed in the azo-polymer system is of interest both from a fundamental polymer dynamics standpoint, and from an applied nano-fabrication standpoint. The fundamental nature of this surface-patterning phenomenon is the focus of this thesis. The work described here involved both eliminating candidate explanations through the use of careful modeling and experiments, as well as fundamentally studying the light-response of these materials, in order to uncover the origin of the driving force. In addition to describing the nature of patterning in azo-polymers, this work also provides crucial insight into the large-scale motions that arise from azobenzene isomerization.

Chapter 3 uses computer modeling and associated analytic expressions to quantify the extent of photo-heating, and the internal temperature gradient, which occur during optical patterning. The purpose of such this study was not only to eliminate purely thermal mechanisms from consideration, but also to place limits on the extent to which thermal effects may play a role in the patterning. For instance, it was necessary to ascertain to what extent heat may be contributing to 'photo-softening.' Chapter 4 then analyzes the effect of confinement on the patterning phenomenon. Again this enables a class of mechanisms to be eliminated, as different mechanisms will imply different size-scales to the phenomenon. In particular, mechanisms involving molecular diffusion can be differentiated from those that involve coordinated motion of material and large-scale stress patterns. Having resolved these issues, chapter 5 then focuses on measuring the extent to which azobenzene materials deform under homogeneous light irradiation. By quantifying the extent of this material motion, it is possible to suggest it as a viable explanation for mass patterning. This chapter thus analyzes in detail how the molecular-scale azobenzene isomerization leads to large-scale dimensional changes in these materials. The effect is also quantified as a function of temperature. Chapter 6 discusses AFM modulus measurements that can be used to set a bound on the extent of photo-softening occurring in these materials. This enables mechanisms that rely on orders of magnitude photo-softening to be eliminated. This chapter also presents results of photo-

patterning as a function of temperature. By combining the results of the previous chapters, it is then possible to make a strong argument that the fundamental origin of surface patterning in these systems is the identified photomechanical deformation. Literature results are analyzed in this context. The final chapter makes suggestions for future research, based upon this newly established correspondence.

1.6. References

(1) Zollinger, H. *Azo and Diazo Chemistry*; Interscience: New York, 1961.

(2) Zollinger, H. *Colour Chemistry, Synthesis, Properties, and Applications of Organic Dyes*; VCH: Weinheim, 1987.

(3) Kwolek, S.; Morgan, P.; Schaefgen, J. *Encyclopedia of Polymer Science and Engineering*; John-Wiley: New York, 1985; Vol. 9.

(4) Möhlmann, G.; van der Vorst, C. *Side Chain Liquid Crystal Polymers*, C. Mcardle ed.; Plenum and Hall: Glasgow, 1989.

(5) Rau, H. In *Photochemistry and Photophysics*; Rebek, J., Ed.; CRC Press: Boca Raton, FL, 1990; Vol. 2, pp 119.

(6) Rau, H. *Berichte der Bunsen-Gesellschaft* **1968**, *72*, 408.

(7) Delaire, J. A.; Nakatani, K. *Chem. Rev.* **2000**, *100*, 1817.

(8) Schulze, F. W.; Petrick, H. J.; Cammenga, H. K.; Klinge, H. *Z. Phys. Chem. (Muenchen, Ger.)* **1977**, *107*, 1.

(9) Mita, I.; Horie, K.; Hirao, K. *Macromol.* **1989**, *22*, 558.

(10) Monti, S.; Orlandi, G.; Palmieri, P. *Chem. Phys.* **1982**, *71*, 87.

(11) Kobayashi, T.; Degenkolb, E. O.; Rentzepis, P. M. *J. Phys. Chem.* **1979**, *83*, 2431.

(12) Lednev, I. K.; Ye, T.-Q.; Hester, R. E.; Moore, J. N. *J. Phys. Chem.* **1996**, *100*, 13338.

(13) Brown, E. V.; Granneman, G. R. *J. Am. Chem. Soc.* **1975**, *97*, 621.

(14) Haberfield, P.; Block, P. M.; Lux, M. S. *J. Am. Chem. Soc.* **1975**, *97*, 5804.

(15) Lamarre, L.; Sung, C. S. P. *Macromol.* **1983**, *16*, 1729.

(16) Shirota, Y.; Moriwaki, K.; Yoshikawa, S.; Ujike, T.; Nakano, H. *J. Mater. Chem.* **1998**, *8*, 2579.

(17) Norikane, Y.; Kitamoto, K.; Tamaoki, N. *J. Org. Chem.* **2003**, *68*, 8291.

(18) Rau, H.; Roettger, D. *Mol. Cryst. Liq. Cryst. Sci. Tech. A* **1994**, *246*, 143.

(19) Rottger, D.; Rau, H. *J. Photochem. Photobiol., A* **1996**, *101*, 205.

(20) Nagamani, S. A.; Norikane, Y.; Tamaoki, N. *J. Org. Chem.* **2005**, *70*, 9304.

(21) Vollmer, M. S.; Clark, T. D.; Steinem, C.; Ghadiri, M. R. *Angew. Chem., Int. Ed.* **1999**, *38*, 1598.

(22) Kerzhner, B. K.; Kofanov, V. I.; Vrubel, T. L. *Zhurnal Obshchei Khimii* **1983**, *53*, 2303.

(23) Funke, U.; Gruetzmacher, H. F. *Tetrahedron* **1987**, *43*, 3787.

(24) Hartley, G. S. *Nature* **1937**, *140*, 281.

(25) Hartley, G. S. *Journal of the Chemical Society, Abstracts* **1938**, 633.

(26) Fischer, E. *J. Phys. Chem.* **1967**, *71*, 3704.

(27) Rau, H.; Greiner, G.; Gauglitz, G.; Meier, H. **1990**, *94*, 6523.

(28) Gabor, G.; Fischer, E. *J. Phys. Chem.* **1971**, *75*, 581.

(29) Eisenbach, C. D. *Macromol. Rapid Commun.* **1980**, *1*, 287.

(30) Hair, S. R.; Taylor, G. A.; Schultz, L. W. *J. Chem. Educ.* **1990**, *67*, 709.

(31) Beltrame, P. L.; Paglia, E. D.; Castelli, A.; Tantardini, G. F.; Seves, A.; Marcandalli, B. *J. Appl. Polym. Sci.* **1993**, *49*, 2235.

(32) Magennis, S. W.; Mackay, F. S.; Jones, A. C.; Tait, K. M.; Sadler, P. J. *Chem. Mater.* **2005**, *17*, 2059.

(33) Xie, S.; Natansohn, A.; Rochon, P. *Chem. Mater.* **1993**, *5*, 403.

(34) Gegiou, D.; Muszkat, K. A.; Fischer, E. *J. Am. Chem. Soc.* **1968**, *90*, 3907.

(35) Rau, H.; Lueddecke, E. *J. Am. Chem. Soc.* **1982**, *104*, 1616.

(36) Naito, T.; Horie, K.; Mita, I. *Macromol.* **1991**, *24*, 2907.

(37) Liu, Z. F.; Morigaki, K.; Enomoto, T.; Hashimoto, K.; Fujishima, A. *J. Phys. Chem.* **1992**, *96*, 1875.

(38) Altomare, A.; Ciardelli, F.; Tirelli, N.; Solaro, R. *Macromol.* **1997**, *30*, 1298.

(39) Fujino, T.; Tahara, T. *J. Phys. Chem. A* **2000**, *104*, 4203.

(40) Fujino, T.; Arzhantsev, S. Y.; Tahara, T. *J. Phys. Chem. A* **2001**, *105*, 8123.

(41) Ho, C.-H.; Yang, K.-N.; Lee, S.-N. *J. Polym. Sci., Part A: Polym. Chem.* **2001**, *39*, 2296.

(42) Angeli, C.; Cimiraglia, R.; Hofmann, H.-J. *Chem. Phys. Lett.* **1996**, *259*, 276.

(43) Jursic, B. S. *Chem. Phys. Lett.* **1996**, *261*, 13.

(44) Ikeda, T.; Tsutsumi, O. *Science* **1995**, *268*, 1873.

(45) Priest, W. J.; Sifain, M. M. *J. Polym. Sci., Part A: Polym. Chem.* **1971**, *9*, 3161.

(46) Paik, C. S.; Morawetz, H. *Macromol.* **1972**, *5*, 171.

(47) Barrett, C.; Natansohn, A.; Rochon, P. *Macromol.* **1994**, *27*, 4781.

(48) Barrett, C.; Natansohn, A.; Rochon, P. *Chem. Mater.* **1995**, *7*, 899.

(49) Sarkar, N.; Sarkar, A.; Sivaram, S. *J. Appl. Polym. Sci.* **2001**, *81*, 2923.

(50) Norman, L. L.; Barrett, C. J. *Journal of Physical Chemistry B* **2002**, *106*, 8499.

(51) Tanaka, K.; Tateishi, Y.; Nagamura, T. *Macromol.* **2004**, *37*, 8188.

(52) Rau, H.; Crosby, A. D.; Schaufler, A.; Frank, R. *Z. Naturforsch., A: Phys. Sci.* **1981**, *36*, 1180.

(53) Malkin, S.; Fischer, E. *J. Phys. Chem.* **1962**, *66*, 2482.

(54) Shen, Y. Q.; Rau, H. *Macromol. Chem. Phys.* **1991**, *192*, 945.

(55) Bortolus, P.; Monti, S. *J. Phys. Chem.* **1979**, *83*, 648.

(56) Yitzchaik, S.; Marks, T. J. *Acc. Chem. Res.* **1996**, *29*, 197.

(57) Levy, D.; Esquivias, L. *Adv. Mater.* **1995**, *7*, 120.

(58) Sisido, M.; Ishikawa, Y.; Harada, M.; Itoh, K. *Macromol.* **1991**, *24*, 3999.

(59) Willner, I.; Rubin, S. *Angew. Chem., Int. Ed. Engl.* **1996**, *35*, 367.

(60) Gallot, B.; Fafiotte, M.; Fissi, A.; Pieroni, O. *Macromol. Rapid Commun.* **1996**, *17*, 493.

(61) Shinkai, S.; Minami, T.; Kusano, Y.; Manabe, O. *J. Am. Chem. Soc.* **1983**, *105*, 1851.

(62) Jung, J. H.; Takehisa, C.; Sakata, Y.; Kaneda, T. *Chem. Lett.* **1996**, 147.

(63) Yamamura, H.; Kawai, H.; Yotsuya, T.; Higuchi, T.; Butsugan, Y.; Araki, S.; Kawai, M.; Fujita, K. *Chem. Lett.* **1996**, 799.

(64) Singh, A. K.; Das, J.; Majumdar, N. *J. Am. Chem. Soc.* **1996**, *118*, 6185.

(65) Chen, S. H.; Mastrangelo, J. C.; Shi, H.; Blanton, T. N.; Bashir-Hashemi, A. *Macromol.* **1997**, *30*, 93.

(66) Chen, S. H.; Mastrangelo, J. C.; Shi, H.; Bashir-Hashemi, A.; Li, J.; Gelber, N. *Macromol.* **1995**, *28*, 7775.

(67) Ichimura, K. *Chem. Rev.* **2000**, *100*, 1847.

(68) Birabassov, R.; Landraud, N.; Galstyan, T. V.; Ritcey, A.; Bazuin, C. G.; Rahem, T. *Appl. Opt.* **1998**, *37*, 8264.

(69) Labarthet, F. L.; Buffeteau, T.; Sourisseau, C. *J. Phys. Chem. B* **1998**, *102*, 2654.

(70) Viswanathan, N. K.; Kim, D. Y.; Bian, S.; Williams, J.; Liu, W.; Li, L.; Samuelson, L.; Kumar, J.; Tripathy, S. K. *J. Mater. Chem.* **1999**, *9*, 1941.

(71) Natansohn, A.; Rochon, P.; Gosselin, J.; Xie, S. *Macromol.* **1992**, *25*, 2268.

(72) Ho, M. S.; Barrett, C.; Paterson, J.; Esteghamatian, M.; Natansohn, A.; Rochon, P. *Macromol.* **1996**, *29*, 4613.

(73) Wang, X.; Chen, J.-I.; Marturunkakul, S.; Li, L.; Kumar, J.; Tripathy, S. K. *Chem. Mater.* **1997**, *9*, 45.

(74) Wang, X.; Kumar, J.; Tripathy, S. K.; Li, L.; Chen, J.-I.; Marturunkakul, S. *Macromol.* **1997**, *30*, 219.

(75) Wang, X.; Balasubramanian, S.; Li, L.; Jiang, X.; Sandman, D. J.; Rubner, M. F.; Kumar, J.; Tripathy, S. K. *Macromol. Rapid Commun.* **1997**, *18*, 451.

(76) Agolini, F.; Gay, F. P. *Macromol.* **1970**, *3*, 349.

(77) Anderle, K.; Birenheide, R.; Eich, M.; Wendorff, J. H. *Makromol. Chem., Rapid Commun.* **1989**, *10*, 477.

(78) Furukawa, J.; Takamori, S.; Yamashita, S. *Angew. Makromol. Chem.* **1967**, *1*, 92.

(79) Bignozzi, M. C.; Angeloni, S. A.; Laus, M.; Incicco, L.; Francescangeli, O.; Wolff, D.; Galli, G.; Chiellini, E. *Polymer Journal (Tokyo)* **1999**, *31*, 913.

(80) Liu, X.-H.; Bruce, D. W.; Manners, I. *Chem. Commun.* **1997**, 289.

(81) Mekelburger, H. B.; Rissanen, K.; Voegtle, F. *Chem. Ber.* **1993**, *126*, 1161.

(82) Junge, D. M.; McGrath, D. V. *Chem. Commun.* **1997**, 857.

(83) Sukwattanasinitt, M.; Wang, X.; Li, L.; Jiang, X.; Kumar, J.; Tripathy, S. K.; Sandman, D. J. *Chem. Mater.* **1998**, *10*, 27.

(84) Teraguchi, M.; Masuda, T. *Macromol.* **2000**, *33*, 240.

(85) Izumi, A.; Teraguchi, M.; Nomura, R.; Masuda, T. *J. Polym. Sci., Part A: Polym. Chem.* **2000**, *38*, 1057.

(86) Izumi, A.; Teraguchi, M.; Nomura, R.; Masuda, T. *Macromol.* **2000**, *33*, 5347.

(87) Morino, S. y.; Kaiho, A.; Ichimura, K. *Appl. Phys. Lett.* **1998**, *73*, 1317.

(88) Altomare, A.; Ciardelli, F.; Gallot, B.; Mader, M.; Solaro, R.; Tirelli, N. *J. Polym. Sci., Part A: Polym. Chem.* **2001**, *39*, 2957.

(89) Tsutsumi, N.; Yoshizaki, S.; Sakai, W.; Kiyotsukuri, T. *MCLC S&T, Section B: Nonlinear Optics* **1996**, *15*, 387.

(90) Ichimura, K.; Momose, M.; Kudo, K.; Akiyama, H.; Ishizuki, N. *Thin Solid Films* **1996**, *284-285*, 557.

(91) Weh, K.; Noack, M.; Ruhmann, R.; Hoffmann, K.; Toussaint, P.; Caro, J. *Chem. Eng. Technol.* **1998**, *21*, 408.

(92) Blinov, L. M.; Kozlovsky, M. V.; Ozaki, M.; Skarp, K.; Yoshino, K. *J. Appl. Phys.* **1998**, *84*, 3860.

(93) Han, M.; Ichimura, K. *Macromol.* **2001**, *34*, 82.

(94) Seki, T.; Sakuragi, M.; Kawanishi, Y.; Tamaki, T.; Fukuda, R.; Ichimura, K.; Suzuki, Y. *Langmuir* **1993**, *9*, 211.

(95) Jianhua, G.; Hua, L.; Lingyun, L.; Bingjie, L.; Yiwen, C.; Zuhong, L. *Supramol. Sci.* **1998**, *5*, 675.

(96) Razna, J.; Hodge, P.; West, D.; Kucharski, S. *J. Mater. Chem.* **1999**, *9*, 1693.

(97) Silva, J. R.; Dall'Agnol, F. F.; Oliveira Jr., O. N.; Giacometti, J. A. *Polymer* **2002**, *43*, 3753.

(98) Evans, S. D.; Johnson, S. R.; Ringsdorf, H.; Williams, L. M.; Wolf, H. *Langmuir* **1998**, *14*, 6436.

(99) Mallia, V. A.; Tamaoki, N. *J. Mater. Chem.* **2003**, *13*, 219.

(100) Naito, K.; Miura, A. *J. Phys. Chem.* **1993**, *97*, 6240.

(101) Shibaev, V.; Bobrovsky, A.; Boiko, N. *Prog. Polym. Sci.* **2003**, *28*, 729.

(102) Sun, S. T.; Gibbons, W. M.; Shannon, P. J. *Liq. Cryst.* **1992**, *12*, 869.

(103) Anderle, K.; Birenheide, R.; Werner, M. J. A.; Wendorff, J. H. *Liq. Cryst.* **1991**, *9*, 691.

(104) Gibbons, W. M.; Shannon, P. J.; Sun, S.-T.; Swetlin, B. J. *Nature* **1991**, *351*, 49.

(105) Ichimura, K.; Hayashi, Y.; Akiyama, H.; Ikeda, T.; Ishizuki, N. *Appl. Phys. Lett.* **1993**, *63*, 449.

(106) Chen, A. G.; Brady, D. J. *Appl. Phys. Lett.* **1993**, *62*, 2920.

(107) Wiesner, U.; Reynolds, N.; Boeffel, C.; Spiess, H. W. *Makromol. Chem., Rapid Commun.* **1991**, *12*, 457.

(108) Stumpe, J.; Mueller, L.; Kreysig, D.; Hauck, G.; Koswig, H. D.; Ruhmann, R.; Ruebner, J. *Makromol. Chem., Rapid Commun.* **1991**, *12*, 81.

(109) Hvilsted, S.; Andruzzi, F.; Kulinna, C.; Siesler, H. W.; Ramanujam, P. S. *Macromol.* **1995**, *28*, 2172.

(110) Yaroschuk, O.; Sergan, T.; Lindau, J.; Lee, S. N.; Kelly, J.; Chien, L.-C. *J. Chem. Phys.* **2001**, *114*, 5330.

(111) Eich, M.; Wendorff, J. *J. Opt. Soc. Am. B* **1990**, *7*, 1428.

(112) Ikeda, T.; Horiuchi, S.; Karanjit, D. B.; Kurihara, S.; Tazuke, S. *Macromol.* **1990**, *23*, 42.

(113) Hayashi, T.; Kawakami, H.; Doke, Y.; Tsuchida, A.; Onogi, Y.; Yamamoto, M. *Eur. Polym. J.* **1995**, *31*, 23.

(114) Kato, T.; Hirota, N.; Fujishima, A.; Frechet, J. M. J. *J. Polym. Sci., Part A: Polym. Chem.* **1996**, *34*, 57.

(115) Shannon, P. J.; Gibbons, W. M.; Sun, S. T. *Nature* **1994**, *368*, 532.

(116) Luk, Y.-Y.; Abbott, N. L. *Science* **2003**, *301*, 623.

(117) Ikeda, T.; Sasaki, T.; Ichimura, K. *Nature* **1993**, *361*, 428.

(118) Fischer, B.; Thieme, C.; Fischer, T. M.; Kremer, F.; Oge, T.; Zentel, R. *Liq. Cryst.* **1997**, *22*, 65.

(119) Villavicencio, O.; McGrath, D. V. *Advances in Dendritic Macromolecules* **2002**, *5*, 1.

(120) Momotake, A.; Arai, T. *Polymer* **2004**, *45*, 5369.

(121) Momotake, A.; Arai, T. *J. Photochem. Photobiol., C* **2004**, *5*, 1.

(122) Ma, H.; Liu, S.; Luo, J.; Suresh, S.; Liu, L.; Kang, S. H.; Haller, M.; Sassa, T.; Dalton, L. R.; Jen, A. K.-Y. *Adv. Funct. Mater.* **2002**, *12*, 565.

(123) Campbell, V. E.; In, I.; McGee, D. J.; Woodward, N.; Caruso, A.; Gopalan, P. *Macromol.* **2006**, *39*, 957.

(124) Jiang, D.-L.; Aida, T. *Nature* **1997**, *388*, 454.

(125) Aida, T.; Jiang, D.-L.; Yashima, E.; Okamoto, Y. *Thin Solid Films* **1998**, *331*, 254.

(126) Junge, D. M.; McGrath, D. V. *J. Am. Chem. Soc.* **1999**, *121*, 4912.

(127) Li, S.; McGrath, D. V. *J. Am. Chem. Soc.* **2000**, *122*, 6795.

(128) Decher, G.; Hong, J. D. *Berichte der Bunsen-Gesellschaft* **1991**, *95*, 1430.

(129) Decher, G.; Schmitt, J. *Prog. Colloid Polym. Sci.* **1992**, *89*, 160.

(130) Decher, G.; Hong, J. D.; Schmitt, J. *Thin Solid Films* **1991**, *210-211*, 831.

(131) Decher, G. *Science* **1997**, *277*, 1232.

(132) Knoll, W. *Curr. Opin. Colloid Interface Sci.* **1996**, *1*, 137.

(133) Decher, G.; Eckle, M.; Schmitt, J.; Struth, B. *Curr. Opin. Colloid Interface Sci.* **1998**, *3*, 32.

(134) Hammond, P. T. *Curr. Opin. Colloid Interface Sci.* **1999**, *4*, 430.

(135) Sukhorukov, G. B.; Schmitt, J.; Decher, G. *Berichte der Bunsen-Gesellschaft* **1996**, *100*, 948.

(136) Lösche, M.; Schmitt, J.; Decher, G.; Bouwman, W. G.; Kjaer, K. *Macromol.* **1998**, *31*, 8893.

(137) Linford, M. R.; Auch, M.; Möhwald, H. *J. Am. Chem. Soc.* **1998**, *120*, 178.

(138) Steitz, R.; Leiner, V.; Siebrecht, R.; Klitzing, R. v. *Colloids Surf., A* **2000**, *163*, 63.

(139) Shiratori, S. S.; Rubner, M. F. *Macromol.* **2000**, *33*, 4213.

(140) Chung, A. J.; Rubner, M. F. *Langmuir* **2002**, *18*, 1176.

(141) Wang, T. C.; Rubner, M. F.; Cohen, R. E. *Langmuir* **2002**, *18*, 3370.

(142) Burke, S. E.; Barrett, C. J. *Langmuir* **2003**, *19*, 3297.

(143) Dubas, S. T.; Schlenoff, J. B. *Macromol.* **1999**, *32*, 8153.

(144) Rmaile, H. H.; Schlenoff, J. B. *J. Am. Chem. Soc.* **2003**, *125*, 6602.

(145) Mendelsohn, J. D.; Barrett, C. J.; Chan, V. V.; Pal, A. J.; Mayes, A. M.; Rubner, M. F. *Langmuir* **2000**, *16*, 5017.

(146) Antipov, A. A.; Sukhorukov, G. B.; Möhwald, H. *Langmuir* **2003**, *19*, 2444.

(147) McAloney, R. A.; Dudnik, V.; Goh, M. C. *Langmuir* **2003**, *19*, 3947.

(148) Dragan, S.; Schwarz, S.; Eichhorn, K.-J.; Lunkwitz, K. *Colloids Surf., A* **2003**, *195*, 243.

(149) Cho, J.; Char, K.; Hong, J.-D.; Lee, K.-B. *Adv. Mater.* **2001**, *13*, 1076.

(150) Lee, S.-S.; Hong, J.-D.; Kim, C. H.; Kim, K.; Koo, J. P.; Lee, K.-B. *Macromol.* **2001**, *34*, 5358.

(151) Chiarelli, P. A.; Johal, M. S.; Casson, J. L.; Roberts, J. B.; Robinson, J. M.; Wang, H.-L. *Adv. Mater.* **2001**, *13*, 1167.

(152) Lee, S.-S.; Lee, K.-B.; Hong, J.-D. *Langmuir* **2003**, *19*, 7592.

(153) Sukhorukov, G. B.; Donath, E.; Lichtenfeld, H.; Knippel, E.; Knippel, M.; Budde, A.; Möhwald, H. *Colloids Surf., A* **1998**, *137*, 253.

(154) Caruso, F. *Adv. Mater.* **2001**, *13*, 11.

(155) Sukhorukov, G. B.; Donath, E.; Davis, S.; Lichtenfeld, H.; Caruso, F.; Popov, V. I.; Möhwald, H. *Polym. Adv. Technol.* **1998**, *9*, 759.

(156) Mermut, O.; Barrett, C. J. *Analyst (Cambridge, U. K.)* **2001**, *126*, 1861.

(157) Richert, L.; Lavalle, P.; Vautier, D.; Senger, B.; Stoltz, J.-F.; Schaaf, P.; Voegel, J.-C.; Picart, C. *Biomacromolecules* **2002**, *3*, 1170.

(158) Jin, W.; Shi, X.; Caruso, F. *J. Am. Chem. Soc.* **2001**, *123*, 8121.

(159) Diaspro, A.; Silvano, D.; Krol, S.; Cavalleri, O.; Gliozzi, A. *Langmuir* **2002**, *18*, 5047.

(160) Thierry, B.; Winnik, F. M.; Merhi, Y.; Tabrizian, M. *J. Am. Chem. Soc.* **2003**, *125*, 7494.

(161) He, J.-A.; Bian, S.; Li, L.; Kumar, J.; Tripathy, S. K.; Samuelson, L. A. *J. Phys. Chem. B* **2000**, *104*, 10513.

(162) Balasubramanian, S.; Wang, X.; Wang, H. C.; Yang, K.; Kumar, J.; Tripathy, S. K.; Li, L. *Chem. Mater.* **1998**, *10*, 1554.

(163) Burke, S. E.; Barrett, C. J. *Biomacromolecules* **2003**, *4*, 1773.

(164) Caruso, F.; Möhwald, H. *J. Am. Chem. Soc.* **1999**, *1212*, 6039.

(165) Lvov, Y.; Ariga, K.; Onda, M.; Ichinose, I.; Kunitake, T. *Langmuir* **1997**, *13*, 6195.

(166) Kotov, N. A.; Dekany, I.; Fendler, J. H. *J. Phys. Chem.* **1995**, *99*, 13065.

(167) Kleinfeld, E. R.; Ferguson, G. S. *Science* **1994**, *265*, 370.

(168) Tang, Z.; Kotov, N. A.; Magonov, S.; Ozturk, B. *Nat. Mater.* **2003**, *2*, 413.

(169) Watanabe, S.; Regen, S. L. *J. Am. Chem. Soc.* **1994**, *116*, 8855

(170) Mattoussi, H.; Rubner, M. F.; Zhou, F.; Kumar, J.; Tripathy, S. K. *Appl. Phys. Lett.* **2000**, *77*, 1540.

(171) Rouse, J. H.; Ferguson, C. S. *Langmuir* **2002**, *18*, 7635.

(172) Advincula, R. C.; Fells, E.; Park, M.-K. *Chem. Mater.* **2001**, *13*, 2870.

(173) Advincula, R. C. In *Handbook of Polyelectrolytes and Their Applications*; Tripathy, S. K.; Kumar, J.; Nalwa, H. S., Eds.; American Scientific Publishers: Stevenson Ranch, Calif., 2002; Vol. 1, pp 65.

(174) Ishikawa, J.; Baba, A.; Kaneko, F.; Shinbo, K.; Kato, K.; Advincula, R. C. *Colloids Surf., A* **2002**, *198-200*, 917.

(175) Advincula, R.; Park, M.-K.; Baba, A.; Kaneko, F. *Langmuir* **2003**, *19*, 654.

(176) Lee, S.-H.; Balasubramanian, S.; Kim, D. Y.; Viswanathan, N. K.; Bian, S.; Kumar, J.; Tripathy, S. K. *Macromol.* **2000**, *33*, 6534.

(177) Saremi, F.; Tieke, B. *Adv. Mater.* **1998**, *10*, 389.

(178) Toutianoush, A.; Saremi, F.; Tieke, B. *Mater. Sci. Eng., C* **1999**, *C8-C9*, 343.

(179) Toutianoush, A.; Tieke, B. *Macromol. Rapid Commun.* **1998**, *19*, 591.

(180) Ziegler, A.; Stumpe, J.; Toutianoush, A.; Tieke, B. *Colloids Surf., A* **2002**, *198-200*, 777.

(181) Van Cott, K. E.; Guzy, M.; Neyman, P.; Brands, C.; Heflin, J. R.; Gibson, H. W.; Davis, R. M. *Angew. Chem., Int. Ed.* **2002**, *41*, 3236.

(182) Mermut, O.; Barrett, C. J. *J. Phys. Chem. B* **2003**, *107*, 2525.

(183) Mermut, O.; Lefebvre, J.; Gray, D. G.; Barrett, C. J. *Macromol.* **2003**, *36*, 8819.

(184) Suzuki, I.; Sato, K.; Koga, M.; Chen, Q.; Anzai, J.-i. *Materials Science and Engineering: C* **2003**, *23*, 579.

(185) Wu, L.; Tuo, X.; Cheng, H.; Chen, Z.; Wang, X. *Macromol.* **2001**, *34*, 8005.

(186) Hong, J.-D.; Jung, B.-D.; Kim, C. H.; Kim, K. *Macromol.* **2000**, *33*, 7905.

(187) Jung, B.-D.; Hong, J.-D.; Voigt, A.; Leporatti, S.; Dähne, L.; Donath, E.; Möhwald, H. *Colloids Surf., A* **2002**, *198-200*, 483.

(188) Wang, X.; Balasubramanian, S.; Kumar, J.; Tripathy, S. K.; Li, L. *Chem. Mater.* **1998**, *10*, 1546.

(189) Wang, H.; He, Y.; Tuo, X.; Wang, X. *Macromol.* **2004**, *37*, 135.

(190) Park, M.-K.; Advincula, R. C. *Langmuir* **2002**, *18*, 4532.

(191) Bian, S.; He, J.-A.; Li, L.; Kumar, J.; Tripathy, S. K. *Adv. Mater.* **2000**, *12*, 1202.

(192) dos Santos Jr., D. S.; Bassi, A.; Rodrigues Jr., J. J.; Misoguti, L.; Oliveira Jr., O. N.; Mendonça, C. R. *Biomacromolecules* **2003**, *4*, 1502.

(193) He, J.-A.; Bian, S.; Li, L.; Kumar, J.; Tripathy, S. K.; Samuelson, L. A. *Appl. Phys. Lett.* **2000**, *76*, 3233.

(194) Dante, S.; Advincula, R. C.; Frank, C. W.; Stroeve, P. *Langmuir* **1999**, *15*, 193.

(195) Zhai, L.; Cebeci, F. Ç.; Cohen, R. E.; Rubner, M. F. *Nano Lett.* **2004**, *4*, 1349.

(196) Nyamjav, D.; Ivanisevic, A. *Chem. Mater.* **2004**, *16*, 5216.

(197) Natansohn, A.; Rochon, P. *Chem. Rev.* **2002**, *102*, 4139.

(198) Uznanski, P.; Kryszewski, M.; Thulstrup, E. W. *Eur. Polym. J.* **1991**, *27*, 41.

(199) de Lange, J. J.; Robertson, J. M.; Woodward, I. *Proc. Roy. Soc. (London)* **1939**, *A171*, 398.

(200) Hampson, G. C.; Robertson, J. M. *Journal of the Chemical Society, Abstracts* **1941**, 409.

(201) Brown, C. J. *Acta Cryst.* **1966**, *21*, 146.

(202) Naito, T.; Horie, K.; Mita, I. *Polymer* **1993**, *34*, 4140.

(203) Weiss, R. G.; Ramamurthy, V.; Hammond, G. S. *Acc. Chem. Res.* **1993**, *25*, 530.

(204) Hugel, T.; Holland, N. B.; Cattani, A.; Moroder, L.; Seitz, M.; Gaub, H. E. *Science* **2002**, *296*, 1103.

(205) Holland, N. B.; Hugel, T.; Neuert, G.; Cattani-Scholz, A.; Renner, C.; Oesterhelt, D.; Moroder, L.; Seitz, M.; Gaub, H. E. *Macromol.* **2003**, *36*, 2015.

(206) Neuert, G.; Hugel, T.; Netz, R. R.; Gaub, H. E. *Macromol.* **2005**, *39*, 789.

(207) Asakawa, M.; Ashton, P. R.; Balzani, V.; Brown, C. L.; Credi, A.; Matthews, O. A.; Newton, S. P.; Raymo, F. M.; Shipway, A. N.; Spencer, N.; Quick, A.; Stoddart, J. F.; White, A. J. P.; Williams, D. J. *Chem.--Eur. J.* **1999**, *5*, 860.

(208) Balzani, V.; Credi, A.; Marchioni, F.; Stoddart, J. F. *Chem. Commun.* **2001**, *18*, 1860.

(209) Tsuchiya, S. *J. Am. Chem. Soc.* **1999**, *121*, 48.

(210) Steinem, C.; Janshoff, A.; Vollmer, M. S.; Ghadiri, M. R. *Langmuir* **1999**, *15*, 3956.

(211) Balasubramanian, D.; Subramani, S.; Kumar, C. *Nature* **1975**, *254*, 252.

(212) Lee, W.-S.; Ueno, A. *Macromol. Rapid Commun.* **2001**, *22*, 448.

(213) Ciardelli, F.; Pieroni, O. In *Molecular Switches*; Feringa, B. L., Ed., 2001; pp 399.

(214) Sisido, M.; Ishikawa, Y.; Itoh, K.; Tazuke, S. *Macromol.* **1991**, *24*, 3993.

(215) Pieroni, O.; Houben, J. L.; Fissi, A.; Costantino, P. *J. Am. Chem. Soc.* **1980**, *102*, 5913.

(216) Houben, J. L.; Fissi, A.; Bacciola, D.; Rosato, N.; Pieroni, O.; Ciardelli, F. *Int. J. Biol. Macromol.* **1983**, *5*, 94.

(217) Malcolm, B. R.; Pieroni, O. *Biopolymers* **1990**, *29*, 1121.

(218) Montagnoli, G.; Pieroni, O.; Suzuki, S. *Polymer Photochemistry* **1983**, *3*, 279.

(219) Yamamoto, H.; Nishida, A. *Polym. Int.* **1991**, *24*, 145.

(220) Fissi, A.; Pieroni, O.; Balestreri, E.; Amato, C. *Macromol.* **1996**, *29*, 4680.

(221) Fissi, A.; Pieroni, O.; Ciardelli, F. *Biopolymers* **1987**, *26*, 1993.

(222) Willner, I.; Rubin, S.; Riklin, A. *J. Am. Chem. Soc.* **1991**, *113*, 3321.

(223) Willner, I.; Rubin, S. *Reactive Polymers* **1993**, *21*, 177.

(224) Inada, T.; Terabayashi, T.; Yamaguchi, Y.; Kato, K.; Kikuchi, K. *J. Photochem. Photobiol., A* **2005**, *175*, 100.

(225) Willner, I.; Rubin, S.; Zor, T. *J. Am. Chem. Soc.* **1991**, *113*, 4013.

(226) Willner, I.; Rubin, S.; Shatzmiller, R.; Zor, T. *J. Am. Chem. Soc.* **1993**, *115*, 8690.

(227) Komori, K.; Yatagai, K.; Tatsuma, T. *J. Biotechnol.* **2004**, *108*, 11.

(228) Harvey, A. J.; Abell, A. D. *Tetrahedron* **2000**, *56*, 9763.

(229) Harvey, A. J.; Abell, A. D. *Bioorg. Med. Chem. Lett.* **2001**, *11*, 2441.

(230) Harada, M.; Sisido, M.; Hirose, J.; Nakanishi, M. *FEBS Lett.* **1991**, *286*, 6.

(231) Hohsaka, T.; Kawashima, K.; Sisido, M. *J. Am. Chem. Soc.* **1994**, *116*, 413.

(232) Wang, L.; Schultz, P. G. *Angew. Chem., Int. Ed.* **2004**, *44*, 34.

(233) Bose, M.; Groff, D.; Xie, J.; Brustad, E.; Schultz, P. G. *J. Am. Chem. Soc.* **2006**, *128*, 388.

(234) Nakayama, K.; Endo, M.; Majima, T. *Bioconjugate Chem.* **2005**, *16*, 1360.

(235) Nakayama, K.; Endo, M.; Majima, T. *Chem. Commun.* **2004**, 2386.

(236) Voinova, M. V.; Jonson, M. *Biosens. Bioelectron.* **2004**, *20*, 1106.

(237) Asanuma, H.; Liang, X.; Yoshida, T.; Komiyama, M. *ChemBioChem* **2001**, *2*, 39.

(238) Liang, X.; Asanuma, H.; Kashida, H.; Takasu, A.; Sakamoto, T.; Kawai, G.; Komiyama, M. *J. Am. Chem. Soc.* **2003**, *125*, 16408.

(239) Liu, M.; Asanuma, H.; Komiyama, M. *J. Am. Chem. Soc.* **2005**, *128*, 1009.

(240) Spörlein, S.; Carstens, H.; Satzger, H.; Renner, C.; Behrendt, R.; Moroder, L.; Tavan, P.; Zinth, W.; Wachtveitl, J. *Proc. Natl. Acad. Sci. U. S. A.* **2002**, *99*, 7998.

(241) Bredenbeck, J.; Helbing, J.; Behrendt, R.; Renner, C.; Moroder, L.; Wachtveitl, J.; Hamm, P. *J. Phys. Chem. B* **2003**, *107*, 8654.

(242) Yu, Y. L.; Ikeda, T. *J. Photochem. Photobiol., C* **2004**, *5*, 247.

(243) Ichimura, K.; Han, M. *Chem. Lett.* **2000**, *29*, 286.

(244) Natansohn, A.; Rochon, P.; Pezolet, M.; Audet, P.; Brown, D.; To, S. *Macromol.* **1994**, *27*, 2580.

(245) Hagen, R.; Bieringer, T. *Adv. Mater.* **2001**, *13*, 1805.

(246) Tawa, K.; Knoll, W. *Macromol.* **2002**, *35*, 7018.

(247) Hore, D. K.; Natansohn, A.; Rochon, P. L. *J. Phys. Chem. B* **2002**, *106*, 9004.

(248) Sekkat, Z.; Wood, J.; Knoll, W. *J. Phys. Chem.* **1995**, *99*, 17226.

(249) Buffeteau, T.; Labarthet, F. L.; Pézolet, M.; Sourisseau, C. *Macromol.* **2001**, *34*.

(250) Hore, D. K.; Natansohn, A. L.; Rochon, P. L. *J. Phys. Chem. B* **2003**, *107*, 2197.

(251) Holme, N. C. R.; Ramanujam, P. S.; Hvilsted, S. *Opt. Lett.* **1996**, *21*, 902.

(252) Lee, T. S.; Kim, D.-Y.; Jiang, X. L.; Li, L.; Kumar, J.; Tripathy, S. *J. Polym. Sci., Part A: Polym. Chem.* **1998**, *36*, 283.

(253) Xu, Z.-S.; Drnoyan, V.; Natansohn, A.; Rochon, P. *J. Polym. Sci., Part A: Polym. Chem.* **2000**, *38*, 2245.

(254) Wu, Y.; Natansohn, A.; Rochon, P. *Macromol.* **2001**, *34*, 7822.

(255) Hildebrandt, R.; Hegelich, M.; Keller, H.-M.; Marowsky, G.; Hvilsted, S.; Holme, N. C. R.; Ramanujam, P. S. *Phys. Rev. Lett.* **1998**, *81*, 5548.

(256) Cimrová, V.; Neher, D.; Hildebrandt, R.; Hegelich, M.; von der Lieth, A.; Marowsky, G.; Hagen, R.; Kostromine, S.; Bieringer, T. *Appl. Phys. Lett.* **2002**, *81*, 1228.

(257) Shi, Y.; Steier, W. H.; Yu, L.; Chen, M.; Dalton, L. R. *Appl. Phys. Lett.* **1991**, *59*, 2935.

(258) Natansohn, A.; Rochon, P. *Adv. Mater.* **1999**, *11*, 1387.

(259) Shi, Y.; Steier, W. H.; Yu, L.; Chen, M.; Dalton, L. R. *Appl. Phys. Lett.* **1991**, *58*, 1131.

(260) Watanabe, O.; Tsuchimori, M.; Okada, A. *J. Mater. Chem.* **1996**, *6*, 1487.

(261) Shishido, A.; Tsutsumi, O.; Kanazawa, A.; Shiono, T.; Ikeda, T.; Tamai, N. *J. Am. Chem. Soc.* **1997**, *119*, 7791.

(262) Eichler, H. J.; Orlic, S.; Schulz, R.; Rübner, J. *Opt. Lett.* **2001**, *26*, 581.

(263) Couture, J. J. A.; Lessard, R. A. *Appl. Opt.* **1988**, *27*, 3368.

(264) Nikolova, L.; Todorov, T.; Ivanov, M.; Andruzzi, F.; Hvilsted, S.; Ramanujam, P. S. *Appl. Opt.* **1996**, *35*, 3835.

(265) Yamamoto, T.; Ohashi, A.; Yoneyama, S.; Hasegawa, M.; Tsutsumi, O.; Kanazawa, A.; Shiono, T.; Ikeda, T. *J. Phys. Chem. B* **2001**, *105*, 2308.

(266) Eaton, D. F. *Science* **1991**, *253*, 281.

(267) Burland, D. M.; Miller, R. D.; Walsh, C. A. *Chem. Rev.* **1994**, *94*, 31.

(268) Dalton, L. R.; Harper, A. W.; Ghosn, R.; Steier, W. H.; Ziari, M.; Fetterman, H.; Shi, Y.; Mustacich, R. V.; Jen, A. K.-Y.; Shea, K. J. *Chem. Mater.* **1995**, *7*, 1060.

(269) Yesodha, S. K.; Pillai, C. K. S.; Tsutsumi, N. *Prog. Polym. Sci.* **2004**, *29*, 45.

(270) Brown, D.; Natansohn, A.; Rochon, P. *Macromol.* **1995**, *28*, 6116.

(271) Meng, X.; Natansohn, A.; Barrett, C.; Rochon, P. *Macromol.* **1996**, *29*, 946.

(272) Blanchard, P. M.; Mitchell, G. R. *Appl. Phys. Lett.* **1993**, *63*, 2038.

(273) Blanchard, P. M.; Mitchell, G. R. *J. Phys. D: Appl. Phys.* **1993**, *26*, 500.

(274) Sekkat, Z.; Kang, C.-S.; Aust, E. F.; Wegner, G.; Knoll, W. *Chem. Mater.* **1995**, *7*, 142.

(275) Jiang, X. L.; Li, L.; Kumar, J.; Tripathy, S. K. *Appl. Phys. Lett.* **1996**, *69*, 3629.

(276) Nunzi, J.-M.; Fiorini, C.; Etilé, A.-C.; Kajzar, F. *Pure Appl. Opt.* **1998**, *7*.

(277) Zhong, X.; Yu, X.; Li, Q.; Luo, S.; Chen, Y.; Sui, Y.; Yin, J. *Opt. Commun.* **2001**, *190*, 333.

(278) Yokoyama, S.; Nakahama, T.; Otomo, A.; Mashiko, S. *J. Am. Chem. Soc.* **2000**, *122*, 3174.

(279) Yamane, H.; Kikuchi, H.; Kajiyama, T. *Polymer* **1999**, *40*, 4777.

(280) Barrett, C.; Choudhury, B.; Natansohn, A.; Rochon, P. *Macromol.* **1998**, *31*, 4845.

(281) Iftime, G.; Labarthet, F. L.; Natansohn, A.; Rochon, P.; Murti, K. *Macromol.* **2002**, *14*, 168.

(282) Steenwinckel, D. V.; Hendrickx, E.; Persoons, A. *Chem. Mater.* **2001**, *14*, 1230.

(283) Prasad, S. K.; Nair, G. G. *Adv. Mater.* **2001**, *13*, 40.

(284) Ruslim, C.; Ichimura, K. *Adv. Mater.* **2001**, *13*, 37.

(285) Nikolova, L.; Todorov, T.; Ivanov, M.; Andruzzi, F.; Hvilsted, S.; Ramanujam, P. S. *Opt. Mater.* **1997**, *8*, 255.

(286) Ivanov, M.; Naydenova, I.; Todorov, T.; Nikolova, L.; Petrova, T.; Tomova, N.; Dragostinova, V. *J. Mod. Opt.* **2000**, *47*, 861.

(287) Nikolova, L.; Nedelchev, L.; Todorov, T.; Petrova, T.; Tomova, N.; Dragostinova, V.; Ramanujam, P. S.; Hvilsted, S. *Appl. Phys. Lett.* **2000**, *77*, 657.

(288) Sackmann, E. *J. Am. Chem. Soc.* **1971**, *93*, 7088.

(289) Everlof, G. J.; Jaycox, G. D. *Polymer* **2000**, *41*, 6527.

(290) Aoki, K. i.; Nakagawa, M.; Ichimura, K. *J. Am. Chem. Soc.* **2000**, *122*, 10997.

(291) Yamamoto, H.; Nishida, A.; Takimoto, T.; Nagai, A. *J. Polym. Sci., Part A: Polym. Chem.* **1990**, *28*, 67.

(292) Arai, K.; Kawabata, Y. *Macromol. Rapid Commun.* **1995**, *16*, 875.

(293) Ebralidze, T. D.; Mumladze, A. N. *Appl. Opt.* **1990**, *29*, 446.

(294) Effing, J. J.; Kwak, J. C. T. *Angew. Chem., Int. Ed. Engl.* **1995**, *34*, 88.

(295) Yang, L.; Takisawa, N.; Hayashita, T.; Shirahama, K. *J. Phys. Chem.* **1995**, *99*, 8799.

(296) Higuchi, M.; Minoura, N.; Kinoshita, T. *Chem. Lett.* **1994**, 227.

(297) Higuchi, M.; Minoura, N.; Kinoshita, T. *Macromol.* **1995**, *28*, 4981.

(298) Angiolini, L.; Caretti, D.; Carlini, C.; Salatelli, E. *Macromol. Chem. Phys.* **1995**, *196*, 2737.

(299) Chen, J. P.; Gao, J. P.; Wang, Z. Y. *J. Polym. Sci., Part A: Polym. Chem.* **1997**, *35*, 9.

(300) Maxein, G.; Zentel, R. *Macromol.* **1995**, *28*, 8438.

(301) Müller, M.; Zentel, R. *Macromol.* **1996**, *29*, 1609.

(302) Higuchi, M.; Minoura, N.; Kinoshita, T. *Colloid Polym. Sci.* **1995**, *273*, 1022.

(303) Siewierski, L. M.; Brittain, W. J.; Petrash, S.; Foster, M. D. *Langmuir* **1996**, *12*, 5838.

(304) Stiller, B.; Knochenhauer, G.; Markava, E.; Gustina, D.; Muzikante, I.; Karageorgiev, P.; Brehmer, L. *Materials Science and Engineering: C* **1999**, *8-9*, 385.

(305) Feng, C. L.; Zhang, Y. J.; Jin, J.; Song, Y. L.; Xie, L. Y.; Qu, G. R.; Jiang, L.; Zhu, D. B. *Langmuir* **2001**, *17*, 4593.

(306) Moller, G.; Harke, M.; Motschmann, H.; Prescher, D. *Langmuir* **1998**, *14*, 4955.

(307) Ichimura, K.; Oh, S.-K.; Nakagawa, M. *Science* **2000**, *288*, 1624.

(308) Jiang, W. H.; Wang, G. J.; He, Y. N.; Wang, X. G.; An, Y. L.; Song, Y. L.; Jiang, L. *Chem. Commun.* **2005**, 3550.

(309) Jiang, W. H.; Wang, G. J.; He, Y. N.; Wang, X. G.; An, Y. L.; Song, Y. L.; Jiang, L. *Chem. Commun.* **2005**, 3550.

(310) Fujita, T.; Iyi, N.; Klapyta, Z. *Mater. Res. Bull.* **1998**, *33*, 1693.

(311) Fujita, T.; Iyi, N.; Klapyta, Z. *Mater. Res. Bull.* **2001**, *36*, 557.

(312) Ivanov, M.; Todorov, T.; Nikolova, L.; Tomova, N.; Dragostinova, V. *Appl. Phys. Lett.* **1995**, *66*, 2174.

(313) Kleideiter, G.; Sekkat, Z.; Kreiter, M.; Lechner, M. D.; Knoll, W. *J. Mol. Struct.* **2000**, *521*, 167.

(314) Eisenbach, C. D. *Polymer* **1980**, *21*, 1175.

(315) Algers, J.; Sperr, P.; Egger, W.; Liszkay, L.; Kogel, G.; de Baerdemaeker, J.; Maurer, F. H. J. *Macromol.* **2004**, *37*, 8035.

(316) Yu, Y.; Nakano, M.; Ikeda, T. *Nature* **2003**, *425*, 145.

(317) Ikeda, T.; Nakano, M.; Yu, Y.; Tsutsumi, O.; Kanazawa, A. *Adv. Mater.* **2003**, *15*, 201.

(318) Yu, Y. L.; Nakano, M.; Maeda, T.; Kondo, M.; Ikeda, T. *Mol. Cryst. Liq. Cryst.* **2005**, *436*, 1235.

(319) Camacho-Lopez, M.; Finkelmann, H.; Palffy-Muhoray, P.; Shelley, M. *Nat. Mater.* **2004**, *3*, 307.

(320) Bublitz, D.; Helgert, M.; Fleck, B.; Wenke, L.; Hvilsted, S.; Ramanujam, P. S. *Appl. Phys. B: Lasers Opt.* **2000**, *70*, 863.

(321) Ji, H. F.; Feng, Y.; Xu, X. H.; Purushotham, V.; Thundat, T.; Brown, G. M. *Chem. Commun.* **2004**, 2532.

(322) Bai, S.; Zhao, Y. *Macromol.* **2001**, *34*, 9032.

(323) Barley, S. H.; Gilbert, A.; Mitchell, G. R. *J. Mater. Chem.* **1991**, *1*, 481.

(324) Sumaru, K.; Inui, S.; Yamanaka, T. *Opt Eng* **1999**, *38*, 274.

(325) Anzai, J.-I.; Osa, T. *Tetrahedron* **1994**, *50*, 4039.

(326) Willner, I.; Willner, B. *Adv. Mater.* **1997**, *9*, 351.

(327) Tokuhisa, H.; Yokoyama, M.; Kimura, K. *Macromol.* **1994**, *27*, 1842.

(328) Zawisza, I.; Bilewicz, R.; Luboch, E.; Biernat, J. F. *Thin Solid Films* **1999**, *348*, 173.

(329) Reynier, N.; Dozol, J.-F.; Saadioui, M.; Asfari, Z.; Vicens, J. *Tetrahedron Lett.* **1998**, *39*, 6461.

(330) Kano, K.; Tanaka, Y.; Ogawa, T.; Shimoura, M.; Okahata, Y.; Kunitake, T. *Chem. Lett.* **1980**, 421.

(331) Abraham, G.; Purushothaman, E. *Indian J. Chem. Technol.* **1998**, *5*, 213.

(332) Sata, T.; Shimokawa, Y.; Matsusaki, K. *J. Membr. Sci.* **2000**, *171*, 31.

(333) Liu, N.; Dunphy, D. R.; Atanassov, P.; Bunge, S. D.; Chen, Z.; López, G. P.; Boyle, T. J.; Brinker, C. J. *Nano Lett.* **2004**, *4*, 551.

(334) Lien, L.; Jaikaran, D. C. J.; Zhang, Z.; Woolley, G. A. *J. Am. Chem. Soc.* **1996**, *118*, 12222.

(335) Wuerthner, F.; Rebek, J., Jr. *Angew. Chem., Int. Ed. Engl.* **1995**, *34*, 446.

(336) Minoura, N.; Idei, K.; Rachkov, A.; Choi, Y.-W.; Ogiso, M.; Matsuda, K. *Macromol.* **2004**, *37*, 9571.

(337) Uznanski, P.; Pecherz, J. *J. Appl. Polym. Sci.* **2002**, *86*, 1459.

(338) Yamamoto, H. *Macromol.* **1986**, *19*, 2472.

(339) Li, Y.; Deng, Y.; Tong, X.; Wang, X. *Macromol.* **2006**, *39*, 1108.

(340) Liu, Z. F.; Hashimoto, K.; Fujishima, A. *Nature* **1990**, *347*, 658.

(341) Dhanabalan, A.; Dos Santos Jr., D. S.; Mendonça, C. R.; Misoguti, L.; Balogh, D. T.; Giacometti, J. A.; Zilio, S. C.; Oliveira Jr., O. N. *Langmuir* **1999**, *15*, 4560.

(342) Sabi, Y.; Yamamoto, M.; Watanabe, H.; Bieringer, T.; Haarer, D.; Hagen, R.; Kostromine, S. G.; Berneth, H. *Jpn. J. Appl. Phys., Part 1* **2001**, *40*, 1613.

(343) Ishikawa, M.; Kawata, Y.; Egami, C.; Sugihara, O.; Okamoto, N.; Tsuchimori, M.; Watanabe, O. *Opt. Lett.* **1998**, *23*, 1781.

(344) Kawata, S.; Kawata, Y. *Chem. Rev.* **2000**, *100*, 1777.

(345) Ramanujam, P. S.; Hvilsted, S.; Ujhelyi, F.; Koppa, P.; Lörincz, E.; Erdei, G.; Szarvas, G. *Synth. Met.* **2001**, *124*, 145.

(346) Zilker, S. J.; Bieringer, T.; Haarer, D.; Stein, R. S.; van Egmond, J. W.; Kostromine, S. G. *Adv. Mater.* **1998**, *10*, 855.

(347) Berg, R. H.; Hvilsted, S.; Ramanujam, P. S. *Nature* **1996**, *383*, 505.

(348) Rochon, P.; Batalla, E.; Natansohn, A. *Appl. Phys. Lett.* **1995**, *66*, 136.

(349) Kim, D. Y.; Tripathy, S. K.; Li, L.; Kumar, J. *Appl. Phys. Lett.* **1995**, *66*, 1166.

(350) Yamaki, S.; Nakagawa, M.; Morino, S.; Ichimura, K. *Appl. Phys. Lett.* **2000**, *76*, 2520.

(351) Yager, K. G.; Barrett, C. J. *Current Opinion in Solid State & Materials Science* **2001**, *5*, 487.

(352) Kim, D. Y.; Li, L.; Jiang, X. L.; Shivshankar, V.; Kumar, J.; Tripathy, S. K. *Macromol.* **1995**, *28*, 8835.

(353) Barrett, C. J.; Natansohn, A. L.; Rochon, P. L. *J. Phys. Chem.* **1996**, *100*, 8836.

(354) Bian, S. P.; Williams, J. M.; Kim, D. Y.; Li, L. A.; Balasubramanian, S.; Kumar, J.; Tripathy, S. *J. Appl. Phys.* **1999**, *86*, 4498.

(355) Fukuda, T.; Matsuda, H.; Shiraga, T.; Kimura, T.; Kato, M.; Viswanathan, N. K.; Kumar, J.; Tripathy, S. K. *Macromol.* **2000**, *33*, 4220.

(356) Sanchez, C.; Alcala, R.; Hvilsted, S.; Ramanujam, P. S. *Appl. Phys. Lett.* **2000**, *77*, 1440.

(357) Jager, C.; Bieringer, T.; Zilker, S. J. *Appl. Opt.* **2001**, *40*, 1776.

(358) Kim, D. Y.; Lee, T. S.; Tripathy, S. K.; Jiang, X. L.; Li, L.; Kumar, J. *Macromol. Symp.* **1997**, *116*, 127.

(359) Kumar, J.; Li, L.; Jiang, X. L.; Kim, D. Y.; Lee, T. S.; Tripathy, S. *Appl. Phys. Lett.* **1998**, *72*, 2096.

(360) Bian, S.; Li, L.; Kumar, J.; Kim, D. Y.; Williams, J.; Tripathy, S. K. *Appl. Phys. Lett.* **1998**, *73*, 1817.

(361) Holme, N. C. R.; Nikolova, L.; Hvilsted, S.; Rasmussen, P. H.; Berg, R. H.; Ramanujam, P. S. *Appl. Phys. Lett.* **1999**, *74*, 519.

(362) Helgert, M.; Wenke, L.; Hvilsted, S.; Ramanujam, P. S. *Appl. Phys. B: Lasers Opt.* **2001**, *72*, 429.

(363) Zettsu, N.; Fukuda, T.; Matsuda, H.; Seki, T. *Appl. Phys. Lett.* **2003**, *83*, 4960.

(364) Naydenova, I.; Nikolova, L.; Todorov, T.; Holme, N. C. R.; Ramanujam, P. S.; Hvilsted, S. *J. Opt. Soc. Am. B* **1998**, *15*, 1257.

(365) Labarthet, F. L.; Bruneel, J. L.; Buffeteau, T.; Sourisseau, C.; Huber, M. R.; Zilker, S. J.; Bieringer, T. *Phys. Chem. Chem. Phys.* **2000**, *2*, 5154.

(366) Labarthet, F. L.; Buffeteau, T.; Sourisseau, C. *J. Appl. Phys.* **2001**, *90*, 3149.

(367) Lagugne-Labarthet, F.; Bruneel, J. L.; Rodriguez, V.; Sourisseau, C. *J. Phys. Chem. B* **2004**, *108*, 1267.

(368) Schaller, R. D.; Saykally, R. J.; Shen, Y. R.; Lagugne-Labarthet, F. *Opt. Lett.* **2003**, *28*, 1296.

(369) Jiang, X. L.; Kumar, J.; Kim, D. Y.; Shivshankar, V.; Tripathy, S. K. *Appl. Phys. Lett.* **1996**, *68*, 2613.

(370) Viswanathan, N. K.; Balasubramanian, S.; Li, L.; Tripathy, S. K.; Kumar, J. *Jpn J Appl Phys 1* **1999**, *38*, 5928.

(371) Jiang, X. L.; Li, L.; Kumar, J.; Kim, D. Y.; Tripathy, S. K. *Appl. Phys. Lett.* **1998**, *72*, 2502.

(372) Lagugne-Labarthet, F.; Buffeteau, T.; Sourisseau, C. *Phys. Chem. Chem. Phys.* **2002**, *4*, 4020.

(373) Labarthet, F. L.; Bruneel, J. L.; Buffeteau, T.; Sourisseau, C. *J. Phys. Chem. B* **2004**, *108*, 6949.

(374) Henneberg, O.; Geue, T.; Pietsch, U.; Saphiannikova, M.; Winter, B. *Appl. Phys. Lett.* **2004**, *84*, 1561.

(375) Pietsch, U.; Rochon, P.; Natansohn, A. *Adv Mater* **2000**, *12*, 1129.

(376) Geue, T.; Henneberg, O.; Grenzer, J.; Pietsch, U.; Natansohn, A.; Rochon, P.; Finkelstein, K. *Colloid Surface A* **2002**, *198-200*, 31.

(377) Geue, T. M.; Saphiannikova, M. G.; Henneberg, O.; Pietsch, U.; Rochon, P. L.; Natansohn, A. L. *J. Appl. Phys.* **2003**, *93*, 3161.

(378) Pietsch, U. *Phys Rev B* **2002**, *66*, 155430.

(379) Watanabe, O.; Ikawa, T.; Hasegawa, M.; Tsuchimori, M.; Kawata, Y.; Egami, C.; Sugihara, O.; Okamoto, N. *Mol. Cryst. Liq. Cryst.* **2000**, *345*, 629.

(380) Ikawa, T.; Mitsuoka, T.; Hasegawa, M.; Tsuchimori, M.; Watanabe, O.; Kawata, Y.; Egami, C.; Sugihara, O.; Okamoto, N. *J. Phys. Chem. B* **2000**, *104*, 9055.

(381) Keum, C. D.; Ikawa, T.; Tsuchimori, M.; Watanabe, O. *Macromol.* **2003**, *36*, 4916.

(382) Yang, S. Z.; Li, L.; Cholli, A. L.; Kumar, J.; Tripathy, S. K. *J Macromol Sci Pure* **2001**, *38*, 1345.

(383) Yang, S.; Jacob, M. M.; Li, L.; Yang, K.; Cholli, A. L.; Kumar, J.; Tripathy, S. K. *Polymer News* **2002**, *27*, 368.

(384) Yang, S. Z.; Li, L.; Cholli, A. L.; Kumar, J.; Tripathy, S. K. *Biomacromolecules* **2003**, *4*, 366.

(385) Nakano, H.; Takahashi, T.; Kadota, T.; Shirota, Y. *Adv Mater* **2002**, *14*, 1157.

(386) Kim, M.-J.; Seo, E.-M.; Vak, D.; Kim, D.-Y. *Chem. Mater.* **2003**, *15*, 4021.

(387) Chun, C. M.; Kim, M. J.; Vak, D.; Kim, D. Y. *J. Mater. Chem.* **2003**, *13*, 2904.

(388) Ando, H.; Takahashi, T.; Nakano, H.; Shirota, Y. *Chem. Lett.* **2003**, *32*, 710.

(389) Ciuchi, F.; Mazzulla, A.; Cipparrone, G. *J. Opt. Soc. Am. B* **2002**, *19*, 2531.

(390) Naydenova, I.; Petrova, T.; Tomova, N.; Dragostinova, V.; Nikolova, L.; Todorov, T. *Pure Appl. Opt.* **1998**, *7*, 723.

(391) Ishow, E.; Lebon, B.; He, Y.; Wang, X.; Bouteiller, L.; Galmiche, L.; Nakatani, K. *Chem. Mater.* **2006**, *18*, 1261.

(392) Ubukata, T.; Seki, T.; Ichimura, K. *Adv Mater* **2000**, *12*, 1675.

(393) Ubukata, T.; Seki, T.; Ichimura, K. *Colloid Surface A* **2002**, *198*, 113.

(394) Ramanujam, P. S.; Holme, N. C. R.; Hvilsted, S. *Appl. Phys. Lett.* **1996**, *68*, 1329.

(395) Archut, A.; Vögtle, F.; Cola, L. D.; Azzellini, G. C.; Balzani, V.; Ramanujam, P. S.; Berg, R. H. *Chem.--Eur. J.* **1998**, *4*, 699.

(396) Andruzzi, L.; Altomare, A.; Ciardelli, F.; Solaro, R.; Hvilsted, S.; Ramanujam, P. S. *Macromol.* **1999**, *32*, 448.

(397) Borger, V.; Kuliskovska, O.; Hubmann, K. G.; Stumpe, J.; Huber, M.; Menzel, H. *Macromol Chem Physic* **2005**, *206*, 1488.

(398) Natansohn, A.; Xie, S.; Rochon, P. *Macromol.* **1992**, *25*, 5531.

(399) Ho, M. S.; Natansohn, A.; Rochon, P. *Macromol.* **1995**, *28*, 6124.

(400) Chen, J. P.; Labarthet, F. L.; Natansohn, A.; Rochon, P. *Macromol.* **1999**, *32*, 8572.

(401) Wu, Y. L.; Natansohn, A.; Rochon, P. *Macromol.* **2001**, *34*, 7822.

(402) Viswanathan, N. K.; Balasubramanian, S.; Li, L.; Kumar, J.; Tripathy, S. K. *J. Phys. Chem. B* **1998**, *102*, 6064.

(403) Geue, T. M.; Saphiannikova, A. G.; Henneberg, O.; Pietsch, U.; Rochon, P. L.; Natansohn, A. L. *Phys Rev E* **2002**, *65*, 052801.

(404) Kameda, M.; Sumaru, K.; Kanamori, T.; Shinbo, T. *J. Appl. Polym. Sci.* **2003**, *88*, 2068.

(405) Sharma, L.; Matsuoka, T.; Kimura, T.; Matsuda, H. *Polym. Adv. Technol.* **2002**, *13*, 481.

(406) Yang, K.; Yang, S. Z.; Wang, X. G.; Kumar, J. *Appl. Phys. Lett.* **2004**, *84*, 4517.

(407) Kumar, G. S.; DePra, P.; Zhang, K.; Neckers, D. C. *Macromol.* **1984**, *17*, 2463.

(408) Bhatnagar, A.; Mueller, J.; Osborn, D. J.; Martin, T. L.; Wirtz, J.; Mohanty, D. K. *Polymer* **1995**, *36*, 3019.

(409) Moniruzzaman, M.; Sabey, C. J.; Fernando, G. F. *Macromol.* **2004**, *37*, 2572.

(410) Forrest, J. A.; Dalnoki-Veress, K. *Adv. Colloid Interface Sci.* **2001**, *94*, 167.

(411) Srikhirin, T.; Laschitsch, A.; Neher, D.; Johannsmann, D. *Appl. Phys. Lett.* **2000**, *77*, 963.

(412) Mechau, N.; Neher, D.; Borger, V.; Menzel, H.; Urayama, K. *Appl. Phys. Lett.* **2002**, *81*, 4715.

(413) Mechau, N.; Saphiannikova, M.; Neher, D. *Macromol.* **2005**, *38*, 3894.

(414) Stiller, B.; Karageirgiev, P.; Geue, T.; Morawetz, K.; Saphiannikova, M.; Mechau, N.; Neher, D. *Phys Low-Dimens Str* **2004**, *1-2*, 129.

(415) Holme, N. C. R.; Nikolova, L.; Ramanujam, P. S.; Hvilsted, S. *Appl. Phys. Lett.* **1997**, *70*, 1518.

(416) Labarthet, F. L.; Rochon, P.; Natansohn, A. *Appl. Phys. Lett.* **1999**, *75*, 1377.

(417) Helgert, M.; Fleck, B.; Wenke, L.; Hvilsted, S.; Ramanujam, P. S. *Appl Phys B-Lasers O* **2000**, *70*, 803.

(418) Geue, T.; Henneberg, O.; Pietsch, U. *Cryst. Res. Technol.* **2002**, *37*, 770.

(419) Geue, T.; Schultz, M.; Grenzer, J.; Pietsch, U.; Natansohn, A.; Rochon, P. *J. Appl. Phys.* **2000**, *87*, 7712.

(420) Henneberg, O.; Geue, T.; Saphiannikova, M.; Pietsch, U.; Rochon, P.; Natansohn, A. *Appl. Surf. Sci.* **2001**, *182*, 272.

(421) Henneberg, O.; Geue, T.; Rochon, P.; Pietsch, U. *J Phys D Appl Phys* **2003**, *36*, A241.

(422) Saphiannikova, M.; Henneberg, O.; Gene, T. M.; Pietsch, U.; Rochon, P. *J. Phys. Chem. B* **2004**, *108*, 15084.

(423) Henneberg, O.; Geue, T.; Saphiannikova, M.; Pietsch, U.; Chi, L. F.; Rochon, P.; Natansohn, A. L. *Appl. Phys. Lett.* **2001**, *79*, 2357.

(424) Stracke, A.; Wendorff, J. H.; Goldmann, D.; Janietz, D.; Stiller, B. *Adv. Mater.* **2000**, *12*, 282.

(425) Kawatsuki, N.; Uchida, E.; Ono, H. *Appl. Phys. Lett.* **2003**, *83*, 4544.

(426) Barrett, C. J.; Rochon, P. L.; Natansohn, A. L. *J. Chem. Phys.* **1998**, *109*, 1505.

(427) Sumaru, K.; Yamanaka, T.; Fukuda, T.; Matsuda, H. *Appl. Phys. Lett.* **1999**, *75*, 1878.

(428) Fukuda, T.; Sumaru, K.; Yamanaka, T.; Matsuda, H. *Mol. Cryst. Liq. Cryst.* **2000**, *345*, 587.

(429) Bublitz, D.; Fleck, B.; Wenke, L. *Appl Phys B-Lasers O* **2001**, *72*, 931.

(430) Saphiannikova, M.; Geue, T. M.; Henneberg, O.; Morawetz, K.; Pietsch, U. *J. Chem. Phys.* **2004**, *120*, 4039.

(431) Pawlik, G.; Mitus, A. C.; Miniewicz, A.; Kajzar, F. *J. Chem. Phys.* **2003**, *119*, 6789.

(432) Mitus, A. C.; Pawlik, G.; Miniewicz, A.; Kajzar, F. *Mol. Cryst. Liq. Cryst.* **2004**, *416*, 113.

(433) Pawlik, G.; Mitus, A. C.; Miniewicz, A.; Kajzar, F. *Journal of Nonlinear Optical Physics & Materials* **2004**, *13*, 481.

(434) Yager, K. G.; Barrett, C. J. *J. Chem. Phys.* **2004**, *120*, 1089.

(435) Schmitt, K.; Benecke, C.; Schadt, M. *Appl. Opt.* **1997**, *36*, 5078.

(436) Ramanujam, P. S.; Pedersen, M.; Hvilsted, S. *Appl. Phys. Lett.* **1999**, *74*, 3227.

(437) Leopold, A.; Wolff, J.; Baldus, O.; Huber, M. R.; Bieringer, T.; Zilker, S. J. *J. Chem. Phys.* **2000**, *113*, 833.

(438) Si, J. H.; Qiu, J. R.; Zhai, J. F.; Shen, Y. Q.; Hirao, K. *Appl. Phys. Lett.* **2002**, *80*, 359.

(439) Baldus, O.; Leopold, A.; Hagen, R.; Bieringer, T.; Zilker, S. J. *J. Chem. Phys.* **2001**, *114*, 1344.

(440) Lefin, P.; Fiorini, C.; Nunzi, J. M. *Opt. Mater.* **1998**, *9*, 323.

(441) Lefin, P.; Fiorini, C.; Nunzi, J. M. *Pure Appl. Opt.* **1998**, *7*, 71.

(442) Pedersen, T. G.; Johansen, P. M. *Phys. Rev. Lett.* **1997**, *79*, 2470.

(443) Pedersen, T. G.; Johansen, P. M.; Holme, N. C. R.; Ramanujam, P. S.; Hvilsted, S. *Phys. Rev. Lett.* **1998**, *80*, 89.

(444) Baldus, O.; Zilker, S. J. *Appl Phys B-Lasers O* **2001**, *72*, 425.

(445) Bian, S. P.; Liu, W.; Williams, J.; Samuelson, L.; Kumar, J.; Tripathy, S. *Chem. Mater.* **2000**, *12*, 1585.

(446) Yang, K.; Yang, S. Z.; Kumar, J. *Phys Rev B* **2006**, *73*.

(447) Ashkin, A. *Phys. Rev. Lett.* **1970**, *24*, 156.

(448) Ashkin, A. *Proc. Natl. Acad. Sci. U. S. A.* **1997**, *94*, 4853.

(449) Chaumet, P. C.; Nieto-Vesperinas, M. *Opt. Lett.* **2000**, *25*, 1065.

(450) Ikawa, T.; Mitsuoka, T.; Hasegawa, M.; Tsuchimori, M.; Watanabe, O.; Kawata, Y. *Phys Rev B* **2001**, *64*.

(451) Gordon, J. P. *Phys. Rev. A* **1973**, *8*, 14.

(452) Matsumoto, M.; Miyazaki, D.; Tanaka, M.; Azumi, R.; Manda, E.; Kondo, Y.; Yoshino, N.; Tachibana, H. *J. Am. Chem. Soc.* **1998**, *120*, 1479.

(453) Hubert, C.; Fiorini-Debuisschert, C.; Maurin, I.; Nunzi, J. M.; Raimond, P. *Adv Mater* **2002**, *14*, 729.

(454) Hubert, C.; Malcor, E.; Maurin, I.; Nunzi, J. M.; Raimond, P.; Fiorini, C. *Appl. Surf. Sci.* **2002**, *186*, 29.

(455) Ciuchi, F.; Mazzulla, A.; Carbone, G.; Cipparrone, G. *Macromol.* **2003**, *36*, 5689.

(456) Zettsu, N.; Ubukata, T.; Seki, T.; Ichimura, K. *Adv Mater* **2001**, *13*, 1693.

(457) Tripathy, S. K.; Viswanathan, N. K.; Balasubramanian, S.; Kumar, J. *Polym. Adv. Technol.* **2000**, *11*, 570.

(458) Rochon, P.; Natansohn, A.; Callendar, C. L.; Robitaille, L. *Appl. Phys. Lett.* **1997**, *71*, 1008.

(459) Stockermans, R. J.; Rochon, P. L. *Appl. Opt.* **1999**, *38*, 3714.

(460) Paterson, J.; Natansohn, A.; Rochon, P.; Callendar, C. L.; Robitaille, L. *Appl. Phys. Lett.* **1996**, *69*, 3318.

(461) Nagata, T.; Matsui, T.; Ozaki, M.; Yoshino, K.; Kajzar, F. *Synth. Met.* **2001**, *119*, 607.

(462) Dumarcher, V.; Rocha, L.; Denis, C.; Fiorini, C.; Nunzi, J.-M.; Sobel, F.; Sahraoui, B.; Gindre, D. *J. Opt. A: Pure Appl. Opt.* **2000**, *2*, 279.

(463) Rocha, L.; Dumarcher, V.; Denis, C.; Raimond, P.; Fiorini, C.; Nunzi, J. M. *J. Appl. Phys.* **2001**, *89*, 3067.

(464) Egami, C.; Kawata, Y.; Aoshima, Y.; Alasfar, S.; Sugihara, O.; Fujimura, H.; Okamoto, N. *Jpn J Appl Phys 1* **2000**, *39*, 1558.

(465) Neumann, J.; Wieking, K. S.; Kip, D. *Appl. Opt.* **1999**, *38*, 5418.

(466) Li, X. T.; Natansohn, A.; Rochon, P. *Appl. Phys. Lett.* **1999**, *74*, 3791.

(467) Kim, M.-H.; Kim, J.-D.; Fukuda, T.; Matsuda, H. *Liq. Cryst.* **2000**, *27*, 1633.

(468) Parfenov, A.; Tamaoki, N.; Ohnishi, S. *J. Appl. Phys.* **2000**, *87*, 2043.

(469) Parfenov, A.; Tamaoki, N.; Ohni-Shi, S. *Mol. Cryst. Liq. Cryst.* **2001**, *359*, 487.

(470) Kaneko, F.; Kato, T.; Baba, A.; Shinbo, K.; Kato, K.; Advincula, R. C. *Colloid Surface A* **2002**, *198*, 805.

(471) Ye, Y. H.; Badilescu, S.; Truong, V. V.; Rochon, P.; Natansohn, A. *Appl. Phys. Lett.* **2001**, *79*, 872.

(472) Yi, D. K.; Kim, M. J.; Kim, D. Y. *Langmuir* **2002**, *18*, 2019.

(473) Yi, D. K.; Seo, E.-M.; Kim, D.-Y. *Langmuir* **2002**, *18*, 5321.

(474) Noel, S.; Batalla, E.; Rochon, P. *J. Mater. Res.* **1996**, *11*, 865.

(475) Hasegawa, M.; Ikawa, T.; Tsuchimori, M.; Watanabe, O.; Kawata, Y. *Macromol.* **2001**, *34*, 7471.

(476) Hasegawa, M.; Keum, C.-D.; Watanabe, O. *Adv Mater* **2002**, *14*, 1738.

(477) Fukuda, T.; Sumaru, K.; Kimura, T.; Matsuda, H.; Narita, Y.; Inoue, T.; Sato, F. *Jpn J Appl Phys 2* **2001**, *40*, L900.

Chapter 2
Temperature-Controlled Neutron Reflectometry Sample Cell Suitable for Study of Photoactive Thin Films

The experimental details relevant for the interpretation and reproduction of the results described in the subsequent chapters can be found in the experimental sections of those chapters. This is true in all cases except for the results of chapter 5, which is a neutron reflectometry study of azo-polymer thin films. For that work, a custom sample cell needed to be built, tested, and validated. This experimental chapter therefore discusses this sample cell, including construction and performance details. This work has been published and is reprinted with permission from:

Yager, K.G.; Tanchak, O.M.; Barrett, C.J.; Watson, M.J.; Fritzsche, H. *Review of Scientific Instruments* **2006**, *77*, 045106. Copyright 2006 American Institute of Physics.

2.1. Abstract

We describe a novel cell design intended for the study of photoactive materials using neutron reflectometry. The cell can maintain sample temperature and control of ambient atmospheric environment. Critically, the cell is built with an optical port, enabling light irradiation or light probing of the sample, simultaneous with neutron reflectivity measurements. The ability to measure neutron reflectivity with simultaneous temperature ramping and/or light illumination presents unique opportunities for measuring photoactive materials. To validate the cell design, we present preliminary results measuring the photo-expansion of thin films of azobenzene-polymer.

2.2. Introduction

Neutron reflectometry is a powerful technique for studying thin films of any composition, including organic thin films, and biological samples. The technique is based upon the detection of grazing-angle specularly reflected neutrons. At very low angles, a neutron beam will be totally reflected by a sample-ambient interface. With increase in the specular reflection angle, oscillations in the reflection amplitude can be seen. These so-called Kiessig fringes[1] are characteristic of the sample's structure, most notably the thickness and neutron refractive index. The neutron refractive index is related to the

scattering length density (SLD) of the material's constituent atoms. Consistent with conventional Fresnel theory, interfaces between differing refractive indices (or, in the case of neutrons, differing SLD) will lead to reflection. The reflectivity as a function of angle is generally expressed in terms of the momentum transfer, or scattering vector:

$$q_z = \frac{4\pi}{\lambda}\sin\theta \tag{2.1}$$

where λ is the wavelength of the incident neutron beam, and θ is the specular scattering angle. The exact shape of the neutron reflectivity curve is a function of the film structure in the normal direction. From this, one can deduce film thickness, density, and roughness. With more elaborate model fitting, one can also deduce multilayer structures or internal material gradients. The technique is applicable to films in the thickness range of about 10 to 2000 Å. Neutrons, unlike x-rays, are sensitive to light elements (such as H, C, N, O), making them more suitable for studying polymers, biological samples, and other soft matter. Additionally, because the scattering length varies with isotope, one can enhance the neutron reflectivity signal by making isotopic substitutions, which often have no effect on chemistry or material properties. One can also perform difference experiments, where two samples that differ only in the isotopic nature of one of their constituent atoms are compared to determine the spatial distribution of that atom. More details on the technique of neutron reflectometry can be found elsewhere.[2]

Neutron reflectometry has additional unique advantages when applied to studying photoactive materials. There is currently considerable interest in thin films that respond to, control, or otherwise interact with light in the ultraviolet (UV), visible and infrared (IR) bands of the electromagnetic spectrum. Such materials find application in telecommunications (as routers, couplers, filters, etc.), in the microelectronics industry (as photoresists), as photo-actuators, photonic bandgap materials, and so on.[3,4] Such materials often cannot be studied using optical techniques, because their interaction with light would confuse the measurement, or, in many cases, the photo-probe would be modifying the sample during measurement. For instance, materials used for photo-resists may undergo photo-polymerization or photo-degradation. Azobenzene materials, which will be described later in more detail, are known to isomerize under illumination, and to photo-align when irradiated with polarized light.[5] Even using nominally non-absorbing

wavelengths, some measure of photo-alignment, hence birefringence, may be induced.[6] This time-varying birefringence makes conventional optical techniques, such as ellipsometry, more difficult to apply to photoactive materials. Similarly, photonic bandgap materials have unique interactions with light that make conventional optical techniques (such as ellipsometry, optical reflectivity, surface plasmon resonance, etc.) difficult to interpret. In some cases, non-perturbing optical measurements are not possible, whereas in other cases, complimentary measurements to confirm optical characterization would be valuable. It is thus of interest to investigate non-optical measurement techniques that can be used on photoactive materials. Ideally, the techniques would allow for light illumination during measurement, which would enable one to measure photo-changes in real time, and without otherwise perturbing the sample. X-ray reflectometry is capable of resolving the structure of a thin film in the normal direction with high accuracy, and could be coupled with simultaneous light illumination. However, since the scattering intensity of X-rays increases with total electron density, hence atomic number, it is a technique best suited to inorganic and metallic thin films. The scattering intensity of neutrons, by contrast, is determined by nuclear properties, and can be very high for lighter elements, including H, C, N, and O. Also, X-rays may lead to material damage for some samples, whereas the lower energy of thermal neutrons minimizes material damage. Thus, neutron reflectivity is, in some cases, better suited to the study of organic and biological samples, compared to X-ray reflectivity. In particular, a great number of photo-functional materials (including resists and photonic bandgap structures) are based on organic polymers. In other cases, the differing scattering properties of a material to X-rays and neutrons can be used for comparative experiments, where ambiguities can be resolved. Overall, neutron reflectivity offers the possibility to study photoactive samples in a nondestructive and unambiguous way, determining any changes in thickness and density due to irradiation.

Given that neutron reflectometry is nearly universally applicable to thin films, experiment design becomes limited only by the availability of appropriate sample environments during scanning. It is thus of interest to explore novel sample cells that can enable measurement of neutron reflectivity at the same time that sample illumination is performed. Simultaneous control of the sample's ambient environment (temperature,

humidity, etc.) is also useful.[7] Here we report on a new sample chamber that was designed to enable neutron reflectivity experiments to be carried out on photoactive materials, without the need to remove the sample from the neutron beam in order to irradiate it. The sample cell additionally enables control of temperature and ambient atmosphere. This sample setup is validated with preliminary experiments measuring non-thermal photo-expansion effects when azobenzene-polymer thin films are irradiated with laser light. Although this sample cell has been conceived of for reflectometry of thin films, it could easily be adapted to other neutron scattering techniques (SANS, diffraction, etc.), where the sample can be irradiated with visible laser light without removing it from the neutron beam.

2.3. Construction and Performance Details

The internal design of the cell is shown in Figure 2.1 (the cell enclosure can be seen in Figure 2.4). The sample is attached to a large copper plate, centered inside an aluminum enclosure. The aluminum sidewalls allow the neutron beam to pass through with very little attenuation. The front port is equipped with a window, allowing for illumination of the sample at normal or near-normal incidence. The window can be made of polymethyl methacrylate (PMMA, also known as Plexiglas or Lucite), glass, quartz, or

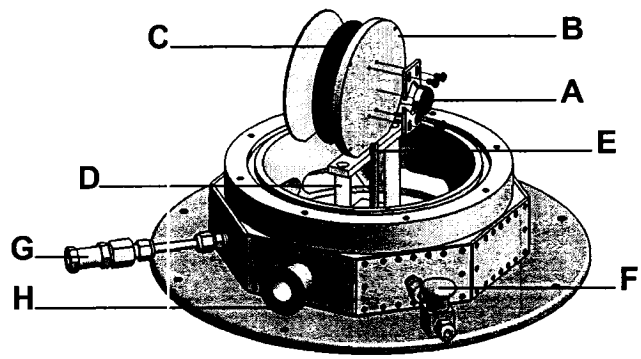

Figure 2.1: Exploded view of the sample disk and environmental control features. The silicon substrate (A) is attached to the copper block (B) with restraints positioned above and below. The block is maintained at the correct temperature by a heating element (C) bonded to the back of the plate. The sample and block are thermally isolated by insulating ceramic posts (D), and can be quenched to lower temperature by flowing gas out of the quench tube (E). The base of the cell can be equipped with a variety of attachments, allowing for supply of quench gas (inlet F and effluent G), evacuation of the cell (vacuum flange H).

other materials as determined by optical requirements. The cell lid and front window rest on rubber O-rings, which form a tight seal when the cell is evacuated. These two pieces can also be screwed securely, enabling the cell to be used with a positive pressure with respect to ambient. The base of the cell is equipped with ports for controlling the cell's atmosphere.

The sample is a silicon wafer, 24 mm in diameter and 6 mm thick, coated with the thin film under investigation. The wafer is secured against a large copper plate using fasteners above and below the sample (A in Figure 2.1). Thermo-conductive paste was used to provide a good thermal conduction between the sample and copper plate. In principle, larger sample sizes could be accommodated in this cell, although the small sample size is advantageous in optical studies (as described later). The back of the copper block has a 125 W resistive heating element clamped to it (C in Figure 2.1). A temperature sensor reads the temperature of the copper block, and a feedback loop ensures that the sample is held at the proper temperature. Measurements were made of the temperature differential between the heating block and the sample by bonding a thermocouple directly on the surface of a Si wafer. It was found that the deviation of the sample temperature from the block temperature increases with increasing temperature, e.g. 2 K deviation at 383 K and 4 K deviation at 453 K. The sample/heating setup is held in place with two Macor® insulating glass-ceramic posts (D in Figure 2.1). This thermally isolates the sample and sample heater from the rest of the cell. The cell environment can be modified using the ports built into the base of the enclosure (F, G, and H in Figure 2.1). Ports allow for evacuation of the cell using a vacuum pump, purging with ambient atmosphere, or the introduction of an arbitrary atmosphere from other equipment (such as gas cylinders). In particular, the quench port exits directly onto the sample, making it ideal for quickly cooling samples down to room temperature using a cool stream of an inert gas.

The cell was specifically designed to enable temperature ramping of the sample. This allows for neutron measurements at a variety of sample temperatures, which can be useful in, for instance, the identification of phase transitions in materials, or the determining of activation energies. For organic thin films, the temperature control also allows the sample to be annealed (or undergo other thermal treatment) without being

removed from the cell and subsequently realigned. This persistence of sample positioning before and after thermal treatment removes some ambiguity in comparing neutron reflectivity curves. It also enables a sequence of experiments to be initiated remotely, or even be completely automated. As can be seen in Figure 2.2, the cell can be ramped up above room temperature smoothly, in a short amount of time, and without significant overshoot of the target temperature. The temperature rise is well described by a simple sigmoid with time constant of 3.7 minutes. Thus the cell can be considered to have reached a stable temperature within 30 minutes of a set-point adjustment. Given that typical neutron reflectivity scans take 8 to 12 hours, this temperature stabilization time is not a major concern. However, additional time may need to be given for any sample response to complete. At a given set-point, temperature stability is excellent. Deviations from the set-point were, at most, 0.02 K (less than 0.01%). This temperature stability is due to the feedback temperature monitoring, but also due to the thermal isolation of the heated sample stage. By evacuating the sample chamber, this thermal isolation can be further enhanced. The cell is able to heat samples to over 200 K above room temperature. For organic thin films, this is typically sufficient to undergo any phase transition of interest. In fact, it is sufficient to degrade most organic materials. The cell can be filled with an inert gas, or entirely evacuated, which helps prevent sample oxidation during

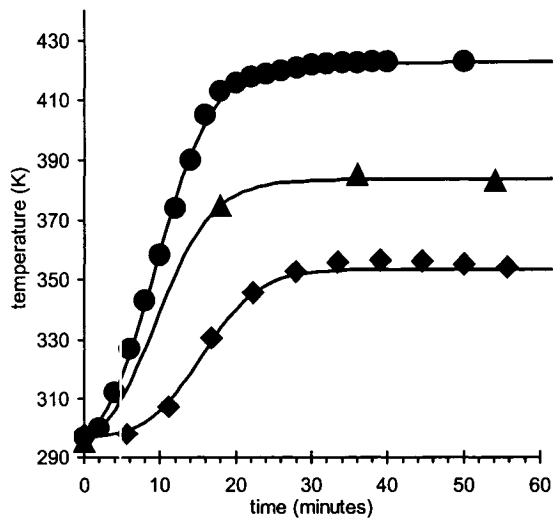

Figure 2.2: Typical temperature ramping behavior of the sealed sample cell. The feedback-loop resistive heater can stabilize at a set-point temperature within 30 minutes. The solid lines are sigmoidal fits to the data.

thermal treatment.

Figure 2.3 shows the decrease of the sample environment back to room temperature, where the resistive heater is no longer active. We measured the temperature decay both with an evacuated sample cell, and with a constant helium purge at 1 bar. This purge exits directly onto the sample/heater block, and serves to efficiently draw off heat from the warm block. In the case of a vacuum environment, the sample temperature decreases slowly, with a time constant on the order of 1.9 hours. This demonstrates the excellent thermal isolation of the sample from the laboratory environment. Even without active temperature control, the sample is maintained at high temperature for a significant period of time. With a steady helium stream, heat is drawn off much more efficiently, and in this case the time constant is ~ 15 minutes. By changing the pressure of the purge gas, the cooling rate can be varied across a wide range.

The transmission characteristics of the 6 mm thick PMMA window were measured. The material is transparent across the visible (~8% absorption and reflection losses) and induces no polarization change in the incident beam. For more precise optical experiments, the internal volume of the sample cell is sufficient to accommodate the

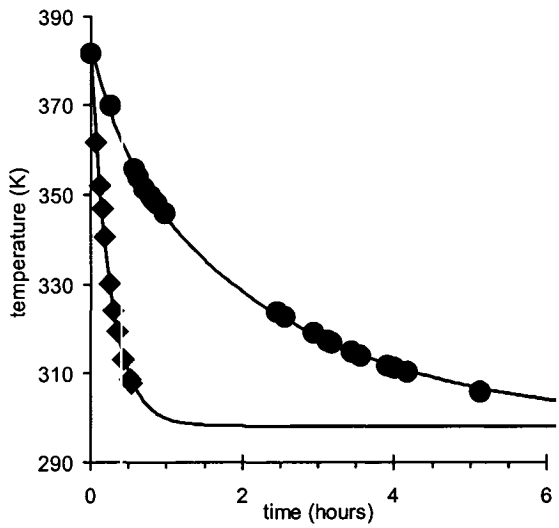

Figure 2.3: Temperature performance of the cell without active heating. Under vacuum (●), the cell holds temperature well, decaying with a time constant of 1.9 hours. With a constant helium purge (◆), the cell's temperature can be quenched to room temperature within one hour (time constant 15 minutes). The solid lines represent an exponential decay fit (for the helium purge data), and a biexponential decay (for the evacuated cell).

placement of optical components inside the housing, after any perturbing effect of the window material. In fact, a series of optical elements could be constructed as a single unit that replaces the window. This versatile design allows any number of optical experiments to be performed.

2.4. Results

The described sample cell was used to study a photoactive polymer thin film. Specifically, thin spin-cast films of an azobenzene polymer, poly(disperse red 1A) (pdr1a) were studied via neutron reflectivity, in order to characterize the photo-deformation behavior of this system. The azobenzene chromophore in pdr1a interconverts

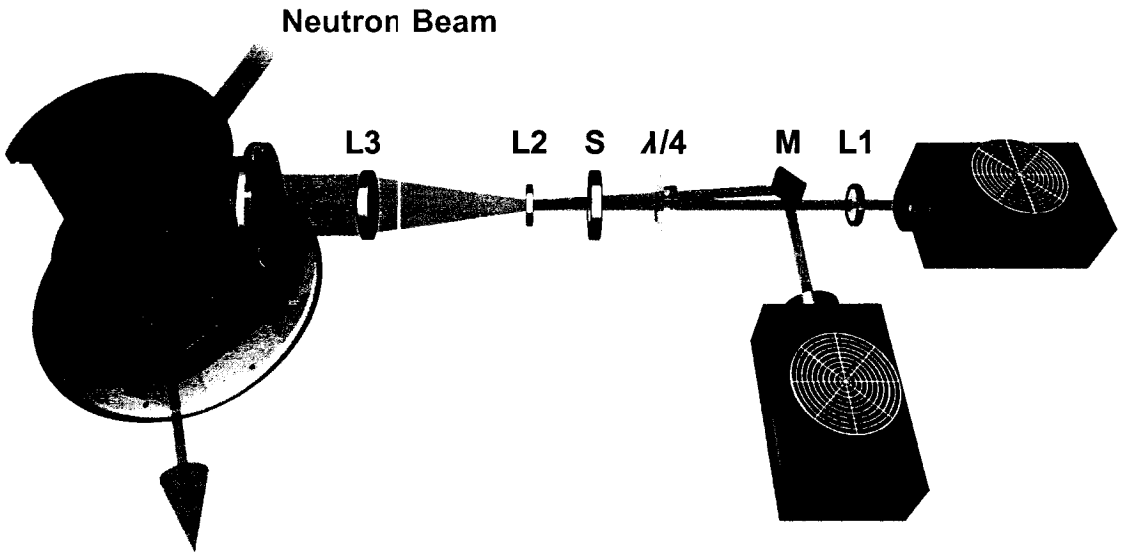

Figure 2.4: Schematic of neutron reflectometry experiment with simultaneous laser irradiation. Two air-cooled Ar^+ lasers (on the right) are used as illumination sources. One laser output is adjusted with a converging lens (L1) in order to account for slight differences in laser divergence. A beam from a second laser is reflected off of a mirror (M), making it nearly collinear with the first beam, and passing through a concerted optical train (the angular difference in the two beams has been exaggerated in the diagram, for clarity). The combined beam is converted from linearly polarized to circularly polarized using a wave plate ($\lambda/4$). A diverging (L2) and converging (L3) lens are then used to expand and collimate the beam, so that it over-illuminates the sample with a uniform light intensity. The beam can be turned on and off via computer control of a shutter (S). On the far left, the sample can be seen attached to the copper heating plate, all enclosed in a sealed cell with a transparent window for laser illumination. The neutron beam passes through the sample housing, reflects off of the sample, and travels into a detector.

between *trans* and *cis* geometric isomers when irradiated with light near its absorption maximum of 467 nm.[8] This efficient and reversible photochemical isomerization reaction leads to modulation of other material properties. For instance, polarized irradiation can be used to photo-orient the azo chromophores.[9] The free surface of an azo film also undergoes spontaneous mass transport when irradiated with a light intensity or polarization gradient.[10] Macroscopically, thin films have been deformed using polarized irradiation.[11,12] Most recently, the photo-expansion of thin films of azo polymer have been probed via optical techniques.[13] This photo-expansion behavior was studied with neutron reflectometry using the present sample cell. In this setup (Figure 2.4), the azo sample (spin cast onto a silicon wafer) is placed inside the evacuated sample cell, with the free surface facing the window port. This allows optical irradiation of the azo sample at any time, even simultaneous with neutron reflectivity measurements. Furthermore, the cell design allows irradiation under inert atmospheric conditions, and at any temperature. Outside the sample cell, a laser and optical setup are used to irradiate the thin film. Two ~150 mW Argon-ion lasers, emitting at 488 nm, were used as light sources. The combination of two lasers was used to increase irradiation power. Additionally, since the two lasers have no coherence relationship to one another, the dual illumination serves to average out any confounding coherence or interference effects, which are known to lead to mass transport phenomena in azo-polymer systems. A mirror is used to direct the two beams nearly collinearly towards a 488 nm $\lambda/4$ plate, which has been adjusted so as to convert the linearly polarized laser beams into a circularly polarized irradiation beam. This circular polarization ensures that no in-plane anisotropy is induced in the azo material (ratio of intensity along the major and minor axes of 1:1.02 was achieved). A shutter allows for computer-controlled activation of the laser as required by experiment design. Finally, a lens system is used to expand the beam to a sufficient size that it illuminates the entire sample surface uniformly. The PMMA window attenuates the 488 nm probe beam by approximately 8%. The collimated beam was measured to fully irradiate the 24 mm diameter sample surface with a uniform intensity of 35 mW/cm^2.

The small sample size is important for studies using optical illumination. A preliminary experiment using a 100 mm silicon wafer gave confounding results. In that experiment, the neutron beam was collimated so as to define a rectangle 77 mm wide by

39 mm tall, on the sample surface. However, over this large area the expanded laser beam was not sufficiently uniform. Thus, some areas of the probed sample saw higher laser intensity than others. The end result was a reflectivity curve that contained contributions from different extents of expansion/contraction. In such a case it is difficult to determine what photo-physical effects are occurring, since the neutron beam probes an incoherent sum of different film regions. By using a smaller sample, and over-illuminating it with the neutron beam, one achieves a better film uniformity over the probed region. Moreover, the smaller sample size makes it possible to irradiate uniformly with laser light. This makes data interpretation obviously more robust.

The azo material was irradiated with laser light for progressively longer periods of time. Typical neutron reflectivity curves, shown in Figures 2.5 and 2.6, show the characteristic fringes due to the thickness and density of the sample. Such curves can be iteratively fit using a variety of models, and using the algorithm developed by Parratt.[14]

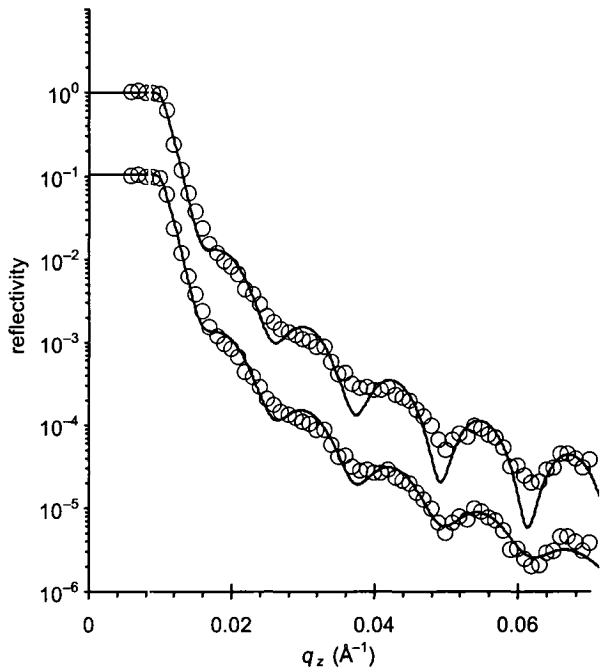

Figure 2.5: Comparison of fits used to analyze the neutron reflectivity curves. The data is the same in both cases (a thin azo film before illumination), but have been offset vertically for clarity. The upper fit is a simple one-box model, which correctly describes the film thickness and density. The lower fit is a more elaborate model that includes a Gaussian distribution of film thickness values. This type of modeling correctly fits both the absolute intensity of the curve, as well as the depth of the minima.

In this case, the Parratt32 (HMI) software was used, in addition to modified versions of neutron reflectivity calculation source code provided by Thad Harroun (Brock University, Department of Physics). A one-box model produces fringe spacing and positions consistent with the experimental data. However, the amplitude of the fringes (specifically the depth of the minima) is not well described by a one-box model. A more elaborate model, which allows for a small distribution of thickness across the sample surface probed by the neutron beam, correctly reproduces the data (see comparison in Figure 2.5). For the samples presented in this paper, a Gaussian thickness distribution of 4.5% (~25Å) was found to be consistent with the data. It should be emphasized that this distribution of thickness is not equivalent to a small-scale sample roughness (which would be modeled with a one-box interfacial distribution, and would lead to substantial decrease in the absolute reflectivity for all q_z values.); it is in fact that different parts of the sample have slightly different thickness, on a size-scale larger than the neutron coherence length (this is modeled with a incoherent sum of reflectivity profiles, which

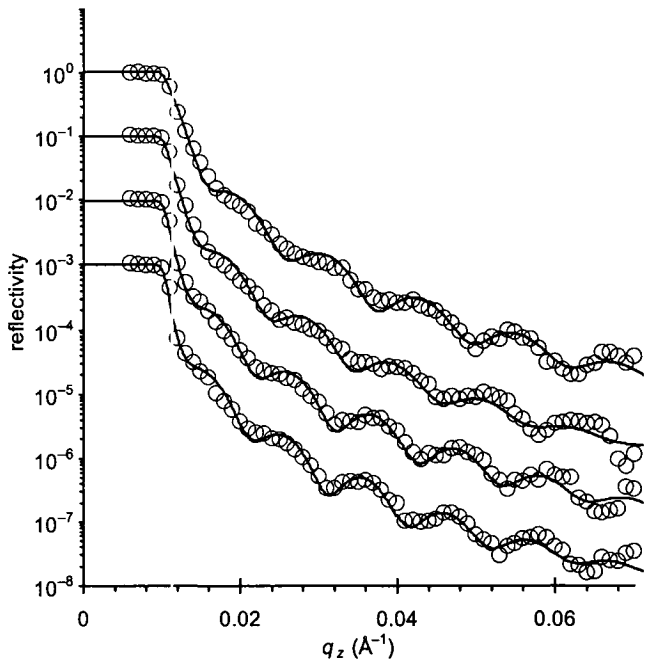

Figure 2.6: Neutron reflectivity curves for an azo film after various amounts of laser illumination. From top to bottom, the curves (offset vertically for clarity) correspond to: before irradiation, after 0.4 hours total irradiation, after 2.5 hours irradiation, and after 7.9 hours irradiation. The solid lines are the corresponding distribution-of-thickness fits. The shift of the fringes indicates that the film photo-expands with increased laser exposure.

causes the minima to be attenuated, without decreasing the absolute reflectivity of the curve). Whether a one-box or a Gaussian distribution of thickness values is used, identical conclusions are obtained.

After irradiation, there is a distinct shift of the fringes (Figure 2.6), which indicates that the film has undergone irreversible photo-expansion. With additional irradiation, the film undergoes further expansion (relative to the initial film thickness), as shown in Figure 2.7. The observed effect is indeed material expansion, as the sample's scattering length density decreased with corresponding expansion (that is, the area under the film profile curve is constant, to within ~2%). The sample cell used, however, allows us to additionally probe the sample during illumination. A typical neutron reflectivity curve requires 8 to 12 hours of data collection, which is far too long to capture the dynamics of the azobenzene photo-expansion. However, one can measure a small portion of the reflectivity curve in order to characterize the behavior over time. We probed the change in neutron reflectivity at specific q_z values, during irradiation with laser light (Figure 2.8). In Figure 2.8 (a), one can see the change in reflectivity at $q_z = 0.02$ Å^{-1}, and in (b), the reflectivity at $q_z = 0.05$ Å^{-1}. The reflectivity at $q_z = 0.05$ Å^{-1} changes in an oscillatory and complex way as laser irradiation proceeds. This is due to the fact that the Kiessig fringes, which are shifting as the film photo-expands, pass in and out of the observation window. By comparison, the monotonic behavior at $q_z = 0.02$ Å^{-1} closely relates to the observed change in thickness. This is because near the critical reflectivity edge, a single fringe is being shifted towards lower q_z. Furthermore, scanning at small q_z is considerably faster than scanning at high q_z, because the much higher absolute reflectivity requires shorter integration times to achieve reasonable statistics. Clearly some regions of the reflectivity curve are more valuable than others for interpreting the kinetics and dynamics of systems. With appropriate choice of q_z, one is able to follow, in real-time, any material changes. This serves two purposes: one, it is possible to determine when a system has reached a stable state, and can then be subjected to a full reflectivity scan (i.e.: the sample will not be changing during the measurement); and two, it is possible to determine the kinetic behavior of material transformations.

Consistent with previous optical investigation of these materials,[13] there is a substantial irreversible photo-expansion, and a secondary elastic expansion of the

material that occurs only when the illuminating light is on. This explains the slight difference between the reflectivity intensity when the laser is on versus off. Such changes

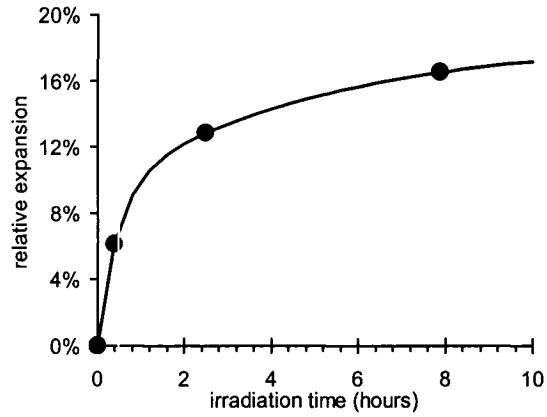

Figure 2.7: Relative expansion of an azo-polymer film as a function of total laser irradiation time, measured using neutron reflectometry. The data was fit with a biexponential rise-to-max.

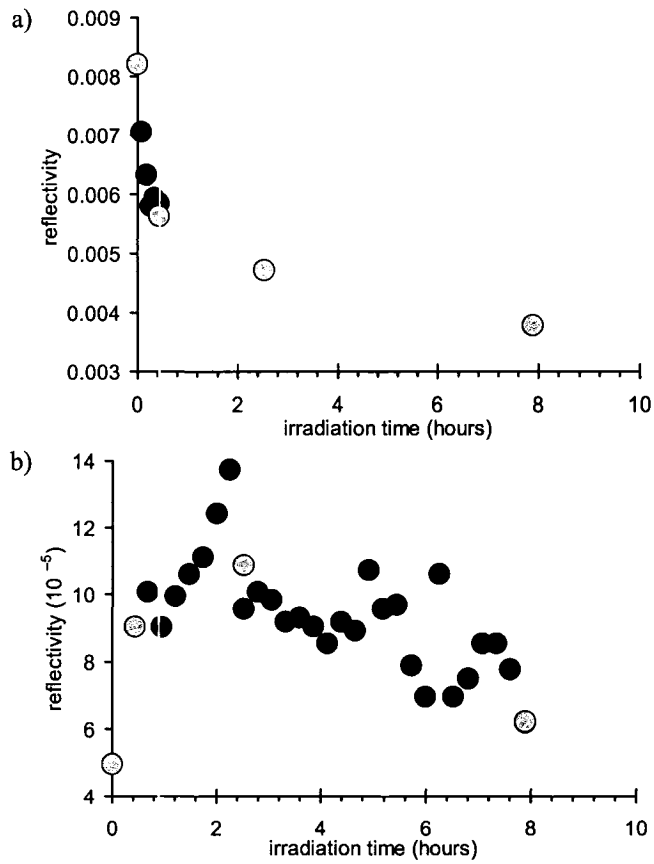

Figure 2.8: Neutron reflectivity signal at q_z = 0.02 Å^{-1} (a), and q_z = 0.05 Å^{-1} (b). The black symbols refer to measurements during laser illumination, whereas the gray symbols refer to measurements in between successive laser irradiation steps. The monotonic data for smaller q_z provides a more meaningful measure of photo-physical change than does the data at larger q_z.

would not be possible to measure if the sample needed to be removed from the neutron beam for light irradiation. In addition to monitoring material changes during light illumination, the present cell enables measurements during temperature ramping, or while maintaining the sample at a given temperature. Figure 2.9 shows an example of a photo-expanded sample that was subsequently treated thermally, which led to contraction of the material. All of these scans were taken without removing the sample from the cell, which makes alignment much faster, and removes any ambiguity that would arise from inconsistent sample placement. The control of the sample atmosphere enabled it to be annealed through its glass transition temperature without any danger of oxidation or other material damage. By controlling environmental parameters, this cell thus offers the possibility of much higher experimental reproducibility.

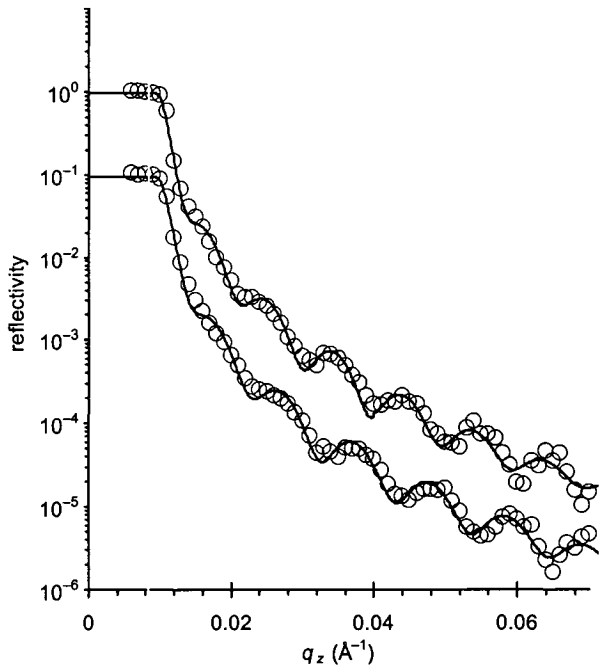

Figure 2.9: Neutron reflectivity curves measured at different temperatures (offset vertically for clarity). The upper curve is a thin film, at room temperature, that has been laser irradiated. The lower curve is the same film, heated to, and maintained at, 353 K. The distribution-of-thickness fits to the data (solid lines) show that the photo-expanded film thermally contracts.

2.5. Conclusion

We have designed, built, and tested a unique neutron reflectometry sample cell, which is able to maintain a sample at a desired temperature under controlled atmospheric conditions, and further allows for simultaneous irradiation or probing with light. The ability to measure neutron reflectivity during illumination and/or temperature adjustments generates new possibilities for experimental studies. This cell is also versatile, accommodating a range of possible optical components, and could even be used with other neutron scattering techniques.

2.6. References

(1) Kiessig, H. *Annalen Der Physik* **1931**, *10*, 769.

(2) Russell, T. P. *Mater. Sci. Rep.* **1990**, *5*, 171.

(3) Eldada, L. *Rev. Sci. Instrum.* **2004**, *75*, 575.

(4) C. López. *Adv. Mater.* **2003**, *15*, 1679.

(5) Ichimura, K. *Chem. Rev.* **2000**, *100*, 1847.

(6) Kempe, C.; Rutloh, M.; Stumpe, J. *J. Phys.: Condens. Matter* **2003**, *15*, S813.

(7) Harroun, T. A.; Fritzsche, H.; Watson, M. J.; Yager, K. G.; Tanchak, O. M.; Barrett, C. J.; Katsaras, J. *Rev. Sci. Instrum.* **2005**, *76*, 065101.

(8) Rau, H. In *Photochemistry and Photophysics*; Rebek, J., Ed.; CRC Press: Boca Raton, FL, 1990; Vol. 2, pp 119.

(9) Natansohn, A.; Rochon, P. *Chem. Rev.* **2002**, *102*, 4139.

(10) Yager, K. G.; Barrett, C. J. *Curr. Opin. Sol. State Mater. Sci.* **2001**, *5*, 487.

(11) Yu, Y.; Nakano, M.; Ikeda, T. *Nature* **2003**, *425*, 145.

(12) Ikeda, T.; Nakano, M.; Yu, Y.; Tsutsumi, O.; Kanazawa, A. *Adv. Mater.* **2003**, *15*, 201.

(13) Tanchak, O. M.; Barrett, C. J. *Macromolecules* **2005**.

(14) Parratt, L. G. *Phys. Rev.* **1954**, *95*, 359.

Chapter 3
Temperature Modeling of Laser-Irradiated Azo-Polymer Thin Films

As a first step to understanding the mechanism of surface patterning in azo materials, it was necessary to quantify to what extent photo-heating plays a role. This chapter discusses modeling used to address this issue. In addition to constraining the possible mechanisms used to explain patterning, these results also enabled improved interpretation of later experiments. Specifically, by establishing the role of photo-heating in different irradiation regimes, these effects can be discounted in the explanation of other photo-physical phenomena identified in the azo system. This material has been published, and is reprinted with permission from:

Yager, K.G.; Barrett, C.J. *Journal of Chemical Physics* **2004**, *120*, 1089.

3.1. Abstract

Azobenzene polymer thin films exhibit reversible surface mass transport when irradiated with a light intensity and/or polarization gradient, although the exact mechanism remains unknown. In order to address the role of thermal effects in the surface relief grating formation process peculiar to azo polymers, a cellular automaton simulation was developed to model heat flow in thin films undergoing laser irradiation. Typical irradiation intensities of 50 mW/cm^2 resulted in film temperature rises on the order of 5 K, confirmed experimentally. The temperature gradient between the light maxima and minima was found, however, to stabilize at only 10^{-4} K within 2 μs. These results indicate that thermal effects play a negligible role during inscription, for films of any thickness. Experiments monitoring surface relief grating formation on substrates of different thermal conductivity confirm that inscription is insensitive to film temperature. Further simulations suggest that high-intensity pulsed irradiation leads to destructive temperatures and sample ablation, not to reversible optical mass transport.

3.2. Introduction

Thin films of polymers containing azobenzene chromophores (azo polymers) have been investigated for over 25 years as nonlinear optical materials, for liquid crystal alignment, and as photoswitchable materials.[1] In 1995, it was observed that the free surface of azobenzene-polymer films could be induced to exhibit surface mass transport if exposed to a light intensity and/or polarization gradient.[2,3] The size scale for this process, which essentially encodes the incoming light modulation pattern into a surface relief pattern, is determined by the geometry and the wavelength of light. A typical inscription setup, shown in Figure 3.1(a), involves interfering two coherent laser beams at the sample surface. The sinusoidal variation of light results in a sinusoidal surface relief grating (SRG) on the sample free surface, as confirmed by atomic force microscopy

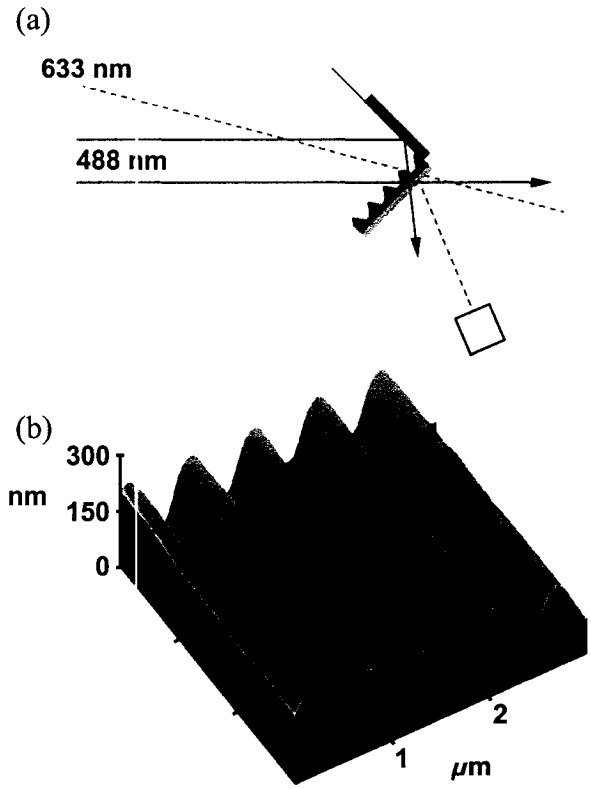

Figure 3.1: (a) Typical experimental setup for inscription of surface relief gratings. A 488 nm laser beam is reflected upon itself to generate an interference pattern at the film surface. The resulting diffraction is monitored with a low power HeNe beam (633 nm). (b) AFM image of the resulting surface relief grating. The spacing is determined by the angle θ and the wavelength of light. The grating amplitude depends on many parameters, including light intensity and polarization.

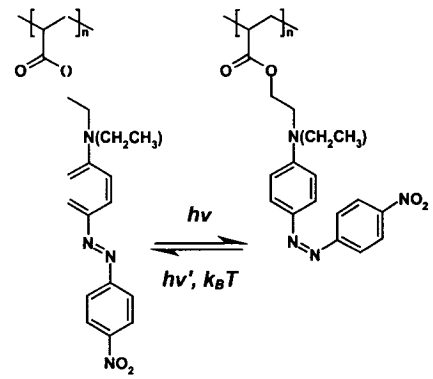

Figure 3.2: Azobenzene chromophores isomerize from the trans to the cis state under irradiation at an absorbing wavelength. The molecule will then thermally relax back to the more stable trans state, or this reconversion can be induced photochemically. Depicted above is poly(disperse red 1 acrylate).

(Figure 3.1(b)). The peak-to-peak spacing is typically on the order of hundreds of nanometers, and peak-to-valley amplitudes of hundreds of nanometers are readily obtained with modest irradiation intensities (<50 mW/cm^2). This unusual material transport occurs in minutes, and at room temperature, which is well below the bulk glass-to-rubber transition temperature (T_g) for these polymers. The optical inscription is fully reversible, as a flat film of the original thickness is recovered upon heating above T_g. Reviews of the many interesting results are available.[4,5] The process critically requires a polymer containing azobenzene moieties. Azobenzene and its derivatives undergo photoinduced isomerization between *trans* and *cis* geometries when exposed to light at an absorbing wavelength (Figure 3.2). Cycling of chromophores between these isomers appears to be required for the mass transport phenomenon, although the exact role of isomerization is not yet clear. The grating amplitude scales with the net exposure energy up to a saturation point, and therefore scales with irradiation power and time.[6] The SRG is phase-shifted with respect to the incident light pattern, with light intensity maxima corresponding to surface relief minima.[7] The grating amplitude depends strongly on the polarization combination used in the writing beams, and it has been observed that even a pure polarization pattern can lead to SRG formation.[8] Mechanisms proposed to explain the mass transport include: isomerization pressure,[9] gradient electric forces,[10] asymmetric diffusion,[11] mean-field forces,[12] and permittivity gradients.[13] In addition to these

mechanisms, the inherent fluid dynamics have been modeled,[14-16] yet the exact nature of the driving force remains unresolved.

Over the course of mechanism investigation, it has generally been assumed that thermal effects do not play a significant role in the inscription process, since inscription is known to depend on the light polarization, yet a purely thermal mechanism would be sensitive only to light intensity. It has recently been suggested, however, that thermal gradients might be responsible for SRG inscription using pulsed irradiation,[17,18] and it may also be that sample heating is assisting the cw photo-induced mass transport phenomenon. It is therefore of interest to consider quantitatively what effect, if any, thermal gradients may have in pulsed and continuous irradiation experiments. These thermal gradients would be created due to the inhomogeneous illumination of the sample surface, but their magnitude and persistence time would be expected to depend strongly on material parameters, geometry, and size-scale. In an effort to understand the role of thermal gradients in the SRG inscription process, we created a straightforward cellular automaton simulation, and used it to predict the temperature gradients for typical inscription conditions. These predictions indicate that thermal gradients are negligible for typical modest irradiations, and that pulsed irradiations are likely causing destructive sample ablation, and not mass transport. We also present the results of our experimental investigation of SRG formation on substrates of markedly different thermal conductivity (plastic and air), which confirm that the grating mechanism is insensitive to film steady-state temperature. The model presented is general, and should allow estimation of temperature rise in a variety of different experiments and geometries.

3.3. Methods

3.3.1 Simulation Procedure

In order to simulate heat flow in the hundreds of nanometers regime, a rectangular grid of cubic cellular automata was implemented, where diffusive heat energy transfer from cells to nearest neighbors is calculated using the Fourier law:

$$J(y,z,t) = -\kappa\left(\frac{\partial T(y,z,t)}{\partial y}\right) - \kappa\left(\frac{\partial T(y,z,t)}{\partial z}\right) \tag{3.1}$$

where $J(y,z,t)$ is the rate of heat flow at position (y,z) and time t, $T(y,z,t)$ is the temperature, and κ is the thermal conductivity (a material property). The validity of this law for short time and distance scales, with minor deviations from bulk thermal conductivity, has been verified experimentally.[19] The typical SRG inscription experiment can be completely simulated using a two-dimensional slice of material, as shown in Figure 3.3. In general, the thin azo film has a free surface (with air above it), and a substrate (such as a glass slide). Approximate bulk material properties for the three layers are shown in Table I.

TABLE I. Simulation parameters

Substance	Heat Capacity C (J/Km^3)	Thermal Conductivity κ (W/mK)	Thermal Diffusivity α (m^2/s)	Extinction Coefficient ϵ_{488nm} (μm^{-1})
Air	1 300	0.026	2.3×10^{-5}	0
Azo	1.60×10^{6}	0.17	1.1×10^{-7}	5.30
Glass	1.56×10^{6}	0.80	5.1×10^{-7}	0

The optical field is simulated inside the azobenzene film only, with a Beer-

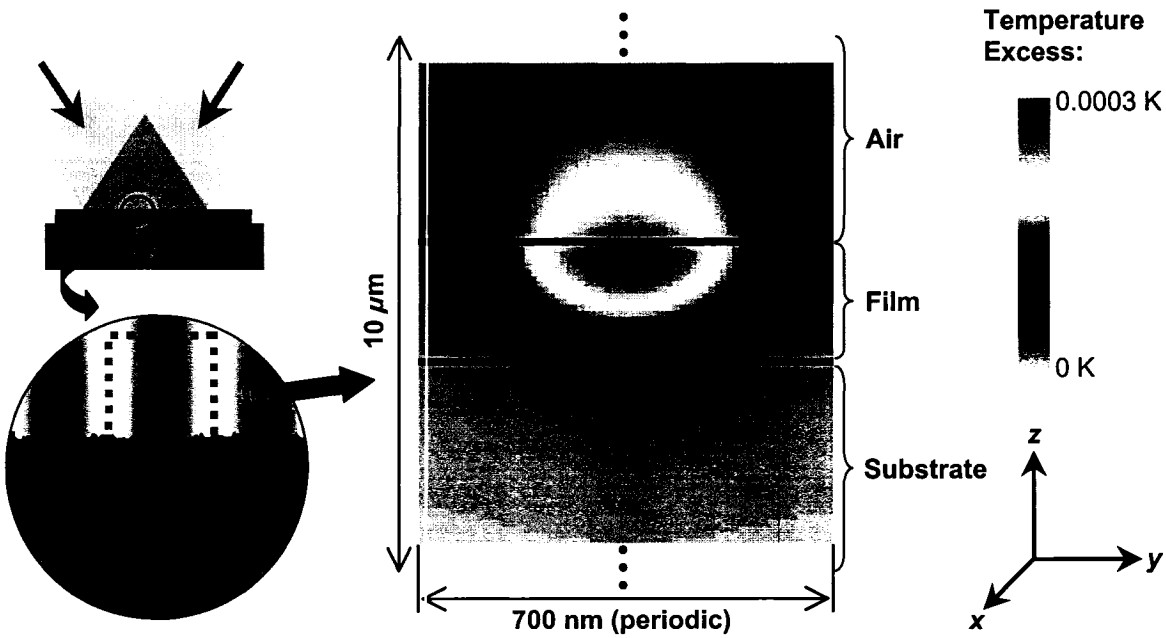

Figure 3.3: Two-dimensional simulation setup. A rectangular simulation region, with periodic boundary conditions, describes a representative section of the azobenzene film. The heat flow calculations predict periodic temperature profiles, as a result of the periodic light pattern at the sample surface. The temperature map shown is the output from a 2D simulation of a 200 nm film, after 10^{-7} s of irradiation with 50 mW/cm^2.

Lambert exponential decrease of light intensity in the z-direction, and a sinusoidal light variation in the y-direction. The left and right-hand sides are coupled, forming periodic boundary conditions in the y-direction, which correctly describes the periodic oscillation of the light field at the sample surface. The width of the simulation was set to 700 nm, which is approximately the periodicity obtained with 488 nm light interfering at 20°. Simulation in the x-direction is not necessary, since no parameters vary along that axis. The top and bottom edges of the simulation rectangle were treated as perfect heat sinks, meaning that any thermal energy in excess of ambient reaching these cells was eliminated. The presence of these heat sinks creates an artifact for any finite simulation size, but as will be discussed later, the results can be interpreted in a way that does not depend on this effect. The results presented here used a vertical simulation size of 10 μm.

Each cell is defined by material properties, specifically thermal conductivity, heat capacity, and extinction coefficient (zero except for the azo film); and by simulation variables, specifically the heat content and temperature at a given timestep. The simulation algorithm consists of, on each timestep: (1) augmenting the heat energy content of each azobenzene-film cell, based on the calculated light energy absorbed by that cell; (2) calculating the cell temperatures, based upon their current heat content and heat capacity; (3) redistributing energy between nearest neighbors, based on the thermal disparity between the cells and the Fourier law; and (4) resetting the upper and lower boundaries to zero excess heat content. It was found that the simulation results were essentially identical, regardless of the exact choice of cell size and timestep duration, so long as these are sufficiently small. For the two-dimensional (2D) simulations presented here, the cells are cubes 10 nm on a side, and the timestep is 10^{-12} s, which were determined to be sufficiently small to avoid resolution artifacts. For long simulation times, a simplified one-dimensional (1D) array of cubic cells was instead used, with cell sizes of 100 nm and a timestep of 10^{-10} s. The 1D results shown here were obtained with a 200 μm linear array.

3.3.2 Thin Film Irradiation

The low molecular weight azobenzene polymer, poly(disperse red 1 acrylate) (pdr1a), was synthesized as described previously.[20] Thin films of pdr1a were spin-coated from filtered solutions (~0.1 mol/L repeat unit concentration) onto freshly cleaved mica

(800 rpm for 35 s, acceleration 1680 rpm/s). The thin film was then floated off onto a water surface, and picked up onto a plastic substrate with an array of 1.5 mm diameter holes. Portions of the thin film suspended over the holes are thereby freestanding, and experience an air substrate. The entire film was exposed for one hour to an interference pattern (θ = 20°) from the 488 nm line of an Ar^+ ion laser (Innova 308, Coherent). The beam was circularly polarized, and the power at the sample surface was 10 mW/cm^2. The resulting SRG, in the areas over the plastic substrate, and over the air substrate, were investigated using atomic force microscopy (BioScope, Digital Instruments). For comparison, a commercially available series of liquid crystal films that exhibit visible color transitions at various temperatures were irradiated with the same laser system.

3.4. Results and Discussion

The two-dimensional simulation procedure is inherently limited by available computational power. Thus, to simulate further in the z-direction and time, it is necessary to simplify the system somewhat. As will be discussed later, it was found that beyond 10^{-5} s, the heat profile in the y-direction had become stabilized. For long simulations, therefore, a simplified one-dimensional array of cells was used. Although the 1D simulation allows access to longer distances and times than the 2D simulation, it is also limited by finite-size artifacts. The simulation results can be compared (at least within order of magnitude) to the analytical result obtained by considering an infinite plane heating a semi-infinite material. For a constant heating rate of w_0, the temperature profile is:[21]

$$T(z,t) = T_i + \frac{2w_0}{\kappa}(\alpha t)^{1/2}\left[\frac{1}{\sqrt{\pi}}e^{-\xi^2} + \xi\,\mathrm{erf}(\xi) - \xi\right] \tag{3.2}$$

where erf is the error function, T_i is the initial temperature of the system, $\alpha \equiv \kappa / C$ is the thermal diffusivity, where C is the heat capacity, and

$$\xi = \frac{z}{2\sqrt{\alpha t}} \tag{3.3}$$

Of specific interest is the temperature of the plane itself, which is:

$$T(0,t) = T_i + \frac{2w_0}{\kappa}\sqrt{\frac{\alpha}{\pi}}t^{1/2} \tag{3.4}$$

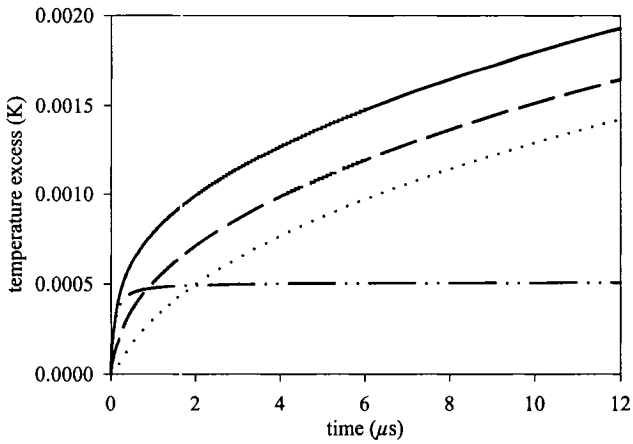

Figure 3.4: Typical heat-flow simulation result, in this case for a 200 nm azo film on glass substrate, irradiated with 50 mW/cm^2 light. The simulation tracks the temperature of the hottest azo cell (solid line), the coldest cell (dotted line), the average of all the azo cells (dashed line), and the temperature difference between the hottest and coldest cells (dot and dash line).

The analytical solution therefore predicts that the temperature of the thin film should rise as $t^{1/2}$.

The temperatures that will be discussed henceforth are excess temperatures, relative to ambient, since the Fourier equation is invariant under uniform temperature offsets. Figure 3.4 shows a typical simulation output, in this case for a 200 nm azo thin film on a glass substrate, irradiated with 50 mW/cm^2 of light. The quantities plotted are the temperature of the hottest cell in the azo film, the temperature of the coldest cell, the simple average of all the azo cells, and the difference between the hottest and coldest cells. This temperature difference was invariably found to correspond to the difference between the maximum and minimum of the light irradiation pattern. Any mechanism attempting to explain SRG formation on thermal grounds would presumably be sensitive only to this temperature difference. As can be seen in Figure 3.4, the overall temperature of the film continues to rise long after the temperature difference has stabilized. One can approximate a characteristic distance for heat diffusion in time t using $\sqrt{\alpha t}$. Using this relation, one would expect heat flow over a distance of 700 nm to stabilize after ~5 μs, in agreement with the simulation results. The overall rise in film temperature eventually reaches a steady-state value, which is necessarily dependent upon the finite simulation size. Larger simulations lead to proportional postponement of the finite-size steady-state artifact. The temperature difference curve, however, is found to be

invariant under simulation size, and in fact sets in before the finite simulation size plays a role. It therefore seems reasonable to decouple questions regarding the heat flow in the *x*-*y* plane and heat flow in the orthogonal *z*-direction. The former relates to the magnitude of thermal gradients inside the film, and the latter to the final absolute temperature of the film.

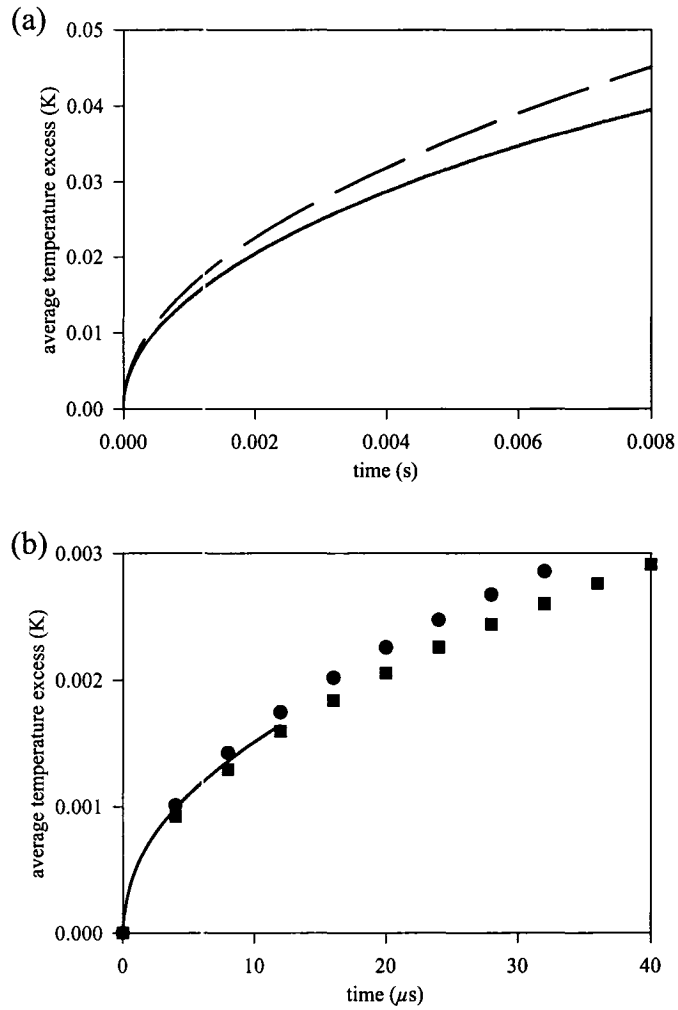

Figure 3.5: Comparison of modeling methods, using a 200 nm film under 50 mW/cm^2 irradiation. (a) The analytical solution (dashed line) is offset slightly from the 1D simulation (solid line) due to different assumptions. (b) The analytical solution (circles), 1D simulation (squares), and 2D simulation (solid line) converge well at short times.

Longer simulation times become accessible using the 1D cell array, and still longer times using the analytical solution. The 2D, 1D and analytical approaches are found to superimpose agreeably (Figure 3.5). The early portion of the 1D simulation is well described by a curve of the form $T = at^{1/2}$, where the pre-factor a is within 10% of the one calculated using Equation 3.4 and the parameters for glass. The discrepancy in the values for a, observable at longer timescales, can be entirely attributed to the fact that the simulation incorporates heat loss into the air as well as the glass substrate. Using $\sqrt{\alpha t}$ as before, one would expect that after milliseconds, the temperature profile would reach a steady-state in the z-direction. Accordingly, at still longer simulation times, finite-size effects cause the 1D curve to deviate from $T = at^{1/2}$ behavior. The agreement of the three approaches (2D, 1D, analytical) lends strong credibility to the simulation results. Overall, it is predicted that the film temperature rises as $t^{1/2}$ indefinitely. For any realistic macroscopic sample one would eventually have to extend the analysis to include the finite sample size (in the x and y directions) and convective heat flow above the sample. These considerations would necessarily limit the achievable steady-state temperature in a thin film irradiation process. The magnitude and scaling indicate, however, that final film temperatures under modest irradiation will not be very large. Specifically, typical inscription conditions involve irradiating an area approximately 1 cm in size with 50 mW/cm^2, for minutes. According to Equation 3.4, after 5 minutes of 50 mW/cm^2 irradiation, the thin film temperature would have risen by ~12 K. More realistically, the finite irradiation size would be expected to play a role when the temperature profile in the z-direction reaches distances similar to the irradiation size. Using Equation 3.3, we predict a substantial (1 K) temperature rise at a distance of 1 cm from the sample after 2 minutes, at which time the film temperature has risen by 5 K. We expect final film temperatures to be on the order of ~5 K above ambient, which is consistent with the measured temperature rise in a thin azobenzene polymer film under 100 mW/cm^2 irradiation.[22] We performed a further verification experiment, by irradiating a series of liquid crystal films that exhibit visible color transitions at different temperatures, and found that irradiation with 20 mW/cm^2 caused a ~7 K temperature rise, and irradiation with 50 mW/cm^2 caused a ~10 K temperature rise. More importantly, the simulations indicate that any thermal gradient will be very small, stabilizing at ~5×10^{-4} K after 2 μs.

It is unlikely that such a small thermal contrast would lead to any interesting spatial variation of material properties. Thermal gradient mechanisms at modest irradiation are therefore effectively ruled out by these results.

3.4.1 Effect of Film Thickness

As film thickness is increased, the fraction of incoming light that is absorbed increases, which leads to an overall increase in the film heat energy content. The very bottom of thicker films, however, sees proportionally less irradiance as the thickness is increased, so that the minimum temperature becomes proportionally lower. The maximum film temperature increases as the film thickness is increased, corresponding to trapping of heat at the sample surface, but this effect eventually saturates to a bulk value (Figure 3.6). The saturation of the film thickness effect can be fit to, for example, a rectangular hyperbolic function. The entire simulation data set, as a function of time t and thickness h is well described by an equation of the form:

$$T_{\max}(t,h) = \left[\frac{bh}{c+h} + \frac{dh}{e+h}\right] t^{1/2} \tag{3.5}$$

where b through e are fitting parameters, and the term in square brackets is essentially the

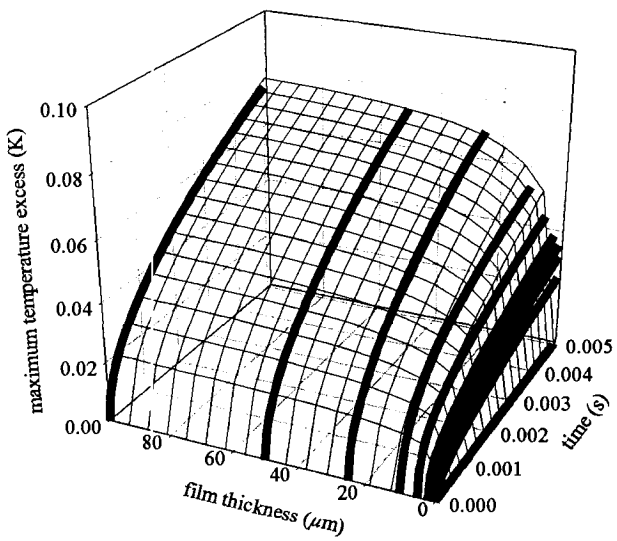

Figure 3.6: Scaling of film temperature with film thickness, based on 1D simulation and 50 mW/cm^2 irradiation. The simulation results (thick lines) are well described by a four-parameter fit (mesh). The maximum temperatures achievable saturate to bulk values for films greater than 50 μm. The $t^{1/2}$ dependence is satisfied for all film thickness values.

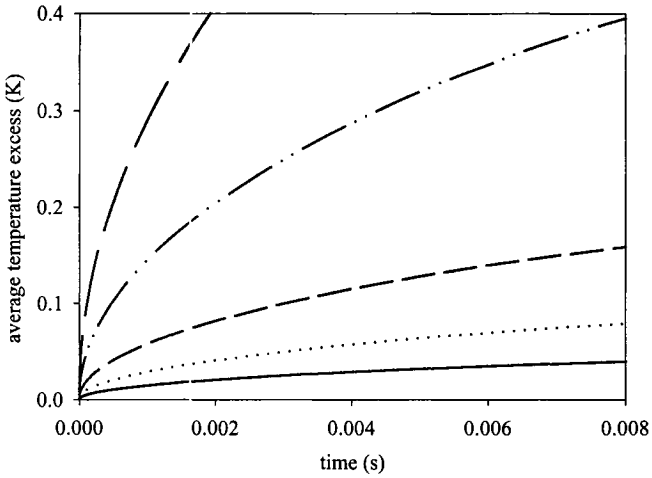

Figure 3.7: Predicted 1D simulation scaling of the temperature in a 200 nm with irradiation power: 50 mW/cm^2 (solid line), 100 mW/cm^2 (dotted line), 200 mW/cm^2 (short dashes), 500 mW/cm^2 (dot and dash line), 1000 mW/cm^2 (long dashes).

parameter *a*. Thus, we can set an upper bound on the temperature rise even in a bulk-like material. This final temperature excess is small even for the thickest films.

3.4.2 Effect of Laser Power

In agreement with the analytical prediction, Equation 3.4, laser power causes a linear scaling of temperature. Laser irradiances above 1 W/cm^2, known experimentally to photo-degrade azo materials, lead to significant temperature rises. From Equation 3.3, irradiation with 1 W/cm^2 leads to a 1 K rise at 1 cm from the film in less than 30 s, at which time the film temperature has increased by 50 K. High laser power densities are known to cause photobleaching by breaking the azo bond. It is possible that photo-induced heating above the material's degradation temperature of 180 °C contributes to sample damage under intense laser light. This prediction is the same order of magnitude as the 15 K temperature rise measured in a thin film polymer light-emitting diode (LED) subjected to 1 W/cm^2 of power input.[23] The agreement is more quantitative when one adjusts for the small size (4 mm^2) of the LED active area compared to the laser spot sizes (~1 cm^2) being considered here. These results also agree with the observed reduction in softening temperature for an azobenzene thin film under 2.4 W/cm^2 laser light illumination, which indirectly suggested a ~12 K photoheating effect.[24] It has been observed that using high laser power, greater than 20 W/cm^2, an in-phase SRG is superimposed upon the out-of-phase SRG obtained under low power irradiation.[6] The in-

phase grating cannot be photoerased, suggesting an irreversible, destructive mechanism. The postulation that this second SRG results from thermal degradation or crosslinking is supported by the present simulations, which predict substantial temperature rises, well above T_g and the degradation temperature (Figure 3.7).

3.4.3 Effect of Substrate (Thermal Conductivity)

Equation 3.4 predicts a ~200-fold difference in film temperatures between the case of glass and air substrates, owing to the markedly different thermal conductivities and heat capacities. Simulation results suggest that the absolute temperature rise of the film will be at least an order of magnitude higher when it is suspended over a good insulator such as air. The lateral temperature difference, however, is not affected by substrate thermal conductivity (Figure 3.8(a)). In order to experimentally investigate

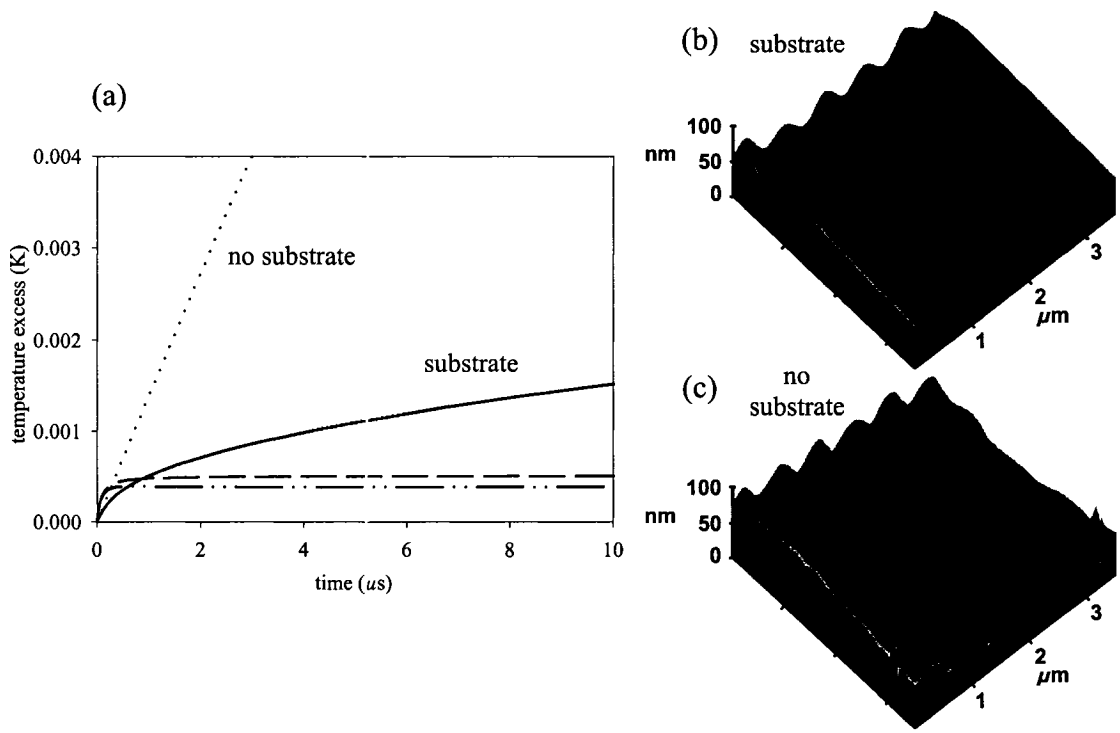

Figure 3.8: (a) Two-dimensional simulation of temperature excess for irradiation (50 mW/cm^2) of a thin film (200 nm) on a glass substrate versus air substrate. The average film temperature for glass substrate (solid line) is much smaller than for air substrate (dotted line), whereas the temperature difference for glass substrates (dashed line) and air substrates (dot and dash line) is identical. There is no experimental difference between the SRG obtained on a plastic substrate (b) versus air substrate (c).

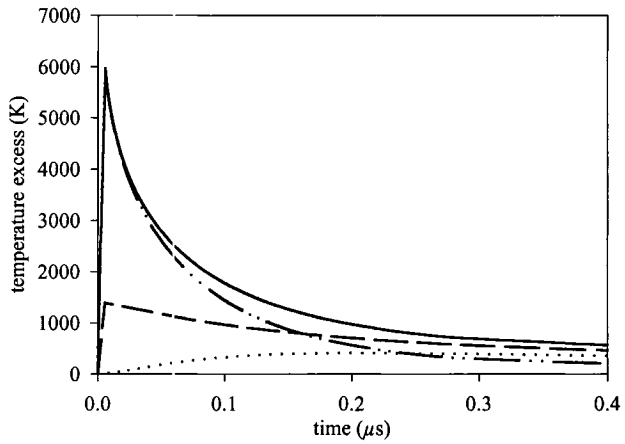

Figure 3.9: Temperature rise predicted by the 2D simulation for a 6 ns laser pulse of total energy 50 mJ/cm^2. The hottest cell (solid line) reaches nearly 6000 K after 6 ns, whereas the coldest cell (dotted line) reaches its maximum temperature after the pulse. The average temperature (dashed line) and temperature difference (dot and dash line) indicate that extremely high temperatures are achieved under pulsed irradiation.

substrate effects, a freestanding polymer film was deposited onto a plastic substrate with holes. The areas of the film on the plastic substrate experience much better thermal conduction (approximately equal to the glass substrate considered in the simulations) than the areas suspended over the holes, which experience an air substrate. The AFM images of SRG inscription in the two areas are shown in Figures 3.8(b) and 3.8(c). Despite the significantly different film temperatures in the two regions, the SRG's are essentially identical. Any photo-thermal effects at play in surface relief inscription are too weak to be observed in this experiment. There is mounting evidence for a photo-induced material softening in azobenzene thin films,[10,24-26] but these simulation results indicate that it has a negligible thermal component.

3.4.4 Pulsed Irradiation

A pulsed irradiation was simulated by using a square-wave light pulse. The photo-energy input was set to be 8.3×10^6 W/cm^2 for 6 ns, corresponding to 50 mJ/cm^2 of energy. The result can be seen in Figure 3.9, where the film temperature rises sharply and nearly linearly for the duration of the pulse. After the pulse, the film cools and redistributes thermal energy. The hottest cells in the film experience a temperature rise of

nearly 6000 K during the pulse, well beyond the typical damage threshold (~180 °C) for these materials. In the polymer photo-ablation literature, temperature increases on the order of 10^3 K have been reported for strongly absorbing samples.[27-30] It therefore seems likely that pulsed experiments on azobenzene polymer thin films are generating thermal gradients of sufficient magnitude to destroy the sample. This is contrary to the postulation that thermal gradients lead to spatial variation of material properties (such as the permittivity), and thereby to optical forces.[18] The foregoing analysis has, however, not included many pertinent effects, such as the non-linear absorption of the azobenzene chromophores at high laser field intensity, and the temperature-dependence of the material properties shown in Table 1. It should also be noted that if ablation is occurring, then the film geometry is changing with time, which the simulation ignores. The simulation nevertheless gives an order of magnitude estimate of sample heating, and strongly suggests that laser pulses are causing material ablation that is in no way unique to azobenzene chromophores.

To verify the pulsed irradiation simulation, we solved analytically for the temperature distribution. Over the course of a 6 ns pulse, the characteristic distance for heat diffusion is $\sqrt{\alpha t} \approx 25$ nm. Given this short distance, the pulsed experiments can be considered in two parts: an irradiation phase where diffusion is neglected, and a diffusion phase after energy input has ceased. The temperature rise at time t during the pulse, assuming no diffusion, can be written:

$$T(y,z,t) = \frac{I_0 t \varepsilon \ln 10}{C}\left[2\sin^2\left(\frac{\pi}{\Lambda}y\right)10^{-\varepsilon(h-z)}\right] \tag{3.6}$$

where I_0 is the incident irradiation intensity, ϵ is the material extinction coefficient, h is the film thickness, and Λ is the spacing of the interference pattern (700 nm for the configurations considered here). The term in square brackets denotes the light distribution pattern inside the film. Using Equation 3.6, one predicts a ~7600 K increase for the hottest point in the film at the end of the pulse, which is within 20% of the result shown in Figure 3.9. The average temperature can be computed as:

$$T_{avg} = \int_0^h \int_0^\Lambda T(y,z,t)dydz \Big/ \int_0^h \int_0^\Lambda dydz$$
$$= \frac{I_0 t}{hC}\left[1 - 10^{-\varepsilon h}\right] \tag{3.7}$$

Using the same parameters as for Figure 3.9, this equation predicts an average film temperature of ~1400 K at the end of the pulse, which is within 2% of the simulation result. The heat diffusion phase can be analyzed by decomposing the temperature distribution that results from the laser pulse into a spatial distribution of instantaneous point heat sources:[31]

$$T(y,z,t) = \frac{Q}{8(\pi\alpha t)^{3/2}} \int_{-\infty}^{\infty} d\bar{x} \int_{-\infty}^{\infty} d\bar{y} \int_0^h d\bar{z} \exp\left(-\frac{(x-\bar{x})^2 + (y-\bar{y})^2 + (z-\bar{z})^2}{4\alpha t}\right)\left[2\sin^2\left(\frac{\pi}{\Lambda}\bar{y}\right)10^{-\varepsilon(h-\bar{z})}\right]$$
$$= \frac{Q}{2\pi\alpha t} \int_{-\infty}^{\infty} \exp\left(-\frac{(y-\bar{y})^2}{4\alpha t}\right)\sin^2\left(\frac{\pi}{\Lambda}\bar{y}\right)d\bar{y} \int_0^h \exp\left(-\frac{(z-\bar{z})^2}{4\alpha t} - \varepsilon \ln 10(h-\bar{z})\right)d\bar{z} \tag{3.8}$$

where the time t now refers to time after the pulse, since the pulse duration is assumed to be negligibly small. Equation 3.8 can subsequently be used as a solution to the heat diffusion law, and the temperature profile during the pulse can be recomputed more rigorously.[32]

Equation 3.8 has implicitly assumed that α is the same everywhere. That is, only a single infinite material is considered. When this equation is compared with a simulation using the same assumption (identical thermal properties in the three regions), the agreement is very good, at all times. At long times (>10^{-7} s), the simulation and analytic results agree to within 2% or better. Near t = 0 s (i.e.: immediately after the pulse), the agreement is between 1% and 15%, depending on the location inside the film. In addition to further validating the simulation procedure presented in this paper, the comparison with analytic results confirms that azo films under pulsed irradiation are likely to achieve temperatures rises of several thousand Kelvin.

3.5. Conclusion

The thermal model developed here for irradiated thin films is simple and robust, appearing to yield reasonable order-of-magnitude estimates for typical situations. Clearly this technique could be extended to other cases, such as consideration of thermal effects

in light propagation down a narrow fiber-optic, NSOM tip, or slab waveguide. With respect to the surface relief inscription process unique to azobenzene polymers, these simulations strongly indicate that thermal effects do not play any appreciable role. Specifically, the overall temperature change under modest irradiation is too small to lead to a change of material properties or softening of the sample. The temperature gradient achieved within the sample is on the order of 10^{-4} K, and does not appear to vary with inscription or geometric conditions. This gradient cannot lead to an appreciable spatial variation of material properties, and certainly does not explain the dependence of SRG inscription on many variables. Surface relief gratings formed under markedly different thermal conditions were essentially identical, further discounting the role of thermal effects. Although there is mounting evidence that azobenzene photo-isomerization leads to material softening, it now seems unlikely that there is an appreciable thermal component. The simulations performed here suggest that pulsed irradiation leads to destructive sample ablation, a well-established phenomenon in strongly absorbing polymer systems, rather than to reversible optical mass transport. Thermal effects in small systems can depend sensitively on many parameters, but it appears that even simple cellular automata, as presented here, can capture much of the behavior at a meso scale in a reasonable way.

3.6. Acknowledgments

Funding for this project was provided by NSERC Canada in the form of grants (CB) and scholarships (KY), by FCAR Quebec in the form of scholarships (KY), and by the Canadian Foundation for Innovation. The authors are grateful to Nasir Ahmad for materials synthesis, and to Peter Grütter for instrument time.

3.7. References

(1) Xie, S.; Natansohn, A.; Rochon, P. *Chem. Mater.* **1993**, *5*, 403.

(2) Rochon, P.; Batalla, E.; Natansohn, A. *Appl. Phys. Lett.* **1995**, *66*, 136.

(3) Kim, D. Y.; Tripathy, S. K.; Li, L.; Kumar, J. *Appl. Phys. Lett.* **1995**, *66*, 1166.

(4) Viswanathan, N. K.; Kim, D. Y.; Bian, S.; Williams, J.; Liu, W.; Li, L.; Samuelson, L.; Kumar, J.; Tripathy, S. K. *J. Mater. Chem.* **1999**, *9*, 1941.

(5) Yager, K. G.; Barrett, C. J. *Curr. Opin. Sol. State Mater. Sci.* **2001**, *5*, 487.

(6) Bian, S. P.; Williams, J. M.; Kim, D. Y.; Li, L. A.; Balasubramanian, S.; Kumar, J.; Tripathy, S. *J. Appl. Phys.* **1999**, *86*, 4498.

(7) Bian, S.; Li, L.; Kumar, J.; Kim, D. Y.; Williams, J.; Tripathy, S. K. *Appl. Phys. Lett.* **1998**, *73*, 1817.

(8) Viswanathan, N. K.; Balasubramanian, S.; Li, L.; Tripathy, S. K.; Kumar, J. *Jpn. J. Appl. Phys., Part 1* **1999**, *38*, 5928.

(9) Barrett, C. J.; Natansohn, A. L.; Rochon, P. L. *J. Phys. Chem.* **1996**, *100*, 8836.

(10) Kumar, J.; Li, L.; Jiang, X. L.; Kim, D. Y.; Lee, T. S.; Tripathy, S. *Appl. Phys. Lett.* **1998**, *72*, 2096.

(11) Lefin, P.; Fiorini, C.; Nunzi, J. M. *Pure Appl. Opt.* **1998**, *7*, 71.

(12) Pedersen, T. G.; Johansen, P. M.; Holme, N. C. R.; Ramanujam, P. S.; Hvilsted, S. *Phys. Rev. Lett.* **1998**, *80*, 89.

(13) Baldus, O.; Zilker, S. J. *Appl. Phys. B: Lasers Opt.* **2001**, *72*, 425.

(14) Barrett, C. J.; Rochon, P. L.; Natansohn, A. L. *J. Chem. Phys.* **1998**, *109*, 1505.

(15) Sumaru, K.; Yamanaka, T.; Fukuda, T.; Matsuda, H. *Appl. Phys. Lett.* **1999**, *75*, 1878.

(16) Bublitz, D.; Fleck, B.; Wenke, L. *Applied Physics B-Lasers and Optics* **2001**, *72*, 931.

(17) Leopold, A.; Wolff, J.; Baldus, O.; Huber, M. R.; Bieringer, T.; Zilker, S. J. *J. Chem. Phys.* **2000**, *113*, 833.

(18) Baldus, O.; Leopold, A.; Hagen, R.; Bieringer, T.; Zilker, S. J. *J. Chem. Phys.* **2001**, *114*, 1344.

(19) Taketoshi, N.; Baba, T.; Ono, A. *Jpn. J. Appl. Phys., Part 2* **1999**, *38*, L1268.

(20) Natansohn, A.; Rochon, P.; Gosselin, J.; Xie, S. *Macromol.* **1992**, *25*, 2268.

(21) Hill, J. M.; Dewynne, J. N. *Heat Conduction*; Blackwell Scientific: Boston, 1987.

(22) Bellavia-Lund, C.; Wudl, F. *J. Am. Chem. Soc.* **1997**, *119*, 943.

(23) Lupton, J. M. *Appl. Phys. Lett.* **2002**, *80*, 186.

(24) Mechau, N.; Neher, D.; Borger, V.; Menzel, H.; Urayama, K. *Appl. Phys. Lett.* **2002**, *81*, 4715.

(25) Srikhirin, T.; Laschitsch, A.; Neher, D.; Johannsmann, D. *Appl. Phys. Lett.* **2000**, *77*, 963.

(26) Kameda, M.; Sumaru, K.; Kanamori, T.; Shinbo, T. *J. Appl. Polym. Sci.* **2003**, *88*, 2068.

(27) Dyer, P. E.; Sidhu, J. *J. Appl. Phys.* **1985**, *57*, 1420.

(28) Gorodetsky, G.; Kazyaka, T. G.; Melcher, R. L.; Srinivasan, R. *Appl. Phys. Lett.* **1985**, *46*, 828.

(29) Danielzik, B.; Fabricius, N.; Rowekamp, M.; Vonderlinde, D. *Appl. Phys. Lett.* **1986**, *48*, 212.

(30) Dijkkamp, D.; Gozdz, A. S.; Venkatesan, T.; Wu, X. D. *Phys. Rev. Lett.* **1987**, *58*, 2142.

(31) Carslaw, H. S.; Jaeger, J. C. *Conduction of Heat in Solids*; Oxford University Press: London, 1986.

(32) Brugger, K. *J. Appl. Phys.* **1972**, *43*, 577.

Chapter 4
Confinement of Surface Patterning in Azo-Polymer Thin Films

The previous chapter described temperature modeling of laser-irradiation of polymer films. It was found that for typical irradiation geometries, photo-heating effects could be ignored. This enabled us, in subsequent experiments, to use temperature as a probe of photo-physical effects, without any confounding effects due to light-driven temperature change. This chapter discusses confinement effects in the patterning of azo materials. With regard to understanding the mechanism of patterning, the previous chapter addressed the effect of photo-heating, whereas this chapter addresses the size-scale of the mass transport phenomenon. In particular, this chapter studies the efficiency of patterning as a function of film thickness, as well as the thermal erasure of surface patterns as a function of thickness. Both techniques demonstrate strong deviations of film dynamics as thickness is decreased, suggesting that the observed material motion is of a size-scale commensurate with the thickness regime studied, that is, on the order of 20–100 nm.

4.1. Abstract

Azobenzene polymer thin films are known to spontaneously generate surface patterns in response to incident light gradients. This peculiar process is investigated in terms of the dynamics of the various azobenzene photo-motions, which occur on different length-scales. In particular, the formation and thermal erasure of surface relief gratings are measured as a function of film thickness, and by using combinatorial samples with thickness gradients. The thermal erasure of gratings in this system provides a direct measure of the glass transition temperature, which is found to deviate substantially from the bulk value. Thin azo films exhibit a glass transition up to 50 K higher than the bulk. These dynamical measurements allow us to probe the length-scale of mass transport, which is found to be ~150 nm. Furthermore, surface mass transport is completely arrested in thin films <40 nm. According to these results, mass transport involves the coordinated motion of many polymer chains in the depth of the sample, rather than surface diffusion of individual chains.

4.2. Introduction

Azobenzene polymers are unique materials that exhibit remarkable photo-physical and photo-mechanical properties.[1,2] Fundamentally, the azo chromophore undergoes a clean and efficient photo-isomerization when irradiated with light anywhere within its broad absorption spectrum (see Figure 4.1). This isomerization converts the stable *trans* azo into a meta-stable *cis* azo state. The *cis* isomer will revert thermally back to the *trans* form, or this back-isomerization can be photo-initiated. For the azo materials studied here (so-called pseudo-stilbenes), the thermal back relaxation has a timescale on the order of seconds, and since the *trans* and *cis* absorption spectra overlap, a single wavelength of light (in the region of 450–490 nm) can be used to induce both the forward and the reverse photo-isomerization simultaneously. This molecular-scale photo-motion leads to a host of larger-scale material motion effects. For instance, the azo chromophore can be photo-aligned with polarized light due to a statistical absorption and reorientation phenomenon (essentially orientational hole burning). This fully reversible chromophore alignment leads to strong dichroism and birefringence in the azo materials, due to the azo's anisotropic structure. The azo photo-motion has been investigated as a photo-switch,[3] to align liquid crystalline systems,[4,5] to bend freestanding thin films,[6,7] and in many other photo-dynamic systems.[2]

In 1995, a further photo-motion was discovered in the azo system.[8,9] It was found that irradiation with a light intensity and/or polarization *gradient* would lead to

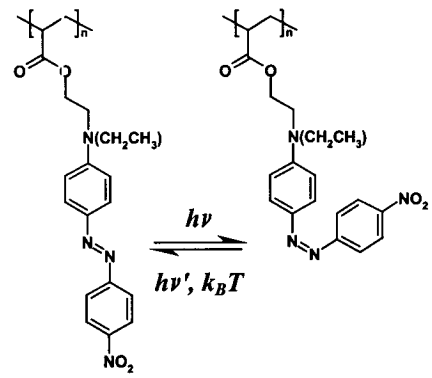

Figure 4.1: Molecular structure of the azobenzene-containing polymer poly(disperse red 1 acrylate) (pdr1a). The azo chromophore isomerizes from the *trans* to the *cis* state when irradiated at an absorbing wavelength. The molecule relaxes thermally back to the stable *trans* state, or can be reconverted photochemically.

spontaneous large-scale motion of polymer material in the thin film, resulting in surface topographical patterning. In the simplest experiment (see Figure 4.2), the sample is exposed to a sinusoidal variation in light intensity, originating from the interference of two coherent laser beams. The end result is that the azo material generates a Surface Relief Grating (SRG), as shown in Figure 4.2. Any incident light field can be used, with the azo material's surface deforming to reproduce the light pattern. The process is strongly polarization dependent,[10] and occurs even at remarkably low laser power (1–100 mW/cm^2). This topographical hologram is stable indefinitely at room temperature, but can be erased by heating the film past its glass-to-rubber transition temperature (T_g), in which case the original film thickness is recovered. This demonstrates that the process in question is a material motion, and not a photo-ablation phenomenon where material is

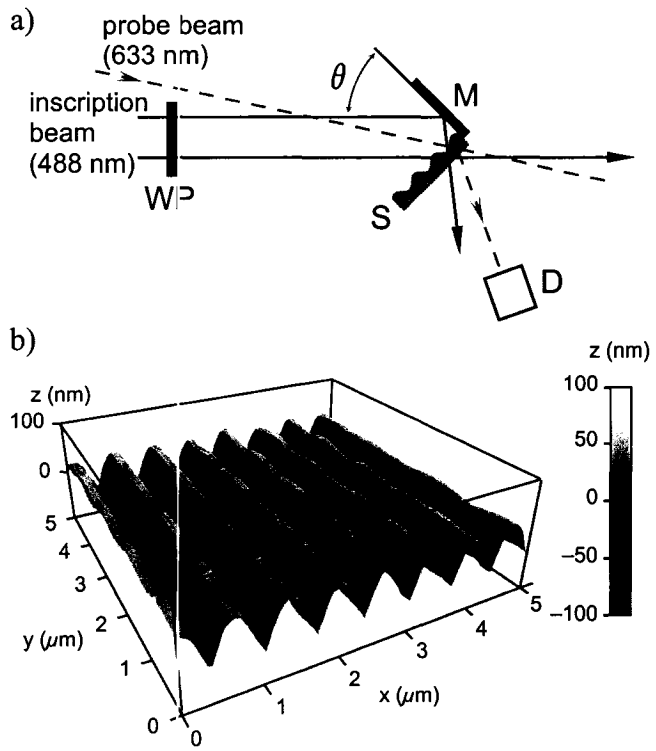

Figure 4.2: (a) Experimental setup for inscription of surface relief gratings in azo thin films. The azo sample (S), cast on a glass slide is placed in proximity to a mirror (M). An inscription laser beam (Ar^+ 488 nm) is circularly-polarized using a quarter-wave plate (WP). The laser beam reflects off of the mirror and interferes with itself at an angle θ. The grating formation can be measured in real-time using a probe laser beam (HeNe 633 nm) that is diffracted into a detector (D). (b) The resulting sinusoidal surface relief grating, inscribed into the azo-polymer surface, as measured using atomic force microscopy.

lost, as would be the case for most materials irradiated at extremely high power. The periodicity of the grating is diffraction limited, being determined by the wavelength of light and the inscription geometry. For typical inscription conditions, a peak-to-peak spacing of 700 nm is obtained. Despite active investigation, the mechanism of this photo-patterning phenomenon has not been fully resolved.[11] Suggested mechanisms include photo-pressure,[12,13] asymmetric diffusion,[14,15] mean-field forces,[16,17] and optical gradient forces.[10,18-20] Not only is the fundamental origin of the driving force not elucidated, but there are still unknowns related to the size-scale and dynamics of the mass transport phenomenon. The present paper attempts to probe these questions using dynamics measurements in films of varying thickness. In particular, we probe the efficiency SRG formation as a function of film thickness, and measure the SRG erasure temperature in this thickness series.

Gratings in thin films can easily be quantified using the intensity of a diffracted probe laser beam. An azo material irradiated with a light intereference pattern will have a number of superimposed gratings inscribed into it. During laser irradiation, the illuminated areas will have a higher *cis*-fraction than the dark regions of the pattern. The *cis* and *trans* isomers have different refractive indices, and this spatially periodic refractive index produces a phase grating. This chemical grating is transient since it will decay after irradiation ceases (since the *cis* isomers will thermally reconvert to the *trans* form). In addition, the polarization-dependant orientation of azo chromophores will lead to a birefringence grating, since the birefringence (hence refractive index measured by the probe laser) is spatially varying. This grating is stable at room temperature, although it experiences a measurable decay after irradiation ceases, due to orientational relaxation.[21] The surface relief grating (topographical grating) is stable at room temperature. The diffraction efficiency of the SRG is very high, owing to the large-amplitude surface modification (up to hundreds of nanometers), and typically the measured diffraction efficiency is dominated by the topographical grating component. More recently, evidence for a density grating inscribed beneath the surface of a SRG has been found.[22,23] This grating was found to form during SRG inscription, but was only measurable after a subsequent thermal treatment step. Apparently the inscription process gives rise to seeding crystallites that grow with thermal treatment, leading to a spatially varying

density in the material. This density grating in principle leads to spatial variation of refractive index. In practice, however, it makes only a small contribution to the visible-light diffraction efficiency (although it is readily measured using x-ray diffraction). Thus the visible-light diffraction efficiency is largely a probe of the surface relief, and the x-ray diffraction a measure of the density grating. The simultaneous existence of these coincident gratings (chemical, birefringence, topographical, and density) necessarily complicates analysis of the diffraction efficiency. However it also provides for independent measures of material dynamics at different size-scales. For instance, the chemical and birefringence gratings are related to molecular-scale motion (azo chromophore isomerization and orientation) whereas the topographical grating involves lateral length-scales on the order of hundreds of nanometers.

Previous investigations have measured the temperature at which photo-induced orientation (i.e.: birefringence) is erased.[24] In these liquid-crystalline systems, the birefringence is stable above the glass-transition temperature, owing to the order of the LC phase, but is erased at the melting temperature for the mesophase. In amorphous systems,[25] it is not possible to maintain photo-orientation above T_g. Thermal erasure of azo-polymer surface relief gratings has recently been probed by simultaneous visible-light diffraction and x-ray diffraction.[26,27] Erasure of the SRG was observed to coincide with the bulk glass-transition temperature in the thin films studied. Evidence was also found for the formation of a buried density grating during SRG formation, which becomes enhanced during the thermal treatment. To further this analysis, we now consider the erasure of surface relief gratings in thin films of varying thickness. The thickness-dependence of the grating erasure provides information about the dynamics of the mass transport phenomenon, and allows us to measure the length-scale associated with the phenomenon.

4.3. Experimental Methods

4.3.1 Sample Preparation

The polymer material, poly(disperse red 1 acrylate) (pdr1a) was synthesized as previously reported.[28] Samples were prepared by spin-coating azo-polymer solutions (pdr1a in THF solvent) onto cleaned glass microscope slides. The solution was placed on

the substrate, and subsequently ramped (acceleration 1260 rpm/s) to 1300 rpm, and maintained for 35 s. Film thickness was varied by adjusting the concentration of the solution (in the range of 10^{-1} to 10^{-3} mol/L, based on repeat unit molecular mass). Thin films were annealed in a vacuum oven at 110°C for 8 hours to remove any residual solvent or flow-induced orientation. Film thickness was measured by imaging a scratch in the thin film by AFM (Digital Instruments Nanoprobe IIIa in contact mode and Asylum MFP-3D in tapping mode). Thickness measurements were corroborated by UV-VIS spectroscopy and knowledge of the material extinction coefficient. Samples prepared with a thickness gradient were obtained using literature methods.[29-31] Briefly, a droplet of polymer solution is placed on a substrate, and a knife-edge held above the surface is used to drag the solution across the substrate. Since the final film thickness depends upon the drag velocity (as well as solution concentration), an acceleration ramp will generate a thin film with a thickness gradient. In this work, a 50 μL drop of polymer solution (5×10^{-2} mol/L, based on repeat unit, pdr1a in THF) was coated onto cleaned glass microscope slides. The gap between the substrate and the blade was maintained at ~100 μm, with a blade angle of 5°. The substrate was ramped from 1 mm/s to 5 mm/s at an acceleration of 0.56 mm/s^2.

4.3.2 SRG Formation

Surface relief gratings (SRGs) were prepared by placing a thin film adjacent to a mirror, which reflected a coherent laser beam onto the surface (experimental setup shown in Figure 4.2). Inscription was performed at room temperature (25°C), and from previous work it is known that the low laser power used does not lead to appreciable sample heating.[32] Laser inscription was performed using the 488 nm line of an Argon-Ion laser (Coherent Innova 308). Unless otherwise specified, the irradiation intensity was 37 mW/cm^2, the inscription angle was θ = 20°, and the irradiation time was 420 s. The incident laser beam was circularly-polarized using a quarter-wave plate. Interference of right and left-handed circularly polarized laser beams is known to give rise to high-efficiency surface relief formation. Grating amplitude during formation was quantified using the diffraction of a probe laser beam (20 mW HeNe 633 nm laser attenuated by an ND 2.0 filter). The height of the final inscribed surface relief grating was measured by AFM.

4.3.3 SRG Erasure

Grating erasure experiments involved measuring the decay of the diffraction of a probe laser beam (10 mW HeNe 633 nm laser attenuated by an ND 2.0 filter) during thermal ramping. The probe beam was attenuated to minimize any possible photo-isomerization or photo-orientation (absorption at 633 nm is small, yet can nevertheless lead to measurable photo-physical effects[33]). Furthermore, a computer-controlled shutter was synchronized with data acquisition, so that the probe beam illuminated the sample only when required. This further minimized sample exposure to the probe beam during the long experiment duration (~24 hours). The sample was fixed inside a heating stage with optical windows on the front and back (INSTEC HCS302), driven by a temperature controller (INSTEC STC200). Good thermal exchange between the sample and the heating block was insured using metal contact spacers. The thin film was ramped from 25°C to 140°C (or 160°C, as required) at a rate of 0.08 °C/min. This ramp-rate was selected based on initial exploratory experiments, where it was determined that the erasure temperature depended on ramp-rate if the rate was too high. For the slow ramp-rate chosen, there is no longer any appreciable dependence on the rate.

4.3.4 Diffraction Efficiency

The diffraction efficiency can be quantitatively related to the height of the induced surface relief grating, and the intensity of the inscribed birefringence and density grating (which both give rise to a spatial variation of refractive index). Specifically, the intensity of the diffracted visible light, for the m-th order diffraction, scales as:[34]

$$I \approx \left| J_m(q_z h) - e^{iq_z d} J_m(q_z \Delta n_m d) \right|^2 \tag{4.1}$$

where the J_m refer to the Bessel functions, h is the grating height, d is the film thickness, and Δn_m is the m-th Fourier component of the refractive index grating. The scattering angles are contained in the momentum transfer:

$$q_z = n\frac{2\pi}{\lambda}(\cos\theta_i + \cos\theta_f) \tag{4.2}$$

where n is the refractive index, λ is the wavelength of the probe beam, and θ_i and θ_f refer to the incident and diffracted angles, respectively (as measured from the surface normal). These equations can be used to describe both the formation and erasure of a surface relief

grating. The Bessel functions can give rise to oscillations in the diffracted signal. The grating heights employed in the present work, however, were kept beneath the first oscillation in the function, which simplifies data fitting.

During grating erasure, the diffraction efficiency is eliminated at a characteristic temperature. Thus the height of the SRG can be assumed to follow an equation of the form:[27,34]

$$h = h_{\max} \frac{1}{1 + \exp\left(\frac{T - T_{g,a}}{E_a}\right)} \tag{4.3}$$

where $T_{g,a}$ is the apparent glass-transition temperature (erasure temperature), h_{max} is the initial grating height (which can be determined from AFM), and E_a is an activation energy, which describes the breadth of the transition. A similar equation exists for the erasure of the Δn grating. However the previous work on fitting grating erasure data has shown that the birefringence component is much smaller than the surface relief component, at least prior to a first melting sequence. It was confirmed here that the results are not appreciably affected if the refractive index grating (Δn term) is ignored for the fits to the erasure data. Using the above equations, we were able to obtain high-quality fits to the thermal grating erasure data.

4.4. Results and Discussion

4.4.1 Grating Formation

The diffraction intensity of a probe laser beam (HeNe 633 nm) was measured during the inscription of surface relief gratings. Representative results can be seen in Figure 4.3. As film thickness is decreased, the diffraction efficiency decreases considerably. Moreover, there is clear evidence that grating formation saturates more quickly in thinner films than it does in thicker films, indicating that material motion is being arrested in thinner films. The decay of the signal seen immediately after the laser is turned off is due to *cis* to *trans* back-relaxation (i.e.: elimination of the chemical grating) and some amount of orientational diffusion (i.e.: relaxation of the birefringence grating).[21] Both of these processes are molecular in origin. In particular, the decay portion of the data is well described by a biexponential function:

$$signal = ae^{-k_{ct}t} + be^{-k_{or}t} \quad (4.4)$$

where t is time after the inscription laser is turned off, $a = 0.22$ is the relative contribution from the chemical grating, and $b = 0.78$ is the relative contribution of the orientational grating. The value for the *cis* to *trans* relaxation is $k_{ct} = 0.24\ s^{-1}$, as reported previously in the literature.[35] The value for the orientational relaxation was fit to be $k_{or} = 0.063\ s^{-1}$. These same values can be used to fit the decay for films of all thickness values, indicating that these relaxation processes are not appreciably affected by thin film confinement in the range of 20 nm to 430 nm. It is worth noting that a previous investigation[36] used the azobenzene *cis* to *trans* relaxation as a probe of mobility in thin polystyrene films. In that work, evidence for enhanced mobility of the isomerization (hence of the polymer network) was detected for thin films <100 nm. This effect was not detected in the present study, although the post-inscription relaxation has a substantial orientational component, which may be unaffected by film thickness in the range probed. In any case, it is evident that the molecular-scale processes are much less sensitive to the film thickness than the larger-scale mass transport phenomenon, as will be shown below.

As discussed in the introduction, laser irradiation generates several kinds of gratings simultaneously. Both a persistent grating, and a transient grating are inscribed. The latter gives rise to the decrease in signal observed after irradiation ceases. The persistent grating results from topographical patterning (SRG) and the birefringence

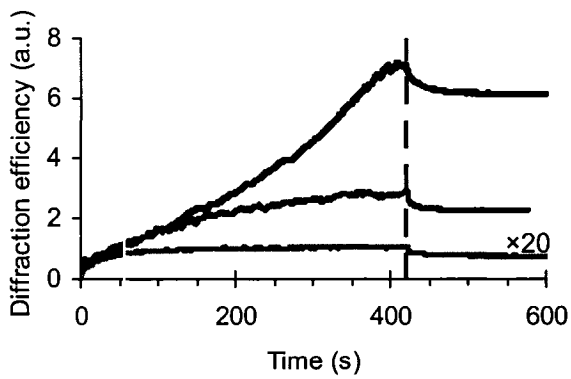

Figure 4.3: Diffraction efficiency (arbitrary units) measured during grating inscription. The irradiation laser was turned on at 0 s, and was turned off at the moment indicated by the dashed line (420 s). The upper curve is for a 427 nm film, the middle curve for a 114 nm film, and the lower curve for a ~20 nm film (this data has been scaled 20-fold for clarity).

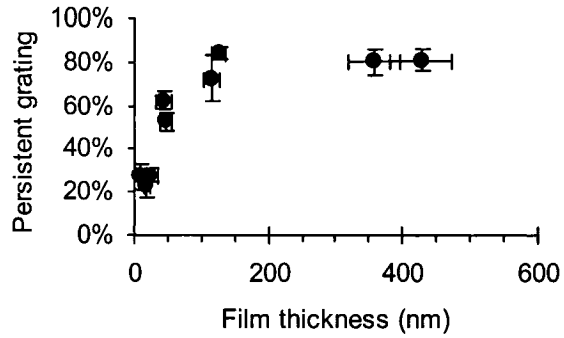

Figure 4.4: Variation of the composition of the measured diffraction signal as a function of film thickness. The extent of the persistent grating (primarily surface relief) relative to the transient grating (primarily chemical) can be quantified using the diffraction efficiency data (see Figure 4.3). In thick films, the diffraction is primarily due to the large-scale SRG, whereas in thin films the molecular-scale chemical grating dominates.

grating. Except in extremely thin samples, the topographical grating is the dominant contributor to the measured persistent diffraction. The transient grating, on the other hand, is due to the *cis/trans* chemical grating, with some contribution from the birefringence grating, which relaxes due to orientational diffusion after the laser is turned off. The SRG by contrast remains fixed after the laser is turned off, and is not part of the observed transient signal. Thus the transient grating is a probe of molecular-scale motion (azo isomerization and azo dipole motion) whereas the persistent grating is a probe of larger-scale motion (involving mass transport of polymer chains). The relative contribution of the persistent and transient gratings can be seen in Figure 4.4. This data provides a measure of the extent to which the various processes (molecular and larger-scale polymer motion) are affected as film thickness decreases. For thick films, the persistent grating (the SRG) accounts for the majority of the observed diffraction, whereas in thin samples it becomes the minor contribution. This indicates that as we scale to thinner samples, the formation of surface-relief is being arrested more significantly than the molecular motions of *cis/trans* isomerization and orientational motion of azo dipoles. In other words, the larger-scale photo-motions of the azo chromophore are being hindered, whereas molecular-scale photo-motions are not.

4.4.2 SRG Height

In order to ascertain the scaling of SRG formation with film thickness, an azo thin film with a macroscopic gradient in thickness across its surface was exposed to interfering laser light (Figure 4.5). This combinatorial experiment allows a range of thickness values to be probed simultaneously. The sample was illuminated with a gradient in light intensity, thereby creating a 2D combinatorial sample that simultaneously probes film thickness and irradiation intensity (and the interplay between these two parameters). As expected, the diffraction efficiency increases with increasing irradiation intensity (the intensity is 2.8 mW/cm^2 near X = 0 mm and increases to 33.7 mW/cm^2 at X = 20 mm). It can also be seen that diffraction efficiency is larger in thicker films (film thickness varies from 30 nm near Y = 25 mm to 60 nm near Y = 40 mm). Direct measurements of surface relief grating height were also conducted using AFM on a series of samples with different thickness values. The data, shown in Figure 4.6, again demonstrate that grating inscription becomes hindered in extremely thin films, regardless of the laser intensity used. In extremely thin films (<40 nm), the SRG height becomes smaller than the film roughness, and is not detectable by AFM. This inability to form surface relief structures in ultra-thin films suggests that a certain size-scale of material motion is required for efficient mass transport.

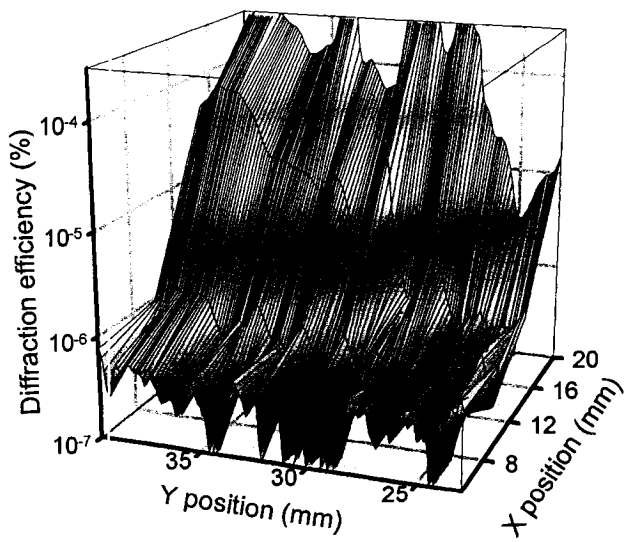

Figure 4.5: Diffraction efficiency (logarithmic scale) for a combinatorial thin film of azo polymer. The sample thickness increases in the +Y direction. The sample was irradiated with a light interference pattern whose intensity increases in the +X direction.

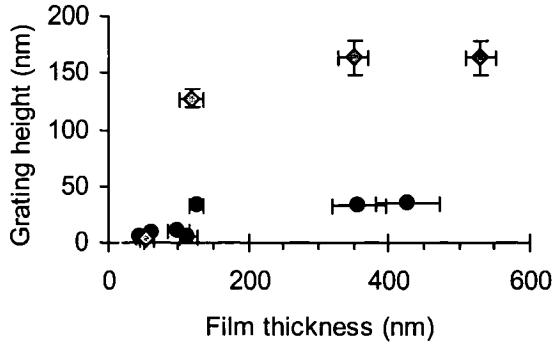

Figure 4.6: Inscribed grating height (SRG amplitude) as a function of film thickness, as measured by AFM. The gray diamonds correspond to a laser irradiation intensity of 120 mW/cm^2, whereas the black circles correspond to 37 mW/cm^2. In both cases a decrease in grating height is seen in thinner samples.

4.4.3 Grating Erasure

To further probe the size-scale dependence of mass transport dynamics in the azo-polymer system, surface relief gratings were thermally erased. Typical grating erasure curves are shown in Figure 4.7. As the thin film is heated, the diffraction efficiency eventually begins dropping, due to material flow that serves to erase the grating (oscillations in the signal are due to thermal expansion of the film and substrate). This elimination of surface relief is undoubtedly a surface-tension driven process. At room temperature the material is an amorphous glass and material motion is impossible. As the glass-transition temperature is approached, coordinated polymer motions become activated and the thin film flattens out any surface patterns. The grating erasure data can be fit using Equations 1–3. The end result of such a fit is the determination of an erasure temperature ($T_{g,a}$) and an activation energy for the process (E_a). For thick films (>350 nm), the erasure temperature corresponds well to the bulk glass-transition temperature (T_g). Specifically, the grating erasure occurs at 102°C, slightly higher than the bulk T_g of 95–97°C. It is worth noting that a decrease in diffraction is observed ~15°C before the $T_{g,a}$ is reached, which is ~10°C below the bulk T_g value.

Figure 4.7 shows a sample of grating erasure curves for films of different thickness. In all cases surface relief gratings were inscribed with identical optical irradiation parameters. As film thickness is decreased, the erasure temperature exhibits a remarkable shift towards higher temperatures. The fit parameters are shown in Figure 4.8.

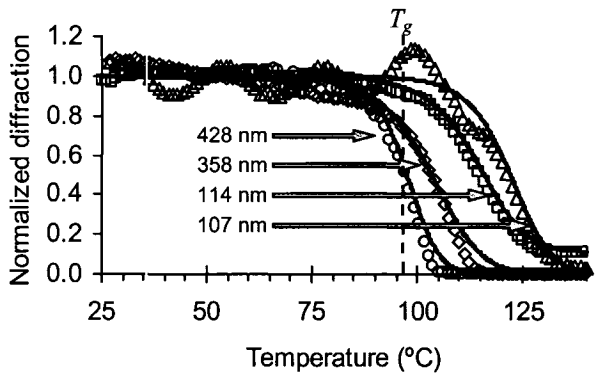

Figure 4.7: Typical grating erasure curves for films of different thickness. The symbols are the experimental data, and the solid lines are the fits. As the film thickness is decrease, the curve is shifted to higher temperatures, corresponding to a higher grating erasure temperature.

The deviation from bulk T_g becomes very large in the thinnest films, with no indication of grating erasure even after passing through the bulk T_g value. For thin films of 46 nm, the measured $T_{g,a}$ is ~50°C higher than the bulk glass-transition. This represents a substantial shift of the film dynamics compared to bulk samples, evidently related to thin-film confinement. The breadth of the transition (described by E_a) is a comparatively insensitive fit parameter. It does not appear to follow any trend with film thickness, with a value of ~8 K reasonably describing all the data.

It is important to emphasize that the change in apparent T_g with film thickness cannot be explained by SRG height alone. For example, in the thinnest films the inscribed gratings are of nearly equal height, yet the apparent T_g is nevertheless strongly sensitive to film thickness in this regime. As a further check, SRGs of various heights were inscribed in films, using different irradiation times. The grating erasure temperature was found to depend upon the film thickness, and not the height of the SRG being erased.

4.4.4 Ultra-thin Films

In extremely thin films (<40 nm), any inscribed surface relief grating is essentially non-existent, as measured by AFM, being smaller than the roughness of the sample surface. In these ultra-thin films, one can nevertheless measure a small rise in diffraction efficiency during laser inscription, and an erasure of this diffraction during the temperature ramping step. In this case, the observed grating is likely entirely due to the inscribed birefringence grating. In extremely thin films (<40 nm), the birefringence

grating is erased at ~110°C, which corresponds to the sample's bulk glass transition temperature. We can again conclude that the molecular-scale motion of azo orientation is not affected by thin-film confinement effects, in marked contrast to the large-scale surface mass transport. Undoubtedly the erasure of the birefringence grating is occurring in samples >40 nm as well, but this erasure appears to be small in size compared to the erasure of the SRG, whose diffraction efficiency is much larger. In fact the gradual decrease in diffraction efficiency as T_g is approached in thicker samples can be attributed to erasure of the weak birefringence grating. Thus for thicker samples (>40 nm) the erasure is dominated by the topographical grating (with a small contribution from a birefringence grating), whereas in thinner samples (<40 nm) the topographical grating cannot be written and the observed diffraction is entirely due to the birefringence grating.

The inability to form gratings in ultra-thin samples is not merely a limitation of irradiation power or time. From Figure 4.6 we can see that even with greater irradiation power, the SRG height decreases to zero near ~40 nm. Furthermore, the grating

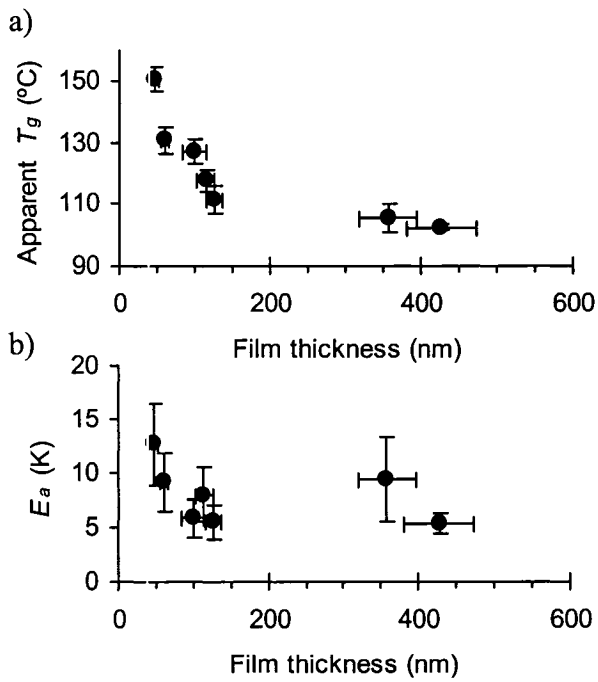

Figure 4.8: Fit parameters for grating erasure data for various film thickness values. (a) The apparent T_g (grating erasure temperature) increases dramatically in thin films <150 nm. (b) The breadth of the erasure (described by E_a) is a comparatively insensitive parameter, and does not vary considerably as a function of film thickness.

inscription curves (Figure 4.3) show faster saturation for the thinner samples, with no further rise in the signal, indicating that even with further irradiation, no SRG would be produced. This was confirmed with extremely long irradiation times (several hours), where no grating could be generated in ultra-thin films. The inability to form gratings in ultra-thin samples is an indication of the size-scale of material motion required to generate an SRG.

4.4.5 Mass Transport Size-scale

The data clearly indicate that the SRG formation and erasure involve motion over a length-scale on the order of 150 nm. This size-scale is much larger than the azo molecule. The azo polymers used for surface patterning are typically low molecular weight chains. In the present study, the polymer molecular weight was approximately 3700 g/mol, corresponding to chains that are 8–12 repeat units long. A minimized molecular model of a 10-mer is shown in Figure 4.9 (generated using the Amber Force Field method from the HyperChem 6.0, Hypercube Inc. software). The size of a typical polymer chain in this system is on the order of 3 nm, considerably smaller than the 150 nm length-scale involved in mass transport. Thus the inhibition of dynamics seen in thin films is not a polymer-chain confinement effect. Instead, the material transport appears to

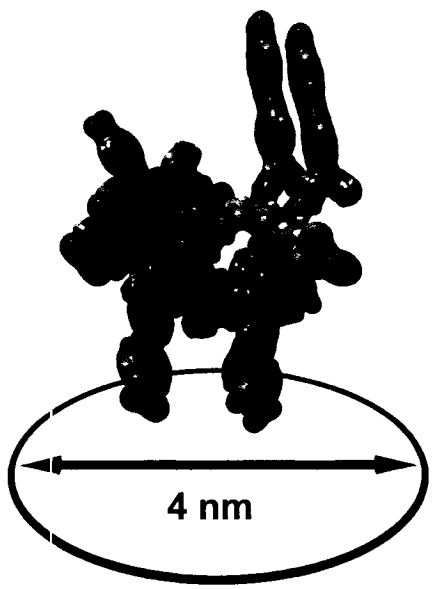

Figure 4.9: Molecular model of a typical pdr1a azo-polymer chain (10 repeat units). The size of a polymer chain is quite small: on the order of 3–4 nm.

involve the coordinated motion of many polymer chains. Such an effect is more naturally described in a hydrodynamic framework. The polymer-substrate interface acts as a pinning surface, preventing material motion at that point. This frictional force prevents material motion well into the material. This effect is in some ways similar to a fluid boundary layer (although by any conventional calculation, the size of the boundary layer in this case is orders of magnitude larger than the film thickness).

4.4.6 Surface Chemistry

If the increase in erasure temperature is due to interaction with the substrate, it is natural to ask whether altering the surface chemistry will affect the observed trends. Glass slides treated with dimethyldichlorosilane present a highly hydrophobic CH_3 terminate surface. In this case the affinity of the polymer for the surface is decreased, and as a result the thin film was found to undergo significant dewetting. Conversely, a glass slide treated with Piranha clearing solution (boiling 3:1 mixture of H_2SO_4 and H_2O_2) presents an oxidized, OH rich, and thus hydrophilic, surface. In this case the polymer does not dewet, but surface affinity is again decreased. As with the untreated glass surfaces, no grating inscription in thin films <40 nm was observed on the highly hydrophilic glass substrates. Whether or not the scaling of the apparent T_g is modified by different surface chemistries (or indeed in free-standing thin films) is an open question that bears further study.

4.4.7 Glass-transition Temperature

It is now well-established that thin freestanding polymer films exhibit depressed T_g relative to the bulk value.[37] This effect has been mapped through the thickness of thin polymer films,[38] where it was determined that the free surface of a polymer film exhibits enhanced dynamics relative to the bulk. This effect was found to penetrate ~20 nm into polystyrene thin films. The existence of this mobile surface layer, combined with the present data, allows us to rigorously exclude a purely surface-layer mass transport phenomenon in azobenzene systems. If the material motion were occurring purely at the surface, the erasure of a SRG would be expected to occur at a $T_{g,a}$ considerably below the bulk value (i.e.: it should occur at the T_g for the surface layer). Instead what is observed here is that even in the thickest films, the grating is erased near the bulk T_g value. This

may be because the surface of these materials does not exhibit substantial deviations from bulk T_g (possibly due to the low molecular weight). However this may also be viewed as substantiation that the length-scale for this material motion is much larger than this mobile surface layer.

The method presented in this paper for measuring dynamics, namely to identify the erasure temperature for a surface relief grating by measuring diffraction, could be applied to a wide variety of systems. In the case of azo-polymers, the formation of a surface relief is especially straightforward, due to the optical patterning process. However in principle nearly any material could have a SRG inscribed onto it in some way, and the diffraction efficiency as a function of temperature could be used to measure the film dynamics. Previous investigations have measured the decay of nanoscale roughness[39] or embossed surface patterns[40] by AFM. Such measurements are obviously laborious, whereas measurement of diffraction efficiency is facile and sensitive. The method of hot-embossing surface patterns into polymer films could be applied to a wide-range of systems, allowing for a new and direct measurement of relaxation-phenomena in thin films. Moreover, novel measurements could be performed. For instance, two-dimensional surface patterns could be imprinted into a film, and the diffraction of a probe beam in the two orthogonal directions could be used to probe anisotropic dynamical properties. In the azo-polymer system, we have used the erasure of an inscribed grating to probe deviations from bulk T_g in thin film. We have measured substantial deviations from the bulk glass transition behavior in thin films <150 nm. For extremely thin films (<50 nm), it would appear that the effective T_g of the thin film is ~50°C higher than the bulk value.

4.5. Summary and Conclusions

Based on the presented results, it is clear that the long-range (hundreds of nanometers) motion of polymer material in azo samples is hindered in thin-films, due to confinement and the pinning effect of the substrate interface. Furthermore, the photo-induced mass transport phenomenon seen in the azobenzene system is arrested in extremely thin films, showing that this process is a long-range effect. In addition to substantial material flow in the film plane directions, it is now clear that the azo photo-motion absolutely requires coordinated motion of material in the film normal direction, over length-scales of ~150 nm.

Previous reports in the literature have attempted to ascertain whether the surface mass transport phenomenon is a surface or bulk phenomenon. In particular, an experiment was performed where a thin film of azo material was capped with a thin transparent polyelectrolyte layer.[41] This thin layer of material was found to noticeably hinder grating formation. Combined with the present results, we now have a more complete picture of the nature of the mass transport phenomenon. In addition to requiring an unrestricted free surface, we now have strong evidence that material motion over larger length-scales (~150 nm) in the film normal direction is required to move material at the sample surface. Furthermore, the efficiency of this process is strongly sensitive to the amount of material beneath the free surface, and not merely the material in proximity to the surface. This demonstrates that the material motion is not localized to the interface, but involves forces and material flow originating at greater distances. This explanation is consistent with the previous study, since capping the free surface of the thin film would be expected to hinder SRG formation due to the higher energy requirement for increasing film surface area. Adding a capping layer to an azo thin film creates a pinning interface analogous to the substrate pinning observed in this study.

With regard to the mechanism of surface relief formation, the present results are most consistent with a hydrodynamic and photo-mechanical model, such as the photo-induced pressure mechanism. Diffusion models, on the other hand, would predict that the process would occur efficiently in a thin surface layer, and would not require coordinated motion within the film bulk. Similarly, models proposing localized forces between azo molecules would not predict a strong thickness dependence to the phenomenon. Instead what is observed here is that a long-range stress buildup in the film is responsible for the observed mass transport. Grating inscription is a manifestly large-scale phenomenon, both in terms of lateral material flow, and in the film normal direction, where cooperation of material over nanometer to micron length-scales is required for efficient photo-induced surface patterning.

4.6. Acknowledgments

We thank Faisal Aldaye for help with molecular modeling, Derek Gray and Emily Cranston for help with the AFM work, Nasir Ahmad for materials synthesis, and Shing

Kwok for performing initial exploratory experiments. Research funds were provided by NSERC Canada and the Canadian Foundation for Innovation.

4.7. References

(1) Natansohn, A.; Rochon, P. *Chem. Rev.* **2002**, *102*, 4139.

(2) Yager, K. G.; Barrett, C. J. *J. Photochem. Photobiol., A* **2006**, *in press*, doi 10.1016/j.jphotochem.2006.04.021.

(3) El Halabieh, R. H.; Mermut, O.; Barrett, C. J. *Pure Appl. Chem.* **2004**, *76*, 1445.

(4) Ichimura, K. *Chem. Rev.* **2000**, *100*, 1847.

(5) Yu, Y. L.; Ikeda, T. *J. Photochem. Photobiol., C* **2004**, *5*, 247.

(6) Ikeda, T.; Nakano, M.; Yu, Y.; Tsutsumi, O.; Kanazawa, A. *Adv. Mater.* **2003**, *15*, 201.

(7) Yu, Y.; Nakano, M.; Ikeda, T. *Nature* **2003**, *425*, 145.

(8) Rochon, P.; Batalla, E.; Natansohn, A. *Appl. Phys. Lett.* **1995**, *66*, 136.

(9) Kim, D. Y.; Tripathy, S. K.; Li, L.; Kumar, J. *Appl. Phys. Lett.* **1995**, *66*, 1166.

(10) Viswanathan, N. K.; Balasubramanian, S.; Li, L.; Tripathy, S. K.; Kumar, J. *Jpn. J. Appl. Phys., Part 1* **1999**, *38*, 5928.

(11) Yager, K. G.; Barrett, C. J. *Curr. Opin. Sol. State Mater. Sci.* **2001**, *5*, 487.

(12) Barrett, C. J.; Natansohn, A. L.; Rochon, P. L. *J. Phys. Chem.* **1996**, *100*, 8836.

(13) Barrett, C. J.; Rochon, P. L.; Natansohn, A. L. *J. Chem. Phys.* **1998**, *109*, 1505.

(14) Lefin, P.; Fiorini, C.; Nunzi, J. M. *Opt. Mater.* **1998**, *9*, 323.

(15) Lefin, P.; Fiorini, C.; Nunzi, J. M. *Pure Appl. Opt.* **1998**, *7*, 71.

(16) Pedersen, T. G.; Johansen, P. M. *Phys. Rev. Lett.* **1997**, *79*, 2470.

(17) Pedersen, T. G.; Johansen, P. M.; Holme, N. C. R.; Ramanujam, P. S.; Hvilsted, S. *Phys. Rev. Lett.* **1998**, *80*, 89.

(18) Kumar, J.; Li, L.; Jiang, X. L.; Kim, D. Y.; Lee, T. S.; Tripathy, S. *Appl. Phys. Lett.* **1998**, *72*, 2096.

(19) Bian, S. P.; Liu, W.; Williams, J.; Samuelson, L.; Kumar, J.; Tripathy, S. *Chem. Mater.* **2000**, *12*, 1585.

(20) Baldus, O.; Zilker, S. J. *Appl. Phys. B: Lasers Opt.* **2001**, *72*, 425.

(21) Matsui, T.; Yamamoto, S.; Ozaki, M.; Yoshino, K.; Kajzar, F. *J. Appl. Phys.* **2002**, *92*, 6959.

(22) Pietsch, U.; Rochon, P.; Natansohn, A. *Adv. Mater.* **2000**, *12*, 1129.

(23) Geue, T.; Henneberg, O.; Grenzer, J.; Pietsch, U.; Natansohn, A.; Rochon, P.; Finkelstein, K. *Colloids Surf., A* **2002**, *198-200*, 31.

(24) Ramanujam, P. S.; Holme, C.; Hvilsted, S.; Pedersen, M.; Andruzzi, F.; Paci, M.; Tassi, E. L.; Magagnini, P.; Hoffman, U.; Zebger, I.; Siesler, H. W. *Polym. Adv. Technol.* **1996**, *7*, 768.

(25) Song, O. K.; Wang, C. H.; Pauley, M. A. *Macromol.* **1997**, *30*, 6913.

(26) Geue, T.; Schultz, M.; Grenzer, J.; Pietsch, U.; Natansohn, A.; Rochon, P. *J. Appl. Phys.* **2000**, *87*, 7712.

(27) Geue, T. M.; Saphiannikova, M. G.; Henneberg, O.; Pietsch, U.; Rochon, P. L.; Natansohn, A. L. *J. Appl. Phys.* **2003**, *93*, 3161.

(28) Natansohn, A.; Rochon, P.; Gosselin, J.; Xie, S. *Macromol.* **1992**, *25*, 2268.

(29) Meredith, J. C.; Smith, A. P.; Karim, A.; Amis, E. J. *Macromol.* **2000**, *33*, 9747.

(30) Meredith, J. C.; Karim, A.; Amis, E. J. *Macromol.* **2000**, *33*, 5760.

(31) Smith, A. P.; Douglas, J. F.; Meredith, J. C.; Amis, E. J.; Karim, A. *J. Polym. Sci., Part B: Polym. Phys.* **2001**, *39*, 2141.

(32) Yager, K. G.; Barrett, C. J. *J. Chem. Phys.* **2004**, *120*, 1089.

(33) Kempe, C.; Rutloh, M.; Stumpe, J. *J. Phys.: Condens. Matter* **2003**, *15*, S813.

(34) Pietsch, U. *Phys. Rev. B: Condens. Matter* **2002**, *66*, 155430.

(35) Barrett, C.; Natansohn, A.; Rochon, P. *Chem. Mater.* **1995**, *7*, 899.

(36) Tanaka, K.; Tateishi, Y.; Nagamura, T. *Macromol.* **2004**, *37*, 8188.

(37) Forrest, J. A.; Dalnoki-Veress, K. *Adv. Colloid Interface Sci.* **2001**, *94*, 167.

(38) Ellison, C. J.; Torkelson, J. M. *Nat. Mater.* **2003**, *2*, 695.

(39) Kerle, T.; Lin, Z. Q.; Kim, H. C.; Russell, T. P. *Macromol.* **2001**, *34*, 3484.

(40) Buck, E.; Petersen, K.; Hund, M.; Krausch, G.; Johannsmann, D. *Macromol.* **2004**, *37*, 8647.

(41) Viswanathan, N. K.; Balasubramanian, S.; Li, L.; Kumar, J.; Tripathy, S. K. *J. Phys. Chem. B* **1998**, *102*, 6064.

Chapter 5
Photomechanical Effects in Azo-Polymers Studied by Neutron Reflectometry

The previous chapter established the size-scale of surface patterning. In particular, it was established that surface mass transport is not a molecular diffusion phenomenon, but requires coordinated motion of polymer material. Combining the results of chapter 3 and 4, it is possible to eliminate certain classes of mechanisms. In particular, those that require photo-heating or thermal softening of the material, as well as those that are based on purely molecular migration, do not fit with the present results. Having eliminated certain mechanisms, it then became necessary to search for evidence of a fundamental photo-induced motion that could give rise to the large-scale motion seen during azo surface patterning. This prompted a detailed investigation, using neutron reflectometry, of the effect that homogeneous irradiation of azo films. Although irradiation of azo films had been extensively studied, neutron reflectometry provides a sensitive measure of film thickness and density, enabling the material response to light irradiation, hence isomerization, to be quantified. In particular, by quantifying the effect as a function of temperature, it is possible to identify the various forces that contribute to material response.

5.1. Abstract

Neutron reflectometry is used to study photomechanical effects in thin films of azobenzene polymer cast onto silicon substrates. A significant photo-expansion effect, up to 17%, is observed at 25°C, due to the free volume requirement of the azobenzene chromophore photo-isomerization. Above a distinct crossover temperature of ~50°C, the material response is inverted and instead photo-contraction effects, of more than –15%, are observed. In this case the combined photo-motion and thermal mobility enables aggregation and crystallization of the azobenzene dipoles. The photomechanical effects, which can be reversed, occur readily using a variety of irradiation powers, incident polarizations, and film thickness values. This photomechanical behavior, which appears to be general to all azo materials, is likely the origin for a wide variety of curious photo-

motions observed in these systems, including macroscopic bending of samples and micron-scale surface mass transport.

5.2. Introduction

Azobenzene polymers exhibit a wide range of photo-responses,[1,2] due to a clean and efficient molecular photo-isomerization (see Figure 5.1). When the azobenzene (azo) chromophore is irradiated within its broad absorption spectrum, the molecule will isomerize into the meta-stable *cis* isomer state. The azo will then thermally relax back into the more stable *trans* state, or this back-isomerization can be induced photo-chemically. For the pseudo-stilbene class of azo molecules (which are the subject of study in this work), the *trans* and *cis* spectra overlap. For these molecules, irradiation with a single wavelength of light (in the range of 450–490 nm) causes continual cycling of the molecules between the two isomeric states. This molecular isomerization generates unique types of material motion at larger length-scales. The azo chromophore can be photo-aligned with polarized light due to a statistical reorientation process (whereby chromophores accumulate perpendicular to the irradiation polarization, since they become inert to the light), which has also been used to photo-align liquid crystalline mesophases.[3,4] In fact, even circularly polarized light will eventually induce some measure of alignment, as chromophores line along the light propagation direction. The azo chromophore can also be used to switch material properties,[5] and thus these systems

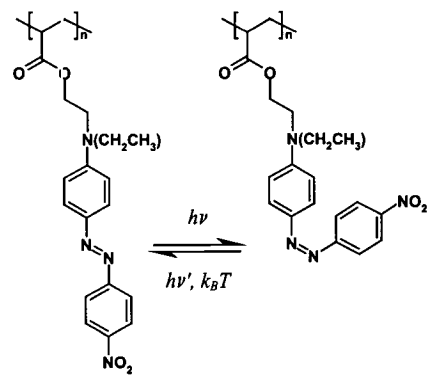

Figure 5.1: Chemical structure of poly(disperse red 1 acrylate) (pdr1a), and its associated photo-isomerization. Azobenzene chromophores will isomerize from the stable *trans* state into the meta-stable *cis* state with light irradiation. The molecule will then thermally relax back to the *trans* state, or may be photo-isomerized into that state.

have been considered in applications ranging from optical devices to sensors. Another unique effect observed in the azo systems is a clean and facile surface topography patterning that occurs when these materials are irradiated with a light intensity gradient. This single-step patterning occurs at room temperature, well below the material's bulk glass transition temperature (T_g). Although extensively studied, this surface mass transport phenomenon is not yet fully understood.[6] The azos have also been shown to generate macroscopic photomechanical effects, such as the expansion of thin films floating on a water surface,[7] the bending of freestanding polymer films irradiated with polarized light,[8,9] and even macroscopic motion of floating films.[10]

Recently we investigated the photomechanical effect in azobenzene thin films by measuring the light-induced expansion of these materials using ellipsometry,[11] an optical technique that determines thickness and refractive index by analyzing the polarization change induced in a probe laser beam upon reflection. It was found that the thin azo films photo-expand during irradiation at an absorbing wavelength, with both a reversible and irreversible contribution (see Figure 5.2). The irreversible expansion persists after illumination ceases, whereas the reversible expansion can be cycled on and off using the pump laser. The extent of expansion can be tuned with irradiation power and time. These experiments demonstrated a decrease in refractive index concomitant with the increase in thickness, corroborating the conclusion of photo-expansion. In these experiments, care

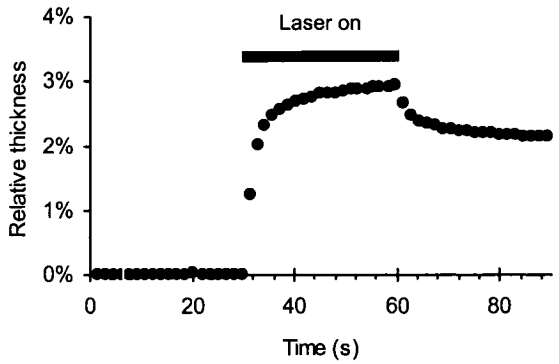

Figure 5.2: Relative thickness measurements, conducted using ellipsometry, measuring a distinct photo-expansion during irradiation with laser light for an azo-polymer thin film of pdr1a. While the laser is on (indicated by the bar in the figure), the material expands. Even when the laser is turned off, some amount of photo-expansion persists, indicating that there is both a reversible and irreversible component to the effect.

was taken to avoid photo-orientation in the material, by using circularly polarized light and modest irradiation times. This was required because ellipsometry, being an optical technique that measures the average refractive index, cannot be easily applied to anisotropic media. Due to the azo's strong optical response, all-optical techniques are limited in their ability to probe these materials. Not only does photo-orientation generate birefringence, which makes optical analysis ambiguous, but optical probes, even at nominally non-absorbing wavelengths, can lead to measurable changes in the material.

In order to resolve these ambiguities, we have probed the photomechanical effect in azobenzene thin films using neutron reflectometry. Because neutron scattering is sensitive to nuclear density (and not electronic properties), it can be used to unambiguously determine thin film thickness and density, regardless of any anisotropy in the electronic refractive index. It also enables extraction of the entire film profile, rather than simply estimating average thickness and density. In this paper, we describe a neutron reflectometry study of the photomechanical phenomenon in azo materials. We employed a custom-built sample cell[12] that allows measurement of neutron reflectivity simultaneous with optical irradiation, and furthermore enables control of the sample temperature. Thus, we quantify the photomechanical response of the material as a function of temperature. In addition to confirming the photo-expansion effect measured optically, we have also found evidence for a unique photo-contraction behavior that occurs at elevated temperature. Using neutron reflectometry, we are able to unambiguously identify the photo-expanded state and the higher-density photo-contracted state.

5.3. Experimental

5.3.1 Sample Preparation

Unless otherwise stated, the azo-polymer material used in this work was poly (disperse red 1 acrylate) (pdr1a), synthesized as previously reported.[13] The chemical structure is shown in Figure 5.1. The 2′ chlorine-substituted analog of this material poly (disperse red 13 acrylate) (pdr13a) was also used for a small number of experiments. The substrates employed were polished single-crystal silicon (111) wafers with a thin (~20 Å) silicon dioxide layer. The wafers were cut into small pucks, 6 mm thick and 24 mm in diameter. This small sample size is necessary in order to ensure that the entire sample is

homogeneously irradiated with laser light. The substrates were cleaned using a warm piranha solution (mixture of 30% H_2O_2 and concentrated H_2SO_4 in 1:3 ratio) for 30 minutes. **Caution:** piranha solution is a powerful oxidizer and reacts violently with organics. This surface treatment also enhances polymer adhesion, greatly improving film homogeneity and decreasing surface roughness.

Samples were prepared by spin-coating azo-polymer solutions (using anhydrous THF as solvent) onto the cleaned silicon substrates. The solution was placed on the substrate, which was then ramped (acceleration 1260 rpm/s) to 1300 rpm, and maintained for 35 s. Film thickness was adjusted by varying the solution concentration (in the range of 10^{-1} to 10^{-3} mol/L, based on repeat unit molecular mass). Film thickness in the range of 200–600 Å was chosen so as to produce high-quality reflectivity curves with a substantial number of Kiessig fringes within the available q_z-range. The cast thin films were annealed in a vacuum oven at 110°C for 8 hours to remove any residual solvent or flow-induced orientation.

5.3.2 Neutron Reflectometry

The neutron reflectivity experiments were performed at Chalk River Laboratories Canada (National Research Council), using the C5 triple-axis spectrometer. Measurements were performed using neutrons of wavelength λ = 2.37 Å, in specular reflection mode. The momentum transfer, $q_z = (4\pi/\lambda)\sin\theta$, was varied between 0.006 $Å^{-1}$ and 0.07 $Å^{-1}$ by varying the specular reflection angle, θ. The collimation slits were opened sufficiently so as to over-illuminate the sample with the neutron beam, such that the sample itself defines the reflected beam profile. Scans were performed in two segments with different slit settings: from q_z = 0.006 $Å^{-1}$ to 0.04 $Å^{-1}$, and from 0.04 $Å^{-1}$ to 0.07 $Å^{-1}$. The relative resolution, $\Delta q_z/q_z$, varies from 0.15 to 0.03 in the first segment, and from 0.05 to 0.03 in the second segment. The two scan regions were found to overlap exactly. A pyrolitic graphite filter was used to suppress the signal from the $\lambda/2$ and $\lambda/3$ components of the monochromator reflection. Furthermore, an analyzer was used to diffract the reflected beam into the detector. This analyzer and detector geometry was found to reduce the background signal considerably. Background scans were performed by offsetting the sample by a fixed angular displacement of +0.5°, and have been

subtracted from all the results presented. The detector count time was varied as a function of q_z in order to maintain uniform and reasonable statistics for the entire scan region. The data were normalized using the critical reflectivity edge.

5.3.3 Experimental Setup

The samples were placed in a custom-built cell that enables neutron scans simultaneous with optical irradiation (refer to Figure 5.3). The details of this cell design have been previously reported.[12] The cell features an aluminum enclosure that is transparent to neutrons, and a PMMA optical window that allows for optical irradiation. The sample was fixed, with thermal contact grease, on a heating block with a thermocouple, allowing for accurate control of temperature. Unless otherwise stated,

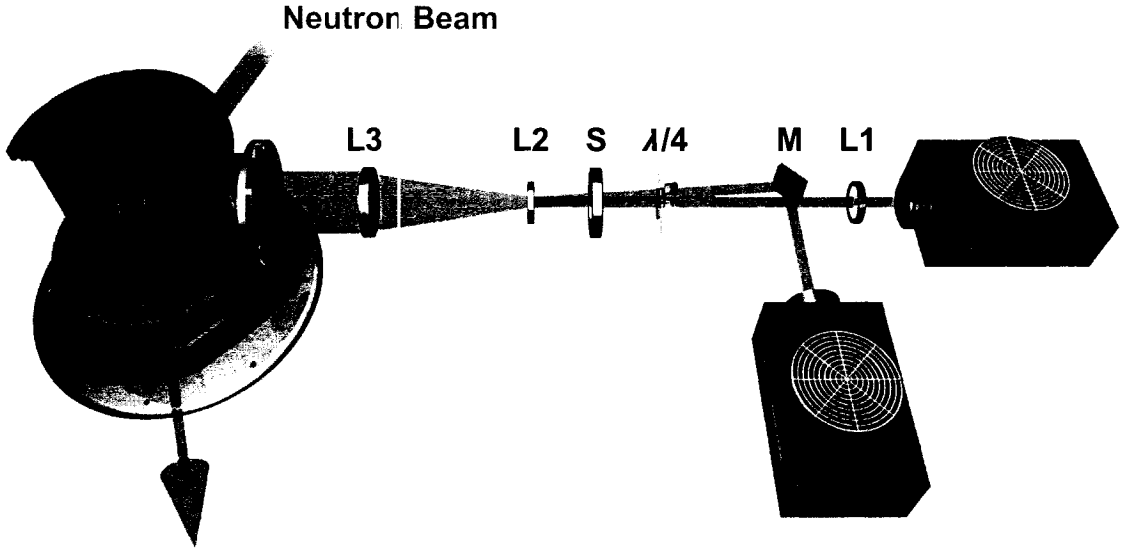

Figure 5.3: Experimental setup for measuring photo-physical changes in azo films using neutron reflectometry. The sample cell (left in the figure) contains a copper heating plate to which the sample wafer is attached. The aluminum enclosure is transparent to neutrons, and an optical window on the front side enables simultaneous optical irradiation. Two air-cooled Ar^+ lasers (on the right), tuned to 488 nm, are used for irradiation. One laser output is adjusted with a converging lens (L1) in order to account for slight differences in divergence. The beam from the second laser is reflected off of a mirror (M), making it nearly collinear with the first beam, and passing through a concerted optical train (the angular difference in the two beams has been exaggerated in the diagram for clarity). The combined beam is converted to circular polarization using a wave plate ($\lambda/4$). A diverging (L2) and converging (L3) lens are then used to expand and collimate the beam, so that it over-illuminates the sample with a uniform light intensity. The beam can be turned on and off via computer control of a shutter (S).

scans were performed at a constant temperature of 25°C (i.e. 'room temperature'). The sample cell was held under vacuum during all temperature ramping to prevent sample oxidation. When required, a flow of inert gas (helium or nitrogen) was used to cool the cell and sample. Optical irradiation was performed using two air-cooled argon-ion lasers, tuned to the 488 nm line. Two lasers were used so as to increase the overall irradiation power, and also to average out any coherence effects. One of the laser beams was reflected off of an adjacent mirror such that both beams become nearly collinear. The output of one laser was adjusted with a lens to account for slight differences in laser divergence. The polarized laser output was converted into circularly polarized light using a $\lambda/4$ wave plate. Circular polarization is used to prevent in-plane orientation of the azo chromophores, known to occur readily when irradiating with polarized light. For those experiments requiring polarized irradiation, the wave plate was removed. A series of lenses was used to expand and collimate the beam such that the sample experienced homogeneous irradiation of the surface. Since neutron reflectivity could be measured during thermal ramping and laser irradiation, we were able to ensure that the sample had stabilized at a new temperature, or after laser irradiation, before beginning the full reflectometry scan.

5.3.4 Data Analysis

The normalized neutron reflectometry curves were fit to scattering length density (SLD) profiles using Parratt's dynamic approach.[14] Initial one-box fits were performed using the Parratt32 software (provided by HMI),[15] however more sophisticated fits were required. These were performed using software code made publicly available by Thad Harroun (Brock University),[16] custom-modified to accommodate our fitting procedure. The instrument resolution was included in the fitting procedure. Data was first fit using a simple one-box model. This fit was then refined by allowing for a Gaussian distribution of thickness across the sample surface. This improved fit was then further refined by allowing the film profile to vary in the film-normal (z) direction. The final fit represents a minimization of the film profile as well as the macroscopic thickness distribution.

5.3.5 Optical Reflectometry

Optical reflectivity scans in the angular range from 20° to 80° were performed on the samples after neutron measurements, using the Multiskop instrument (Optrel, Germany). By using the thickness measured from neutron reflectometry, the optical reflectometry data could be fit with very little ambiguity. The three orthogonal refractive indices were then extracted by fitting the curves using custom-written software that implements the transfer matrix formalism for layered optical media.[17]

5.4. Results and Discussion

5.4.1 Fitting Procedure

Thin films of azo-polymer, spin-coated onto silicon substrates, were measured using neutron reflectometry. The resulting reflectivity curves contained numerous oscillations (so-called Kiessig fringes[18]) which result from interference between neutron reflections from sample interfaces. Lacking absolute phase information, neutron reflectivity data cannot be directly inverted. Instead, a range of models must be considered. The final selected model must describe the experimental data and provide a physically reasonable description of the system. Figure 5.4a shows a typical neutron reflectometry curve, and various possible fits to the data, presented in order to assess the quality of four different fitting models. The first possibility (uppermost curve) is a simple one-box model, where the thin film is taken to be a microscopically rough (22 Å), but otherwise a homogeneous and flat slab of material on top of the substrate, which in turn is modeled as a thin layer of silicon dioxide on top of an infinite slab of silicon. This fit correctly describes the film thickness, as indicated by the spacing of the oscillations in the data. However, the fit does not fully match the experimental data. In particular, the minima of the oscillations in the fit are much deeper than the actual data. This mismatch is not merely a matter of microscopic roughness blurring the reflectivity curve, as shown by the second fitting model. In the second model (second curve from the top in Figure 5.4a), a one-box film with increased roughness (double the initial model, i.e. 44 Å) is compared to the data. As can be seen, this causes a significant decrease in the absolute reflectivity of the model curve, and it no longer describes the experimental data. In fact it was found that, with this model, no combination of film thickness, scattering length

density (SLD), and film roughness could match the profile minima and maxima. However roughness in these calculations is modeled as a smearing of the interface, which properly describes the coherent averaging that the neutron beam probes when surface variation is smaller than the neutron coherence length. In cases when surface variations are larger than the neutron coherence length, there is no interference between the

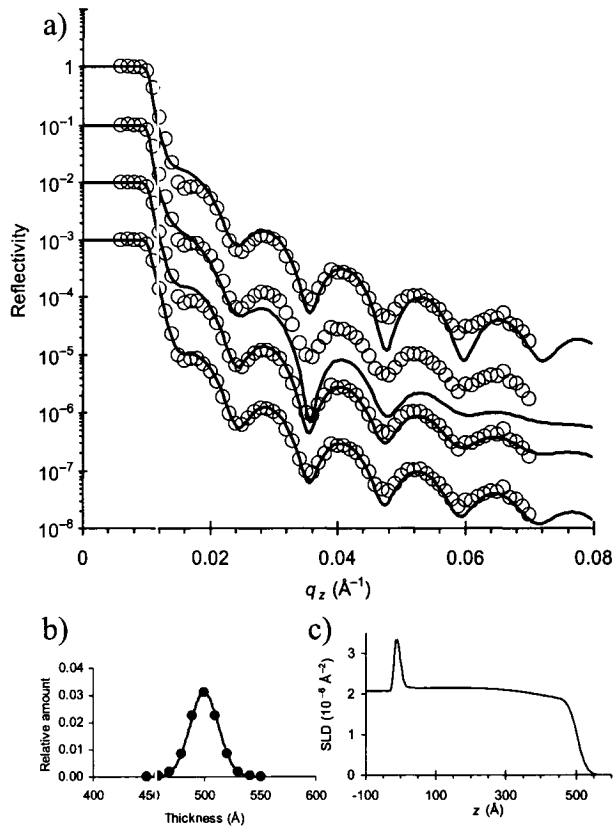

Figure 5.4: (a) Comparison of the quality of model fits. In all four curves, the open symbols are the same experimental data, whereas the solid line is a model reflectivity curve based on a particular SLD profile. In the uppermost curve, a one-box model (thickness 499 Å, surface roughness 22 Å) is simulated. The position and spacing of the Kiessig fringes matches the data (indicating that the model film thickness is correct). However the minima in the fit data are much deeper than the experimental data. The second curve shows a similar one-box model with double the surface roughness (44 Å). The absolute reflectivity decreases substantially, demonstrating that this 'blurring' of the minima in the data is not due to effective roughness. The third curve shows that by allowing for a Gaussian distribution of film thickness values across the sample surface, the data can be fit properly. The corresponding thickness distribution is shown in (b). The final model allows not only for a macroscopic thickness distribution, but also for a more complex SLD profile. The fit in this case properly reproduces all features of the data. The corresponding SLD profile is shown in (c).

reflections from distinct film regions. In such a case, modeling involves a sum and average of the distinct neutron reflectivity curves, rather than a sum and average of the SLD profiles. This is an incoherent average, where we are summing the relative reflection intensities, instead of a microscopic coherent average, where one would sum the relative reflection amplitudes. The third model (third curve in Figure 5.4a) fit to the data shows the result of allowing for this macroscopic variation of sample thickness. In particular, a Gaussian distribution of film thickness values (centered about the nominal thickness from the one-box model) involves averaging a distribution of neutron reflectivity curves. This averaging does indeed reduce the depth of the minima, without decreasing the absolute reflectivity. This assumption allows us to generate much more reliable and reasonable fits to the data. The lateral extent of the neutron coherence varies as a function of angle as $L_{coh} = 2\pi/(\Delta q_z \sin\theta)$, which corresponds to 45–230 μm for the present data. Thus the fits indicate that the sample thickness varies across the macroscopic sample surface, with a size scale larger than ~230 μm. Although the spin-casting technique used to generate the samples creates highly homogeneous films with consistent thickness, it is nevertheless quite reasonable to suggest that the sample thickness varies by ~20 Å across the 23 mm sample surface. Moreover, this large-scale thickness variation is easily confirmed using optical techniques. A slightly better fit to the data can be obtained by augmenting the thickness-distribution model by allowing for a small variation of the sample profile in the film normal (z) direction. The lowest curve in Figure 5.4 shows such a model, with the corresponding Gaussian thickness-distribution and nominal film profile shown below. The fit to the data is very good, and the film profile (with a slight decrease of film density near the surface) is reasonable. It should also be noted that merely allowing for complex profiles in the z-direction (without a thickness-distribution) cannot properly reproduce the intensity of the measured reflectivity. All the fits presented are thus the result of allowing for both thickness distribution and some small density variation in the film profile. It is also worth noting that the film SLD, obtained from the best fits, was always in the range 2.2–2.4×10^{-6} $Å^{-2}$, corresponding to a physical density of 1.2–1.3 g/cm^3, which is consistent with previous measurements on these materials.[19]

5.4.2 Photo-expansion

In the previous ellipsometry study of photo-expansion in azo materials,[11] it was found that the material expanded as a result of laser irradiation of sufficient power, if the wavelength was inside the azo absorption band. Both a reversible photo-expansion, which occurs only when the laser light illuminates, and an irreversible photo-expansion, which persists even after irradiation ceases, were identified. The present experiments used a unique sample cell to enable neutron measurements simultaneous with optical irradiation. Because a full neutron reflectivity scan requires 8–12 hours, it was not possible to fully characterize the material state during irradiation using this technique. However, the present sample cell enabled us to measure at particular values of the momentum transfer, q_z, during irradiation.[12] Consistent with the ellipsometry data, a shift in reflectivity is observed when the laser light was active, indicating some amount of physical change. With both techniques, it was observed that this small reversible photo-expansion was superimposed on top of a larger light-induced expansion that did not relax after the irradiation ceased. The irreversible photo-expansion was readily probed by neutron reflectometry by measuring a thin film before and after illumination. Because the sample cell enabled this to be performed without removing the sample, the instrument and sample alignment are identical for all the scans, thereby removing this ambiguity from data fitting.

Figure 5.5a shows reflectivity curves for a thin azo-polymer film as it is irradiated with 488 nm laser light (circularly polarized, 38 mW/cm^2) for progressively longer periods of time. The scans were performed after the illumination light was deactivated and the material allowed to relax. The corresponding film profiles are shown below. As can be seen in Figure 5.5b, the neutron reflectivity data immediately confirms the ellipsometry data. The film thickness increases substantially with irradiation, and a corresponding decrease in the film density is also recorded. By integrating the area beneath the SLD profile, we confirmed that mass is conserved in the photo-expansion process. The extent of expansion is shown in Figure 5.5c, where it can be seen that the thin film expansion saturates to ~17% after ~8 hours irradiation. In the previous ellipsometry work, irradiation times were more modest and the extent of expansion was correspondingly smaller, and consistent with the neutron data. The SLD profiles also

enable us to analyze this photomechanical phenomenon as a function of depth into the film. Because the azobenzene chromophore is a strong absorber (extinction coefficient $\varepsilon_{488nm} = 5.30 \mu m^{-1}$), the intensity of laser light decreases exponentially as the beam travels through the film. This creates a light intensity gradient inside the material. Because the experiments were performed on polished silicon substrates, the incident beam will be reflected and travel through the material a second time. For the films considered here, the intensity of laser light at the substrate is ~40% lower than at the film surface. The film profiles shown in Figure 5.5b indicate that the surface region, where light intensity is greater, expands preferentially. For the ~30 minute illumination, the density of the surface region has decreased compared to the initial value, whereas the bulk of the film has not changed. With greater irradiation time, the entire film becomes photo-expanded in a nearly uniform way. This demonstrates that there is a power

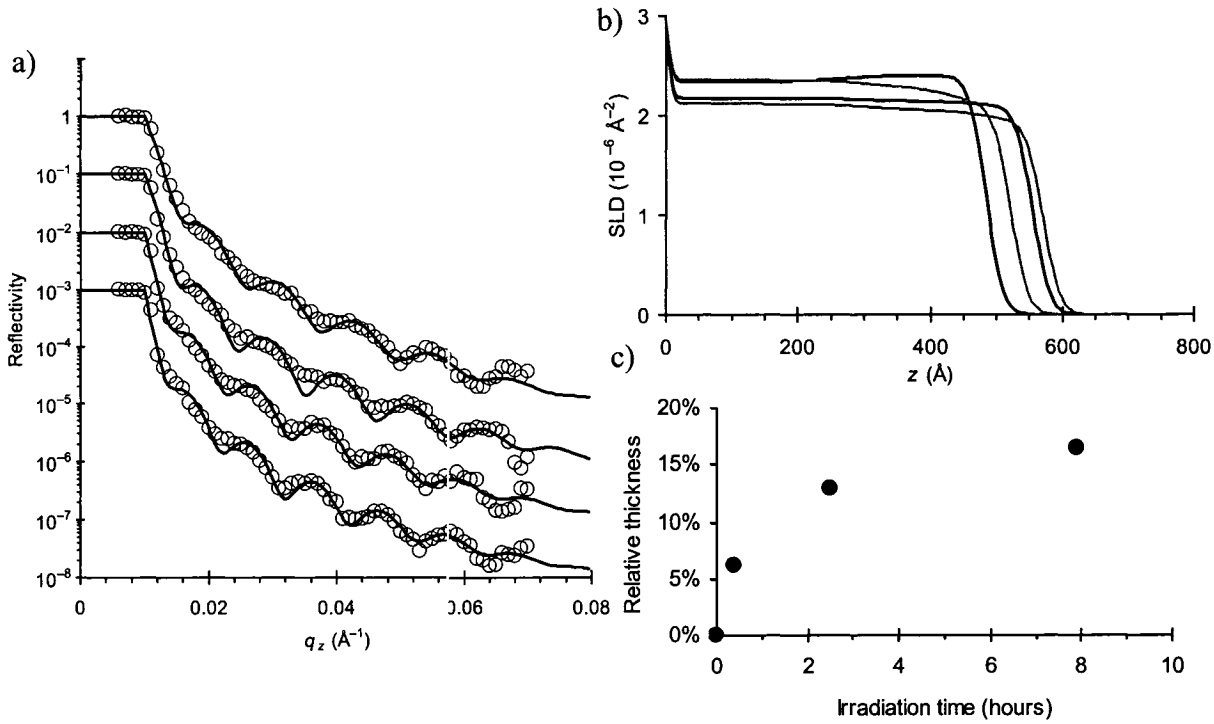

Figure 5.5: (a) Neutron reflectivity data (open symbols) and corresponding fits (solid lines) for a thin azo-polymer film irradiated at room temperature with 38 mW/cm^2 laser light for progressively longer periods of time. The total irradiation time for the curves (going from top to bottom) is 0 hours, 0.4 hours, 2.5 hours, and 7.9 hours. (b) The associated SLD profiles clearly show that the thin film is expanding with increased irradiation. (c) The total change in film thickness saturates with irradiation time.

dependence to the photo-expansion, but also proves that the entire film is able to expand with sufficient irradiation time and/or power.

5.4.3 Photo-contraction

A unique material response was discovered here for thin films of azo-polymer irradiated at elevated temperatures. In Figure 5.6a, reflectivity curves are shown for a thin film held at 85°C, before (upper curve) and after (lower curve) irradiation with 62 mW/cm^2. The film SLD profiles, corresponding to the fits, are shown in Figure 5.6b. At

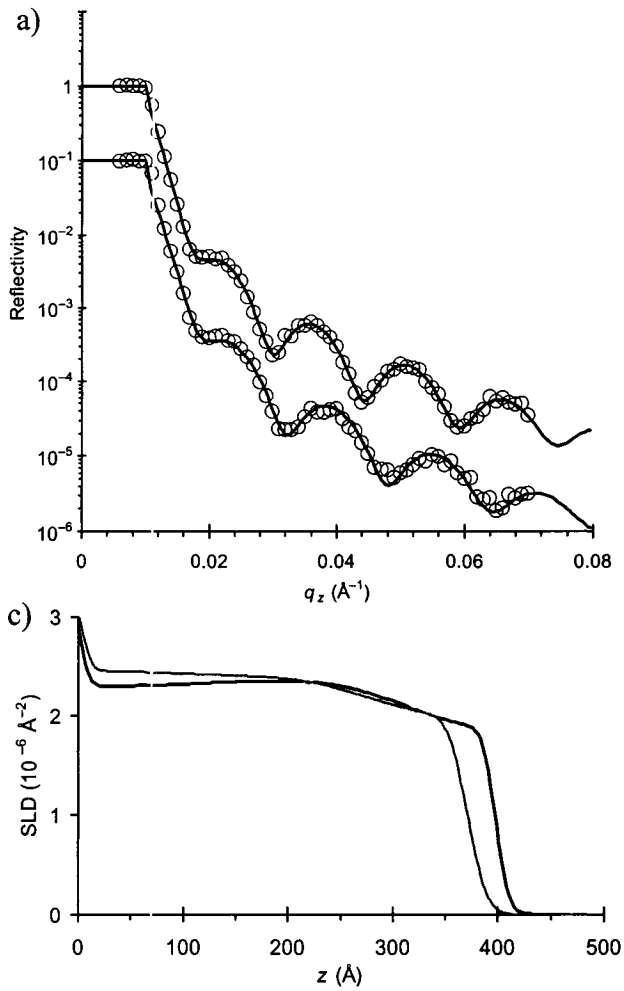

Figure 5.6: (a) Neutron reflectivity data (open symbols) and corresponding fits (solid lines) for a thin azo-polymer film held at 85°C. The upper curve is before laser illumination, and the lower curve is after 2 hours irradiation with 62 mW/cm^2 laser light. (b) The SLD profiles show clearly that irradiation at this temperature leads to a photo-contraction (black curve before, grey curve after), with decrease in film thickness and a corresponding increase in film density.

this temperature, the laser irradiation has generated a significant photo-contraction, rather than the photo-expansion established at room temperature (25°C). By integrating the area under the SLD profile, we can again confirm that this is a mass-conserving transformation. The neutron reflectivity data provide a sensitive probe of density, and in this case indicate that the material has become denser than the usual bulk value (~0.02 g/cm^3 denser near the center of the film). This densification is likely due to reorganization of the azobenzene chromophores, with the azo groups undergoing dipole pairing and aromatic stacking.

This photo-contraction effect was observed in a wide variety of samples. In Figure 5.7, data is presented for a thin film held at 80°C, as it is irradiated with laser light

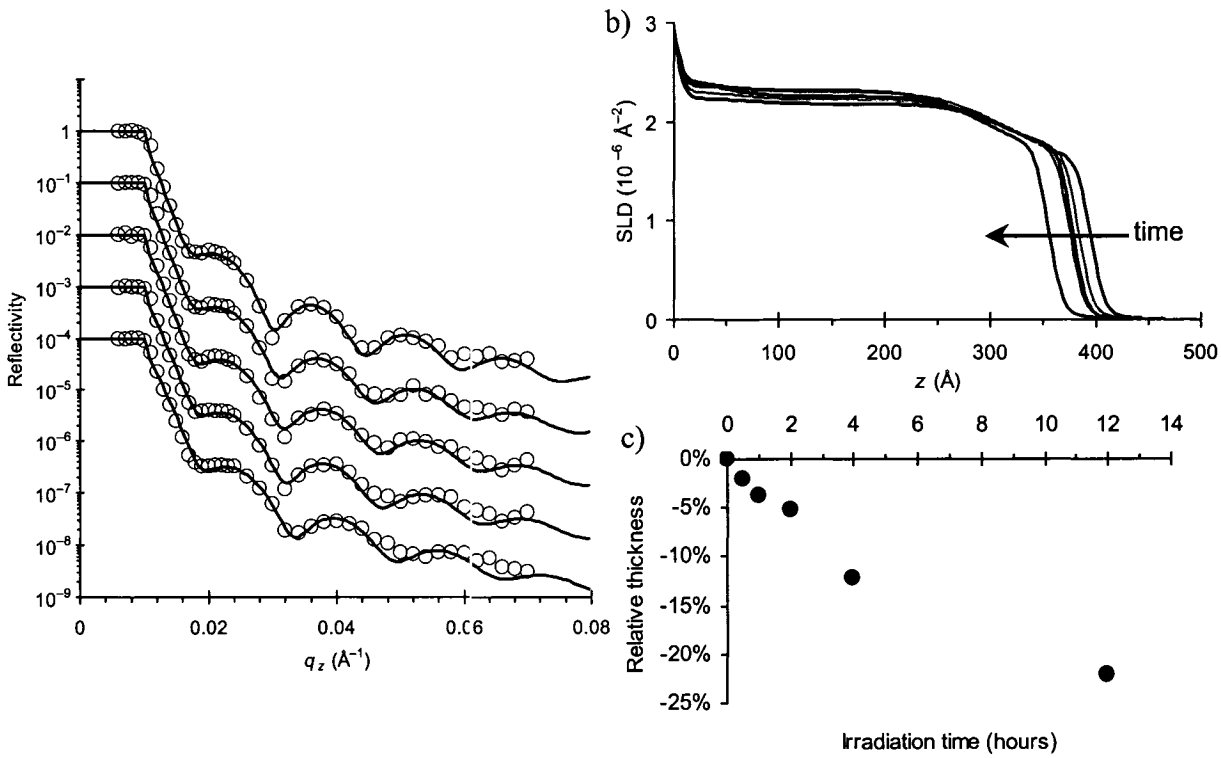

Figure 5.7: (a) Neutron reflectivity data (open symbols) and corresponding fits (solid lines) for a thin azo-polymer film held at 80°C, and irradiated with 62 mW/cm^2 laser light for progressively longer periods of time. The total irradiation time for the curves (going from top to bottom) is 0 hours, 0.5 hours, 1 hour, 2 hours, and 4 hours. (b) The corresponding SLD profiles show film contraction and associated densification. (c) The photo-contraction scales with irradiation time. Note that the final data point (12 hour irradiation) was obtained from a different azo-sample. For this long-time irradiation at elevated temperature, some amount of material loss from the film was detected.

(circularly polarized, 62 mW/cm^2) for progressively longer periods of time. Again a mass-conserving photo-contraction effect is observed, that becomes larger in magnitude as irradiation time proceeds. Note that although mass was conserved for most irradiation times (integrated area under the SLD profile deviates from the initial value by <1%), for extremely long irradiation times at elevated temperatures (notably 12 hour irradiation at 80°C) there is a measurable (~4%) decrease in the integrated SLD area. Since these films were annealed (at 110°C) before measurement, and because this effect only appears with irradiation, it is likely related to some form of photo-initiated cleavage of the azo bond, with subsequent thermal release of the cleavage products. This is entirely consistent with the usual optical observation of color loss seen for azo films subjected to extreme conditions. For this reason, the irradiation times were kept below these extreme levels for all other experiments. The film profiles shown in Figure 5.7b do not show any evidence for preferential contraction near the surface of the film or the substrate. The densification appears throughout the material in a uniform way. Figure 5.7c shows that substantial amounts of photo-contraction (~15%) can be obtained with a few hours of irradiation.

5.4.4 Photomechanical Effect

The observed photo-expansion and photo-contraction can be viewed as two manifestations of a photomechanical phenomenon in azo-polymer systems. Figure 5.8

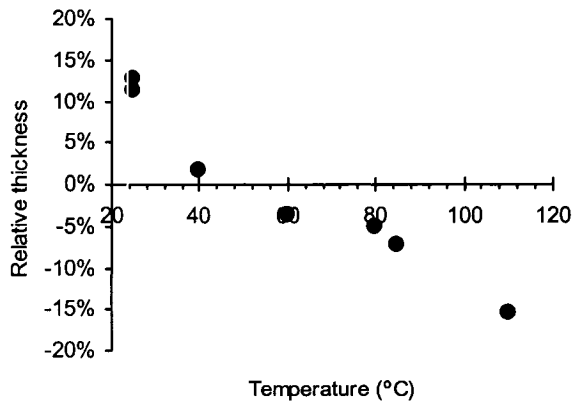

Figure 5.8: Magnitude of the photomechanical effect (photo-expansion or photo-contraction) as a function of the temperature at which irradiation takes place. The relative change in film thickness is shown, based on a variety of thin films all irradiated with 62 mW/cm^2 of 488 nm circularly polarized light for 2 hours. A crossover from photo-expansion to photo-contraction occurs at ~50°C.

shows the photomechanical response (expansion or contraction) of azo films irradiation for 2 hours with 62 mW/cm^2 laser light. A photo-expansion effect is observed at lower temperatures, whereas a distinct photo-contraction occurs at sufficient temperature. The steady change in response (with a crossover at ~50°C) suggests a competition between two effects. At low temperatures, the azobenzene molecular isomerization forces expansion of the local polymer network, in order to accommodate the free volume requirements of the azo isomerization. Larger-scale motion in the polymer network is, however, impossible, and the resultant expanded state is frozen in. While the azo chromophores are somewhat mobile within their respective free volume pockets, larger scale migration of the chromophores is not possible. As temperature is increased, the higher polymer mobility allows for relaxations in the network that counteract the expansion effect (as discussed later, the thermal expansion coefficient of the material is negligible). At sufficient temperatures (above ~50°C), the combined effect of photo-induced motion and thermal motion enables the chromophores to move within the polymer matrix, aggregate, and form a denser contracted state. Figure 5.9 shows a molecular modeling study of two azobenzene polymer chains. As can be seen, the low-energy state occurs when the azo chromophore dipoles are aligned and undergo aromatic stacking. This azo dipole association is well established in the liquid crystal literature,

Figure 5.9: Molecular model of two chains of the azo-polymer pdr1a (generated using the Amber Force Field method from the HyperChem 6.0, Hypercube Inc. software). The aromatic stacking and interdigitation of the azo chromophore side groups (seen in the center of the image) is likely the origin of the denser photo-contracted state.

although this crystalline state is not typically accessible to amorphous polymers. Based on our present results, it appears that irradiation with light at elevated temperatures enables the azo chromophores to reorient and overcome an energy barrier, such that they aggregate and crystallize. It should be noted that this photo-induced aggregation is occurring well below the material's glass-to-rubber transition temperature (T_g). Similar behavior has been observed in the azo system for other types of photo-motions, such as photo-orientation and surface patterning, which are both readily initiated below T_g.

Figure 5.10 shows reflectivity data for different types of thermal treatment. The upper two curves represent a thin film held at 25°C (uppermost curve), and the same film after thermal ramping to 80°C (second curve). The two curves are identical (and can be fit with the same film model), demonstrating that thermal treatment alone does not give rise to any measurable change in film thickness or density. Thus the physical changes being observed here are due to the azobenzene isomerization, and not merely annealing. The denser photo-contracted state is not achieved with heat treatment alone, which suggests

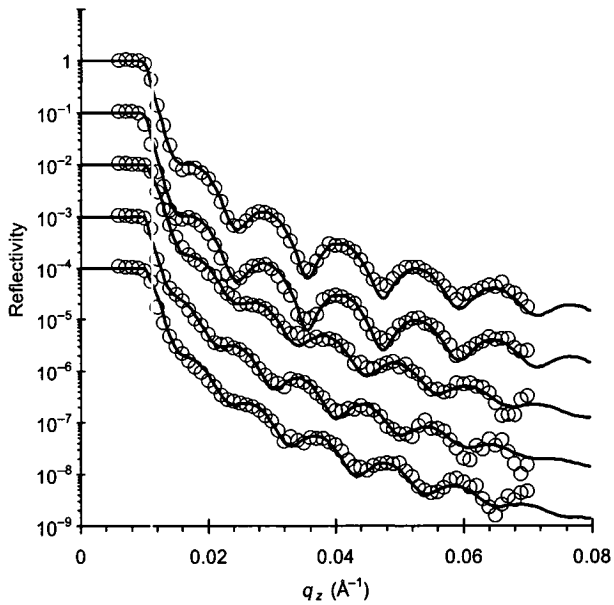

Figure 5.10: Analysis of the thermal component of photomechanical changes. The upper two curves are a thin film measured at room temperature (upper curve) and again at 80°C. The two curves are identical (and are described using the same model data), showing that thermal treatment alone does not give rise to any material changes. The third curve corresponds to a thin film before irradiation (25°C), and the fourth curve shows the same sample after photo-expansion (2 hours irradiation, 38 mW/cm^2) at 25°C. The final curve shows the same film heated to 80°C, where a contraction effect is observed without laser illumination.

that photo-induced alignment is required in some way. It is likely that photo-orientation generates seed crystals, which can then be thermally annealed and grown into a higher-density state. The lower three curves in Figure 5.10 show a thin film that has been irradiated with 38 mW/cm^2 at room temperature (which leads to an expansion) and subsequently heated to 80°C. This purely thermal treatment step has evidently caused the thin film to contract. This effect is not merely a reversal of the expanded state: with sufficient thermal treatment, various films were found to thermally contract to a state thinner than the original film thickness. This was only observed, however, in films that had been irradiated with laser light. This effect was also seen by ellipsometry, where, for instance, an irradiated thin film annealed above T_g was found to be ~3.5% thinner than the original film thickness.

The formation of a denser state with combined heat and light treatment has also been seen in the formation of surface relief gratings (SRGs).[20,21] In that work, a stable surface pattern was generated at room temperature and then thermally erased. During this heat treatment, a density grating, coincident with the original SRG but buried beneath the surface of the material, was found to form. This indicates that light treatment generates some form of seeding crystals that can then be thermally annealed into a higher-density semi-crystalline state. Similarly, we have observed that photo-irradiation (which certainly induces some measure of chromophore orientation) seeds the material, such that subsequent thermal treatment induces contraction and densification.

5.4.5 Thermal Considerations

An experiment was performed where the azo film was irradiated using a 15 mW/cm^2 broadband incoherent light source. In this case the neutron reflectivity curve showed no appreciable difference before, during, or after irradiation. Furthermore, samples that had been irradiated to the point of being photo-bleached (which involves destruction of the azo bond) became unresponsive to laser illumination. Previous calculations[22] also allow us to neglect photo-heating effects. Given the present irradiation conditions, a temperature rise of only a few degrees would be expected. For the samples held at elevated temperatures, the changes in film density are again directly related to laser irradiation of the azo material. Merely changing the sample temperature caused essentially no change in the reflectivity curve (relative thickness difference <0.4%). The

thermal expansion of the thin film can also be neglected, since it is orders of magnitude smaller than the observed effect (the thermal expansion coefficient of a polymer is typically $<10^{-5}$ K^{-1}). It is thus clear that the observed changes are due to laser illumination, and not merely sample heating. Moreover, it is clear that the effects are related to the azobenzene chromophore and its molecular isomerization.

5.4.6 Other Variables

The photomechanical effects are sensitive to laser power for short irradiation times. However for the long irradiation times considered here (>30 minutes), it was found that the extent of thickness change was not strongly related to irradiation intensity, whereas it was sensitive to the irradiation time. This indicates that for the powers considered here (>30 mW/cm^2), the material response is saturated, and the process of expansion or densification is limited not by isomerization frequency or efficiency, but by the reorganization of the azo side-groups, and motion of polymer chains in the material. The photomechanical effects were observed in all thin azo films studied, across the thickness range from 200 Å to 600 Å. The relative amount of photo-expansion and photo-contraction, after 2 hours irradiation, was not found to depend on film thickness. Instead it again appears that the studied irradiation power (>30 mW/cm^2) is sufficient to fully expand films in this thickness range. It should be noted that in the previous ellipsometry study,[11] the photo-expansion was sensitive to both irradiation power and film thickness. However the irradiation times in that study were considerably shorter, and it is likely that the entire film volume was not undergoing saturated photomechanical change. For the longer irradiation time and relatively high irradiation power considered here, a saturated response is measured.

The observed photomechanical effects appear to be general to azo polymers. A similar extent of photo-expansion was measured with thin films of poly(disperse red 13 acrylate) (pdr13a). This polymer is similar to pdr1a, except that it has a Cl substituent at the 2′ position of aromatic ring. Given that the azobenzene's other unique motions (such as photo-orientation and surface mass transport) are quite general and appear in nearly all samples, these photomechanical effects are likely present in all azo-polymer systems. In fact, a large number of the unusual photo-motions observed in azo systems are probably related to this photomechanical effect. For instance, the macroscopic bending and

unbending of liquid crystalline azo films[8,9] may be a manifestation of the photo-contraction effects described here. The free surface of these films contracts to a greater extent than the bulk (since the light intensity is higher at the surface, owing to sample absorption), and this gradient in contraction leads to macroscopic deformation. It appears to be a general trend that liquid crystalline azo samples will photo-contract with irradiation, rather than photo-expand as amorphous systems tend to.[7,23] This is likely occurring because the liquid crystalline samples, being highly mobile, are above the expansion-to-contraction crossover temperature even at room temperature. It is possible that these samples, if cooled sufficiently, will exhibit photo-expansion behavior instead. For typical amorphous polymers well below T_g, the molecular mobility is arrested and photo-contraction effects cannot occur. Instead, the frustrated azo motion leads to deformation of the polymer matrix and a net expansion.

5.4.7 Linear Polarization

The effect of incident laser polarization was also studied. Figure 5.11 shows an example of a thin film irradiated with 38 mW/cm^2 at 25°C, and a thin film irradiated with

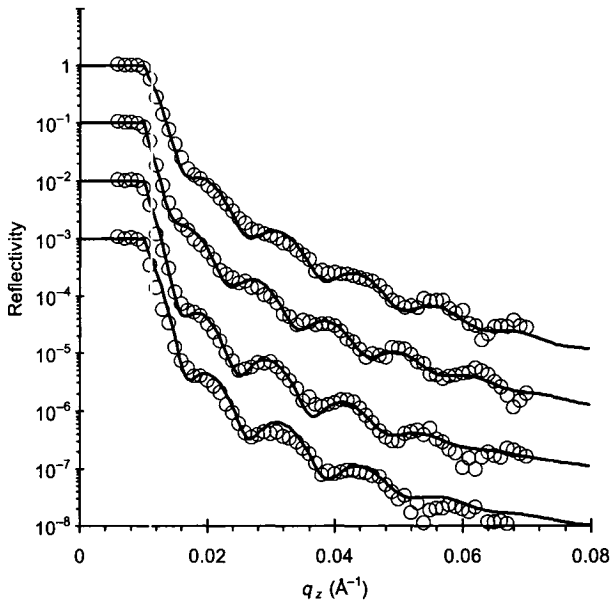

Figure 5.11: Effect of irradiating azo films with linearly polarized light. The upper two curves represent a thin film before (upper curve) and after (second curve) irradiation at 25°C. The bottom two curves represent a thin film before (third curve) and after (final curve) irradiation at 80°C. The effects are identical to those measured with circularly polarized light, where photo-expansion occurs at room temperature, whereas photo-contraction occurs at elevated temperatures.

62 mW/cm^2 at 80°C, for 2 hours. In both cases, the thin films respond similarly to irradiation with circularly polarized light. That is, the thin film at 25°C photo-expanded by 10%, whereas the film at 80°C photo-contracted by 8%. Although the photo-contraction phenomenon is attributed to photo-alignment, irradiation with linearly polarized light (which typically induces greater ordering and alignment) did not increase the magnitude of the contraction effect. This may be because photo-orientation necessarily decreases the fraction of azo chromophores undergoing isomerization (since they are no longer addressed by the incident light), which would tend to decrease the photo-motion required for photomechanical effects. It is also worth noting, however, that the final amount of photo-orientation is quite small. Using the thickness measured with neutron reflectivity, one can fit optical reflectivity reliably to determine the three orthogonal components of the refractive index (n_x, n_y, n_z). Figure 5.12 compares the optical reflectivity data for a thin film photo-contracted using circularly polarized light

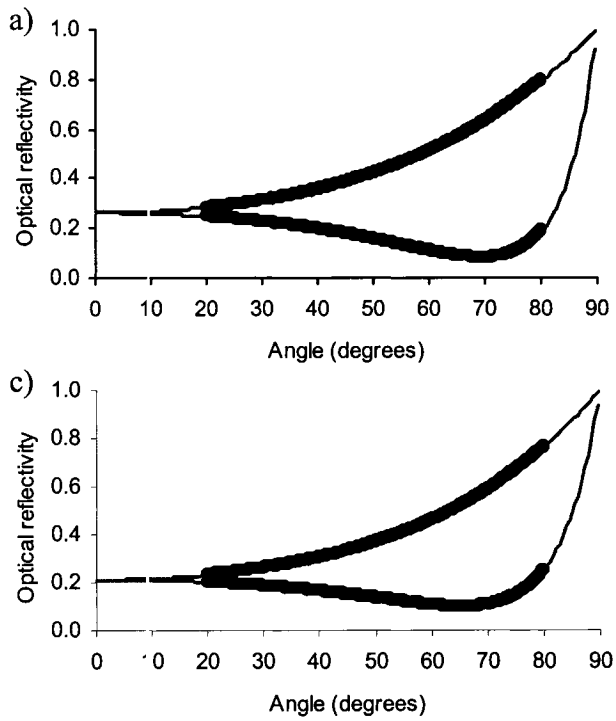

Figure 5.12: Optical reflectivity data (solid black lines) and associated model fits (thin gray lines) for azo-polymer films after photo-contraction. The model fits were obtained using the thickness from neutron reflectivity, and allowing the three orthogonal refractive indices to vary. In both the case of a sample photo-contracted with circularly polarized light (a) and linearly polarized light (b) the final sample is isotropic.

compared to linearly polarized light. In both cases, the data are well described by assuming only an isotropic refractive index ($n_x = n_y = n_z$). Thus the higher-density azo crystallites have an isotropic orientational distribution. We attempted to directly detect the azo crystallites by using the neutron spectrometer's triple-axis mode, and scanning for Bragg peaks arising from the azo crystal spacing. Although the Bragg peak due to the Silicon substrate was detected, no peaks due to the azo film were detected in films irradiated with either circularly or linearly polarized light. Detection of Bragg peaks in the selected geometry would require that the azo crystals be oriented with their spacing normal to the sample surface. The lack of a Bragg peak could be due to the formation of a single azo crystal that is not within the selected scattering plane. However the more likely explanation is that the azo crystallites are oriented randomly (i.e. the sample is polycrystalline), and the Bragg peak intensity is therefore too weak to be detected. Future experiments using powder diffraction on a sufficient sample volume might be able to detect the crystals.

5.4.8 Reversibility

The photomechanical effect studied here appears to be partially reversible. For thin films photo-expanded at room temperature, photo-contraction at elevated temperatures was thereafter possible. For instance, an initial 545 Å film was photo-expanded (2 hours at 38 mW/cm^2) by 11% at 25°C. A subsequent irradiation at 80°C (2 hours at 38 mW/cm^2) caused a contraction to a state 5% thinner than the original film thickness. The photo-contracted state persists regardless of thermal treatment, including annealing above the polymer T_g. In fact, any thermal treatment step (after irradiation) leads to further material densification (up to a certain saturation limit). However the photo-contracted state can evidently be partially reversed by irradiating again below the crossover temperature. For instance, an initially 395 Å film was photo-contracted at 85°C (2 hours at 62 mW/cm^2) to a state 7% thinner than the original film, then further photo-contracted at 110°C (2 hours at 62 mW/cm^2) to a state 15% thinner than the original film. This film was then irradiated at 25°C (2 hours at 62 mW/cm^2), where it photo-expanded to a state 2% thicker than the original film. Thus irradiation can be used to reverse the contracted state to some extent, although the efficiency of the process appears reduced. It is not known whether greater irradiation time or power could be used to expand the film

to the ~17% saturation limit. Again it appears that at low temperature the matrix cannot relax and reorganize. The azo isomerization breaks the dipole pairing, creating free volume pockets, and expanding the polymer matrix. However the material cannot relax back into a densified state without the addition of some thermal mobility.

5.5. Conclusions

Using neutron reflectometry, we have identified two competing photomechanical effects in azo polymer systems: one that causes expansion of the polymer matrix, and one that induces contraction of the material. We are able to measure the expansion and contraction effects unambiguously, since neutron reflectometry probes the physical density rather than the optical refractive index (which may be anisotropic and time-varying). Temperature can be used to alter the relative importance of the two photomechanical effects, switching from photo-expansion behavior below a characteristic crossover temperature, to photo-contraction behavior above this temperature. Both effects (expansion and contraction) are stable over time, although they can be reversed with subsequent light irradiation steps. We attribute the photo-expansion to the azobenzene molecular isomerization, which requires a certain free volume to proceed, and thereby induces a local pressure in the material. The polymer matrix then expands to accommodate this molecular motion, but cannot relax at low temperature. We attribute the photo-contraction to the formation of seed crystals due to photo-orientation; that is, pairing and aggregation of the azo dipoles, which are able to crystallize and thereby increase material density. This photo-motion and relaxation of the polymer matrix is only possible when the combined effects of light-induced and thermally-enabled motion reaches a critical value. For the materials studied here, this crossover temperature is ~50°C.

With regard to applications, such as photo-actuation, the identified photomechanical effect offers some unique features. With the addition of localized temperature control (which could also be laser-based), the range of motion is quite large: from −15% to +15%. The photomechanical transformations have both reversible and irreversible aspects, which can each be exploited as required by device characteristics (two-state values or reversible actuation). Importantly, by using light one may actuate a device remotely and without other energy requirements.

Given that nearly all the photo-motions discovered for azo materials are general (occurring in all cases where photo-isomerization occurs), it is likely that this photomechanical phenomenon is present in most azobenzene systems. In fact, it may very well be that numerous effects observed with azos can in fact be explained in the context of this photomechanical effect. For instance, the macroscopic bending of freestanding liquid crystalline azo films was attributed to contraction at the film surface.[8,9] That these materials photo-contract at room temperature is consistent with the present findings, given that the highly mobile liquid crystalline systems probably have a low crossover temperature, and thus are in the photo-contraction regime at room temperature. Similarly, findings that showed that a liquid crystalline and a similar amorphous system had opposite macroscopic expansion/contraction behavior[7] can be attributed to a difference in crossover temperature. According to this explanation, the liquid crystalline samples should exhibit photo-expansion if cooled sufficiently.

Importantly, the present results identify that the photomechanical effect is localized and occurs in nanometer-sized samples. This thus links the macroscopic observations of photomechanical phenomenon, to the microscopic photo-motions that have been characterized in azo materials. In particular, the all-optical formation of surface relief structures that occurs when azo materials are irradiated with light gradients may in fact be due to the photomechanical effect. Spatial variation of light intensity would generate an internal stress distribution in the material (owing to a gradient in expansion/contraction effects), which would then drive material motion. This is essentially equivalent to the isomerization-pressure model already presented to account for azo surface patterning,[24,25] with now the inclusion of a microscopic explanation for the driving force.

5.6. Acknowledgments

Neutron fitting software code was generously made available by Thad Harroun (Brock University). We thank Mike Watson for design and construction of the sample cell, Faisal Aldaye for help with molecular modeling, and Nasir Ahmad for materials synthesis. Research funds were provided by NSERC Canada, the FQRNT Centre for Self-Assembled Chemical Structures, and the Canadian Foundation for Innovation.

5.7. References

(1) Natansohn, A.; Rochon, P. *Chem. Rev.* **2002**, *102*, 4139.

(2) Yager, K. G.; Barrett, C. J. *J. Photochem. Photobiol., A* **2006**, *in press*, doi 10.1016/j.jphotochem.2006.04.021.

(3) Ichimura, K. *Chem. Rev.* **2000**, *100*, 1847.

(4) Yu, Y. L.; Ikeda, T. *J. Photochem. Photobiol., C* **2004**, *5*, 247.

(5) El Halabieh, R. H.; Mermut, O.; Barrett, C. J. *Pure Appl. Chem.* **2004**, *76*, 1445.

(6) Yager, K. G.; Barrett, C. J. *Curr. Opin. Sol. State Mater. Sci.* **2001**, *5*, 487.

(7) Bublitz, D.; Helgert, M.; Fleck, B.; Wenke, L.; Hvilsted, S.; Ramanujam, P. S. *Appl. Phys. B: Lasers Opt.* **2000**, *70*, 863.

(8) Yu, Y.; Nakano, M.; Ikeda, T. *Nature* **2003**, *425*, 145.

(9) Ikeda, T.; Nakano, M.; Yu, Y.; Tsutsumi, O.; Kanazawa, A. *Adv. Mater.* **2003**, *15*, 201.

(10) Camacho-Lopez, M.; Finkelmann, H.; Palffy-Muhoray, P.; Shelley, M. *Nat. Mater.* **2004**, *3*, 307.

(11) Tanchak, O. M.; Barrett, C. J. *Macromol.* **2005**, *38*, 10566.

(12) Yager, K. G.; Tanchak, O. M.; Barrett, C. J.; Watson, M. J.; Fritzsche, H. *Rev. Sci. Instrum.* **2006**, *77*.

(13) Natansohn, A.; Rochon, P.; Gosselin, J.; Xie, S. *Macromol.* **1992**, *25*, 2268.

(14) Parratt, L. G. *Phys. Rev.* **1954**, *95*, 359.

(15) Braun, C., version 1.5; HMI Berlin, 1999; www.hmi.de/bensc/instrumentation/instrumente/v6/refl/parratt_en.htm.

(16) Harroun, T., version 1.3; Brock University, 2006; http://www.physics.brocku.ca/faculty/harroun/parratt/index.html.

(17) Hecht, E. *Optics*, 4th ed.; Addison Wesley, 2002.

(18) Kiessig, H. *Ann. Phys.-Berlin* **1931**, *10*, 769.

(19) Brown, D.; Natansohn, A.; Rochon, P. *Macromol.* **1995**, *28*, 6116.

(20) Geue, T.; Henneberg, O.; Grenzer, J.; Pietsch, U.; Natansohn, A.; Rochon, P.; Finkelstein, K. *Colloids Surf., A* **2002**, *198-200*, 31.

(21) Pietsch, U.; Rochon, P.; Natansohn, A. *Adv. Mater.* **2000**, *12*, 1129.

(22) Yager, K. G.; Barrett, C. J. *J. Chem. Phys.* **2004**, *120*, 1089.

(23) Holme, N. C. R.; Nikolova, L.; Hvilsted, S.; Rasmussen, P. H.; Berg, R. H.; Ramanujam, P. S. *Appl. Phys. Lett.* **1999**, *74*, 519.

(24) Barrett, C. J.; Natansohn, A. L.; Rochon, P. L. *J. Phys. Chem.* **1996**, *100*, 8836.

(25) Barrett, C. J.; Rochon, P. L.; Natansohn, A. L. *J. Chem. Phys.* **1998**, *109*, 1505.

Chapter 6
Photomechanical Surface Patterning in Azo-Polymer Materials

The last chapter discussed the use of neutron reflectometry to identify and characterize new photomechanical effects in azo-polymers. These effects represent a fundamental photo-physical effect that gives rise to material motion over considerable length-scales. It is thus natural to investigate them as the driving force for surface patterning in these systems. This chapter presents a set of experiments chosen to demonstrate a correspondence between the photomechanical effect, and the surface patterning. In particular, the same material used for the neutron reflectometry study is photo-patterned in a localized way, which enables the direction of material motion to be imaged by AFM. These surface expansion/contraction results compare favorably to the photomechanical effects described in the last chapter. In particular, surface patterning is shown to invert from photo-expansion to photo-contraction at the same crossover temperature as identified for the photomechanical effect. AFM nano-indentation experiments are also presented to discount photo-softening effects during patterning. This chapter therefore argues that the photomechanical effect is the driving force for surface patterning, and moreover shows how this supposition can explain a variety of literature results.

6.1. Abstract

The elastic modulus of an azobenzene-polymer thin film is measured before and during laser irradiation using AFM indentation experiments. It is found that there is no significant change in elastic modulus with laser illumination, indicating that photo-softening can be neglected in these systems. In particular, this eliminates mechanisms that require photo-softening as candidate explanations for azo surface patterning. AFM measurements of patterning in azo-polymer thin films, irradiated at various temperatures, are compared to recent neutron reflectometry measurements of photomechanical effects in the same material. The magnitude and sign of the patterning exactly matches the literature trend for photomechanical effects. This represents the first report of measuring both photo-expanded and photo-contracted surface patterns in the same material, at

different temperatures. These results are interpreted to mean that the unexplained surface mass transport phenomenon observed in the azobenzene system is in fact due to this newly identified photomechanical effect. Previous patterning results are discussed in terms of this explanation, and it is shown that the photomechanical effect can explain the vast majority of the literature results to date.

6.2. Introduction

Azobenzene chromophores exhibit a wide variety of photo-physical and photo-switching effects.[1,2] The azo unit undergoes an efficient photo-induced isomerization between its *trans* and *cis* geometric isomers. This clean photochemistry gives rise to a variety of unique photo-switching and photomechanical effects. For instance, the material can be photo-oriented with polarized light (which induces birefringence), or thin films can be induced to macroscopically bend or unbend[3] (which has also been used to generate macroscopic locomotion[4]). The azobenzene unit is typically incorporated into a polymer system, whether amorphous or liquid crystalline, to improve processability and photo-physical stability. In 1995, a remarkable effect was discovered in the azo-polymer materials.[5,6] Specifically, when the material was irradiated with two coherent laser beams (which generate a sinusoidally varying light pattern at the sample surface), the materials spontaneously deformed so as to generate a sinusoidal Surface Relief Grating (SRG). An AFM image of a typical SRG is shown in Figure 6.1. This single-step all-optical surface patterning was found to be reversible, as the original film thickness could be recovered

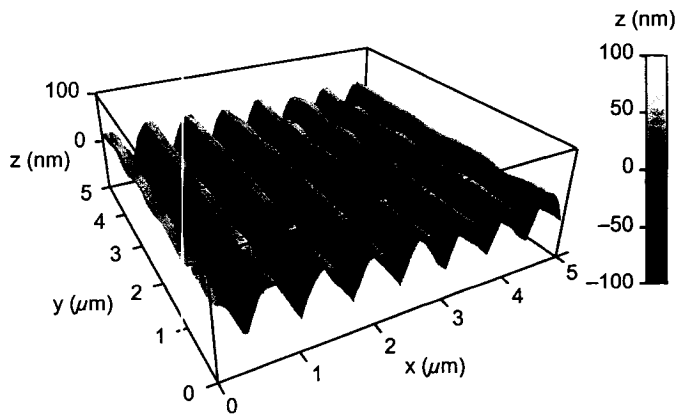

Figure 6.1: Atomic force micrograph of a surface relief grating (SRG) inscribed on an azo-polymer film by irradiating with a sinuisoidal light pattern.

upon heating the material past its glass-to-rubber transition temperature (T_g). Thus the process represents polymer motion over length-scales of hundreds of nanometers, occurring readily at temperatures well below T_g. The facile patterning is a general phenomenon, with any incident light intensity and/or polarization pattern converted into a topography pattern. Various mechanisms have been proposed to explain the effect, although each has certain shortcomings. Thermal mechanisms have been discounted based on modeling of the temperature gradient during irradiation.[7] Gradient electric force mechanisms[8] naturally include the polarization dependence, but the predicted force density is too small.[9] An asymmetric diffusion model[10,11] was formulated, but would seem to imply that the process would be most efficient for small-molecule materials, whereas in practice relatively high molecular weight polymers can be photo-patterned. A mean-field model[12,13] predicts the correct phase behavior for liquid-crystalline systems, but not for amorphous polymers. A proposed isomerization pressure model[14,15] does not naturally include the polarization dependence of the patterning. A fundamental shortcoming of all presented explanations is that they cannot account for the phase relationship between the incident light field and the resultant patterning. In particular, all the models presented to date predict one phase relationship or the other (either material accumulates in the illuminated regions or in the dark regions), whereas experimentally both are observed in different systems. As a general rule, amorphous systems exhibit a 'common' phase relationship (material accumulates in the dark regions of an incident light pattern) whereas the liquid crystalline azo systems exhibit an 'inverted' phase relationship (material accumulation in the illuminated regions).[16] Some mechanisms imply that a form of photo-softening must be occurring during laser irradiation, in order to explain the material motion well below the glass-transition temperature. For instance, viscoelastic modeling assumed that the modulus decreased by three orders-of-magnitude during irradiation.[9] Thus, despite active research, the fundamental nature of the driving force remains unresolved.[17]

Recently, photo-expansion in thin films of azo-polymer was measured using ellipsometry.[18] The material was found to expand during laser illumination, with a large irreversible component that persists after illumination ceases, and a smaller reversible component that exists only while the irradiating beam is active. This photomechanical

effect was found to be directly related to the isomerization of the azo chromophores. A subsequent neutron reflectometry study analyzed this effect in more detail.[19] In addition to unambiguously confirming the photo-expansion of azo materials during light irradiation at room temperature, it was discovered that at elevated temperatures (above a distinct crossover at ~50°C), the material instead contracted and became more dense when irradiated with laser light. The trend of this photomechanical effect (changing from expansion at low temperature to contraction at high temperature) is shown in Figure 6.2, and suggests a competition between two driving forces. At low temperature, the free volume requirement of the azobenzene isomerization induces a pressure on the polymer matrix and a subsequent expansion of the material. At these low temperatures, the polymer matrix cannot relax and the modification is persistent. Above the crossover temperature, however, the combination of photo-induced motion and thermally-enabled motion are sufficient to allow the azo chromophores to migrate, aggregate, and eventually crystallize into higher-density states.

In this paper, we describe AFM measurements of the elastic modulus of azo materials before and during laser irradiation. These measurements indicate that photo-softening effects are quite small, which establishes a constraint on mechanisms proposed to explain surface mass patterning. We propose here that the photomechanical effect observed during homogeneous irradiation of azo films is the fundamental driving force

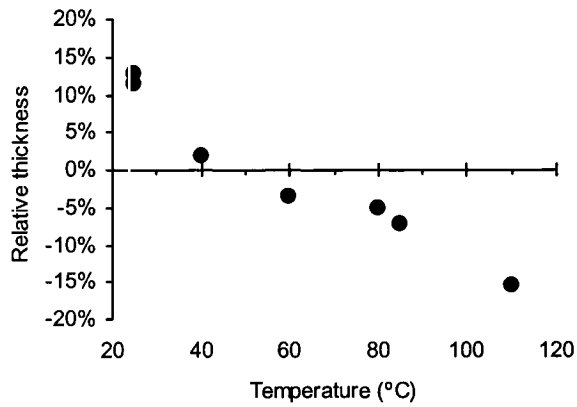

Figure 6.2: Relative film thickness (expansion or contraction) for thin azo films after irradiation with homogeneous laser light, as measured using neutron reflectometry. Below a crossover temperature (~50°C for this material) the film photo-expands, whereas above the crossover, samples photo-contract instead.

for mass transport observed when the same materials are irradiated with light gradients. In order to critically test this theory, we conducted photo-patterning experiments through a transmission mask, at various sample temperatures. The trend of the photo-patterning, including both amplitude and sign, precisely matches the photomechanical trend. Moreover the proposed patterning mechanism, with the exclusion of photo-softening, can be used to explain a variety of results in the azo-patterning literature, that previously appeared contradictory.

6.3. Experimental

6.3.1 Sample Preparation

The azo-polymer material, poly(disperse red 1 acrylate) (pdr1a) was synthesized as previously reported.[20] Samples for patterning were prepared by spin-coating the azo-polymer solutions (pdr1a in anhydrous THF solvent) onto cleaned glass microscope slides. The spin-coater acceleration was 1260 rpm/s, with a final velocity of 1300 rpm maintained for 35 s. Thin films were annealed in a vacuum oven at 110°C for 8 hours to remove any residual solvent or flow-induced orientation. Film thickness was measured by imaging a scratch in the thin film by AFM.

6.3.2 AFM Modulus Measurements

The elastic modulus of azo-polymer films was measured using AFM in force-distance mode (Nanoscope 3A, Digital Instruments), and applying a data analysis method already described in the literature.[21,22] Measurements were performed in a fluid cell (filled with ultrapure water) at room temperature, in order to reduce adhesion artifacts. Measurements were performed before and during irradiation from a 532 nm diode laser. The laser light was coupled into the glass substrate that the thin film was cast onto. Internal reflections inside the glass substrate allowed the light to exit the film and irradiate the probed area. Successful irradiation of the probed region was confirmed visually, and by irradiating for a long period of time, after which significant photo-patterning was observed in the vicinity of the AFM tip. The AFM cantilevers were SiN probes with nominal tip radius 20–60 nm, and a nominal spring constant of 0.12 N/m. All the data reported in this paper were acquired using a single probe, thereby eliminating variability in the tip radius or spring constant. Although the inherent assumptions of tip

geometry and spring constant introduce an uncertainty into the reported modulus values, using a single tip enables us to draw robust relative conclusions. The indentation rate was 0.2 Hz, and the indentation depth (<30 nm) was always considerably smaller than the film thickness (~200 nm). A large number of force indentation curves were recovered, and analyzed using automated fitting software. Only those curves free of adhesion or other artifacts were automatically selected for further analysis. The final modulus values thereby obtained are spread across a certain range, owing to differences in the various indentation curves. A histogram of the results is thus used to analyze the statistical behavior. Each force curve is analyzed by extrapolating the linear non-contact region and the linear 'infinitely stiff' region so as to identify the nonlinear elastic response region. This transition from the linear non-contact region to the nonlinear elastic response region is taken as the initial contact point. By assuming the AFM tip can be modeled as a sphere, the nonlinear region is fit to a force-distance equation of the form:

$$F_{sphere} = \frac{4E\sqrt{R}}{3(1-\sigma^2)}\delta^{3/2} \quad (1)$$

where F is the measured force as a function of sample indentation δ, σ is the Poisson ratio for the material (taken to be 0.5, typical for polymers), R is the nominal tip radius, and E is the elastic modulus to be determined. Note that modeling the tip as a cone instead of a sphere provides a slightly different equation and thus modulus estimate. A cone model does not reproduce the data as faithfully as the selected sphere model, but in any case would not alter the relative conclusion being drawn from the force-distance data in this paper.

6.3.3 Neutron Reflectometry

The neutron reflectometry measurements are described in detail in another publication.[19] The samples were held in a custom-built cell that enables neutron measurements simultaneous with optical irradiation.[23] The cell further allows control of sample environment, including ambient atmosphere and temperature. The presented photomechanical data was obtained for thin films maintained at various temperatures, under vacuum, and are based on comparison of the reflectivity curves before and after irradiation at those temperatures.

6.3.4 Transmission Mask Patterning

A single film of pdr1a (330 nm thick) was cut into small segments for the patterning experiment. The sample was placed inside a heating stage with optical windows on the front and back (INSTEC HCS302), driven by a temperature controller (INSTEC STC200). Good thermal exchange between the sample and the heating block was insured using metal contact spacers. A transmission mask (VECO 0400-Copper TEM grid, pitch 63 μm, hole size 30 μm) was secured 10 μm above the sample surface. Irradiation took place for 2 hours at 40 mW/cm^2, using the circularly-polarized beam from a water-cooled Argon-ion laser (Coherent Innova 308) tuned to 488 nm. The film surface patterns were then imaged using AFM (Asylum MFP-3D in tapping mode).

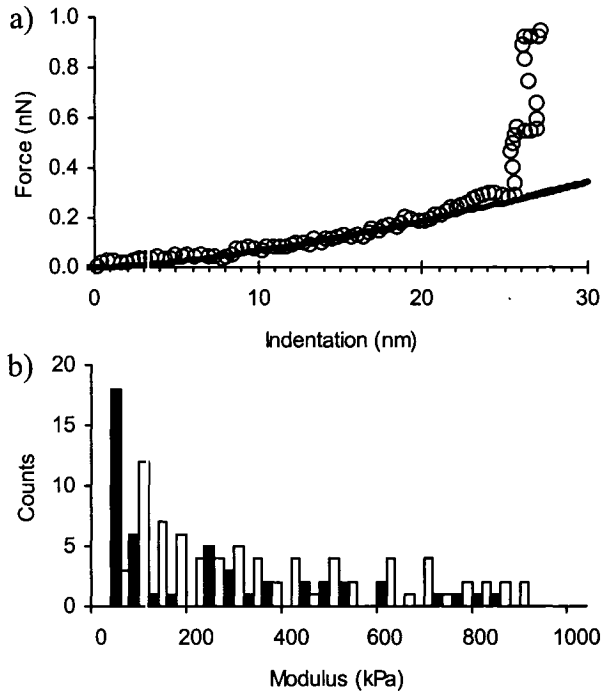

Figure 6.3: (a) Typical force-distance curve obtained by indenting an AFM tip into an azo-polymer thin film. The open circles are the experimental data, and the black line a fit to the data. The sharp rise in the later part of the curve represents the 'infinitely stiff' response of the sample/substrate and is not considered in the analysis. (b) Histogram of AFM modulus events, based on the fits to the force-distance data. Measurements without laser irradiation (black bars) and during irradiation with a 532 nm diode laser (white bars) are shown. The two distributions are not significantly different, indicating that photo-softening is a limited effect.

6.3.5 Surface Relief Gratings

Surface relief gratings were formed by securing a sample inside the heating stage, and placing it adjacent to a laser-quality mirror. An expanded laser beam was used to illuminate both the sample and the mirror, such that the mirror reflection would interfere with the incident beam at the sample surface. The incident laser power was 40 mW/cm^2, and the beam was circularly-polarized. Thus the sample surface experiences an interference between right-handed and left-handed circular light, which results in the formation of a high-efficiency SRG at room temperature. The inscription angle was 20°.

6.4. Results

6.4.1 Photo-softening

Figure 6.1 shows a surface relief grating (SRG) formed by irradiating an azo-polymer film with a sinusoidally varying light intensity pattern. This well-established surface-patterning phenomenon still lacks a satisfactory explanation, despite extensive research. In an attempt to identify the origin of this patterning, we undertook a series of atomic force microscopy measurements. The all-optical patterning of azo films can occur with high efficiency well below the material's glass-transition temperature (T_g). Polymer motion is generally completely hindered below T_g, and it therefore often suggested that patterning involves some sort of 'photo-plasticization' or 'photo-softening' whereby the azobenzene molecular isomerization substantially decreases the elastic modulus of the host polymer network, thereby enabling a comparatively small molecular force to drive patterning. Recent literature reports of the change in modulus, measured by quartz crystal microbalance[24] and electromechanical spectroscopy,[25,26] however, show quite modest (<10%) decrease in bulk elastic modulus. We investigated this phenomenon by performing AFM force-distance measurements, which allow one to deduce the elastic properties of thin films by performing nano-indentation (a typical curve is shown in Figure 6.3a). By fitting the shape of many indentation and retraction curves, a range of modulus values were calculated, which is depicted as a histogram Figure 6.3b. From this distribution, we calculate that the average modulus of the film is 219±70 kPa before irradiation, whereas it is 336±62 kPa during irradiation. From both this average and the overall distribution, we conclude that there is no statistically significant difference

between the two cases. Thus, consistent with the other studies, there appears not to be an orders-of-magnitude decrease in the modulus. We confirmed that we were in fact irradiating the sample volume probed by the AFM by leaving the irradiating light active for a long period of time, after which AFM topography measurements showed significant photo-patterning in the vicinity of the AFM tip. It should be noted, however, that the timescale of these modulus measurements (seconds) is smaller than the typical timescale for material motion (minutes). The lack of substantial photo-softening indicates that the material motion does not involve a decrease in the bulk elastic properties of the material. Instead, it relies upon localized, molecular scale rearrangements. Evidently the azobenzene isomerization induces a sufficient molecular pressure to distort the polymer matrix locally, rather than softening the bulk matrix substantially. This helps explain why the observed photo-expansion and surface patterning persist at room temperature: the polymer matrix is still rigid and cannot relax. These results also eliminate any model that relies upon significant photo-softening to explain mass transport.

6.4.2 Temperature Dependence of Patterning

Our recent work using ellipsometry[18] and neutron reflectometry[19] has identified two competing photomechanical effects in azobenzene materials. Thin films of azo-polymer were irradiated homogeneously with laser light at a wavelength close the azo's absorption maximum. Below a characteristic crossover temperature, the material exhibited photo-expansion behavior, whereas above this temperature, the same material instead photo-contracted. The expansion can be attributed to molecular isomerization, which induces a molecular pressure on the surrounding polymer matrix, forcing it to expand. Since the polymer matrix cannot relax at low temperature, the expansion remains fixed. At a certain temperature, however, the combination of light-induced motion and thermally-enabled motion is sufficient to allow the azobenzene dipoles to reorient, aggregate, and thereby crystallize into higher-density domains. The temperature dependence of the photomechanical effect, measured for thin films of poly(disperse red 1 acrylate) (pdr1a) is shown in Figure 6.2. As can be seen, a crossover from photo-expansion to photo-contraction occurs at ~50°C. The phenomenon was also found to occur in the azo-polymer pdr13a, and it is likely that it is a generic effect that occurs in all azo materials. It should also be noted that this effect, which involves a large-scale change

in material dimensions and density, occurs well below the glass-transition temperature, and apparently without the aid of photo-softening.

These neutron reflectometry measurements prompted us to similarly study the temperature dependence of surface patterning in azo materials. The previous study measured expansion and contraction effects that occurred when the films were homogeneously irradiated with laser light. However the photomechanical effect is clearly localized, as it occurs readily in thin films even 20 nm thick. It is thus natural to consider the connection between these photomechanical motions, and the surface mass transport patterning well documented in the azo system. To that end, we irradiated the same

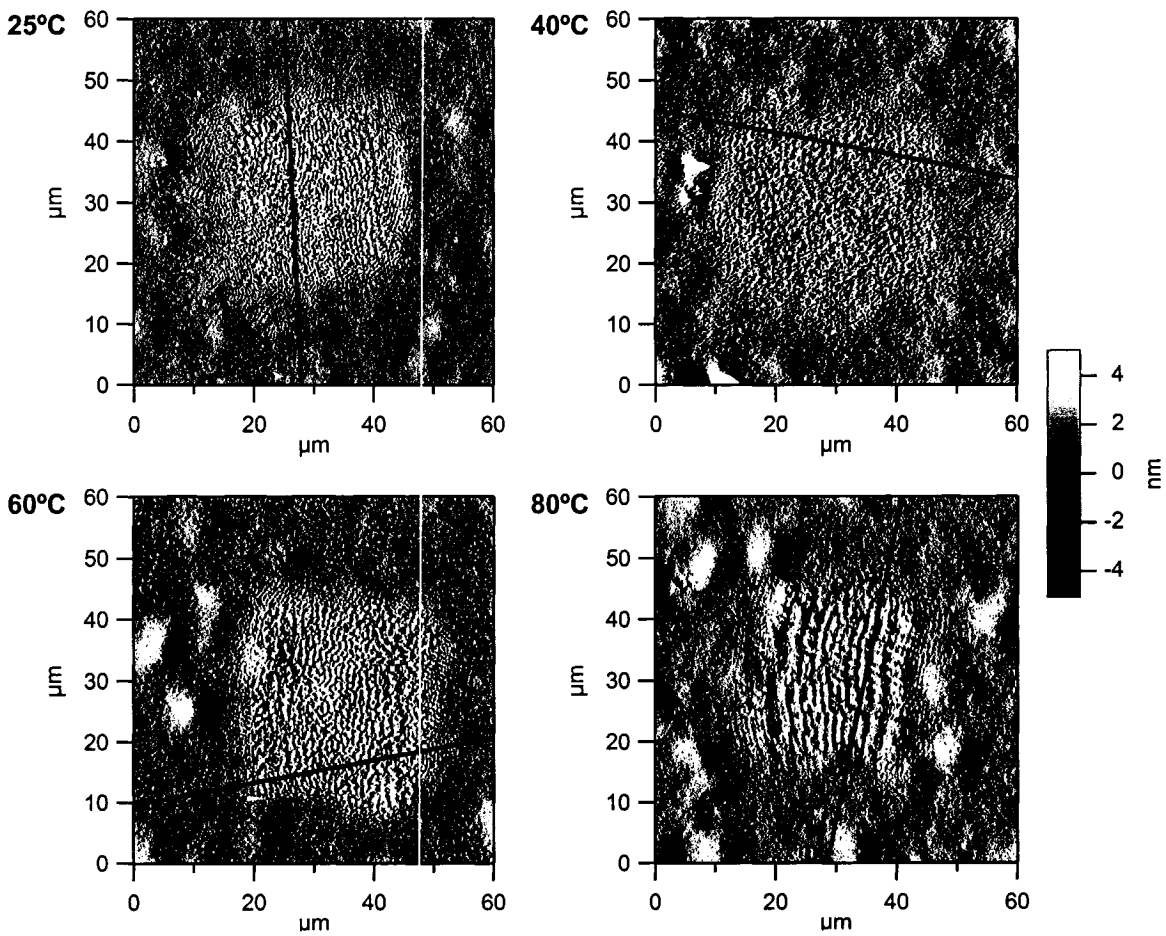

Figure 6.4: Atomic force microscopy amplitude images (all shown using the same vertical scale) of an azo surface irradiated through a mask with square holes. Irradiation was performed at 25°C, 40°C, 60°C, and 80°C. The central region in each image is rougher because it has become photo-patterned by the incident laser light. The surrounding area was not irradiated with laser light. The black line through each figure refers to the cross-sections shown in Figure 5.

polymer material (pdr1a) through a transmission grid, so that the photomechanical transformations would be spatially localized. Figure 6.4 shows atomic force micrographs of the resultant changes in topography when films held at various temperatures are irradiated. In each case, the thin film was irradiated for 2 hours using 40 mW/cm^2 laser light at 488 nm. The amplitude images show clearly that the irradiated region (center square in the images) has become considerably rougher than the surrounding un-irradiated polymer surface. Similar photo-induced roughening[25] or spontaneous patterning[27-29] has been observed during homogeneous irradiation of related systems. It is likely due to surface patterning owing to the interference between the edge diffractions and the back-reflections from the substrate. Some amount of photo-roughening may also be caused by spontaneous buckling of the sample surface to relieve the stress caused by the photomechanical deformation (whether expansion or contraction) that is occurring. Figure 6.5 shows the root-mean-square (RMS) roughness of the corresponding height data for the irradiated regions. For comparison, the RMS roughness of the un-irradiated polymer surface is 15 nm. By comparing the data in Figure 6.2 to Figure 6.5, it is clear that the patterning observed by AFM follows the same temperature dependence as the photomechanical effect measured with neutron reflectometry. Specifically, the competition between the two effects causes the surface patterning to be inefficient near the crossover temperature (~50°C), whereas it becomes more efficient further from the crossover.

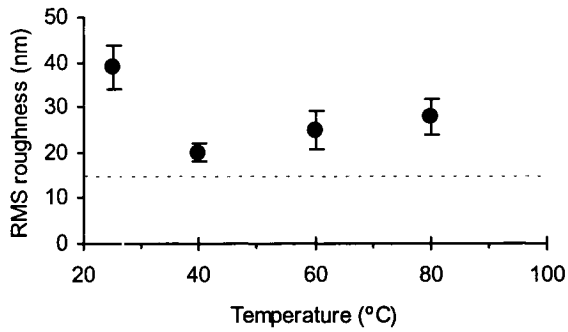

Figure 6.5: Root-mean-square (RMS) roughness inside the patterned regions shown in Figure 3. For reference, the roughness of the surrounding (un-irradiated) film is 15 nm, and is shown using a dashed line. The RMS roughness can be used as a measure of patterning efficiency. The patterning is inefficient near the crossover temperature.

The height cross-sections (see Figure 6.6a) provide a more direct indication of nature of the surface patterning. At 25°C, the patterning clearly involves the formation of surface relief that is higher than the surrounding polymer material. This occurs because the irradiated film region is expanded relative to the un-irradiated material. At 40°C, the competition between the photo-expansion and photo-contraction effects makes the photomechanical response quite modest, and the surface patterning is correspondingly smaller, being the result of a small amount of photo-expansion. At 60°C, the surface patterning extends below the original film thickness. At 80°C, the effect is even more pronounced, with the patterning phenomenon clearly arising due to contraction of the material in the irradiated region. Thus for all temperatures a light-induced surface-

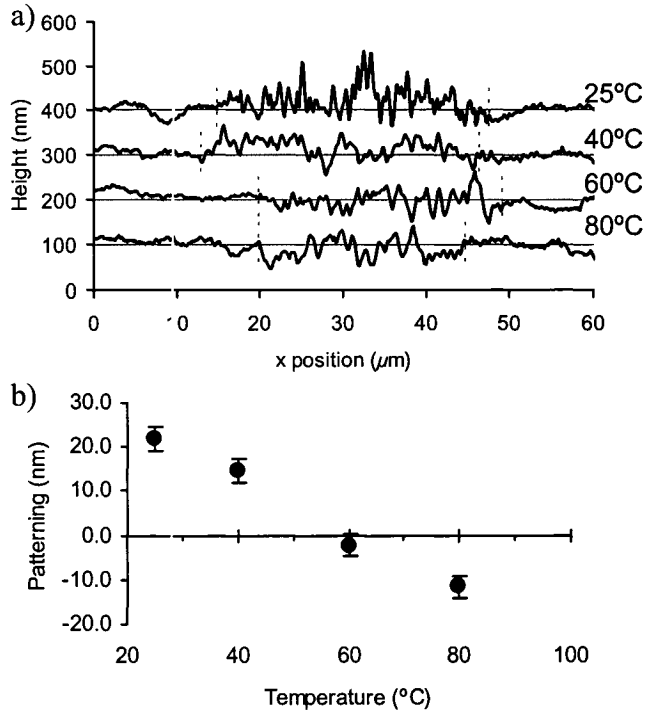

Figure 6.6: (a) Atomic force microscopy height cross-sections, taken through the corresponding images shown in Figure 3. The sections have been offset vertically for clarity. The gray horizontal line represents the nominal film height in each case. The vertical dashed lines for each section represent the approximate boundaries of the illuminated regions, as determined from the amplitude data in Figure 3. (b) By integrating the area under the curve in the patterned region (and normalizing to the associated span), the magnitude and sign of the effect can be quantified. The patterning trend, as a function of temperature, exactly matches the photomechanical trend seen in Figure 2. The error bars are based on a similar analysis performed on the un-irradiated film region.

patterning phenomenon is apparent. However the phase of the patterning is opposite on either side of the crossover temperature. The patterning analysis can be made more quantitative by integrating the area under the AFM height profiles (the curves are offset so that the un-irradiated film surface corresponds to a height of zero). The trend of this value as a function of patterning temperature (see Figure 6.6b) exactly matches the photomechanical trend observed using neutron reflectometry (Figure 6.2).

6.4.3 Photomechanical Mechanism

Given the correspondence between the photomechanical data and the surface patterning data, we propose that the well-established surface mass transport phenomenon is in fact a manifestation of localized photomechanical deformation. Specifically, a light intensity gradient will generate a corresponding photomechanical stress gradient inside the azo material, which will serve to drive the motion of polymer material. Below the crossover temperature, photo-expansion in the illuminated regions will lead to a positive pressure gradient. Above the crossover temperature, photo-contraction in the illuminated regions will lead to a negative pressure and a phase-inverted version of the patterning. The existence of two patterning mechanisms, one phase inverted relative to the other, has been identified in the literature. The proposed below-crossover patterning mechanism is in fact well described by the isomerization pressure mechanism[14,15] described in the literature, and the related hydrodynamic modeling studies. The proposed above-crossover mechanism is essentially the same, with the inclusion of a phase-inverted stress pattern. It should also be noted that the proposed densification-based patterning, initiated by photo-orientation, is similar to the mean-field model[12,13] proposed in the literature. Thus the previously proposed isomerization pressure and mean-field models are limiting cases in the general framework of a photomechanical mechanism. It is important to note that photomechanical effects measured in azo systems, and now identified as the origin of surface-patterning, occur in these materials well below T_g, and without the aid of photo-softening.

In the literature, it has been found that liquid crystalline systems exhibit opposite expansion/contraction effects relative to a similar amorphous system.[16,30] This is now easily explained with the photomechanical data, with the suggestion that liquid crystalline systems are, owing to their high mobility, above their crossover temperature even at room

temperature, and thus exhibit photo-contraction behavior. Similarly, the bending of freestanding liquid crystal films is due to photo-contraction.[3] Amorphous systems, on the other hand, will typically exhibit an opposite photo-expansion behavior because they are below their crossover temperature. A similar argument can be made to explain the phase of surface relief patterning. Liquid crystalline systems have typically be seen to have the opposite phase behavior to amorphous systems. In LC systems, the material tends to accumulate in the irradiated regions, whereas in amorphous systems the material moves into the dark regions. This can be explained in the context of a pressure gradient. Although homogeneous irradiation (or large-scale irradiation, as shown in Figure 6.4) causes net expansion of a material below the crossover temperature, a local gradient in expansion creates a stress gradient that moves material out of the region of high stress (irradiation). The opposite behavior would be seen for a small-scale negative stress gradient in a material above the crossover temperature. Here, the contraction occurring in illuminated regions would serve to draw in more material, causing an accumulation and corresponding depletion from nearby regions. Thus the phase-inverted patterning seen for some systems can be attributed entirely to the specific position of their crossover temperature. This enables us to also explain the rare cases where amorphous systems exhibit phase-inverted patterning,[31] or where LC systems exhibit the usual patterning.[32,33] Similarly, the creation of phase-inverted surface relief gratings when irradiating with extremely high laser power[34] (>300 W/cm^2) can be attributed to localized heating, which drives the material above the crossover temperature. From modeling studies,[7] it is known that there is a modest (<5 K) change in sample temperature for most irradiation powers. At high laser power, however, one can calculate that the sample temperature will increase considerably, and could be driven above the crossover temperature. Thus the phase-inverted SRG (and thus double-period SRG) that was formed in that study is due to photo-heating combined with photo-patterning.

It is well established that the surface-patterning phenomenon is strongly polarization dependant.[35] Both the efficiency of the process (as measured by topography height) and the exact shape of structures are affected by the incident polarization state. In essence, the topography encodes both the incident light intensity pattern, and the polarization pattern. The presented photomechanical mechanism does not obviously

include any polarization dependence. Presumably the extent of photomechanical response would be related only to the light intensity, and not the polarization vector. However a number of additional considerations can explain the influence of incident polarization. It has been determined that azo chromophores become photo-oriented by incident polarized light during surface patterning.[36-38] Azo chromophores tend to accumulate perpendicular to the incident polarization at any given position, as those chromophores that fall into these orientations will no longer be able to absorb incident photons, and will therefore no longer undergo isomerization and photo-motion. This orientational photo-depletion can explain in some cases the low grating efficiency observed (for instance in the case of forming a SRG with two *s*-polarized beams), because the chromophores become photo-aligned and cease to isomerize. In the context of the proposed competing photomechanical mechanism, it is also possible, however, that photo-orientation increases the efficiency of the photo-contraction component. For some polarization combinations this may actually increase the overall efficiency, if the photo-contraction causes accumulation of material in the same direction as the photo-expansion drives material flow. Additionally, it is worth considering anisotropy in the restoring force. It is generally agreed that surface tension is the restoring force that eventually arrests the surface-patterning phenomenon. Even if the driving force is isotropic (no polarization dependence), polarization patterns may develop if the restoring force is anisotropic (has a polarization dependence). For instance, if azobenzene orientation causes the surface tension to be anisotropic (locally different along the molecular axis, as compared to against it), this can explain the observed polarization patterns. Specifically, irradiation geometries that do not induce spatial variation of the azo orientation (such as the *s*:*s* combination, or the RCP:RCP combination) will have a homogeneous surface tension across the surface, which will arrest the surface mass transport. Irradiation geometries that induce a spatially varying surface tension, due to a spatially varying polarization pattern and hence azo orientation (which includes the +45°:–45° and RCP:LCP combinations) will have an additional driving force to deform the sample surface, namely that the gradient in surface tension represents an additional instability that can drive material flow. In other words, a gradient in surface tension (with, importantly, lower than bulk surface tension at some positions in the pattern) will not arrest material flow as

efficiently as a homogeneous surface tension. This suggestion is similar to the experimental observation of macroscopic droplet motion on azo-polymer surfaces that have photo-driven surface energy gradients.[39]

It is possible that further experiments measuring the temperature dependence of SRG inscription, with different polarization states, could help to determine the relative contribution of the photo-expansion and photo-contraction mechanisms under each set of conditions. For instance, Figure 6.7 shows the SRG height for gratings formed using the highly efficient RCP:LCP polarization combination. What can be seen is that this polarization combination is inefficient at elevated temperatures, possibly because it is driven by the photo-expansion process, and not efficient in a photo-contraction context.

Although initial analysis of surface patterning suggested that volume was conserved,[34] subsequent studies have shown that this is not the case,[31] with evidence of densification and compressible fluid behavior. Modeling also suggests that the process requires a compressible fluid.[9] Moreover, a sequence of measurements on the thermal erasure of surface relief gratings demonstrated that during heat treatment, a density grating, coincident with the initial SRG but buried beneath the surface, develops.[40,41] This suggests that the initial photo-patterning and related photo-orientation creates seeding crystals that can be grown, with chromophores aggregating, during thermal treatment. This is precisely analogous to the observed photomechanical effect, where the combination of light-induced orientation and heat-enabled mobility generates a photo-contracted state.

6.5. Conclusion

AFM force-distance measurements have been used to argue that photo-softening effects are negligibly small in azo materials, which limits the range of mechanisms that can be used to explain surface patterning in these systems. The recently characterized photomechanical response of azo materials, which involves competition between photo-expansion and photo-contraction, was used to explain the surface-patterning phenomenon seen in azobenzene systems. By irradiating through a grid-like mask, we have shown that surface-patterning can occur both above and below the photomechanical crossover temperature. The phase of the patterning effect is opposite in the two cases, with photo-expansion driving mass transport below the crossover, and photo-contraction driving

mass transport above the crossover temperature. This observation allows us to explain the peculiar phase dependence observed in the literature. Specifically, systems which exhibit the 'common' patterning phase relationship (material motion into the dark) are constrained systems that are below their crossover temperature during patterning, whereas those that exhibit the 'inverted' phase relationship (material motion into the light) are mobile systems that are above their crossover temperature.

The proposed photomechanical explanation for surface patterning agrees with the large body of literature that has been developed on azo patterning and SRG formation, and does not require the introduction of a hypothetical photo-softening effect. Some of the previously proposed mechanisms can be viewed as limiting cases of this general photomechanical patterning. By including considerations of the anisotropy in the restoring force, it is also possible to explain the polarization dependence seen in azo patterning.

6.6. Acknowledgments

Neutron fitting software code was generously made available by Thad Harroun (Brock University). The neutron reflectometry data was acquired in collaboration with Helmut Fritzsche of the NRC Chalk River labs, and with the help of Oleh M. Tanchak and Christopher Godbout. Polymer synthesis was performed by Nasir Ahmad. We would also like to thank Derek Gray and Emily Cranston for help with AFM imaging, and Ozzy Mermut for help with force-distance measurements. Research funds were provided by NSERC Canada and the Canadian Foundation for Innovation.

6.7. References

(1) Natansohn, A.; Rochon, P. *Chem. Rev.* **2002**, *102*, 4139.

(2) Yager, K. G.; Barrett, C. J. *J. Photochem. Photobiol., A* **2006**, *in press*, doi 10.1016/j.jphotochem.2006.04.021.

(3) Yu, Y.; Nakano, M.; Ikeda, T. *Nature* **2003**, *425*, 145.

(4) Camacho-Lopez, M.; Finkelmann, H.; Palffy-Muhoray, P.; Shelley, M. *Nat. Mater.* **2004**, *3*, 307.

(5) Rochon, P.; Batalla, E.; Natansohn, A. *Appl. Phys. Lett.* **1995**, *66*, 136.

(6) Kim, D. Y.; Tripathy, S. K.; Li, L.; Kumar, J. *Appl. Phys. Lett.* **1995**, *66*, 1166.

(7) Yager, K. G.; Barrett, C. J. *J. Chem. Phys.* **2004**, *120*, 1089.

(8) Kumar, J.; Li, L.; Jiang, X. L.; Kim, D. Y.; Lee, T. S.; Tripathy, S. *Appl. Phys. Lett.* **1998**, *72*, 2096.

(9) Saphiannikova, M.; Geue, T. M.; Henneberg, O.; Morawetz, K.; Pietsch, U. *J. Chem. Phys.* **2004**, *120*, 4039.

(10) Lefin, P.; Fiorini, C.; Nunzi, J. M. *Opt. Mater.* **1998**, *9*, 323.

(11) Lefin, P.; Fiorini, C.; Nunzi, J. M. *Pure Appl. Opt.* **1998**, *7*, 71.

(12) Pedersen, T. G.; Johansen, P. M. *Phys. Rev. Lett.* **1997**, *79*, 2470.

(13) Pedersen, T. G.; Johansen, P. M.; Holme, N. C. R.; Ramanujam, P. S.; Hvilsted, S. *Phys. Rev. Lett.* **1998**, *80*, 89.

(14) Barrett, C. J.; Natansohn, A. L.; Rochon, P. L. *J. Phys. Chem.* **1996**, *100*, 8836.

(15) Barrett, C. J.; Rochon, P. L.; Natansohn, A. L. *J. Chem. Phys.* **1998**, *109*, 1505.

(16) Holme, N. C. R.; Nikolova, L.; Hvilsted, S.; Rasmussen, P. H.; Berg, R. H.; Ramanujam, P. S. *Appl. Phys. Lett.* **1999**, *74*, 519.

(17) Yager, K. G.; Barrett, C. J. *Curr. Opin. Sol. State Mater. Sci.* **2001**, *5*, 487.

(18) Tanchak, O. M.; Barrett, C. J. *Macromol.* **2005**, *38*, 10566.

(19) Yager, K. G.; Tanchak, O. M.; Godbout, C.; Fritzsche, H.; Barrett, C. J. *Macromol.* **2006**, *submitted*.

(20) Natansohn, A.; Rochon, P.; Gosselin, J.; Xie, S. *Macromol.* **1992**, *25*, 2268.

(21) Domke, J.; Radmacher, M. *Langmuir* **1998**, *14*, 3320.

(22) Akhremitchev, B. B.; Walker, G. C. *Langmuir* **1999**, *15*, 5630.

(23) Yager, K. G.; Tanchak, O. M.; Barrett, C. J.; Watson, M. J.; Fritzsche, H. *Rev. Sci. Instrum.* **2006**, *77*.

(24) Srikhirin, T.; Laschitsch, A.; Neher, D.; Johannsmann, D. *Appl. Phys. Lett.* **2000**, *77*, 963.

(25) Mechau, N.; Neher, D.; Borger, V.; Menzel, H.; Urayama, K. *Appl. Phys. Lett.* **2002**, *81*, 4715.

(26) Mechau, N.; Saphiannikova, M.; Neher, D. *Macromol.* **2005**, *38*, 3894.

(27) Lagugne-Labarthet, F.; Buffeteau, T.; Sourisseau, C. *Phys. Chem. Chem. Phys.* **2002**, *4*, 4020.

(28) Hubert, C.; Fiorini-Debuisschert, C.; Maurin, I.; Nunzi, J. M.; Raimond, P. *Advanced Materials* **2002**, *14*, 729.

(29) Hubert, C.; Malcor, E.; Maurin, I.; Nunzi, J. M.; Raimond, P.; Fiorini, C. *Appl. Surf. Sci.* **2002**, *186*, 29.

(30) Bublitz, D.; Helgert, M.; Fleck, B.; Wenke, L.; Hvilsted, S.; Ramanujam, P. S. *Appl. Phys. B: Lasers Opt.* **2000**, *70*, 863.

(31) Keum, C. D.; Ikawa, T.; Tsuchimori, M.; Watanabe, O. *Macromol.* **2003**, *36*, 4916.

(32) Zettsu, N.; Fukuda, T.; Matsuda, H.; Seki, T. *Appl. Phys. Lett.* **2003**, *83*, 4960.

(33) Helgert, M.; Wenke, L.; Hvilsted, S.; Ramanujam, P. S. *Appl. Phys. B: Lasers Opt.* **2001**, *72*, 429.

(34) Bian, S. P.; Williams, J. M.; Kim, D. Y.; Li, L. A.; Balasubramanian, S.; Kumar, J.; Tripathy, S. *J. Appl. Phys.* **1999**, *86*, 4498.

(35) Jiang, X. L.; Kumar, J.; Kim, D. Y.; Shivshankar, V.; Tripathy, S. K. *Appl. Phys. Lett.* **1996**, *68*, 2618.

(36) Lagugne-Labarthet, F.; Bruneel, J. L.; Buffeteau, T.; Sourisseau, C. *J. Phys. Chem. B* **2004**, *108*, 6949.

(37) Lagugne-Labarthet, F.; Bruneel, J. L.; Buffeteau, T.; Sourisseau, C.; Huber, M. R.; Zilker, S. J.; Bieringer, T. *Phys. Chem. Chem. Phys.* **2000**, *2*, 5154.

(38) Lagugne-Labarthet, F.; Bruneel, J. L.; Rodriguez, V.; Sourisseau, C. *J. Phys. Chem. B* **2004**, *108*, 1267.

(39) Ichimura, K.; Oh, S.-K.; Nakagawa, M. *Science* **2000**, *288*, 1624.

(40) Geue, T.; Henneberg, O.; Grenzer, J.; Pietsch, U.; Natansohn, A.; Rochon, P.; Finkelstein, K. *Colloids Surf., A* **2002**, *198-200*, 31.

(41) Pietsch, U.; Rochon, P.; Natansohn, A. *Adv. Mater.* **2000**, *12*, 1129.

Chapter 7
Conclusions and Perspectives

7.1. Conclusions and Contributions to Original Knowledge

This dissertation describes careful studies performed on azo-polymer materials, with the intent to understand the fundamental nature of the driving force that gives rise to surface patterning in these systems. In order to explain this phenomenon, a number of fundamental questions were first answered. A recurring theme in the research is the use of temperature as a probe of dynamics in materials. Temperature variation allowed the relative contribution of different dynamical motions to be considered. A necessary prerequisite for such a thermal analysis, however, is knowledge of the photo-induced heating phenomena that may accompany laser-based patterning. The modeling presented in this dissertation establishes that for a wide variety of experimental conditions, photo-heating effects can be neglected. The modeling formalism is simple, robust, and quite general, allowing it to be applied to a wide variety of organic materials and irradiation geometries.

Having delineated the regimes where photo-heating can be neglected, fundamental studies of mobility confinement in thin films were undertaken. Using thermal treatment to activate material motion, the size-scale of mass transport in the azo system was studied. It was found that while molecular-scale motions are not appreciably affected by confinement in the range 20–150 nm, the large-scale motions of polymer chains, involved in surface patterning, are greatly affected. In particular, mass transport becomes arrested in extremely thin films. Quantitative deviations of the apparent glass-transition temperature were recorded. This establishes a size-scale for the phenomenon, indicating that mass transport requires the coordinated motion of polymer chains over 40–100 nm, and not merely surface diffusion of individual polymer chains. The reported methodology for measuring thin film dynamics, and quantifying the glass-transition temperature, is quite general, and could be applied to other organic systems. For instance, any polymeric material could have a surface relief grating embossed into it, with the thermal erasure temperature of this surface structure being used to quantify dynamics.

Neutron reflectometry measurements were used to unambiguously identify photomechanical effects in azobenzene systems. This work has, for the first time, identified the photo-contraction events that lead to densification of azo materials. Furthermore, this work shows that azo materials exhibit two competing photomechanical effects: one that drives towards material expansion, and another that leads to contraction. Temperature was again exploited to probe the competing dynamics, and it was shown that there exists a smooth crossover from one behavior to the other. The process appears to be a general feature of azobenzene photochemistry, and helps explain many literature results. The described sample cell and experimental methodology are obviously applicable to other photo-active organic systems. Thus this work serves as a starting point for further studies of photo-dynamics in organic systems.

The newly discovered photomechanical phenomenon was used to explain the surface mass patterning effects seen in the azobenzene materials. The scaling and phase of surface patterning was found to exactly match the observed photomechanical trend. This thus represents a conclusive description of the curious surface mass transport that was discovered over 10 years ago, and which remained unexplained until now. This new explanation resolves a number of controversies and contradictory results that had appeared in the literature.

In addition to finally resolving numerous controversies in the azobenzene literature, it should be noted that the experimental techniques described here are not only applicable to the azobenzene system. The measurement techniques could be applied to a wide variety of polymeric or organic systems. Thus this dissertation contributes the fundamental study of dynamics in organic systems. In particular, it emphasizes techniques to use temperature as a probe, either theoretically or experimentally, to study novel systems.

7.2. Future Research Directions

This thesis has argued that the fundamental origin of the surface patterning is a photomechanical phenomenon. This theory produces a number of predictions that could be tested to further validate it. For instance, the assumption that all azo materials exhibit a crossover from photo-expansion effects to photo-contraction effects could be verified by cooling liquid crystalline systems, and observing the phase of their photomechanical

response and/or patterning. Also, it would be worthwhile to study the full range of polarization combinations used to form Surface Relief Gratings, as a function of temperature. It may be found that some polarization combinations become more efficient at higher temperature, whereas others see decreased efficiency. This data would allow one to determine the relative contribution from the photo-expansion and photo-contraction phenomena in driving surface patterning. In particular, it may provide evidence that the polarization dependence is, for instance, primarily related to the photo-contraction effect. This data would allow for rational design of micro-lithographic patterning of azo materials, by selecting the incident polarization and inscription temperature to suit a particular need. It may also allow for novel types of surface patterning. For instance, the doubling of grating period observed in the formation of some SRGs can now be attributed to an overlap of an out-of-phase (photo-expansion) and in-phase (photo-contraction) grating. Rational design could in principle allow one to create surface patterns below the usual diffraction limit, by exploiting the two competing mechanisms that have a tightly controlled phase relationship. This work has also demonstrated that the patterning phenomenon is sensitive to film thickness and the nature of the underlying substrate. Thus an azo film cast on top of a patterned substrate would exhibit spatially varying patterning efficiency. In addition to being useful for probing questions of dynamics and confinement in polymer systems, such an experimental geometry could also be useful for new modes of micro-lithography. In essence, careful registry between a sub-surface micro-fabricated structure, and an incident light field, could be used to create novel nano-structures.

The presented argument with regard to photomechanical patterning suggested that an anisotropy in the surface tension might be playing a role. To further investigate this supposition, it would be instructive to perform azo photo-patterning while the material is immersed in different liquids. By controlling the interfacial tension, the role of this parameter in the mass transport phenomenon could be fully elucidated. The entire mass transport phenomenon can now also be fully modeled and simulated. It is now apparent that the model can neglect photo-heating effects, but must absolutely model the azo material as a compressible fluid. In fact the model must include both expansion and contraction effects, based upon laser irradiation and temperature, and simulate the

resultant internal stress field. A successful model may also need to include the effect of an anisotropic surface tension. Combined, these parameters would be expected to reproduce the observed surface mass patterning.

Now that it is more fully characterized, the azobenzene photomechanical effect could be studied from an applied standpoint. The effect could be exploited in a photo-actuation device, such as a microfluidic chip. Such a device would have the advantages of fast and remote activation (being photo-driven) and could exploit either the reversible or the irreversible component of the photomechanical response, depending on device requirements. In such an investigation, it would be critical to accurately measure the long-term reversibility, reproducibility, and stability of the photomechanical response. It is currently known that the photo-expanded and photo-contracted states can be reversed with appropriate treatment, but it is not known what limits exist to the long-term cycling between states. For instance, it may be that cycling will lead to the formation of azo crystals that are difficult to disassemble.

Now that the azobenzene photomechanical effect and associated patterning phenomenon has been carefully characterized, it can be exploited in a variety of ways. It opens up the possibility for both fundamental studies of polymer dynamics, and applied device fabrications, where light is converted into useful mechanical work at small size-scales, or for reversible surface patterning.